Stent-Graft Behaviour During Complex Endografting Procedures



Jakub Kwiecinski
Department of Engineering Science
St. Anne's College

Supervisor: Prof. Zhong You

A thesis submitted for the degree of
Doctor of Philosophy

Michaelmas Term 2018

Stent-Graft Behaviour During Complex Endografting Procedures

Jakub Kwiecinski

St. Anne's College
University of Oxford

A thesis submitted for the degree of
Doctor of Philosophy

Michaelmas Term 2018

Abstract

Treatment of ascending aorta and aortic arch aneurysms represents one of the most technically challenging subsets of minimally invasive endovascular repair. The complex biomechanics and morphology of the dynamic proximal aorta pose significant challenges to even the most experienced clinical teams. To manage high-risk patients, surgeons have augmented traditional endografting techniques. The use of off-the-shelf devices deployed in a parallel configuration, known as chimney thoracic endovascular aortic repair, has been described to treat patients in both emergent and elective settings. Despite a growing level of experience with these procedures, device related peri- and post-operative complications persist. This thesis is concerned with elucidating the structural device-device and device-artery interactions arising during parallel endografting, to better understand the appropriate management of aortic disease.

To investigate stent-graft mechanics, two categories of sophisticated analysis tools have been developed. In the first, a computational framework based on the finite element method has been established for predicting device behaviour in a virtual environment. The simulation techniques have been elaborated to a cardiac modelling platform, enabling numerical analysis of stent-graft behaviour in a realistic manner. In the second, experimental methods have been employed to physically characterise parallel endografting in both a benchtop and an *in vitro* model of the aortic vasculature. Using these tools, the behaviour of stent-grafts has been quantified using metrics analogous to clinically reported complications, namely endoleak and graft lumen compression.

Structural interactions during parallel endografting are shown here to be significantly affected by device design and configuration. It has been demonstrated that increased aortic wall loading, likelihood of endoleak, and excessive device deformations are dominated by the radial stiffness of endografts. Furthermore, these phenomena are both spatially and temporally dependent. Indeed, careful selection of both endograft combination and configuration is necessary to improve long-term treatment outcomes associated with the chimney technique.

Acknowledgements

Professor Zhong You, for his supervision and support

Drs. R. Uberoi and M. Hadi of the John Radcliffe Hospital, for their clinical expertise and enthusiasm for this work

Professor Christopher Cheng of Stanford University, for his insightful discussions and thoughtful comments

Oxford Endovascular Ltd., for the unrestricted research scholarship

St. Anne's College, for the conference funding and travel grants

Colleagues in Jenkin 11, for making time spent in the lab so memorable

Contents

Abstract i

Acknowledgements ii

List of Figures vii

List of Tables x

1 Introduction 1
- 1.1 Thoracic Aortic Aneurysms . . . 1
- 1.2 Surgical Treatment of TAAs . . . 3
  - 1.2.1 Open Surgical Repair . . . 4
  - 1.2.2 Thoracic Endovascular Aortic Repair (TEVAR) . . . 5
  - 1.2.3 Emerging Technologies and Surgical Techniques . . . 7
  - 1.2.4 Chimney Thoracic Endovascular Aortic Repair (ch-TEVAR) . . . 9
- 1.3 Aim of Doctoral Research . . . 9
- 1.4 Organization of the Thesis . . . 11

2 Stent-Graft Mechanics 13
- 2.1 What is a Stent-Graft? . . . 13
  - 2.1.1 Functional Requirements of Stent-Grafts . . . 15
  - 2.1.2 Commercially Available Stent-Graft Systems . . . 16
  - 2.1.3 Clinical Performance of TEVAR Devices . . . 17
  - 2.1.4 Limitations of Current Stent-Graft Systems . . . 17
  - 2.1.5 Next Generation Stent-Graft Design . . . 22
- 2.2 *In Vitro* Evaluation of Stent-Grafts . . . 23
  - 2.2.1 Delivery, Deployment, and Positioning . . . 24
  - 2.2.2 Fixation, Stent-Graft Migration, and Endoleak . . . 27
  - 2.2.3 Material Durability . . . 32
- 2.3 *In Silico* Evaluation of Stent-Grafts . . . 35
  - 2.3.1 Delivery, Deployment, and Positioning . . . 35
  - 2.3.2 Fixation, Stent-Graft Migration, and Endoleak . . . 37
  - 2.3.3 Material Durability . . . 40
- 2.4 Summary and Thesis Objectives . . . 41

3 A Computational Framework for Stent-Graft Modelling 43

3.1 Material Behaviour . . . 43
3.1.1 Stent Devices: Nitinol . . . 44
3.1.1.1 Numerical implementation . . . 46
3.1.1.2 Uniaxial tension testing of nitinol . . . 49
3.1.1.3 UMAT Calibration . . . 51
3.1.1.4 Other stent materials . . . 55
3.1.2 Graft Material: PET . . . 56
3.1.2.1 Numerical implementation . . . 56
3.1.3 Arterial Material: Ascending Thoracic Aorta . . . 59
3.1.3.1 Numerical implementation . . . 59
3.2 Stent-Graft Performance . . . 66
3.2.1 Stent Crimping . . . 66
3.2.1.1 Materials and methods . . . 67
3.2.1.2 Results and discussion . . . 70
3.2.2 Stent-Graft Bending . . . 72
3.2.2.1 Materials and methods . . . 73
3.2.2.2 Results and discussion . . . 74
3.2.3 Stent Deployment into an Artery . . . 77
3.2.3.1 Materials and methods . . . 77
3.2.3.2 Results and discussion . . . 79
3.3 Parallel Stent-Graft Deployment . . . 81
3.3.1 Clinical Motivation . . . 81
3.3.2 Materials and Methods . . . 82
3.3.3 Results and Discussion . . . 85
3.4 Summary . . . 89

4 Parallel Stent-Graft Behaviour When Subjected to Uniform Radial Load 90
4.1 Introduction . . . 90
4.2 Materials and Methods . . . 92
4.2.1 Endografts . . . 92
4.2.2 Device Characterisation . . . 93
4.2.3 Radial Loading During ch-TEVAR . . . 95
4.2.4 Mechanical Deformations of Parallel Endografts . . . 96
4.2.5 “Ideal” Aortic Diameter . . . 97
4.2.6 Influence of Post-Dilation and Repeatability . . . 100
4.3 Results . . . 100
4.3.1 Device Characterisation . . . 100
4.3.2 Radial Loading Profiles of ch-TEVAR . . . 103
4.3.3 Deformation Behaviour of Parallel Endografts . . . 107
4.3.4 Influence of Post-Dilation and Repeatability . . . 111
4.4 Discussion . . . 111
4.4.1 Device Characterisation . . . 111
4.4.2 Benchtop ch-TEVAR . . . 113
4.4.3 Chronic Outward Force During ch-TEVAR . . . 115
4.4.4 Mechanical Deformations During ch-TEVAR . . . 116
4.4.5 Limitations . . . 117

4.5 Supplement: Stent Ring Design & FEA Validation . . . 118
4.5.1 Stent Ring Design . . . 118
4.5.2 FEA Validation . . . 119
4.6 Summary . . . 123
4.7 Acknowledgements . . . 123

5 *In Vitro* Quantification of Stent-Graft Behaviour During ch-TEVAR 124
5.1 Introduction . . . 124
5.2 Methods . . . 126
5.2.1 *In Vitro* Thoracic Aortic Model . . . 126
5.2.2 Hemodynamic Circuit . . . 129
5.2.3 Image Acquisition: ECG-Gated CT . . . 130
5.2.4 *In Vitro* ch-TEVAR Procedures . . . 130
5.2.5 Evaluation of ch-TEVAR Gutters . . . 132
5.2.6 Evaluation of Device Interactions (Deformations) . . . 136
5.2.7 Statistical Analysis . . . 137
5.3 Results . . . 138
5.3.1 *In Vitro* Model Characterisation . . . 138
5.3.2 Gutter Phenomena During the Cardiac Cycle . . . 140
5.3.3 Endograft Compression During the Cardiac Cycle . . . 144
5.3.4 Repeatability . . . 149
5.4 Discussion . . . 150
5.5 Summary . . . 154
5.6 Acknowledgements . . . 155

6 Simulating Ascending Aorta Endografting in a Dynamic Heart Model156
6.1 Introduction . . . 156
6.2 Materials and Methods . . . 157
6.2.1 The Living Heart Human Model . . . 157
6.2.2 Chimney TEVAR in the LHHM . . . 164
6.2.3 Experimental Design . . . 167
6.3 Results . . . 168
6.3.1 Mechanical Behaviour of the LHHM . . . 168
6.3.2 Simulating ch-TEVAR in the LHHM . . . 171
6.4 Discussion . . . 177
6.5 Summary . . . 180
6.6 Acknowledgments . . . 181

7 Conclusions and Future Work 182
7.1 Conclusions . . . 183
7.1.1 A Computational Framework for Stent-Graft Modelling . . . 183
7.1.2 Radial Loading of Parallel Endografts . . . 184
7.1.3 *In Vitro* Evaluation of ch-TEVAR . . . 185
7.1.4 Realistic Simulation of Ascending Aortic Endografting . . . 186
7.2 Future Work . . . 186
7.2.1 Enhancing the Computational Framework . . . 186
7.2.2 Hemodynamics and Fluid-Structure Interactions . . . 187

7.2.3 Validation with Clinical Data 187

A Mesh Convergence **188**

References **190**

List of Figures

1.1 Structure and composition of the arterial wall . . . 2
1.2 Normal anatomy and thoracic aortic aneurysm (TAA) . . . 3
1.3 Open surgical repair of thoracic aortic aneurysm . . . 5
1.4 Thoracic Endovascular Aortic Repair (TEVAR) . . . 6
1.5 Types of thoracic aortic aneurysms . . . 7
1.6 Emerging technology and techniques . . . 8
1.7 Stages of chimney thoracic endovascular aortic repair . . . 10

2.1 Typical thoracic aortic stent-graft . . . 14
2.2 Branched stent-graft technologies . . . 23
2.3 Thoracic aortic stent-graft conformability . . . 26
2.4 Apparatus for TAA stent-graft dislodgement testing . . . 28
2.5 Experimental setup for measuring Type I endoleak . . . 30
2.6 Flow phantom for thoracic aortic stent-graft assessment . . . 31
2.7 In vitro chimney endografting experiments . . . 32
2.8 Mechanical failure of an endograft following ch-TEVAR . . . 32
2.9 Virtual deployment of a bifurcated stent-graft . . . 36
2.10 Hemodynamics of endovascular aortic arch repair . . . 39

3.1 Structural analysis domain of TEVAR . . . 44
3.2 Nitinol superelastic-plastic material behaviour . . . 45
3.3 Uniaxial tension testing of nitinol . . . 50
3.4 Single element unit cube for nitinol calibration . . . 52
3.5 Nitinol material model calibration . . . 53
3.6 Robustness of nitinol material model . . . 54
3.7 Comparison of nitinol material models . . . 55
3.8 PET graft material behaviour . . . 57
3.9 Schematic of simulated arterial segments . . . 61
3.10 Simulated uniaxial tensile testing of thoracic aortic tissue . . . 62
3.11 Stress-stretch behaviour of ascending thoracic aortic tissue . . . 63
3.12 Distensibility and compliance of aortic tissue . . . 65
3.13 Z-stent geometry definition and implementation in Abaqus . . . 68
3.14 Z-stent crimping via finite element analysis . . . 69
3.15 Computed radial outward force of Z-stent devices . . . 71
3.16 Global-local stress analysis of a Z-stent . . . 72
3.17 Local stress-strain response at a Z-stent apex . . . 72

3.18 Stent-graft bending boundary conditions . . . 74
3.19 Simulated stent-graft behaviour during bending . . . 75
3.20 Stent-graft lumen reduction during bending . . . 75
3.21 Computed torque required for stent-graft bending . . . 76
3.22 Virtual stent deployment into an artery . . . 78
3.23 Maximum arterial and device von Mises stress post stent deployment . . . 79
3.24 Influence of stent design and oversizing on arterial stresses . . . 80
3.25 Representative illustration of parallel stent-graft deployment . . . 82
3.26 Computational analysis of parallel stent-graft deployment . . . 84
3.27 Cross-sectional analysis of parallel stent configurations . . . 86

4.1 Endografts investigated using benchtop ch-TEVAR . . . 92
4.2 MSI RX650 radial loading test system . . . 94
4.3 Schematic of single chimney TEVAR subjected to radial load . . . 96
4.4 Geometric approximation of "ideal" aortic diameter for ch-TEVAR . . . 99
4.5 Main endograft characterisation: radial deformation-load profiles . . . 101
4.6 Chimney graft characterisation: radial deformation-load profiles . . . 102
4.7 Radial deformation-load profiles of single chimney TEVAR . . . 104
4.8 Radial deformation-load profiles of double chimney TEVAR . . . 105
4.9 Deformations of single chimney parallel endografts . . . 108
4.10 Deformations of double chimney parallel endografts . . . 110
4.11 Influence of post-dilation and repeatability . . . 111
4.12 Medtronic Valiant stent ring radial deformation-load profiles . . . 119
4.13 Medtronic Valiant stent ring reconstruction . . . 120
4.14 Medtronic Valiant stent ring virtual crimping experiment . . . 121
4.15 Finite element analysis validation . . . 122

5.1 *In vitro* thoracic aortic model geometry . . . 127
5.2 Hemodynamic circuit . . . 130
5.3 *In vitro* ch-TEVAR setup . . . 131
5.4 Representative CT reconstructions of *in vitro* ch-TEVAR . . . 133
5.5 Gutter quantification . . . 134
5.6 Gutter quantification workflow . . . 135
5.7 Surface deviation workflow . . . 136
5.8 Determination of endograft compression . . . 137
5.9 Thoracic aorta model wall thickness analysis . . . 139
5.10 Aortic pressure profile generated using a pulse duplicator . . . 140
5.11 *In vitro* double chimney TEVAR gutter volumes . . . 141
5.12 Geometrical ch-TEVAR gutter analysis . . . 143
5.13 Co-registration of diastolic-systolic gutters . . . 143
5.14 D-ratios of Ankura-BeGraft/Viabahn ch-TEVAR combinations . . . 145
5.15 Endograft lumen major and minor axes . . . 148
5.16 Pulse duplicator repeatability . . . 149
5.17 D-Ratio measurement repeatability . . . 150

6.1 The Living Heart Human Model (LHHM) . . . 158
6.2 Generalized active stress of cardiac tissue . . . 161
6.3 Stress-stretch behaviour of LHHM ascending aortic tissue . . . 162

6.4 Aortic arch pressure profile in the LHHM 164
6.5 Mechanical response of the LHHM 169
6.6 Pulsatile behaviour of the LHHM ascending aorta 170
6.7 Single chimney TEVAR in the LHHM 171
6.8 Mechanical deformations of endografts during the cardiac cycle 172
6.9 Contact normal forces acting on the aortic wall 174
6.10 Aortic wall maximum principal stress during ch-TEVAR 176

A.1 Stent mesh convergence study 188
A.2 Artery mesh convergence study 189

List of Tables

2.1 Commercially available thoracic aortic stent-grafts 18
2.2 Peripheral devices commonly used as chimney grafts 19
2.3 Clinical performance of select TEVAR devices 20
2.4 Categorization of endoleak 21

3.1 Parameters describing the superelastic behaviour of nitinol 46
3.2 Nitinol tube properties derived from uniaxial tensile tests. 51
3.3 Calibrated nitinol material model parameters 53
3.4 Material properties of 316L stainless steel 56
3.5 PET graft material properties 58
3.6 Summary of HGO material model parameters 60
3.7 Ascending thoracic aortic tissue HGO material parameters 62
3.8 Stent geometric and computational features 68
3.9 Maximum von Mises stress of Z-stents upon radial crimping 70
3.10 Comparison of simulated ch-TEVAR gutter areas 85
3.11 Comparison of simulated chimney graft compression 87
3.12 Comparison of simulated main graft infolding 88

4.1 Endograft specifications and characteristics 93
4.2 Chimney TEVAR combinations and the "ideal" aortic diameter 99
4.3 Endograft COF, RRF, and RS characterisation values 103
4.4 Chimney TEVAR chronic outward force 106
4.5 Single chimney TEVAR deformation measures 109
4.6 Double chimney TEVAR deformation measures 109
4.7 Nitinol material model for Valiant stent ring FEA validation 122

5.1 *In vitro* thoracic aortic model characterisation 138
5.2 *In vitro* thoracic aortic model geometric indices 140
5.3 Gutter volumes during ch-TEVAR 142
5.4 Geometrical variation in gutter volumes 144
5.5 Main and chimney endograft D-ratios 146

6.1 Constitutive parameters of the passive cardiac material response 159
6.2 Constitutive parameters of the active cardiac material response 161
6.3 Stent geometric and computational features 165
6.4 Material properties of main and chimney endografts 166
6.5 Experimental design for studying chTEVAR in the LHHM 168

6.6 Range of peak contact normal force on the aortic wall 173
6.7 Peak maximum principal stress at the ascending aortic lumen surface . . . 175

To my family for getting me here, and
to Bernadette for getting me through.

Chapter 1

Introduction

Within the human body there exists a complex vascular network transporting blood to organs and tissue. Conditions affecting this network - aptly known as (cardio)vascular disease - have fatal consequences and are the leading cause of death worldwide [1, 2]. One significant manifestation of cardiovascular disease is the occurrence of thoracic aortic aneurysms (TAAs), a pathology disrupting the normal arterial wall architecture.

1.1 Thoracic Aortic Aneurysms

Healthy arterial walls consist of three distinct layers: the *tunica intima*, the *tunica media*, and the *tunica adventitia*, as illustrated in Figure 1.1. The tunica intima is the thinnest, innermost structure built-up of a single layer of endothelial cells, which are in direct contact with blood flow. The tunica media comprises smooth muscle cells surrounded by a matrix of elastin and collagen fibres, providing mechanical strength to the intima. The outermost layer, the tunica adventitia, forms a protective boundary around the vessel and contains connective tissue with elastin and collagen fibres [3].

In general, the behaviour and integrity of an artery is determined by the biomechanical properties of its constituents, primarily elastin and collagen fibres. As its name suggests, elastin is a distensible fibre which is load-bearing at low pressures and responsible for the elastic recoil of arteries. In contrast, collagen is 1000 times stiffer and is load-bearing at high pressures, acting to prevent over-dilation and rupture of vessels. Indeed, it is the elastin-to-collagen ratio which is the principal determinant of vessel wall mechanics. As such, the degradation of both elastin and collagen contributes to the weakening of the arterial wall and the eventual formation of permanent localized dilations [5]. These arterial dilations, which can take on numerous shapes and sizes, are known as aneurysms.

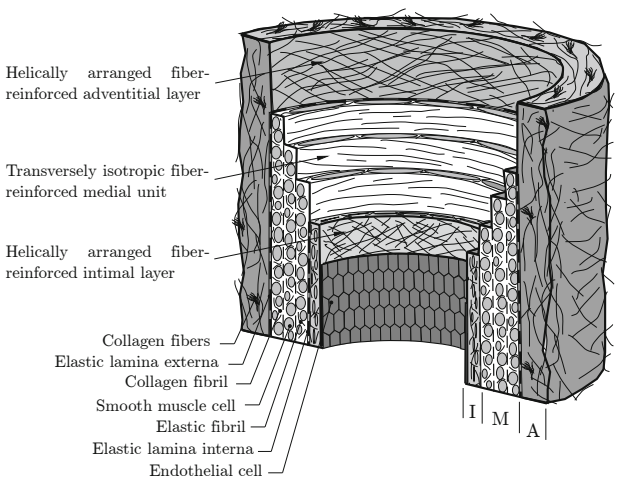


Figure 1.1: Structure and composition of a healthy arterial wall cross-section. Illustrated are the three arterial layers (intima, media, and adventitia) and collagen fibre orientations within the wall. Image adapted from [4].

Clinically, an aneurysm is diagnosed as an increase in arterial diameter which is at least 50% greater than the normal expected size [6]. Within the arterial system, aneurysms commonly present along the aorta (the main artery of the body, carrying oxygenated blood from the heart) and are known as aortic aneurysms. These aneurysms can be further categorized by location, and include abdominal aortic aneurysms (AAAs), thoracoabdominal aortic aneurysms (TAAAs), and thoracic aortic aneurysms (TAAs) [7]. Diseases of the aorta, such as the aneurysm illustrated in Figure 1.2, pose a significant challenge to cardiovascular surgeons due to the complexity of the condition, tortuous vascular anatomy, and the formidable operative procedures required in treating them. This is particularly true of TAAs, and as such, deserve special attention.

The natural history of thoracic aortic aneurysm is one of progressive weakening of the aortic wall and simultaneous expansion, typically leading to rupture [9]. From a biomechanical perspective, aneurysm rupture occurs when aortic wall stresses exceed wall strength. Although the direct cause of thoracic aortic aneurysm formation is considered to be multifactorial, the pathogenesis of arterial vessel change is primarily the result of age related medial layer degeneration, as previously mentioned. Elastin fragmentation and collagen induced fibrosis reduces the strength and integrity of the aorta resulting in a weakened arterial wall [10]. In addition to these histological changes, other factors contributing to TAA formation include genetic predisposition, connective tissue disorder, as well as environmental exposure/lifestyle [11]. Although the underlying pathological

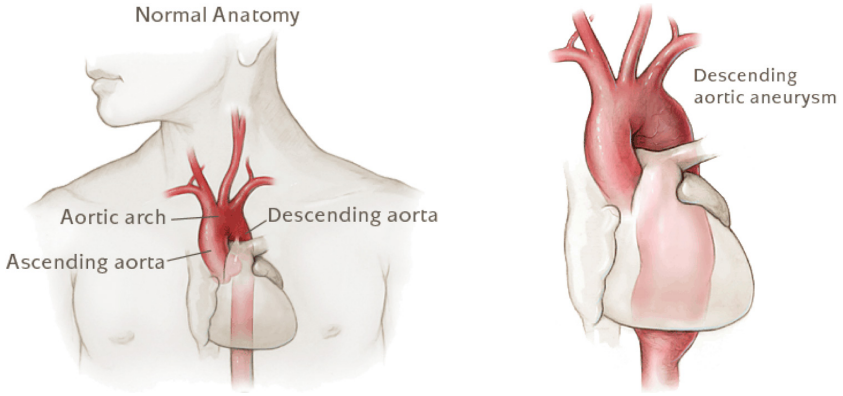


Figure 1.2: The thoracic aorta. (Left) Healthy aortic anatomy depicting ascending, arch, and descending thoracic aortic segments. (Right) diseased dilation of the descending segment, commonly known as thoracic aortic aneurysm (TAA). Image adapted from [8].

processes may differ among individuals, the ultimate aneurysmal disease process is the same for all: progressive aortic dilation and eventual rupture. Unfortunately, it is difficult to identify signs and symptoms that warn of the presence of aortic disease; most often, TAAs are asymptomatic and are diagnosed by chance [12].

Thoracic aortic aneurysms generally occur in the elderly and have thus been increasing in incidence as the population ages and diagnostic capabilities improve. With a reported frequency of 10.4 per 100 000 persons per year, it is evident that TAAs are a prevalent vascular disease [13]. Likewise, with an associated mortality rate of 94% [14, 15], TAA rupture is almost certainly a fatal event. The 5-year survival rate of unoperated TAA patients is only 13%, whereas historical data suggest 70% - 79% of those who undergo elective surgical intervention are alive at 5 years [9, 16–18]. Thus, the risk and outcome of aneurysm rupture requires consideration for surgical repair. Unfortunately, traditional operative techniques used to treat aortic aneurysms are associated with substantial long-term morbidity and mortality [19], necessitating the need for improvement.

1.2 Surgical Treatment of TAAs

The purpose for treating TAAs is two-fold: to prevent rupture, and in the case of patients who are in fact symptomatic, to alleviate symptoms resulting from compression of the surrounding anatomy [20]. Surgical treatment of aortic disease is warranted when the risk of aneurysm rupture outweighs the risk of operation. As such, the indication for

elective surgical repair depends substantially on the risks of the procedure as well as the long-term treatment outcomes [21].

Aneurysm diameter, growth, and location are the primary considerations in treatment planning. In asymptomatic patients, the decision to consider surgical repair is based principally on aneurysm diameter. To prevent rupture, elective operation is recommended when the aneurysm diameter is greater than 60mm or when the rate of dilation exceeds 3mm per year. In patients with connective tissue disorders, the threshold for operation is lower for both absolute size and growth rate. Symptomatic patients, however, are at increased risk of rupture and thus require immediate evaluation and urgent aneurysm repair, regardless of aneurysm size [9, 22].

Currently, there are two surgical options available for the treatment of TAAs: open surgical repair, and thoracic endovascular aortic repair (TEVAR). These techniques are detailed below.

1.2.1 Open Surgical Repair

Open surgical repair with prosthetic vascular graft interposition is considered the traditional treatment for patients with TAAs [20]. This approach was introduced in the 1950s after Swan, Lam, and DeBakey successfully reported segmental aortic resection and graft placement [23–25]. This highly invasive procedure entails general anesthesia, thoracotomy, left lung collapse, and aortic cross-clamping to fully access the diseased portion of the aorta (and thus referred to as "open" repair) [26]. Essentially, the aneurysmal portion of the aorta is exposed, removed, and replaced with a synthetic substitute. The primary stages of this procedure are depicted in Figure 1.3.

Although advances in diagnostic capabilities, surgical techniques, and perioperative care have resulted in improved outcomes, open surgical repair of TAAs is still associated with significant long-term morbidity and mortality, as previously mentioned. Severe postoperative complications such as paraplegia and stroke are common, and intensive care unit and hospital admission stays are considerable. Five- and 10-year survival estimates based on contemporary data are only 60% and 38%, respectively [28].[1] Additionally, the time taken for recovery to the preoperative state of well-being is often lengthy [29].

[1]The discrepancy in 5-year survival estimates reported in this Chapter is attributed to differences between the referenced historical and contemporary datasets.

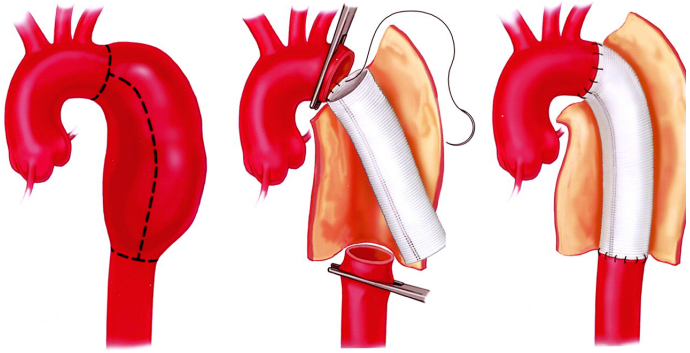


Figure 1.3: Stages of open surgical repair for thoracic aortic aneurysm. *Left to right*: Identification of diseased thoracic aorta, resection of aneurysm, and complete replacement of aortic segment with a synthetic graft. Image adapted from [27].

Due to its highly invasive nature, open surgical repair requires considerable physiological reserve. As a result, patients who are elderly and/or present with multiple comorbidities (e.g. compromised cardiac, pulmonary, or renal status) are often not eligible for treatment [26, 30]. For this reason, as well as the postoperative complications and unsatisfactory long-term outcomes detailed above, a less invasive treatment for aortic disease is required.

1.2.2 Thoracic Endovascular Aortic Repair (TEVAR)

In an effort to improve outcomes of surgically treating aortic disease, the concept of deploying endovascular prostheses to exclude an aneurysm from systemic circulation has gained acceptance. Reported by Parodi et al. in 1991 for the treatment of AAAs [31], treatment of TAAs using endovascular prostheses was described by Dake and colleagues in 1994 [32]. This minimally invasive surgical technique, known as thoracic endovascular aortic repair (TEVAR), entails the transluminal placement of one or more stent-graft devices across the longitudinal extent of the aneurysmal aorta. The primary stages of this procedure are illustrated in Figure 1.4. Essentially, a stent-graft is delivered through a remote access vessel (typically the femoral artery via a small incision in the groin) and is subsequently deployed along the aortic curvature, bridging the aneurysmal sac by forming a hemostatic seal between the stent-graft and vessel wall.[2] As a result, the aneurysm

[2]The primary mode of stent-graft fixation is through device oversizing, forming an interference fit with the arterial wall.

is excluded from high-pressure aortic blood flow allowing for sac thrombosis, possible remodelling of the aortic wall, and dramatically reducing the likelihood of rupture [9].

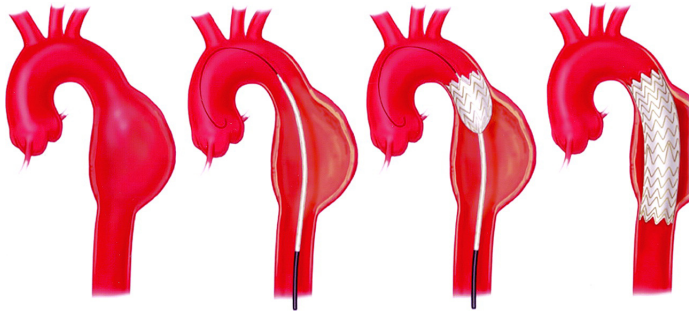


Figure 1.4: Stages of TEVAR. *Left to right*: Descending thoracic aortic aneurysm, minimally invasive device delivery, initiation of stent-graft deployment, and complete device deployment excluding the diseased aortic segment from systemic circulation. Image adapted from [27].

Originally devised for high-risk patients who were not eligible for open repair, the ongoing refinement of TEVAR as an alternative has greatly expanded treatment options for patients with TAAs. This minimally invasive approach eliminates the need for thoracotomy, aortic cross-clamping, left-lung collapse, and their associated physiological perturbations. Consequently, the physical insult of the surgery is greatly reduced [21].

To evaluate outcomes of TAA treatment strategies, Cheng et al. [33] compared reported results of TEVAR with open surgery across 42 nonrandomized studies involving 5888 patients. In that meta-analysis, the 30-day mortality rate was found to be 7.9% versus 15.2%, the 1-year mortality rate was 19.4% versus 31.7%, and overall complications were 20.6% and 33.2%, (in TEVAR versus open surgical repair, respectively). A separate meta-analysis [34] comparing endovascular treatment with open surgery further confirmed the effectiveness of TEVAR, reporting incidence of stroke at 4.1% versus 10.2%, and paraplegia at 3.1% versus 5.5%. Additionally, a single-centre study [35] also provided long-term data, reporting survival rates of 94%, 90%, and 83%, at 1-, 5-, and 10-years after TEVAR, respectively. Such results have revealed minimally invasive TEVAR to be an effective alternative to open repair with beneficial outcomes.

Although favourable early- and mid-term results of TEVAR demonstrate its utility, peri- and post-operative complications persist. Long-term device durability, occurrence of so-called endoleak, and stent-graft migration are the critical issues which remain to be fully resolved; notably, these device-related complications are inherently absent

from open surgical repair [12]. Despite these concerns, stent-graft treatment is already the best option for a large number of patients with thoracic aortic diseases who are poor candidates for traditional surgery [36]. Indeed, it appears that minimally invasive surgery is rapidly becoming the treatment option of choice for those diagnosed with TAAs, particularly as refinements to current stent-graft systems are made.

1.2.3 Emerging Technologies and Surgical Techniques

In its primary form, TEVAR is limited to the treatment of aneurysms located along the descending aorta. The requirement of an adequate proximal "landing zone" to anchor the stent-graft generally precludes its applicability for use in complex TAA cases.[3] Specifically, aneurysms located along the ascending aorta and aortic arch (aTAAs), such as those illustrated in Figure 1.5, require careful consideration to ensure continuous perfusion of the supra-aortic branch vessels.

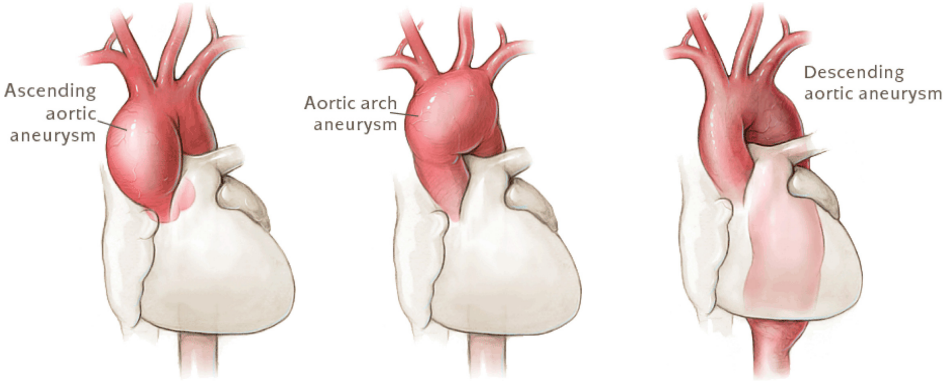


Figure 1.5: Types of thoracic aneurysms as classified by anatomical location. *Left to right*: Ascending, arch, and descending thoracic aortic aneurysm. Imaged adapted from [8].

Until recently, treatment of these aneurysms was limited to open surgical repair or challenging hybrid procedures combining both open surgery and endovascular techniques. Given the necessity to include aspects of open repair in these strategies, treatment of aTAAs is also associated with significant morbidity and mortality [37].

As TEVAR technologies continue to evolve and surgeon skill grows, the development of an entirely minimally invasive technique for the treatment of these complex aneurysms

[3] Arterial segments in which the proximal and distal sections of a stent-graft are deployed are commonly known as landing zones. Healthy landing zones are essential for TEVAR.

is being explored. Specifically, two new categories of endovascular devices, aimed specifically at branch vessel inclusion, have recently emerged: (1) so-called "fenestrated" stent-grafts, and (2) branched stent-grafts [38, 39]. In the former, a standard thoracic aortic stent-graft is modified to include fenestrations (holes) along its greater curvature through which secondary endografts are deployed after positioning in the supra-aortic vessels. Similarly, these devices can also feature customized "scallops" whereby select portions of the endograft remain uncovered (typically located at the proximal device edge) as to eliminate branch vessel coverage. In the latter category, new stent-graft designs have been proposed which include intra-lumenal channels for dedicated branch device deployment, or in a separate embodiment, the incorporation of so-called "sealing-cuffs" for branch device integration. These technologies are illustrated in Figure 1.6.

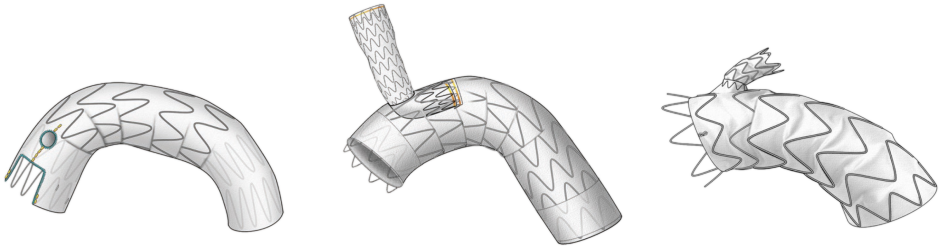


Figure 1.6: Emerging aTAA technology. *Left to right*: fenestrated thoracic stent-graft with proximal scallop (Cook Medical), dedicated branch device featuring an internal channel (W.L. Gore), branch device featuring integrated "sealing-cuff" (Medtronic). Image adapted from [40].

A recent systematic review of endovascular arch repair by Spanos and co-workers [41] described good early- and reasonable mid-term outcomes using these technologies and their associated surgical procedures. However, adverse events such as endoleak, stroke, spinal cord ischemia, and aortic wall damage (retrograde dissection) remain prevalent. Also of note is the lack of clinical data reporting on the mid- and long-term efficacy of branched devices [42].

Unfortunately, the wide-spread adoption of total endovascular repair for complex aTAAs is limited by two main factors. First, the few devices which are available for use are typically custom-made; procedures requiring multiple fenestrations/branches must be patient-specific so as to account for exact aortic anatomy. These devices are therefore costly and subject to long manufacturing times. Secondly, for branch devices which have been designed to offer an "off-the-shelf" solution (i.e. readily available at the time of repair), all current technologies are considered to be investigational. That this, they

have not gained the requisite regulatory approvals, and so are restricted to use in a select number of interventional centers [39]. As such, there is a clear need for a readily available, off-the-shelf solution to treat complex aortic disease.

1.2.4 Chimney Thoracic Endovascular Aortic Repair (ch-TEVAR)

To overcome these limitations, surgeons have proposed chimney thoracic endovascular aortic repair (ch-TEVAR). Originally reported by Greenberg [30] and Criado [43, 44] as a so-called "bail-out" procedure, this endovascular approach employs the use of standard off-the-shelf devices deployed in a "parallel" (or "nested") fashion. Specifically, chimney stent-grafts (CGs) are placed in the supra-aortic branch vessels, sized with sufficient length to extend proximally into the ascending aorta/arch, and run adjacent to the primary endograft. The intended result is a sufficient aortic seal zone excluding the diseased aorta whilst maintaining supra-aortic branch vessel perfusion. A representative illustration demonstrating the primary steps of ch-TEVAR is given in Figure 1.7.

Recent registries [46], reviews [47, 48], and single-center studies [49, 50] have described the technical feasibility of ch-TEVAR and reported on promising mid-term outcomes, demonstrating the utility of this approach in treating high-risk patients.

Critically, life-threatening complications such as endoleak and chimney graft occlusion, which are inherent to this technique, persist. Regarding endoleak in ch-TEVAR, this phenomena is associated with the formation of so-called "gutters": channels which form between the aortic wall and endografts, through which blood can continue to flow, compromising the aortic seal (see Figure 1.7F). Conversely, CG occlusion is thought to result from excessive lumenal compression stemming from adjacent deployment to the thoracic endograft; disruption of normal hemodynamics can lead to in-stent thrombosis. Indeed, these complications mandate a deeper understanding of how parallel endograft devices behave in the complex anatomy of the ascending aorta and aortic arch.

1.3 Aim of Doctoral Research

This research is motivated by the clinical need to better understand stent-graft technologies for complex endografting procedures. The primary aim is to elucidate stent-graft

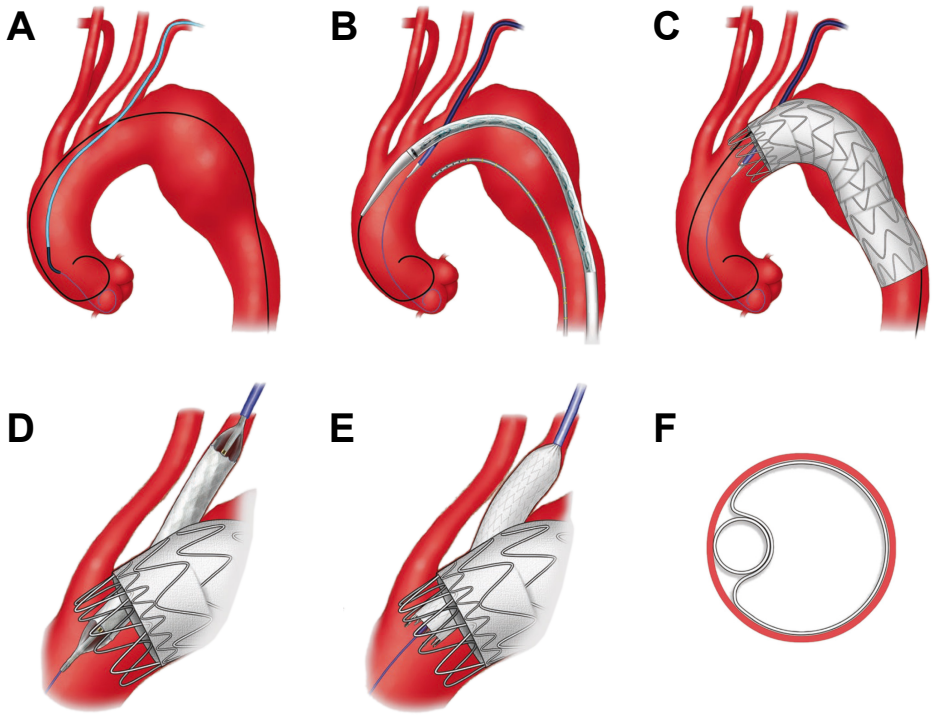


Figure 1.7: Procedural steps of representative chimney TEVAR. (A) Standard arterial access and guidewire advancement through the thoracic aorta and left subclavian artery. (B) Thoracic and chimney devices delivered to target positions. (C) Deployment of thoracic aortic stent-graft. (D-E) Deployment of chimney stent-graft: devices can be either balloon-expandable (*left*) or self-expandable (*right*) covered stents. (F) Resulting vessel lumen cross-section illustrating so-called gutters (i.e. gaps between endografts and aortic wall). Image adapted from [45].

behaviour when used to treat ascending aorta and aortic arch aneurysms via chimney thoracic endovascular aortic repair (ch-TEVAR).

As such, this thesis is concerned with developing two categories of sophisticated tools for investigating stent-graft mechanics: (1) computational methodologies for predicting device behaviour in a virtual environment, and (2) experimental techniques for assessing device-artery and device-device interactions. Using such tools, the structure-function relationship of stent-grafts and their suitability for use in procedures to treat ascending aorta and aortic arch aneurysms can be explored. This work will contribute to the overall effort of establishing an effective treatment strategy for managing complex vascular disease.

1.4 Organization of the Thesis

Given the aim, this thesis is organized as followed:

- **Chapter 2:** *Stent-Graft Mechanics*

  An in-depth discussion of stent-graft mechanics is provided. Attention is drawn to the specific requirements of stent-grafts, as well as limitations facing current device designs. The reported *in vitro* and *in silico* techniques used to quantify stent-graft functionality are discussed, providing the necessary foundation on which this research is based. As such, this Chapter formally introduces the reader to stent-grafts, identifies gaps in the current knowledge, and establishes research objectives for the thesis.

- **Chapter 3:** *A Computational Framework for Stent-Graft Modelling*

  In this Chapter, numerical strategies to investigate stent-graft behaviour are developed. First, the phenomenological material models which govern the underlying behaviour of each component in the "stent-graft-artery" domain are described. Following this, a series of finite element analysis (FEA) case studies examining various aspects of stent-graft performance are established. Finally, a novel simulation approach to assess the behaviour of stent-grafts deployed in a parallel configuration, representative of chimney thoracic endovascular aortic repair (ch-TEVAR), is proposed and results presented.

- **Chapter 4:** *Parallel Stent-Graft Behaviour When Subjected to Radial Load*

  In this Chapter, experimental methodologies are detailed to study the *in vitro* deformation characteristics of stent-graft devices. Specifically, the behaviour of stent-grafts when deployed in a parallel configuration and subjected to uniform radial load is investigated. First, a conventional benchtop technique is used to characterise four commercially available endografts: two main thoracic aortic devices, and both self- and balloon-expandable covered chimney stents. The benchtop protocol is then extended to analyse the loading response and mechanical deformations of endografts during representative chimney thoracic endovascular aortic repair (ch-TEVAR). Results reporting clinically relevant evaluation metrics are presented to demonstrate the influence of stent design/configurations on anticipated *in vivo* performance. Finally, taking advantage of the available experimental setup, a baseline validation of the finite element analysis methods employed in the previous Chapter is included as a supplement to the primary study.

- **Chapter 5:** *In Vitro Quantification of Stent-Graft Behaviour During ch-TEVAR*

  In this Chapter, the previously described experimental techniques to investigate parallel stent-graft interactions are elaborated to a more clinically relevant case. Specifically, representative double chimney TEVAR procedures are performed in a physiological model of the thoracic aorta with retrospective electrocardiography-gated computed tomography used to evaluate endograft behaviour. First, the clinical context for this study is provided. Following this, the experimental setup and

procedural protocol are described. A rigorous analysis of the *in vitro* ch-TEVAR procedures is then presented, with particular attention given to the quantification of gutter dynamics and endograft deformations at critical time points during the cardiac cycle. Finally, a detailed discussion of the findings is provided, highlighting the influence of endograft design and configuration on device behaviour.

- **Chapter 6:** *Simulating Ascending Aorta Endografting in a Dynamic Heart Model*

  The objective of this Chapter is to report on *realistic* simulation strategies for the evaluation of TAA stent-graft designs and associated surgical procedures. The FEA methods used in Chapter 3 employ traditional analysis techniques, whereby devices and procedures are simulated in a quasi-static fashion neglecting cardiac-induced biomechanics. In this Chapter, a complete finite element representation of an adult male human heart and its surrounding vasculature is detailed. The dynamic response of the heart is governed by realistic electrical, structural, and fluid flow physics via a sequentially coupled electrical-mechanical analysis. Results investigating the use of such a model for evaluating multiple chimney thoracic endovascular aortic repair configurations are presented and discussed.

- **Chapter 7:** *Conclusions and Future Work*

  This concluding Chapter consolidates the main research findings and original contributions presented throughout the thesis. It also outlines prospective directions for future work in the field of stent-graft mechanics and treatment of complex aortic disease.

In this thesis, Chapters 3 - 6 have been presented in a manner such that they can be read independently of each other. Although introductory sections have been minimized, some repetition is inevitable given the clinical motivation on which this work is based (e.g. thoracic aortic aneurysm, description of ch-TEVAR, etc.).

Finally, it should be noted that the *in vitro* and *in silico* models presented throughout this work generally make use of healthy thoracic aortic anatomy. Given that a healthy aortic landing zone is a prerequisite for endovascular repair, and that complications during ch-TEVAR are most likely to be associated with device behaviour at the landing zone, use of such models were deemed to be appropriate.

Chapter 2

Stent-Graft Mechanics

In this Chapter, an in-depth discussion of stent-graft mechanics is presented. Attention is drawn to the specific requirements of stent-grafts, as well as limitations facing current device designs. The reported *in vitro* (experimental) and *in silico* (computational) techniques used to quantify stent-graft behaviour are detailed, providing the necessary foundation on which this research is based. As such, this Chapter serves as a literature review; it formally introduces the reader to stent-grafts, identifies gaps in the current knowledge, and establishes research objectives for the thesis.

2.1 What is a Stent-Graft?

A stent-graft is a tubular endovascular prosthesis designed to form an internal bypass between sections of the vascular system, protecting weakened arterial walls from rupture. These devices have two primary characteristics for use in minimally invasive surgery: (1) they can be packaged to small dimensions for atraumatic delivery, and (2) they can be deployed (implanted) within a vessel with a high degree of accuracy. Typically, endovascular prostheses used for the treatment of thoracic aortic aneurysms (TAAs) consist of a metallic wire frame (the stent), covered by a synthetic sheath (the graft), and are known as thoracic aortic stent-grafts [51]. A representative thoracic aortic stent-graft is shown in Figure 2.1. In general, stent-graft designs can be categorized according to their deployment mechanism, geometrical (stent) shape, and material selection.

Mechanism of deployment. In terms of device deployment, stents can be either balloon-expandable (BE) or self-expanding (SE). Balloon-expandable stents are those that are initially crimped down over a balloon catheter, subsequently delivered to an aneurysm, and then plastically deformed to a target diameter via balloon inflation. On the other



Figure 2.1: Typical stent-graft for minimally invasive repair of thoracic aortic aneurysms. (Left) Partially deployed device constrained within its delivery catheter. (Right) Device fully deployed. Note: the stent frame is sutured to the graft covering. Image adapted from [52].

hand, self-expanding stents are those manufactured from materials that can undergo large elastic deformations which are fully recoverable. Here, stents are typically made from shape memory alloys and can withstand strains in excess of 9%. As such, SE devices are well suited to packaging (i.e. diameter substantially reduced) within a so-called delivery catheter for use during minimally invasive surgery. When deployed, these stents expand to their pre-packaged shape as they recover their deformation [51].

Geometric design. Various stent-graft designs exist that can be best described by the geometry of their stent frames. In general, the latest generation of aortic stent-grafts can be categorized as those that employ either: (i) multiple "Z-stents" (as seen in Figure 2.1), (ii) multiple "ring-stents", (iii) a single helical coil, or (iv) a "Spiral-Z" design consisting of a single helical coil containing a zig-zag pattern. These stent frames are most commonly manufactured (formed) using medical-grade metallic wire. Additional details of stent-graft frame designs have been detailed elsewhere (for example, see [53]).

Peripheral stent-grafts, such as those used as part of chimney thoracic endovascular aortic repair (ch-TEVAR), are typically manufactured (laser cut) from a single piece of medical-grade tubing and can incorporate either a "closed-cell" or "open-cell" design. In the former, all internal inflection points of the structural members are connected (via so-called peak-to-peak connections). In the latter, only select internal inflection points of the structural members are connected (leading to periodic peak-to-peak, or peak-to-valley, connections or a combination thereof). Indeed, the chosen stent cell design

greatly influences its mechanical behaviour. For example, closed-cell designs can exhibit superior radial strength, whilst open-cell designs can exhibit superior flexibility [54].

Stent materials. Briefly, stent-graft materials are required to be biologically inert/biocompatible. They must also be radiopaque as to enable visualization during deployment. The material chosen for a specific stent also depends on the aforementioned deployment mechanism; BE stents must deform plastically during deployment, whereas SE stents must be able to recover considerable elastic deformation. For balloon-expanding stents, the most widely used materials satisfying these criteria are 316L stainless steel and cobalt chromium. For self-expanding stents, the most commonly used material is a nickel-titanium alloy, known as nitinol (NiTi) [51]. These materials have excellent biocompatibility and sufficient radiopacity. Additionally, nitinol has the ability to be detected via magnetic resonance imaging (MRI) without introducing unwanted artifacts [55]. Graft materials are required to be flexible and thin, such that the stent can be folded down to small dimensions for minimally invasive surgery. Additionally, strength and durability is required to withstand aortic blood flow and to avoid long-term material damage. The most common biocompatible synthetic materials used for grafts today include ePTFE (expanded polytetrafluoroethylene) and PET (polyethylene terephthalate, commonly known as Dacron) [56].

2.1.1 Functional Requirements of Stent-Grafts

The morphology and biomechanics of the thoracic aorta create specific demands on endovascular device design and performance. Given their close proximity to the heart, TAA stent-grafts are subjected to aggressive hemodynamic forces as well as cardiac and respiratory induced motions. Consequently, the potential for device migration, kinking, and structural failure (i.e. fatigue) must be appropriately accounted for. Lally and co-workers [51] have commented on the various functional/design requirements which should be considered in the development of stents. Those relevant to TAA stent-graft design, and so devices for use during ch-TEVAR, include:

1. *Adequate Radial Strength:* The stent-graft should provide adequate outward force to ensure sealing and fixation while not damaging the vessel wall.

2. *Good Flexibility:* The packaged stent-graft and delivery catheter must be sufficiently flexible such that it can be delivered to the deployment site. The deployed device must be able to conform to tortuous vessel geometry and should not straighten (or damage) the vessel.

3. *Low Stent Profile:* The packaged stent-graft and delivery catheter should have a low profile to accommodate arterial access and prevent excessive flow disturbances during delivery and once deployed.

4. *Good Trackability:* Trackability is a measure of the ease of a delivery catheter to follow a tortuous path to its ultimate destination. Stent-graft delivery should not induce injury to the vessel wall.

5. *Minimal Foreshortening:* The length of a stent-graft may shorten as the device expands radially, which may affect both the final position and deployed (implanted) length of the stent. The degree of device foreshortening should be minimized to enhance the positioning/deployment accuracy.

6. *Material:* The device should be radiopaque, biocompatible, corrosion-resistant, and have excellent fatigue properties; stent-grafts must withstand at least 380 million cyclic loading cycles (equivalent to 10 years of *in vivo*).

Meeting these (non-exhaustive) criteria has proven to be a difficult task throughout the evolution of stent-graft development. Clinicians, researchers, and medical device companies alike are still in pursuit of the optimal stent-graft design.

2.1.2 Commercially Available Stent-Graft Systems

The initial experience with minimally invasive endovascular repair of TAAs was gained by using home-made devices. Technology in this field has advanced at a brisk pace, and an increasing number of companies have developed and marketed endovascular prostheses. Currently, there are seven commercially available stent-grafts for the treatment of thoracic aortic disease. A list of these devices, a summary of their primary design characteristics, as well as their approved indications are presented in Table 2.1. Similarly, a list a peripheral stent-grafts, which are used as so-called “chimney grafts” during chimney TEVAR, are presented in Table 2.2 with key characteristics reported.

It is critical to note that there exists no readily available nor approved stent-graft device for the treatment of ascending aortic or aortic arch aneurysms. When performing ch-TEVAR (using a combination of stent-grafts as listed in Tables 2.1 and 2.2), devices are used "off-label". That is, the devices are implanted in a manner outside of the intended use conditions for which they were explicitly designed.

2.1.3 Clinical Performance of TEVAR Devices

Assessing the relative performance of currently available TAA stent-grafts is difficult due to a lack of large-scale, randomized clinical trials as well as inconsistencies in reporting methods. Nevertheless, the available data have been reviewed and the clinical performance of select TAA stent-graft systems are presented in Table 2.3. Data reported are the most clinically relevant outcomes, namely incidence of: paraplegia, stroke, 30-day and 1-year mortality, as well as evidence of endoleak at 30-days and 1-year. Note that the performance of peripheral stent-grafts is not reviewed here as the clinical trials associated with these devices strictly report on outcomes when used as indicated (and so are not directly relevant to aortic repair). Regarding ch-TEVAR, there are no available clinical studies reporting on best device combinations nor size configurations, representing a significant gap in the knowledge.[1]

Although TEVAR is an improvement over open surgical repair, it is apparent that currently available stent-graft systems are (still) associated with substantial complication rates. Such performance mandates the refinement of current stent-graft designs, particularly if TEVAR of ascending aorta and aortic arch aneurysms is to be successful.

2.1.4 Limitations of Current Stent-Graft Systems

As previously mentioned, the anatomy and motion of the thoracic aorta create specific challenges to successful stent-graft delivery, deployment, and fixation. Current stent-graft systems present with multiple deficiencies associated with these challenges that remain to be resolved. Desai and colleagues [67] have reported an extensive review of endovascular aortic prostheses, highlighting their limitations and failure mechanisms.

[1] Recent clinical studies have reported on the influence of device combination [59] and size configuration [60] on outcomes during chimney repair of abdominal aortic aneurysm (AAA, known as ch-EVAR); however, the applicability of those findings to the thoracic aorta and ch-TEVAR remain to be established.

Table 2.1: Comparison of commercially available thoracic aortic stent-graft systems. Adapted from [57, 58].

Manufacturer	Device	Stent Material	Graft Material	Staged Tip Release	Proximal Landing Zone	Arch Radius of Curvature	Available Diameters	FDA Approved Indications
Cook Medical	Zenith Alpha	Nitinol	PET	Yes	20mm	>20mm	24-46mm	Aneurysm, PAU
Cook Medical	Zenith TX2	Stainless Steel	PET	Yes	20mm	>35mm	28-42mm	Aneurysm, PAU
Jotec GmbH	E-vita 3G	Nitinol	PET	Yes	n/s	n/s	24-44mm	Non-FDA *(CE Mark Only)*
Medtronic	Valiant	Nitinol	PET	Yes	20mm	n/s	22-46mm	Aneurysm, PAU, Dissection, TAI
Terumo Aortic	RelayPlus	Nitinol	PET	Yes	15, 20, 25mm*	>15mm	22-46mm	Aneurysm, PAU
Terumo Aortic	RelayNBS	Nitinol	PET	Yes	22, 25, 30mm*	>15mm	22-46mm	Non-FDA *(CE Mark Only)*
W.L. Gore	cTAG	Nitinol	ePTFE	No	20mm	n/s	21, 26, 28, 31, 34, 37, 40, 45	Aneurysm, PAU, Dissection, TAI

All listed devices are self-expandable; *n/s* - not specified; *dependent on graft diameter; diameters increase in 2mm increments unless otherwise noted; *ePTFE* - expanded polytetrafluoroethylene; *PET* - polyethylene terephthalate; *PAU* - penetrating aortic ulcer; *TAI* traumatic aortic injury

Table 2.2: Commercially available peripheral covered stents commonly used as chimney grafts. Adapted from [58].

Manufacturer	Device	Deployment Method	Stent Material	Graft Material	Available Diameters	Indications
Bard PV	LifeStream	BE	Stainless Steel	ePTFE	5-10, 12mm	Atherosclerotic lesions in the common and external iliac arteries*
Bard PV	Flair	SE	Nitinol	ePTFE	6-9mm	Stenoses at the venous anastomosis of synthetic AV access grafts*
Bard PV	Fluency	SE	Nitinol	ePTFE	5-10, 12, 13.5mm	In-stent restenosis in the venous outflow of hemodialysis patients*
Bentley GmbH	BeGraft	BE	Cobalt Chromium	ePTFE	5-10mm	Aneurysms, acute perforations, ruptures, and fistulas of iliac and renal arteries
Jotec GmbH	E-Ventus BX	BE	Cobalt Chromium	ePTFE	5-10mm	Renal and iliac ruptures, dissections, and aneurysms
Maquet Getinge	Advanta V12 (Atrium iCast)	BE	Stainless Steel	PTFE	5-10mm	Renal, Iliac
W.L. Gore	VBX	BE	Stainless Steel	Fluoro-polymer	5-11mm	Restenotic lesions found in the iliac arteries*
W.L. Gore	Viabahn	SE	Nitinol	ePTFE	5-11, 13mm	Improving blood flow in symptomatic peripheral arterial disease in SFA lesions*

BE - balloon-expandable; *SE* - self-expandable; *ePTFE* - expanded polytetrafluoroethylene; *PET* - polyethylene terephthalate; *SFA* - superficial femoral artery;
*Denotes device with FDA approval for listed indication

Table 2.3: Clinical performance of select commercially available TEVAR devices.

Device	No. of Patients	Paraplegia (%)	Stroke (%)	Mortality at 30 Days (%)	Mortality at 1 Year (%)	Endoleak at 30 Days (%)	Endoleak at 1 Year (%)
Zenith Alpha [61]	110	0	4.5	0	4.5	n/a	5.5
Zenith TX2 [62]	160	5.6	2.5	1.9	8.4	4.8	3.9
Valiant [63]	160	2.5	2.5	3.1	12.6	15.8	13
RelayPlus [64]	133	1.5	4.5	5.3	n/a	0.8	0.9
RelayNBS [65]	56	3.6	1.8	n/a	n/a	8.9	n/a
TAG [66]	142	3	4	1.5	16	3.5	7

n/a - no data available; 1-year mortality reported for overall survival

The key findings of that review are summarized below and have been organized chronologically according to the procedural order in which they would be encountered (i.e. preoperatively, perioperatively, postoperatively). The overlap with the design requirements outlined in Section 2.1.1 should be apparent.

Delivery, deployment, and repositioning. A major challenge still facing stent-graft systems is that the remote access sites required for minimally invasive surgery (femoral and/or iliac arteries) are often small and tortuous; current delivery systems experience difficulty navigating such vasculature. Furthermore, as all commercially available TAA stent-grafts are self-expanding, with most employing rapid-deployment systems, repositioning of the device cannot be performed once the graft has been fully deployed. Such mechanisms can result in inaccurate/undesirable deployment increasing the probability of endoleak (see below), or inadvertent branch vessel coverage.

Endoleak and stent-graft migration. Endoleak is recognized as the main risk associated with stent-grafts, and is a key metric for quantifying stent-graft performance in clinical trials. Essentially, an endoleak allows blood to flow around or through the prosthesis, thus allowing the aneurysmal sac to remain pressurised. Such leakage can cause aneurysm rupture and is the primary cause of aneurysm-related mortality post TEVAR. Four categories of endoleak exist, and are described in Table 2.4.

Table 2.4: Categorization of endoleak as reported by Desai et al. [67].

Endoleak	Definition
Type I	Inadequate seal at graft ends, resulting in leaks at the proximal or distal anchorage sites
Type II	Residual blood flow into aneurysm sac from patent arteries
Type III	Integrity of graft compromised; leakage between modular components
Type IV	Porous/perforated graft material

In relation, stent-graft migration (i.e. significant unwanted displacement/longitudinal movement from the implanted position) is associated with graft kinking, endoleak, and late aneurysm rupture. Migration of stent-grafts is due to inadequate aortic wall fixation when subjected to a force or pressure (e.g. blood flow), or is the result of material failure (e.g. fatigue).

Material durability. Mechanical failure (i.e. device component damage) remains an issue for stent-graft systems. A historical study carried out by Jacobs et al. [68] examined stent-graft fracture over a 10-year period. In that work, over 10% of all devices fractured within 4 years, and a further 4% presented graft material failure (i.e. suture fracture, or graft holes). Although endograft durability has improved (a recent clinical trial reported fracture rates of 1.5% [64]), these failure modes persist.

Resolving these issues through continued device refinement is of paramount importance for improving the long-term outcomes of TEVAR and effectively applying stent-graft technologies to complex aortic disease.

2.1.5 Next Generation Stent-Graft Design

As introduced in Section 1.2.3, stent-graft designs with the potential for treating ascending aorta and aortic arch aneurysms have recently emerged. For the sake of completeness, a descriptive overview of branched endografts is presented here.

The distinguishing characteristic of these next-generation devices is the ability to maintain supra-aortic blood flow in an endovascular manner. This is achieved by incorporating a modular secondary stent-graft, forming an additional conduit to the branch vessel. A survey of these new devices reveals that there exist a variety of mechanisms for branch graft deployment. In one embodiment (e.g. the Medtronic Mona LSA), the device can incorporate an externally orientated "sealing cuff" through which the secondary graft is deployed. In another variation (e.g. the Gore Branched TAG), devices can be constructed with an "inner-portal" through which a secondary stent-graft is guided and deployed. With such designs the manner in which branch vessels are vascularized differ. In the case of the Medtronic Mona LSA, blood flow is maintained in a physiological (antegrade) fashion, whereas the Gore Branched TAG maintains flow in a retrograde fashion. Likewise, the surgical techniques required for device implantation are distinct. When employing a sealing-cuff design, the branch component is positioned and deployed via the target (branch) artery. In the case of a retrograde inner-portal, branch components are delivered via femoral access. Figure 2.2 illustrates these next-generation designs.

These new technologies, in addition to the off-label use of standard devices deployed during chimney endografting technique, are playing a formative role in how complex

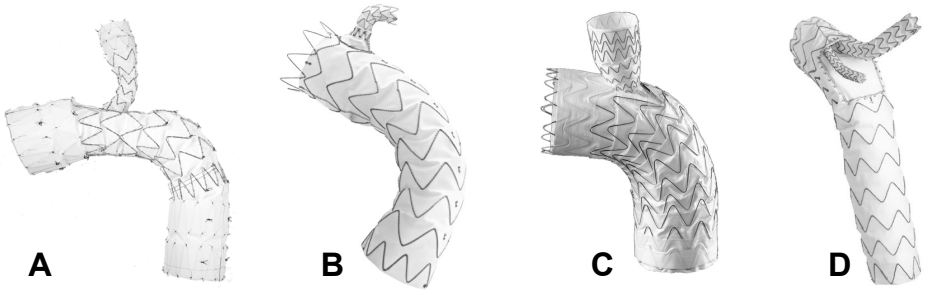


Figure 2.2: Branched technologies for the aortic arch. (A) Cook Medical inner-branched arch stent-graft, (B) Medtronic Mona LSA thoracic stent-graft, (C) Gore TAG thoracic branch endograft, and (D) Bolton Medical double inner-branched arch stent-graft. Adapted from [69].

aortic disease is managed. However, the clinical success of such interventions remains to be fully elucidated. The use of the aforementioned devices are currently limited to small-scale feasibility studies (for example, see [70, 71]). As such, their wide-spread use (outside of dedicated, specialist centers) remains some years away. In an effort to assist surgical decision making and bring endovascular treatments to patients sooner, it is critical to assess these devices in a preclinical environment so as to investigate anticipated behaviour, predict long-term outcomes, and offer potential design/technique improvements.

2.2 *In Vitro* Evaluation of Stent-Grafts

Preclinical evaluation of medical devices is a critical stage of the research and development process when designing novel technologies and establishing the viability of new surgical techniques. Commonly known as *in vitro* (or "benchtop") testing, the primary objective here is to replicate the *in vivo* environment in an experimental manner as to fully characterise device behaviour prior to surgical use. Indeed, there exist numerous guidelines and international standards for conducting such tests (e.g. ASTM International, the FDA, and ISO all prescribe various methods for vascular device testing [72–75]). Likewise, before any device is approved for human use, its design is subjected to rigorous review by regulatory agencies who scrutinize its *in vitro* performance as an indicator of its clinical safety and (potential) effectiveness.

Given the proprietary nature of medical device design and development, manufacturer specific test results are (almost) always confidential. However, experimental studies

in the literature do exist presenting fundamental aspects of stent-graft mechanics. The reports most relevant to complex endografting are reviewed in the following sections and have been organized according to the mechanical characteristics which they examine, namely: (i) delivery, deployment, and positioning, (ii) fixation, stent-graft migration, and endoleak, and (iii) material durability.

2.2.1 Delivery, Deployment, and Positioning

Navigating a thoracic aortic stent-graft to its target location is no trivial task. The entire delivery system must be safely advanced through tortuous vascular anatomy minimizing any risk of arterial trauma. In an experimental environment, the mechanics of device delivery are assessed via a "trackability" test whereby an entire stent-graft system is advanced through a representative vascular model and the displacement/interaction forces recorded [76]. In a similar fashion, a "torquability" test is used to evaluate the torque required to align/position a delivery catheter when it is within the vasculature at the site of deployment (typically, adjustments to the proximal device position are required; however, this can only be achieved via fine manipulation of a distal handle through which all actions must be transmitted). Although such tests are common for device manufacturers, there have been no comparative studies in the literature reporting on the trackability or torquability of TAA stent-graft systems.

As previously mentioned, passive fixation upon deployment via an interference fit with the aortic wall is the primary method used to ensure positional stability of a stent-graft. In clinical practice, stent-grafts are typically oversized by 10 - 20% in relation to the target vessel diameter when treating aneurysmal disease. In doing so, they impose a radial outward force (ROF) onto the arterial wall, which provides fixation. However, recent clinical studies have suggested that excessive radial loads can lead to vessel wall damage and aortic neck dilation [77, 78], increasing the risk of TEVAR failure (e.g. development of type I endoleak). Indeed, there exists a careful balance between the necessary radial loads to ensure device fixation whilst not inadvertently injuring the aortic wall. To correlate device oversizing to ROF, De Bock et al. conducted a comparative study of four different AAA stent-grafts using a radial crimping apparatus [79]. Radial load values between 10.1 - 20.0N (at 20% oversizing, capturing both loading and unloading regimes) were reported across the four device types tested. From this work, general conclusions

regarding the impact of device design on passive fixation were drawn: it was suggested that stent designs offering a high radial strength at the sealing location, but lower radial force at the secondary fixation points, could have better long-term outcomes.

A similar investigation was recently conducted by Morris and colleagues [80] who also reported on the radial load-unload profiles of various AAA stent-grafts. Moreover, the influence of implanted device type on resulting aortic compliance was also studied in that work. Devices were deployed in a physiological silicone vascular model with pulsatile flow and the difference in model compliance was compared pre- and post-implantation. They noted that loss of arterial compliance is an important cardiovascular risk factor, and so devices used in clinical practice should not influence native arterial behaviour. Indeed, substantial differences were found between device types (i.e. deployment of specific devices resulted in statistically significant reductions in arterial compliance), suggesting that the use of different stent-grafts may result in different long-term outcomes.

With regard to endograft positioning, Canaud et al. assessed the conformability - or aortic arch apposition - of four TAA devices in an *ex vivo* model [81].[2] Specifically, device-wall apposition, measured as the (free) distance between the device and inner aortic curvature, was correlated to aortic arch angulation and degree of device oversizing. Representative results showing device conformability from that study are shown in Figure 2.3. Importantly, this study revealed the (potential) superior performance of specific devices when used in highly angulated thoracic anatomies; as made evident in the Figure below, different devices behave differently at acute aortic angulations. This again suggests the potential influence of device type on long-term treatment outcomes. Notably, the experimental findings were also compared to previous results reported by the same group [82], providing commentary on the progression and improvement of TAA stent-graft design.

To isolate the influence of specific device designs on mechanical behaviour, Demanget [83] and Guan [84] have both described novel apparatus for subjecting endografts to bending. In the first instance, stent-grafts were subjected to uniform bending via equivalent and opposite rotations applied to each device end. Coupled with micro-computed tomography, this setup was used to qualify the behaviour of two different stent-graft designs

[2]Ideally, a stent-graft will perfectly conform to the aortic wall with no appreciable gap forming between the device-artery interface; non-apposition in the aortic arch, typically seen on the inner aortic curvature, is referred to as the "bird-beak" phenomena.

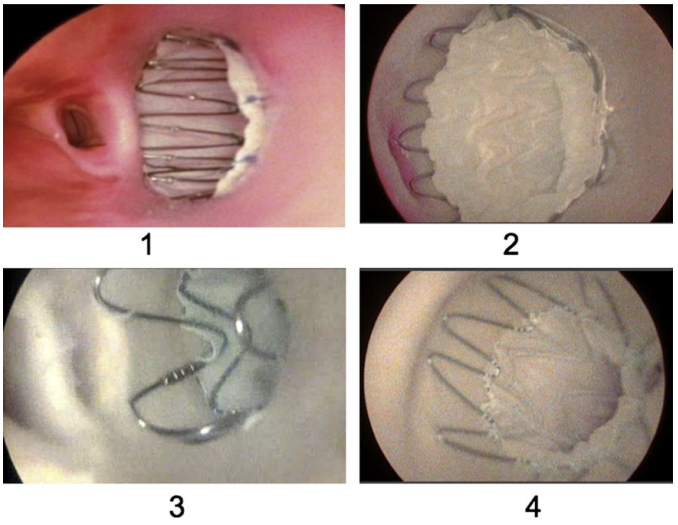


Figure 2.3: Thoracic aortic stent-graft conformability as reported by Canaud et al. Intraluminal views of (1) Cook Zenith, (2) Gore cTAG, (3) Bolton Relay, and (4) Medtronic Valiant endografts in cadaveric aortas demonstrating proximal device-wall apposition. Image adapted from [81].

when subjected to non-pulsatile deformations. To quantify similar behaviour, the latter setup subjected a single device end to rotation and simultaneous measured the bending (and subsequent "spring-back") forces at the opposite device end. Although those studies were limited to testing devices of smaller diameters (i.e. those more commonly used for iliac indications), they provide compelling insights into pure device mechanics when bent (e.g. stent frame structures for improved flexibility). Indeed, such behaviour is directly applicable to complex TEVAR; deploying thoracic devices in the aortic arch leads to an inherently bent device configuration.

Finally, to provide a more detailed (and patient-specific) assessment of factors influencing stent-graft mechanics in the aortic arch, Pasta et al. [85] recently employed an *in vitro* flow model to analyse a thoracic aortic endograft when deployed in a manner leading to poor conformability (i.e. representative of multiple "bird-beak" configurations). Using this approach, factors related to endograft infolding/collapse, which are associated with poor device-artery apposition, were studied. Most notably, it was also found that hemodynamic variables such as aortic pulsatility and cardiac output contributed significantly to device behaviour. Indeed, the salient observations of that study emphasize it is not only the structural characteristics of a device which may influence treatment outcomes, but also the highly variable physiological factors with which they must contend.

2.2.2 Fixation, Stent-Graft Migration, and Endoleak

As stent-graft migration is a contributing factor to Type I and Type III endoleak, considerable effort has been made to quantify the fixation strength of endografts. These studies aim to determine the force required to dislodge/pullout a deployed device from an artery, and hence their likelihood to migrate.

Using bovine arteries, Bosman et al. [86] compared the proximal fixation strength of three AAA stent-grafts. In that study, it was found that dislodgement forces were dependent on the so-called "landing zone" length, and moreover, was influenced by the device type (i.e. design). This suggested that specific devices may be better suited for short landing-zones. In a more comprehensive analysis, Melas et al. [87] studied seven different AAA stent-graft systems in cadaveric models attempting to further elucidate which endograft designs exhibit the best fixation. That study concluded devices incorporating barbs/hooks and those which were subjected to balloon-molding (i.e. additional dilation post implantation) exhibited increased dislodgement forces. Employing a similar benchtop approach, Rahmani and co-workers [88] recently quantified that an increase in aortic angulation decreases stent-graft fixation strength. Although these three studies investigated devices used for AAA repair, they do provide critical insight into the mechanical interactions of stent-grafts with the aorta.

To assess the behaviour of TAA specific devices, Chiang et al. [89] described an experimental setup to evaluate the dislodgement forces of stent-grafts at varying neck angulations and oversizing. The proximal segment of three thoracic aortic endografts (Cook Zenith TX2, Gore TAG, and Medtronic Valiant), in a range of diameters, were deployed in four silicone fixtures representing increasing levels of aortic neck angulation. The fixtures were mounted onto a universal tensile test system, and the devices subsequently dislodged with force-displacement data collected. The experimental setup used in that study is shown in Figure 2.4. Significant differences in dislodgement forces between device types and degree of oversizing were reported. Furthermore, it was found that aortic neck angulation has a negative correlation with thoracic stent-graft fixation (similar to the findings of Rahmani et al.). In other words, devices which are deployed in tortuous anatomy, such as the aortic arch, are more likely to migrate, and the likelihood of migration may be influenced by device type.

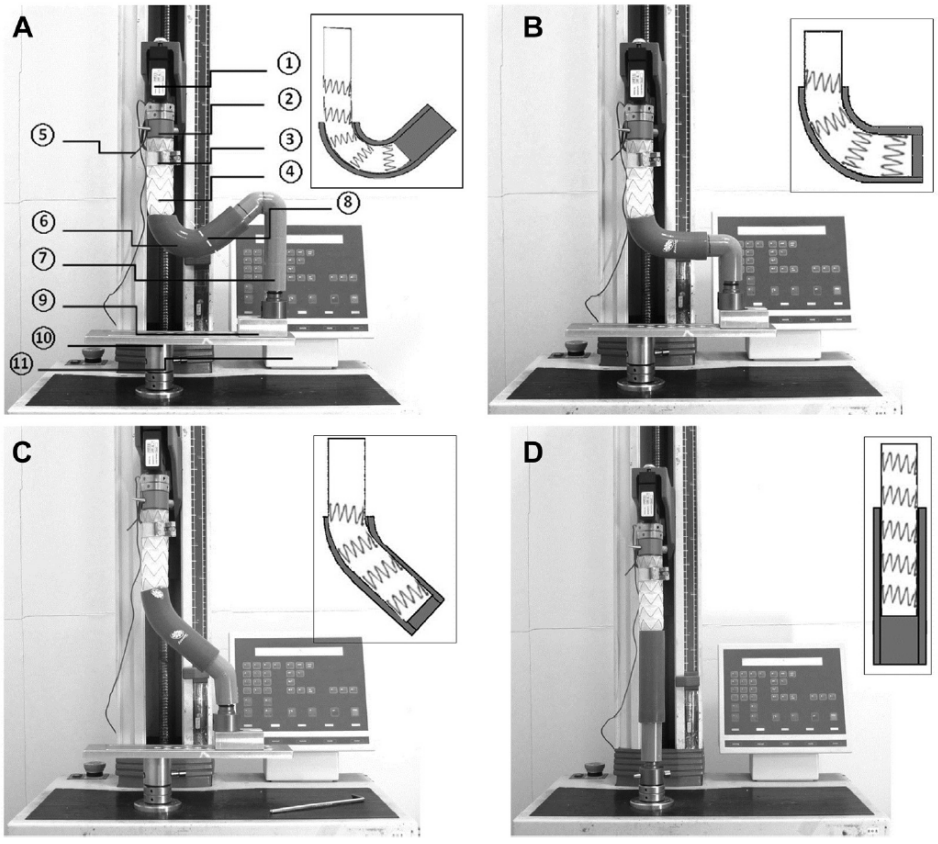


Figure 2.4: Apparatus for TAA stent-graft dislodgement testing as reported by Chiang et al. Devices are deployed in silicone fixtures equivalent to (A) 135°, (B) 90°, (C) 45°, and (D) 0° aortic neck angulations, are mounted on a universal test system, and subsequently dislodged with force-displacement data measured. Image adapted from [89].

It should be noted, however, that the findings reported in the aforementioned studies are limited by the fact that they were conducted in non-aneurysmal (or silicone) arteries where blood flow and pressure were not considered. In an effort to assess stent-graft fixation under physiological conditions, Corbett et al. conducted multiple *in vitro* experiments employing silicon mock vessels connected to a pulsatile flow loop [90–92]. Indeed, those studies demonstrated the significant influence pulsatile flow and arterial wall properties have on stent fixation. In cases where pulsatile flow was induced, and arterial wall compliance was increased, fixation strength was compromised. Across those studies, a general range of 2.5 - 8.5N was required to dislodge the tested devices.

Moving from "global" experiments investigating aspects of device-artery interactions, a number of studies evaluating device-device interactions have also been described. In the first instance, Hinchliffe et al. [93] assessed the fixation strength of modular stent-graft

components. Dislodgement tests of six EVAR systems were conducted (separating the iliac limb from the main body stent-graft), and pullout forces ranging from 2.4 - 23.7N were reported. Following this, Cinà et al. [94] compared modular component pullout forces between standard stent-grafts and those deployed in a "multi-manufacturer hybrid" configuration. Interestingly, it was found that hybrid configurations performed as well as, or better than, standard configurations. This suggests that a range of device designs may offer unique advantages when complex anatomy must be considered. Finally, Grenville and colleagues [95] presented a study examining pullout forces of so-called "bridging" stents commonly used in complex thoracoabdominal and iliac endografting procedures (here, a bridging stent is synonymous to a secondary branched stent-graft, and is deployed into the main stent-graft via portals/channels). This group reported median pullout forces (to dislodge the bridging stent from the main body stent-graft) of 1.17 - 3.82N for a range devices, noting statistically significant differences between device types. Again, this provides insight into the potential fixation strengths of branched arch aTAA devices, given the similarities of the technologies examined.

In a similar line of research, the Liverpool Group [96–99] conducted a series of benchtop experiments to elucidate mechanical aspects of fenestrated endografting.[3] Across that work: (1) the fixation strengths of standard and fenestrated devices were compared; (2) the ability of different peripheral stents to resist fenestrated graft migration was quantified; (3) the forces acting on peripheral stents due to fenestrated device misalignment were determined; and (4) the interactions of modular fenestrated device components assessed. Most recently, Crawford et al. [100] continued research into the influence of fenestrated stent-graft misalignment, reporting that increased levels of device mismatch (i.e. where the fenestration does not properly align with the target branch artery) can lead to luminal narrowing of the main device as well as loss of wall apposition.

To characterise the factors associated with, and mechanics of, endoleak Schurink et al. [101] were among the first to use *in vitro* techniques to investigate the relationship between stent-graft design and aortic seal. Specifically, they reported that "endoleak channels" (i.e. folds of the graft material through which blood can flow) form as a result of device oversizing. As an oversized device does not fully expand to its unconstrained diameter, the material between the stent rings remains folded such that the device

[3] As described in Section 1.2.3, fenestrated stent-grafts are constructed with specific holes (fenestrations) through which secondary (peripheral) devices are deployed to maintain branch vessel perfusion.

cannot form an adequate seal with the aorta. Evidence of this phenomena can be seen in Figure 2.3. These findings present an interesting contradiction in stent-graft use: clinicians advocate oversizing the device to prevent device migration, while the same oversizing may lead to inadequate sealing.

In a complementary study, Leigh et al. [102] investigated the impact of seal length and graft material configuration on Type I endoleak. In that work, endoleak rates were found to be significantly affected by neck length and graft attachment pattern. By increasing coverage length and adopting a "zigzag" graft design (i.e. following the Z-shaped configuration of the stent ring, rather than a simple straight edge approach) endoleak was significantly reduced. In the same year, Albertini et al. [103] shed more light on the mechanisms contributing to Type I endoleak quantifying the relationship between neck angulation and fluid loss in an experimental setup, as seen in Figure 2.5. There, it was found that as neck angulation increased, endoleak increased. This behaviour was attributed to the formation of gaps between the stent-graft and (mock) vessel wall at increased neck angulations, thereby compromising the seal and allowing endoleak. This study is of particular relevance to TAA stent-graft mechanics during complex endovascular repair of the aortic arch, as these devices are required to be placed along a curved aortic segment, where high angulation is inevitable.

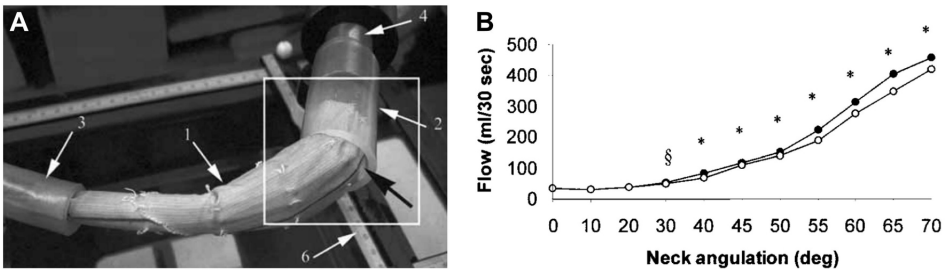


Figure 2.5: Benchtop setup for measuring Type I endoleak as described by Albertini et al. (A) Stent-graft deployed in silicone tube sections, with (B) reported fluid loss (endoleak) measured according to increasing stent-graft angulation. Image adapted from [103].

It should be noted that the aforementioned (endoleak) studies were all conducted using simplistic (non-anatomical) vessels. That is, no consideration was given to the geometry of the simulated artery, thus limiting the clinical utility of their findings. To address this, Sulaiman et al. [104] described the development of a physiological "flow phantom" replicating the anatomical structure of an aneurysmal thoracic aorta. This model was

then used for assessing endoleak immediately after stent-graft deployment. Briefly, medical image processing and rapid prototyping was employed to create a patient-specific silicone model of the thoracic vasculature. The phantom was then connected to an extracorporeal circulation pump and an *in vitro* stenting procedure was performed. To assess the aortic seal, contrasting dyes where injected into the circulatory system, allowing stent positioning and freedom from endoleak to be confirmed via absence of dye in the simulated aneurysmal sac. This setup is shown in Figure 2.6.

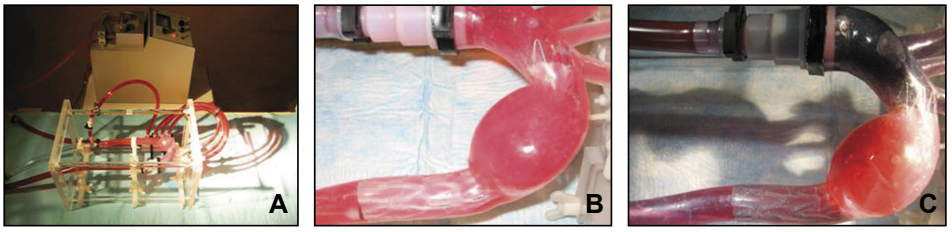


Figure 2.6: *In vitro* flow phantom for thoracic aortic stent-graft assessment as described by Sulaiman et al. (A) Silicone vascular model connected to extracorpreal circulation, (B) stent-graft deployment, and (C) assessment of endoleak after dye injection. Image adapted from [104].

In what is considered to be the most relevant series of *in vitro* studies to this thesis, the groups of Mestres [105, 106], Blankensteijn [107, 108], and Reijnen [109, 110] have reported on the mechanical interactions of stent-grafts during chimney endografting. In those influential works, the behaviour of endografts when deployed in a "parallel" (or "nested") configuration were detailed. Specifically, the mechanical descriptors "gutters", "parallel-stent compression", and "endograft infolding" were described in the context of an experimental setup and related to the clinical scenario. In each of those studies, various combinations of primary and chimney (peripheral) stent-grafts, at various degrees of oversizing, were assessed to determine the configuration that would likely reduce *in vivo* complications such as endoleak and secondary graft occlusion. A representative experimental setup and evaluation is shown in Figure 2.7. Indeed, compelling insights were reported as to device type and sizing which may lead to improved long-term outcomes after chimney endografting. For example, Mestres recommended that main endografts should be oversized by 30% relative to the native aortic diameter (and so substantially greater than the common clinical practice for standard endovascular repair) to limit gutter formation. Likewise, it was reported that gutter size can be minimized by using self-expandable rather than balloon-expandable chimney stents; however, chimney occlusion may be more likely in these combinations due to increased graft compression.

Unfortunately, these studies focused specifically on ch-EVAR (i.e. chimney endografting of the abdominal aorta). As such, there is a significant gap in the knowledge regarding parallel endograft behaviour in the thoracic aorta, which is inherently more complex.

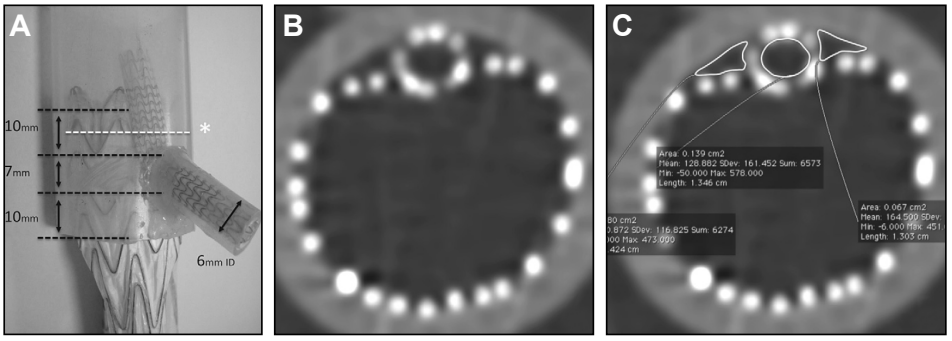


Figure 2.7: *In vitro* chimney endografting as reported by Mestres et al. (A) Endograft and chimney graft deployed within silicone artery; (B) CT reconstruction of chimney graft model; and (C) measurement of gutter areas and parallel stent compression. Image adapted from [105].

2.2.3 Material Durability

To meet regulatory requirements, endovascular prostheses must withstand 380 million (cardiac) load cycles - equivalent to 10 years *in vivo* - without failure. To this end, fatigue durability testing is routinely performed to characterise the integrity and long-term safety of a device. Endograft failure, such as that shown in Figure 2.8, can lead to life-threatening complications for a patient and so must be avoided.

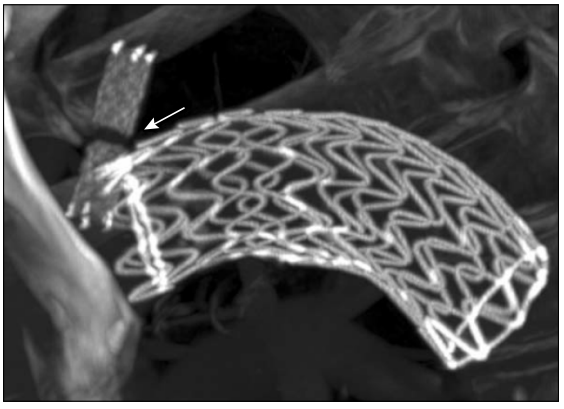


Figure 2.8: Example of mechanical stent-graft failure *in vivo*. Chimney stent fracture (arrow) in the left subclavian artery detected at 18-months follow-up. Image adapted from [111].

To evaluate stent durability, specialist accelerated fatigue testers are employed. Briefly, devices are implanted into compliant silicone vessels. These are in turn mounted onto a system capable of driving a fluid volume into (and out of) the vessels in a pulsatile manner. The silicone vessels thereby act as volumetric springs, which deform in tandem with the displaced fluid. Thus, the implanted stents are subjected to cyclic radial loads via pulsatile vessel deflections. By carefully specifying the degree of silicone vessel distension during testing, *in vivo* loading regimes can be reproduced. Similarly, by appropriately controlling the frequency of fluid displacement, it is possible to simulate 10 years of service life in a matter of months. Using such an apparatus, characterisation of stent integrity is straightforward; macroscopic (visual) inspection is often sufficient to determine if a device has meet durability requirements. Recently, Zhang et al. [112] presented a preliminary case study describing the use of such a system to evaluate mechanical aspects of chimney TEVAR fatigue.

Comparatively, establishing graft (textile) durability of an endovascular prosthesis is a more challenging task. Not only must the graft withstand pulsatile aortic pressures and maintain an impermeable boundary, it must also withstand abrasive contact with the stent frame and its connecting sutures. To characterise and quantify the failure modes of stent-graft textiles, a European explant retrieval program has been established by Chakfé and colleagues. The most current data from that program [113], focused on analysing second- and recent-generation devices, revealed that a majority of grafts exhibited age-related degradation. Likewise, textile failure modes could be categorized as either tears, holes, or suture rupture, and were attributed to either device compression (i.e. when constrained within a delivery system prior to deployment) or abrasion.

In an effort to elucidate the influence of stent design on graft failure, Lin et al. [114] conducted an *in vitro* buckling test comparing Z- and ringed-stent types. In that study, it was reported that contact between the apices of adjacent Z-stents resulted in significant damage to the textile structure, whereas ringed stents did not cause graft failure. In a related study, Chenesseau et al. [115] quantified the influence of the aforementioned device compression within a delivery system and stent design on graft degradation, noting that both device type and duration of compression influenced textile degradation.

When considering the use of stent-graft devices during fenestration procedures, clinicians often modify standard devices *in situ*, purposely perforating the graft (rather than using

a customized device). Recently, Jayet and colleagues [116] evaluated the behaviour of how various stent-grafts respond to such perforations. In that study, it was reported that *in situ* fenestration results in significant textile damage. Moreover, a clear position statement was made, warning against the use of physician-made fenestrations outside of investigational studies.

These durability findings have implications for all endograft devices, but are even more critical for those used during ascending aorta and aortic arch repair. Indeed, multi-component branched TAA devices as well as those used in chimney TEVAR are inherently subjected to additional device-device contact. These complex interactions, coupled with the dynamic behaviour of the thoracic aorta, are likely to increase the risk of mechanical device failure and so warrants further research.

Finally, Schlösser et al. [117] have provided insightful commentary on the applicability of current stent-grafts for use in parallel endografting procedures,[4] stating:

> "Stent-grafts used for chimney and periscope stent-grafting have not been designed for that specific purpose and are outside of the instructions for use... It is unclear what the consequences will be of the long-term mechanical interaction between the aortic and periscope/chimney stent-grafts. Additionally, it is yet to be determined what the impact will be of the aortic arch motion on chimney and periscope stent-grafts during long-term follow-up. There may be a role for stent-grafts designed for the specific use as chimney or periscope stent-grafts."

Unfortunately, given the high costs and long product development life-cycle, developing new devices is no trivial task. To accelerate endovascular innovation, numerical tools to simulate endograft mechanics, known as *in silico* evaluation, are playing an increasingly central role in both the research and development phases of device design.

[4] Chimney and periscope endografting are analogous surgical techniques; however, to revascularize branch vessels, chimneys are deployed in an antegrade fashion whilst periscopes deployed retrograde.

2.3 *In Silico* Evaluation of Stent-Grafts

Computational modelling of endovascular prostheses can be broadly categorized into three domains. In general, these domains are delineated by the physical phenomena examined and the associated numerical methods employed. The first is concerned with analysing structural/mechanical aspects of stent behaviour, and is most commonly performed using the Finite Element Method (FEM).[5] The second is focused on analysing the influence stent-graft implantation on hemodynamics, and employs Computational Fluid Dynamics (CFD) to solve the governing fluid flow relations. The third field couples the interaction between the fluid flow and structural domains, and is aptly termed Fluid-Structure Interaction (FSI).

Using these methods it is possible to comprehensively analyse stent-graft mechanics in a virtual environment. The most relevant FEA, CFD, and FSI studies, as related to complex endografting procedures, are reviewed in the following sections. Again, these have been organized according to the stent-graft characteristics which they examine, namely: (i) delivery, deployment, and positioning, (ii) fixation, stent-graft migration, and endoleak, and (iii) material durability.

2.3.1 Delivery, Deployment, and Positioning

To study the effects of guidewire insertion into a vessel as performed in clinical practice (e.g. prior to stent-graft delivery), Gupta et al. [118] reported on FEA methods to simulate such a procedure. Using various numerical tools, that work illustrated the deformations (straightening) a vessel undergoes prior to stent-graft deployment. Such changes in vessel anatomy have implications for the subsequent deployment of a stent-graft; given their elastic nature, vessels will (attempt to) recover their original anatomy/shape after guidewire withdrawal. In turn, this may effect stent-graft position, fixation, etc., and has the potential to effect the long-term treatment outcomes. Unfortunately, that study only reported on computational methodologies pertaining to guidewire insertion, and so has a rather limited scope regarding overall stent-graft mechanics.

[5]The computational implementation of FEM is known as Finite Element Analysis (FEA).

In a more comprehensive study, De Bock et al. [119] reported on the virtual implantation of a AAA stent-graft into a silicone vascular model. There, the main body of a bifurcated endograft was crimped, positioned within the abdominal aorta, and subsequently deployed. The output of that simulation strategy is shown in Figure 2.9. From the analysis, measures such as neck dilation, stent-artery contact forces, and strains in the stent-graft wires could be evaluated. The main limitation of that work, however, was the method by which device delivery was modelled: rather than simulate the (realistic) insertion over a guidewire and subsequent release, it was simply "bent" into place according to the vessel geometry and deployed. As such, the results must be viewed with some caution: the natural (strain) history of the device is not realistically captured.

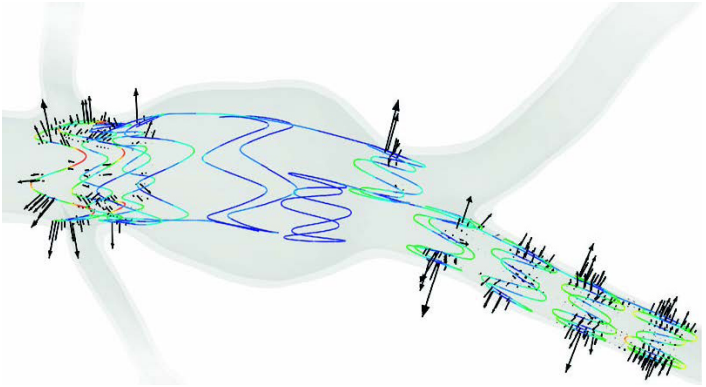


Figure 2.9: Virtual deployment of a bifurcated stent-graft as described by De Bock et al. Using finite element analysis, it is possible to analyse principal strains in the device wires as well as contact force vectors (arrows) exerted by the stent onto the artery. Image adapted from [119].

Demanget and colleagues conducted a series of FEA studies to investigate the (free) bending behaviour of aortic stent-grafts. In that work, techniques for accurately modelling graft material response were proposed. Using those methods, endograft characteristics such luminal reductions, torque required for bending, and maximal membrane strains/von Mises stresses were analysed. Across that work, specific conclusions were drawn about the relationship between stent-graft design and flexibility: in general, endografts employing a spiral or helical frame offer superior behaviour over conventional Z-stents [53, 83, 120]. Following this, the same group extended those methodologies to evaluate stent-graft deployment in patient-specific AAA scenarios. Specifically, numerically determined endograft mechanics were compared to postoperative medical imaging data of the physical procedure [121, 122].

Similar patient-specific methods have also been described by the Pavia group, further demonstrating the utility of FEA for analysing stent-graft behaviour. Notably, those works were concerned with elaborating on the deployment mechanics of various endograft designs when used in the ascending aorta [123], and with comparing numerical predictions with postoperative outcomes [124]. Furthermore, they reported on the use of FEA methods to establish suitable CFD models for evaluating thoracic hemodynamics post TEVAR [125].

Indeed, the results of the aforementioned studies demonstrate the robustness of current numerical techniques to accurately predict stent-graft behaviour. Critically, however, FEA has yet to be used for analysing complex procedures such as chimney endografting.

2.3.2 Fixation, Stent-Graft Migration, and Endoleak

In an effort to reveal (some of) the mechanics associated with stent-graft fixation, Vad et al. [126] performed matching *in vitro* and *in silico* dislodgement tests, from which the stent/vessel coefficient of friction could be determined. For three different endograft designs, the experimental pullout forces ranged from 3-12N, which corresponded to a numerically determined coefficient of friction range of 0.00025-0.07. Interestingly, it was reported that the coefficient of friction decreased with increasing device oversizing; this behaviour was broadly attributed to the fact that contact interactions occur between materials having large differences in stiffness (i.e. between a compliant polymeric tube and a comparatively stiffer endograft). Overall, it was concluded that coefficients of friction, pullout forces, and contact pressures are all influenced by device oversizing, geometry, and material properties.

It should be noted that most computational research attempting to quantify displacement forces acting on stent-grafts employ CFD methods. Naturally, evaluating phenomena that may influence endoleak and (fluid driven) stent-graft migration is best analysed using CFD strategies; these numerical tools are inherently able to account for hemodynamic forces (i.e. those caused by blood flow). In general, such work aims to determine the so-called "drag force" acting on stent-grafts, as generated by the efflux of fluid momentum and the friction on the graft wall due to shear stresses.

To begin, Lam et al. [127] studied the effect of vessel diameter, deployment position, and aortic arch curvature on drag forces experienced by a (simplistic) thoracic aortic stent-graft. It was found that all three parameters affected resultant drag forces, with stent-graft size and deployment position having the most significant influence. Larger devices and those deployed more proximally experienced greater drag. Of note, a (theoretical) maximum drag force of 27N was reported. Given the current clinical trend towards stent-graft deployment in the ascending aorta and aortic arch, these data raise cause for concern. Notably, the computationally determined drag forces acting on thoracic stent-grafts appear greater than their supposed fixation strengths (dislodgement forces) that have been determined experimentally.

Building on this work, Figueroa and co-workers reported two CFD studies further examining factors influencing displacement forces acting on AAA [128] and TAA [129] stent-grafts. Between these studies, it was found that increases in stent-graft curvature, diameter, and length all increased displacement forces (and so, were in general agreement with the work reported by Lam). The most significant contribution, however, was the determination of displacement force orientation: in TAA stent-grafts, the displacement force is orientated cranially rather than caudally. This is counter intuitive to the notion that displacement forces act in the downward direction of blood flow, and so deserves special consideration for branched devices in the ascending aorta and aortic arch.

Regarding ascending aorta/arch endografting, three recent CFD studies have detailed hemodynamic performance post endovascular aortic arch repair [130–132]. In those studies, various arch branch endograft configurations were simulated, with hemodynamic metrics such as flow and pressure waveforms, wall shear stresses, and platelet activation (via particle tracking) were analysed. A representative hemodynamic analysis of different surgical scenarios is given in Figure 2.10. It was demonstrated that the selected surgical approach/resulting endograft configuration can significantly influence hemodynamic phenomena (and hence, potential long-term outcomes). Notably, in the study presented by Nardi et al., an ascending aortic chimney graft configuration was analysed. Unfortunately, the distinct lack of structural mechanics incorporated in those studies (e.g. device-device and device-artery interactions, which may influence lumen geometries) limit their realism, representing a significant gap in the current knowledge.

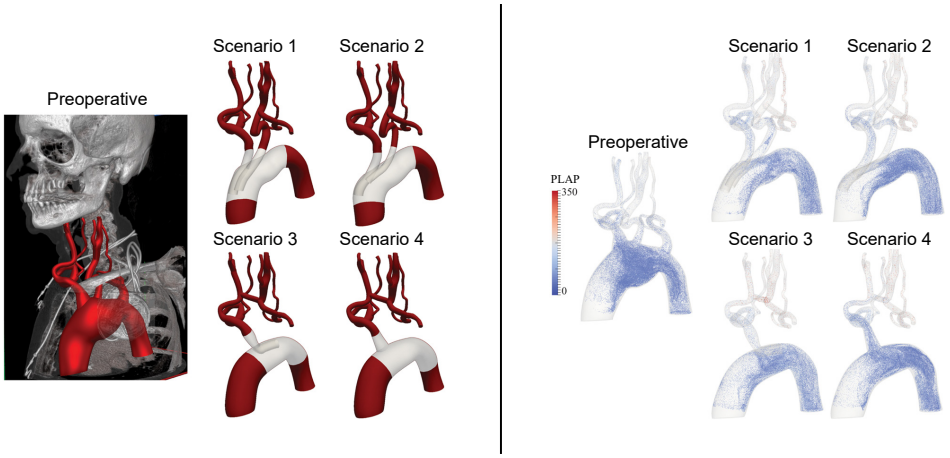


Figure 2.10: Hemodynamics of endovascular aortic arch repair. (Left) Geometric models of the clinical case and four repair scenarios. (Right) Particle tracking via CFD quantifying platelet activation potential (PLAP) to assess risk of thrombus formation. Image adapted from [132].

To assess the mechanics of Type III endoleak, Prasad et al. [133] studied the hemodynamic and mechanical forces acting on the intermodular junctions of a multi-component TAA stent-graft. Specifically, CFD techniques were employed to quantify displacement forces acting on the device. FEA techniques were then used to determine contact stresses between the different components, from which frictional instabilities could be evaluated. Although it was possible to predict the location of endoleak (the study was based upon a retrospective endoleak case), numerous modelling simplifications were made limiting the wide-spread utility of methods used. For example, material properties were simplified, an unrealistic stent-graft deployment procedure was simulated, and typical stent-artery fixation was neglected. With this in mind, it becomes evident that realistically capturing all aspects of *in vivo* stent-graft mechanics in a virtual environment is no trivial task.

In the above study, the CFD analysis and FEA were performed independently, with the CFD results serving as input boundary conditions for the subsequent structural analysis. Using more sophisticated computational techniques, these domains can be directly coupled in so-called fluid-structure interaction analyses, as previously mentioned.

In what is considered to be the seminal collection of FSI work in the stent-graft field, Li and co-workers reported a series of studies exploring the relationship between AAA hemodynamics and device design. Initially, a study investigating the effects of aneurysm

morphology on blood flow, pressure distributions, and aneurysm wall stresses was performed, demonstrating the significant role that aneurysm geometry plays on local biomechanics [134]. Employing the same methods, the influence of (virtual) stent-graft deployment on the same biomechanical factors were analysed and served to quantify the benefits of minimally invasive aortic repair [135, 136]. These studies also reported on stent-graft drag forces, and analysed the factors contributing to potential device migration such as aneurysm and endograft geometry. Finally, using the same techniques, factors contributing to the development of Type II endoleak were assessed [137]. Although those studies focused on AAA aneurysm geometries and related stent-graft designs, their general findings still deserve special consideration for the development of next-generation stent-grafts for complex aortic repair.

Finally, building on their (uncoupled) fluid and solid mechanics work, Prasad et al. [138] detailed a partitioned FSI study of AAA stent-grafts. That study was the first to report the use of specific contact formulations between the stent-graft and artery wall. Furthermore, it introduced the so-called "instability index" for numerically quantifying the positional stability of an endograft. Using this index, it was possible to more accurately analyse the influence of fixation lengths, curvature, and frictional coefficients on potential stent-graft migration.

2.3.3 Material Durability

Fatigue-life prediction of medical grade nitinol and stents has been widely reported (for example, see [139–141]). Of these studies, the most relevant to computational stent-graft mechanics was presented by Kleinstreuer et al. [142] who described methods to predict fatigue behaviour (i.e. the safety factor) of a generic device when designed with different stent (nitinol) and graft (ePTFE, PET) materials. In that study, it was determined that the selection of both stent and graft properties play an important role in device behaviour and predicted long-term performance. For example, a nitinol stent with a PET graft may offer better long-term durability than an equivalent device with an ePTFE graft. Unfortunately, the stent-graft geometry used to quantify such performance was simplistic and not representative of a typical (commercial) design, thereby limiting the scope of that study's findings.

The work by Kleinstreuer is the only reported computational study to date examining the influence of graft properties on stent-graft durability. This is surprising given the rise of chimney endografting and that these procedures are associated with high-risk device related complications. As such, there remains much to do in predicting the long-term behaviour of devices when used in such procedures.

Finally, when employing computational strategies to evaluate stent-graft mechanics, it is of paramount importance to verify and validate the methods used [143]. That is, the analyst must ensure the predicted (computational) behaviour accurately reflects the real-life scenario. To this end, it is often the case that the results of *in silico* simulations are compared to their *in vitro* counterpart to increase confidence in the numerical predictions.

2.4 Summary and Thesis Objectives

In this Chapter, the functional requirements of stent-grafts have been described and the state-of-the-art in endograft technology reviewed. Methods and key findings of the reported *in vitro* and *in silico* studies detailing aspects of stent-graft mechanics have been consolidated.

It is apparent that identifying the optimal stent-graft configuration for endovascular repair of thoracic aortic disease is no trivial task: functional requirements are complex, multifactorial, and often contradictory. Unsurprisingly, there exist numerous mechanical factors which affect device behaviour, and thus, influence their clinical effectiveness.

In an effort to elucidate stent-graft mechanics, much work has been done across the experimental and computational domains. This review, however, has revealed significant gaps in the current knowledge concerning thoracic aortic devices and their use in complex endovascular procedures. Specifically, there is a distinct lack of detailed TAA device characterisation. Moreover, there does not exist a robust engineering analysis of how thoracic aortic devices behave when used in off-label surgical procedures such as chimney endografting. This paucity of data is of particular concern given the trend towards minimally invasive repair of aortic arch aneurysms using such devices.

This thesis will explore distinct aspects of thoracic aortic stent-graft behaviour by developing computational and experimental tools capable of capturing the complex interactions that arise during endografting procedures. The specific objectives are:

Objective 1: to establish a computational framework employing the finite element method able to predict thoracic aortic stent-graft behaviour.

Objective 2: to characterise the loading response of thoracic stent-grafts alone and in combination with chimney stents. In the case of parallel configurations, to quantify mechanical deformations in terms of clinically relevant metrics.

Objective 3: to evaluate thoracic aortic chimney endografting in an *in vitro* model accounting for cardiac biomechanics.

Objective 4: to describe advanced numerical simulations, elaborating on the methods developed in Objective 1 and the behaviour characterised in Objectives 2 and 3, to assess aspects of complex endografting in a dynamic FEA model.

This research represents a significant opportunity to further the understanding of endograft mechanics, thereby contributing to the fields of biomedical engineering and (endo)vascular surgery. This work serves to benefit device manufacturers, surgeons, and patients alike.

Chapter 3

A Computational Framework for Stent-Graft Modelling

In this Chapter, numerical strategies to investigate stent-graft behaviour are developed. First, the phenomenological material models which govern the underlying behaviour of each component in the "stent-graft-artery" domain are described. Following this, a series of finite element analysis (FEA) case studies examining various aspects of stent-graft performance are established. Finally, a novel simulation approach to assess the behaviour of stent-grafts deployed in a "parallel" configuration, representative of chimney thoracic endovascular aortic repair (ch-TEVAR), is proposed and results presented.

3.1 Material Behaviour

To accurately predict stent-graft behaviour using computational techniques, it is of paramount importance to correctly describe the underlying material behaviour of each component included within the analysis. Likewise, when developing sophisticated numerical tools to evaluate multiple components and complex interactions, it is advisable to adopt an incremental approach whereby simple models are established in the first instance, than built upon to the achieve the level of complexity required. Thus, the logical starting point to develop a computational framework for stent-graft modelling is to begin by evaluating the material behaviour of the constituent components subjected to simplistic test cases.

When assessing the structural domain of thoracic endovascular aortic repair (TEVAR), there are two "components" of interest: (*i*) the stent-graft device (consisting of two distinct members itself), and (*ii*) the artery with which the device interacts. Figure 3.1

illustrates the various stages of TEVAR (i.e. device delivery, positioning, and deployment) and depicts the analysis domain. In this section, the phenomenological models used to describe nitinol, PET, and aortic tissue are presented. Specifically, the unique properties and behaviour of each material is described, followed by a discussion of their numerical implementation where finite element analysis (FEA) is used to assess their behaviour in the general sense.

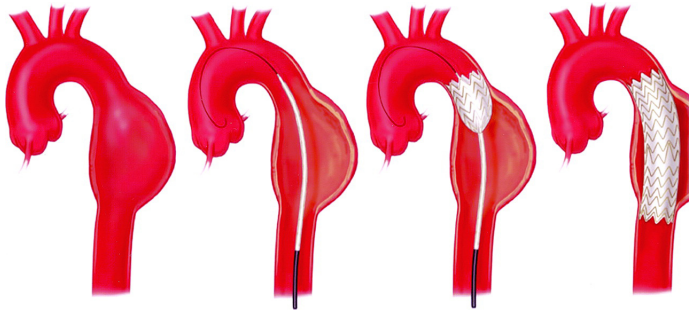


Figure 3.1: Stages of thoracic endovascular aortic repair (TEVAR) of a descending thoracic aortic aneurysm. Panel four illustrates the "stent-graft-artery" components comprising the structural analysis domain. Image adapted from [27].

3.1.1 Stent Devices: Nitinol

The properties of nickel-titanium, commonly known as nitinol, and its use in medical devices has been described in detail elsewhere (for example, see [144–148]). Recently, Bonsignore summarized the functional characteristics of this unique material as applicable to endovascular technologies. Briefly, nitinol of suitable composition and processing exhibits "superelastic" behaviour related to a stress induced martensite phase transition. Most notably, superelastic nitinol can be deformed in excess of 9% strain and return to its original shape when the deformation force is released. Such behaviour is inherently advantageous for minimally invasive medical applications, such as stents and stent-grafts, as these devices must undergo large recoverable deformations [149].

The distinct stress-strain curve of superelastic nitinol is shown in Figure 3.2. Elaborating on this generalized behaviour, Azaouzi described the phenomena occurring at each loading-unloading stage [150] and is detailed hereafter. Referring to the Figure below and parameters in Table 3.1, medical grade nitinol presents itself in an austenite phase up to a critical threshold (1). When loaded mechanically beyond a certain stress σ_{tL}^{S}

and at a temperature greater than T_{Af} (the austenite transformation temperature, not shown), the austenite phase transforms into a martensite phase (2). The transformation produces a substantial amount of strain, which upon unloading is reversible (regions 4 and 5) as the martensite is not stable for T > T_{Af}. Since the transformation strains are large (of the order of 6%) compared to elastic strains in typical metals, the material is said to be superelastic [151]. When the direct and inverse transformations take place, the stress remains uniformly constant over a large range of deformation (known as the upper and lower plateaus, respectively). Loading beyond the superelastic limit reveals plastic behavior within the martensite phase (3). If a compressive load is applied, a similar behavior is observed (6), with the exception that the stress levels required to produce the transformations are higher while the transformation strain is lower.

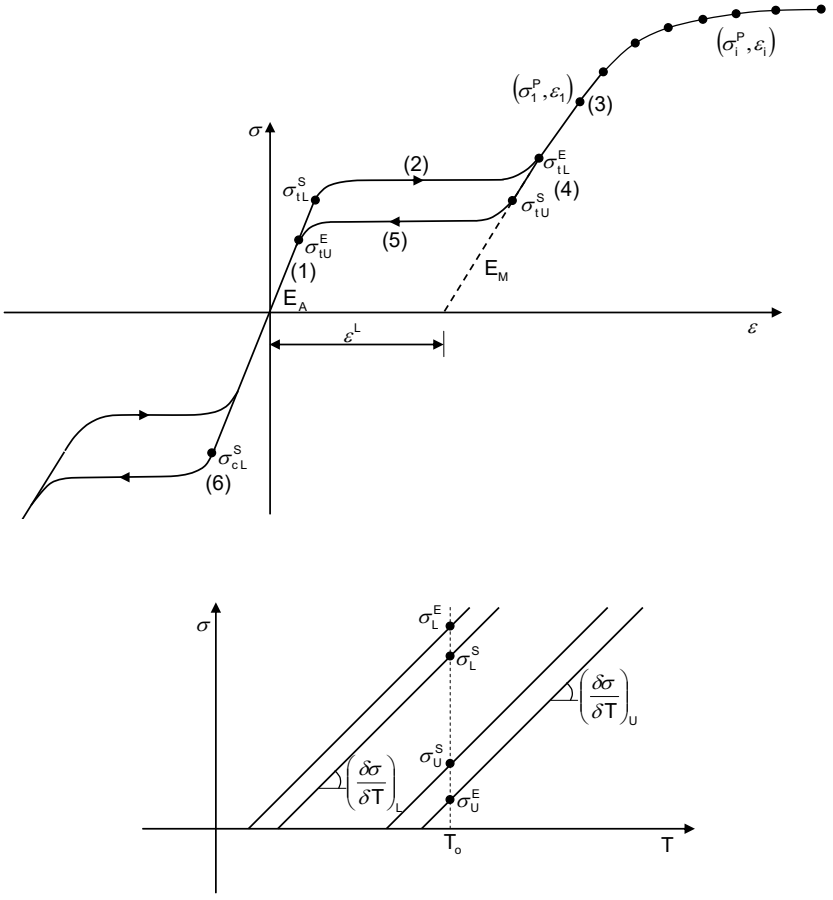


Figure 3.2: Superelastic-plastic material response of nitinol. (Top) Uniaxial tension-compression behaviour; (bottom) stress *vs.* temperature curve. Image adapted from [152].

When considering the construction of stent-grafts, it is the metallic stent component which dominates the mechanical characteristics of the device. It is therefore necessary

Table 3.1: Parameters describing the superelastic behaviour of nitinol.

Parameter	Description
E_A	Austenite elasticity
E_M	Martensite elasticity
ε^L	Transformation strain
σ^S_{tL}	Start of transformation loading
σ^E_{tL}	End of transformation loading
σ^S_{tU}	Start of transformation unloading
σ^E_{tU}	End of transformation unloading
σ^S_{cL}	Transformation stress (compression)
$\left(\sigma^P_i, \varepsilon_i\right)$	Yield stress - plastic strain pairs
T_o	Temperature
$(\delta\sigma/\delta T)_L$	Temperature-stress relation (loading)
$(\delta\sigma/\delta T)_U$	Temperature-stress relation (unloading)

to model this unique material behaviour accurately if a rigorous stent analysis is to be performed. As nitinol is considered to be the material of choice for stent-graft frames, it is used as the primary stent material for the analysis presented in this work.

3.1.1.1 Numerical implementation

To model the material behaviour of nitinol via finite element analysis (FEA), a dedicated user material subroutine (UMAT) is implemented in the Abaqus Unified FEA code (Dassault Systèmes Simulia Corp., Providence, RI, USA), which is used for all computational studies presented throughout this work. Originally proposed by Auricchio and Taylor [153, 154], the superelastic model is based upon the uniaxial stress-strain response of phase transforming materials. For the sake of completeness, the underlying details of this subroutine as reported in [152] are described below.

As previously mentioned, in a load-free state nitinol is in the austenite phase and is assumed to follow isotropic linear elasticity. Upon loading, the austenite phase starts transforming into martensite beyond a certain stress. Martensite is also assumed to follow isotropic linear elasticity. During the phase transformation, elastic properties are calculated from the elastic constants of austenite and martensite, following the rule of mixtures:

$$E = E_A + \zeta \left(E_M - E_A \right), \tag{3.1}$$

$$\nu = \nu_A + \nu \left(\nu_M - \nu_A \right), \tag{3.2}$$

where ζ is the fraction of martensite, E_A is the Young's modulus of austenite, E_M is the Young's Modulus of martensite, ν_A is the Poisson's ratio of austenite, and ν_M is the Poisson's ratio of martensite. After a certain stress, austenite is completely transformed into martensite, which deforms elastically thereafter. Therefore, the deformation follows the elastic constants of austenite when the fraction of martensite is zero and follows the elastic constants of martensite if the fraction of martensite is one (i.e. at full transformation). Upon unloading, martensite transforms back into austenite and the transformation strain is fully recovered. However, the stress at which the reverse transformation occurs is different from the stress at which the austenite to martensite transformation occurred.

In this model the total strain increment $\Delta\varepsilon$, is assumed to be the sum of the elastic strain increment, $\Delta\varepsilon^{el}$, and the increment in transformation strain, $\Delta\varepsilon^{tr}$:

$$\Delta\varepsilon = \Delta\varepsilon^{el} + \Delta\varepsilon^{tr}. \tag{3.3}$$

The increment in transformation strain is calculated using the following flow rule:

$$\Delta\varepsilon^{tr} = \Delta\zeta \frac{\partial G^{tr}}{\partial \sigma}, \tag{3.4}$$

where G^{tr} is the transformation flow potential. The transformation potential is assumed to follow the Drucker-Prager form:

$$G^{tr} = q - p \; tan \; \psi, \tag{3.5}$$

where $q = \sqrt{\frac{3}{2} S : S}$ is the von Mises equivalent stress, and $p = -\frac{1}{3} \; trace \; \sigma$ is the equivalent pressure stress.

The transformation surface, F^{tr}, is also assumed to follow the Drucker-Prager form, and it varies linearly with temperature, T:

$$F^{tr} = q - p\ tan\ \beta. \tag{3.6}$$

In the case of tensile loading, F^{tr} should lie between σ^S_{tL} and σ^E_{tL}; during unloading, F^{tr} should lie between σ^S_{tU} and σ^E_{tU}. A difference in the response of the specimen during loading in tension and compression can be obtained by specifying a value of σ^S_{cL}, which is different from σ^S_{tL}. The angles β and ψ are calculated from the tensile and compressive transformation stress levels, the uniaxial transformation strain, and the volumetric transformation strain.

The stress levels at which the transformation takes place are with respect to a specified reference temperature, T_o. These stress levels are assumed to vary linearly with temperature.

Notably, the formulation described above pertains to the superelastic material response of nitinol. To account for plasticity, that is loading beyond the elastic limit of the martensite phase, the total strain increment, $\Delta\varepsilon$, is assumed to be the sum of the elastic strain increment, $\Delta\varepsilon^{el}$, the increment in transformation strain, $\Delta\varepsilon^{tr}$, and the increment in plastic strain, $\Delta\varepsilon^{pl}$:

$$\Delta\varepsilon = \Delta\varepsilon^{el} + \Delta\varepsilon^{tr} + \Delta\varepsilon^{pl}. \tag{3.7}$$

The increment in plastic strain is calculated using a nonassociated flow rule:

$$\Delta\varepsilon^{pl} = \Delta\bar{\varepsilon}^{pl}\frac{\partial G^{pl}}{\partial\sigma}, \tag{3.8}$$

where G^{pl} is the plastic flow potential. G^{pl} is equal to the von Mises stress, q,

$$G^{pl} = q. \tag{3.9}$$

The yield surface, F^{pl}, is assumed to follow the Druker-Prager formulation with hardening driven by the equivalent plastic strain,[1] $\bar{\varepsilon}^{pl}$:

$$F^{pl} = q - p\ tan\ \beta - F^{Y}\left(\Delta\bar{\varepsilon}^{pl}\right), \tag{3.10}$$

where p is the pressure and β is the friction angle. The initial yield stress is the stress at which the transformation of austenite into martensite ends, σ^{E}_{tL}.

To implement the superelastic material model, 14 user specified variables based upon the stress-strain behaviour of nitinol are required. As such, an experimental testing protocol to characterise nitinol and calibrate the user material subroutine has been undertaken.

3.1.1.2 Uniaxial tension testing of nitinol

To characterise the behaviour of nitinol, uniaxial tensile testing of nitinol tube specimens was performed. The specific test protocol chosen for this characterisation follows the well established methodology described by ASTM F2516 [155].

Briefly, three nitinol tube specimens (4.164mmOD x 50μmWT, 15mm gauge length) were mounted onto a standard uniaxial tensile tester (ZwickRoell AllroundLine Test System Z020, Zwick GmbH & Co. KG, Ulm, Germany) with mandrels inserted into each end segment to prevent crushing during fixation. Specimens were then subjected to tensile loading (at a loading rate of 2mm/min), with strain measurements taken via clip-on extensometers. For each specimen, two testing cycles were performed. In the first cycle, the specimen was elongated to 6% strain followed by unloading to 7 MPa. In the second cycle, the specimen was pulled to failure. Testing was performed at $22 \pm 2°C$.

In addition to collecting stress-strain data, nitinol upper plateau strength (UPS, at 3% strain), lower plateau strength (LPS, at 2.5% strain), residual elongation (El_r, at 7 MPa after unloading), ultimate tensile strength (UTS), and uniform elongation (El_u, strain at maximum load) was also analysed to fully characterise the experimentally derived material behaviour.

[1] Equivalent plastic strain is a scalar quantity which describes the degree of inelastic deformation in a material. Additional details can be found in [152].

The stress-strain response of the tested specimens is given in Figure 3.3. The additional material characteristics as outlined above are given in Table 3.2. Upon assessment of the collected data, the uniaxial tensile behaviour of the nitinol tube specimens tested here demonstrate the distinct stress-strain behaviour commonly reported in the literature (for example, see [140, 145, 156]). Good agreement was found between all test samples for the region of interest required to calibrate the nitinol subroutine (i.e. specimen behaviour up to El_u). Specimen 3 was noted to have failed earlier than Specimens 1 & 2. This was likely caused by a local inhomogeneity in the tube sample; an imperfection on the inner tube surface due to manufacturing (e.g. tube drawing) can create a microcrack in the circumferential direction leading to early specimen failure [157]. Nevertheless, for nitinol material tested per ASTM F2516, elongation is not evaluated at failure, therefore confirming the repeatability of the nitinol material behavior assessed.

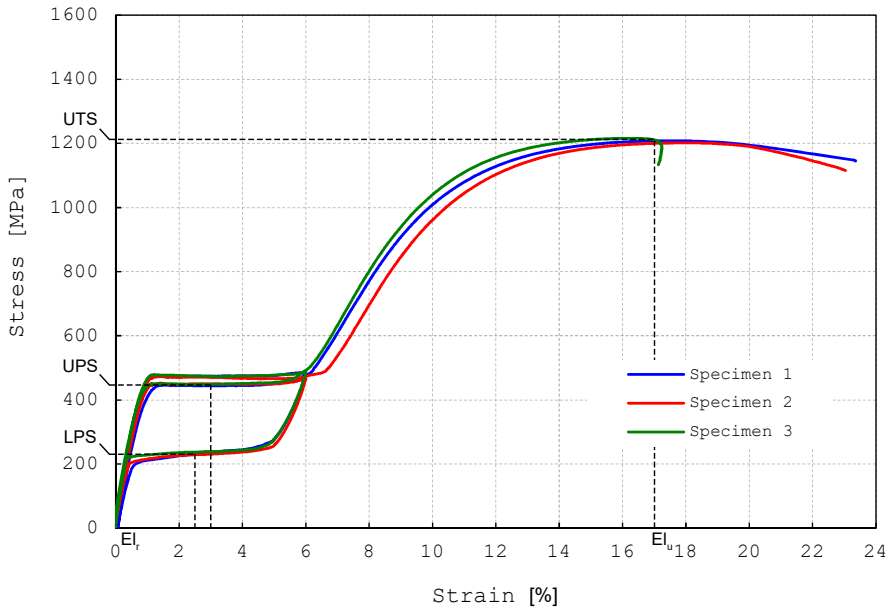


Figure 3.3: Nitinol material characterisation. Uniaxial stress-strain behaviour of three nitinol tube specimens subjected to tensile load as per ASTM F2516. Annotated properties include: lower plateau strength (LPS), upper plateau strength (UPS), ultimate tensile strength (UTS), residual elongation (EL_r), and uniform elongation (El_u).

Also of interest is the difference in UPS noted between the initial and secondary loading cycles (where $UPS_{Cycle\ 1} > UPS_{Cycle\ 2}$). In the first cycle, stress-induced martensite (SIM) forms the first time. Once the load is reversed at 6% strain the SIM transforms back into austenite, but not completely, which is described by El_r (i.e. permanent set).

Table 3.2: Nitinol tube properties derived from uniaxial tensile tests.

Specimen ID	UPS [MPa]*	LPS [MPa]	El_r[%]	UTS [MPa]	El_u [%]
1	474.0	231.0	0.1	1208.0	17.4
2	470.0	229.0	0.0	1202.0	18.3
3	474.0	237.0	-0.1	1216.0	16.1
mean	427.7	232.0	0.0	1216.0	17.3
SD	2.3	4.2	0.1	7.0	1.1

*UPS reported for Cycle 2; mean - arithmetic mean; SD - standard deviation

The transformation into SIM during the second cycle is somewhat "easier" as the loading path has been initialised, thus resulting in a decrease in UPS [157].

3.1.1.3 UMAT Calibration

Employing the stress-strain data collected via uniaxial tensile testing, it is possible to calibrate the parameters necessary to define the nitinol user material subroutine within Abaqus. For the purposes of this calibration, the unloading portion of the first cycle and the complete second cycle up to El_u are used to describe nitinol behaviour. It is appropriate to neglect the initial loading cycling (with an associated higher UPS as noted previously), as stent devices will have already undergone a preliminary loading cycle during device packaging. Hence, during the service life of a stent-graft, the experienced stresses will be associated with the loading behaviour of cycle 2. Of note, prior to calibration it is necessary to convert the experimental test data from engineering stress-strain to true stress-strain, as Abaqus computes Cauchy "true" stress as its stress measure.

To conduct the calibration, a simple simulation strategy is adopted in Abaqus/Standard (v2017) whereby a single continuum element (reduced integration, type C3D8R) is subjected to the same loading regime as the physical test protocol. Specifically, nodal displacements are prescribed for the "top" element face in the U2 direction to replicate tensile testing, while nodes lying on "bottom" element face (i.e. on the U1-U3 plane) are appropriately constrained. Figure 3.4 illustrates the single element (also known as "unit cube") simulation approach. As mentioned above, output from the simulation are

true stresses and logarithmic strains computed at the element integration point during uniaxial loading-unloading.

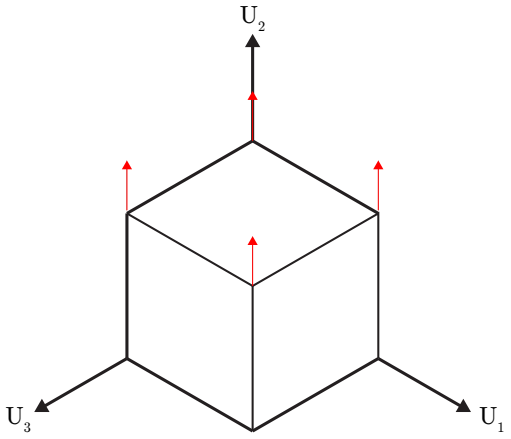


Figure 3.4: Simulation strategy for nitinol material model calibration. Representative single element unit cube subjected to uniaxial tensile loads via nodal displacements (*red arrows*).

Using an initial parameter estimation based on the defined data points specified in Figure 3.2, the procedure used to calibrate the material model is based on an iterative updating scheme. Variables are passed to the built-in subroutine and are continuously updated until agreement is achieved between the experimental data and simulation output.

Upon completion of the calibration procedure, excellent agreement was obtained between the physical test data and numerical response, as shown in Figure 3.5. The 14 superelastic parameters of the calibrated material model are given in Table 3.3.

To demonstrate the robustness of this model, the single element simulation strategy was adapted to evaluate the response of the UMAT to three additional test cases. In the first instance, the imposed temperature was increased from 22°C (i.e. experimental test temperature) to 37°C (the temperature experienced by the element throughout the simulation can be modified through specified predefined fields as implemented in the FEA code). Testing this change to the model is particularly relevant given that nitinol is a temperature-dependent material and that stent-graft devices are subjected to loading at physiological temperatures (i.e. different to the temperature at which material model calibration was conducted). Following this, cyclic loading at increasing levels of strain was simulated. Capturing this behaviour within the material model is of critical importance given that stent devices are subjected to pulsatile loading, which influences

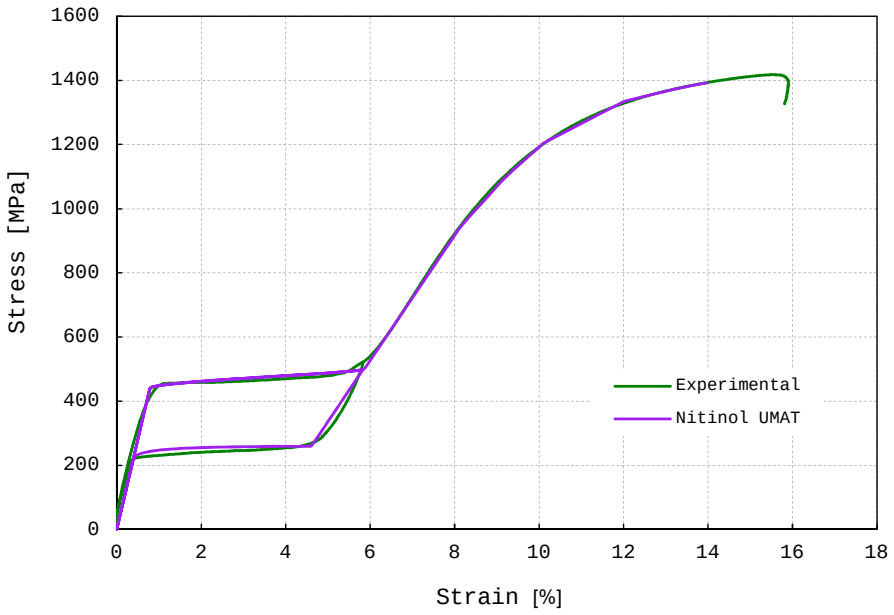


Figure 3.5: Nitinol user material subroutine calibration. Stress-strain response to uniaxial tension via experimental determination (*green*), and single element simulation strategy (*purple*).

Table 3.3: Calibrated nitinol material model parameters.

Parameter	Value
Calibrated Nitinol UMAT	
Density ρ	6450 Kg/m^3
Austenite elasticity E_A	56000 MPa
Austenite Poisson's ratio ν_A	0.33
Martensite elasticity E_M	19500 MPa
Martensite Poisson's ratio ν_M	0.33
Transformation strain ε^L	0.033
Loading $(\delta\sigma/\delta T)_L$	6 MPa/°C
Start of transformation loading σ_L^S	440 MPa
End of transformation loading σ_L^E	500 MPa
Temperature T_o	22°C
Unloading $(\delta\sigma/\delta T)_U$	6 MPa/°C
Start of transformation unloading σ_U^S	260 MPa
End of transformation unloading σ_U^E	220 MPa
Transformation stress (compression) σ_{CL}^S	660 MPa
Volumetric transformation strain ε_V^L	0.0

fatigue life (a key consideration when evaluating the performance and functionality of medical implants) [139]. Finally, the effects of inducing plasticity, followed by unloading, were analysed. Again, the ability to capture plasticity effects is crucial, given the design criteria imposed on stent devices (e.g. the device may need to be packaged to extremely small diameters to facilitate minimally invasive surgery, inadvertently loading the device beyond its elastic limit). The response of the material model to these three additional test cases is given in Figure 3.6.

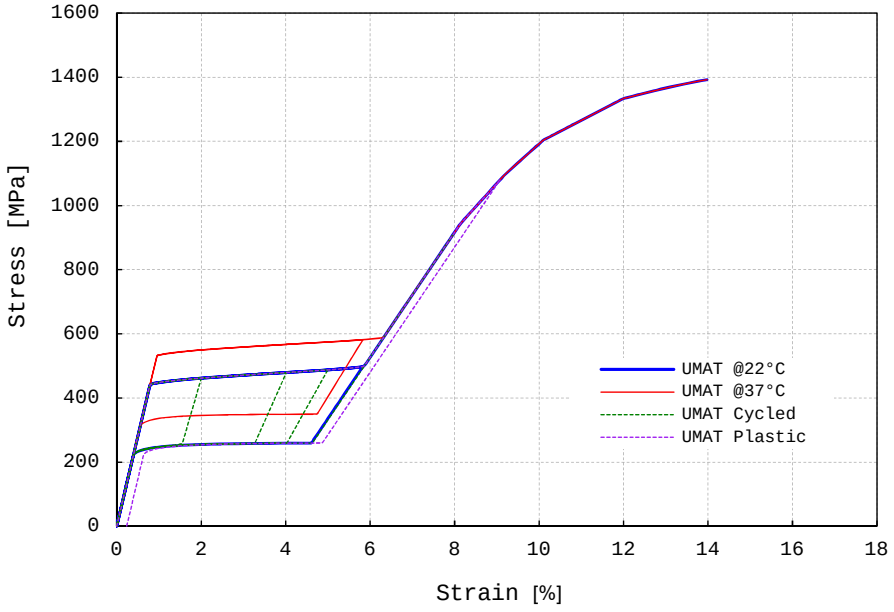


Figure 3.6: Stress-strain response of a single element unit cube. Robustness of the calibrated material model as subjected to physiological temperature (37°C), cyclic loading (at increasing levels of transformation strain), and plasticity (loading beyond the elastic limit of martensite).

The results presented in Figure 3.6 clearly demonstrate the robustness of the calibrated material model. Increasing the temperature to physiologically relevant levels produces the anticipated upward shift in the stress-strain response [145]. Subjecting the model to multiple loading cycles at various level of strain results in repeatable behaviour (i.e. follows the same loading-unloading path consistently). Likewise, loading beyond the elastic limit of the material results in plasticity, as demonstrated by the permanent deformation seen upon unloading.

Finally, for completeness, the calibrated model presented here was compared against other user subroutine parameters reported in the literature. As can be seen in Figure 3.7, the calibrated model is in general agreement with those previously described [156, 158,

159]. Specifically, a direct match between austenite modulus can be observed, with upper and lower plateaus falling within the median range. The only apparent difference is that of the martensite modulus, which is somewhat lower than those reported elsewhere, but nevertheless follows the same general trend.

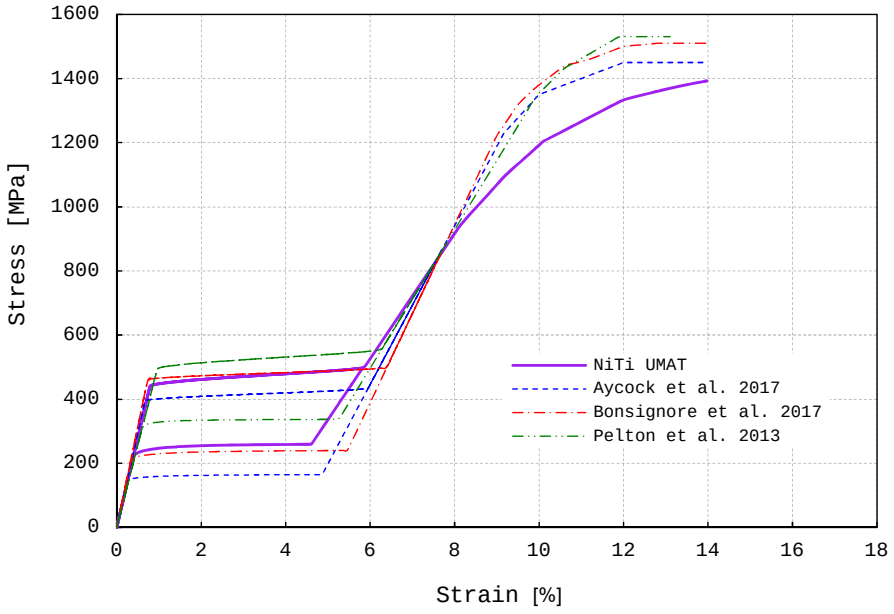


Figure 3.7: Stress-strain response of a single element nitinol unit cube subjected to uniaxial tensile load. Comparison of experimentally calibrated user subroutine material parameters to those reported in the literature.

3.1.1.4 Other stent materials

It is important to note that although nitinol is the primary material of stent-graft frames used in TEVAR procedures, other stent materials also exist. In particular, 316L stainless steel can be found in some thoracic aortic aneurysm (TAA) devices used in clinical practice today. Fortunately, the numerical implementation of this material is straightforward, as it exhibits an elastoplastic behaviour common to conventional metals. The properties of this material are given in Table 3.4, and are used in subsequent simulations presented in this Chapter.

Table 3.4: Material properties of 316L stainless steel as reported in [53].

Parameter	Value
316L stainless steel	
Density ρ	7900 Kg/m^3
Young's modulus E	210000 MPa
Poisson's ratio ν	0.3
Yield stress σ_e	1550 MPa

3.1.2 Graft Material: PET

As the stent component dominates the mechanical characteristics of stent-graft devices, it is the graft covering of the device which ensures its clinical efficacy. Not only must the graft be impermeable, such that it can effectively exclude the aneurysmal portion of the aorta from blood flow, it must also be thin and flexible as to facilitate packaging for minimally invasive surgery, deliverability, and conformability against the vessel wall.

The graft material most commonly used in conventional devices is Polyethylene Terephthalate, PET (also known as Dacron). In a typical graft construction, fibres of PET are woven together to form a synthetic textile. As with any woven fabric construction, the resulting graft is constituted of fibres aligned along the "warp" and "weft" directions. Given this distinct construction, graft materials made from PET fibres exhibit anisotropic behaviour [160].

3.1.2.1 Numerical implementation

To characterise the material properties of a PET graft and effectively implement its behaviour in the computational framework presented here, the data and methods originally reported by Demanget et al. [120] are adopted in this work. For the sake of completeness and to ensure correct implementation, it is appropriate to corroborate the originally described numerical methodology, and so it is detailed below.

Using data reported in [161], based on pure and plane strain tensile tests of graft specimens at differing orientations along the warp (longitudinal) and weft (circumferential) directions, the anisotropic behaviour of PET is illustrated in Figure 3.8.

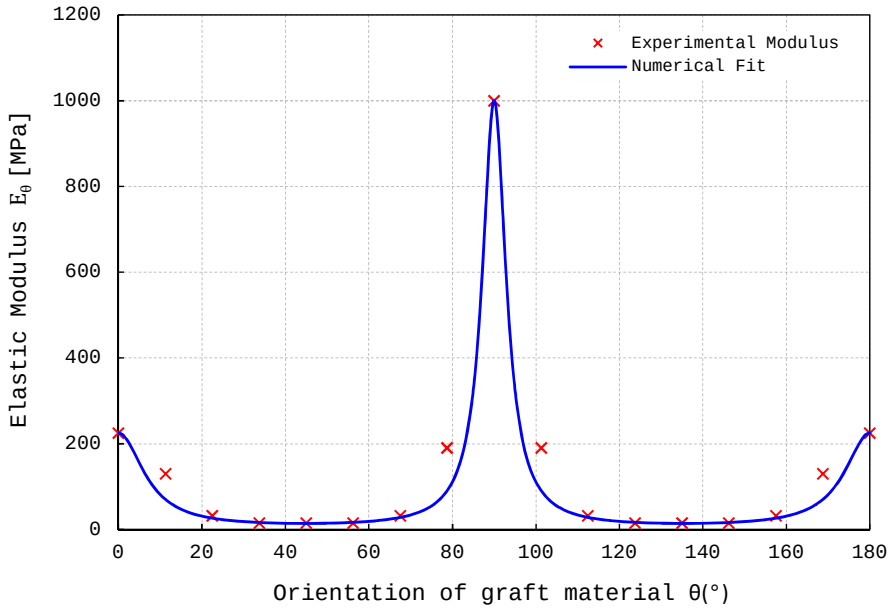


Figure 3.8: PET graft material characterisation as originally reported by Demanget [120]. Experimentally determined elastic moduli derived from uniaxial tensile tests of graft specimens at nine orientations (*red*), and numerical fit (*blue*). *Note*: mechanical response assumed to be symmetric about 90° orientation plane.

Given the material response, it is appropriate to consider the in-plane graft behaviour using an elastic orthotropic plane stress model following the form

$$\begin{pmatrix} \varepsilon_{LL} \\ \varepsilon_{CC} \\ 2\varepsilon_{LC} \end{pmatrix} = \begin{pmatrix} 1/E_L & -\frac{\nu_{LC}}{E_L} & 0 \\ -\frac{\nu_{CL}}{E_C} & 1/E_C & 0 \\ 0 & 0 & 1/G_{LC} \end{pmatrix} \begin{pmatrix} \sigma_{LL} \\ \sigma_{CC} \\ \sigma_{LC} \end{pmatrix} \tag{3.11}$$

where E_L is the longitudinal elastic modulus, E_C the transverse elastic modulus, ν_{LC} and ν_{CL} the major and minor Poisson's ratio, respectively, and G_{LC} the shear modulus.

To fully specify the parameters of the orthotropic elasticity model, the classical analysis of a lamina can be used

$$\frac{1}{E_\theta} = \frac{cos^4\theta}{E_L} + \frac{sin^4\theta}{E_C} + \frac{1}{4}\left(\frac{1}{G_{LC}} - \frac{2\nu_{LC}}{E_L}\right) sin^2\left(2\theta\right), \tag{3.12}$$

where E_L and E_C are taken directly from the reported tensile data in Figure 3.8, and ν_{LC} derived from plane tensile tests. A curve fitting routine is implemented to evaluate

the shear modulus G_{LC} as to achieve agreement with the reported experimental data. Using the material properties in Table 3.5, the constitutive relation gives good agreement with the experimental data given in Figure 3.8.

Table 3.5: Material properties of a PET graft based on data reported in [120].

Parameter	Values
Density ρ	650 Kg/m^3
Longitudinal elastic modulus E_L	225 MPa
Transverse elastic modulus E_C	1000 MPa
Poisson's ratio ν_{LC}	0.2
Shear modulus G_{LC}	3.6 MPa

It is also necessary to appropriately account for graft bending behaviour as a woven textile has negligible compressive stiffness compared to its tensile properties. Again, following the methods described by Demanget [161], this is achieved by artificially adjusting both the graft thickness and elastic moduli. Indeed, according to Kirchhoff-Love theory, the bending rigidity D of the graft (considered to be a shell) is specified as

$$D = \frac{Et^3}{12\,(1-\nu^2)}\,, \tag{3.13}$$

where E is the elastic modulus (E_L, E_C), t the graft thickness, and ν the Poisson's ratio. In this work, a scaling factor of 10 was applied: the graft thickness was reduced to achieve an appropriate bending behaviour, while the elastic moduli increased as to not inadvertently affect in-plane response. Finally, the orthotropic plane stress model described above was numerically implemented in Abaqus for all subsequent simulations employing the "Lamina" material model type.

Of course, the results described in this section reflect those presented elsewhere [120, 161], as they are based on the data and methods reported in those studies. Although those studies were dedicated to modelling iliac devices, it is appropriate to detail the applicable methodology here as to fully describe the computational framework for thoracic aortic stent-graft evaluation.

3.1.3 Arterial Material: Ascending Thoracic Aorta

Having described in the preceding sections the material behaviour of both the stent and graft constituents in the TEVAR domain, it is now necessary to detail the behaviour of arterial tissue with which stent-graft devices interact. Indeed, accurately modelling arterial tissue when developing numerical tools for stent-graft analysis is of critical importance; it is the pulsatile deformations of the vessel that largely influence device durability, and consequently, determines the long-term success of TEVAR treatment. Given the biological nature of vessels, and thus their highly complex structure, modelling this soft tissue is no trivial task.

Indeed, experimental characterisation of arterial tissue as well as the development of constitutive models describing its behaviour have been active areas of research for many decades. Such work, however, is beyond the scope of this study. Nevertheless, appropriate material properties and numerical models considering the most recent advances in soft tissue mechanics have been adopted for the computational framework presented here as to ensure a rigorous analysis of stent-graft behaviour.

3.1.3.1 Numerical implementation

In this work an incompressible, anisotropic, hyperelastic model has been adopted to describe the mechanical behaviour of the ascending thoracic aorta/aortic arch.[2] The implementation is based on the fibre-reinforced hyperelastic material model proposed by Holzapfel, Gasser, and Ogden [3, 4] (and so commonly referred to as the HGO model), which has been shown to accurately capture the behaviour of blood-vessel inflation under internal pressurisation. For completeness, this model is detailed below.

Briefly, the aortic tissue is assumed to be composed of a matrix material with two families of embedded fibres, each of which has a preferred direction. The fibre directions (γ) can be mathematically described using two unit vectors. The strain-energy function takes the form

[2] Detailed descriptions of hyperelastic materials can be found in [162]. Typical stress-stretch behaviour of hyperelastic arterial tissue is presented in Figure 3.11.

$$U = C_{10}\left(\bar{I}_1 - 3\right) + \frac{1}{D}\left(\frac{\left(J^{e\ell}\right)^2 - 1}{2} - lnJ^{e\ell}\right) + \frac{k_1}{2k_2}\sum_{\alpha=1}^{N}\left\{exp\left[k_2\left\langle\bar{E}_\alpha\right\rangle^2\right] - 1\right\}, \quad (3.14)$$

where

$$\bar{E}_\alpha \stackrel{\text{def}}{=} \kappa\left(\bar{I}_1 - 3\right) + (1 - 3\kappa)\left(\bar{I}_{4(\alpha\alpha)} - 1\right), \quad (3.15)$$

and $\bar{I}_1$ is the first deviatoric strain invariant, $J^{e\ell}$ is the elastic volume ratio, and $\bar{I}_{4(\alpha\alpha)}$ are pseudoinvariants of $\bar{C}$ and A_α (the directions of the fibres, noting the fibre orientation angle (γ) is part of $\bar{I}_{4(\alpha\alpha)}$).

Here, C_{10}, D, k_1, k_2, and κ are material parameters. C_{10} is a stress-like material parameter, D is inverse to the bulk modulus K, k_1 is a stress-like parameter, k_2 is a dimensionless parameter, and κ describes the level of fibre dispersion. For clarity, the material parameters defining the constitutive model are summarized in Table 3.6, as described by [163].

Table 3.6: Summary of HGO hyperelastic material model parameters as described in [163].

Material model parameter	Physical interpretation
C_{10} $(C_{10} > 0)$	Stress-like material parameter (Pa)
k_1 $(k_1 > 0)$	Stress-like parameter (Pa)
k_2 $(k_2 > 0)$	Dimensionless parameter
κ $(0 \leq \kappa \leq 1/3)$	Level of fibre dispersion
γ $(0 \leq \gamma \leq 90°)$	Fibre orientation angle (°)
K $(K > 0)$	Bulk modulus (Pa)

To ensure the correct implementation of this material model within the computational framework, a simulation representative of uniaxial arterial testing was conducted, following the strategy proposed by [4] and again in [152].

Briefly, the numerical analysis consists of representative arterial strips cut along their axial and circumferential directions subjected to uniaxial tension. The arterial strips are appropriately constrained as to ensure their end faces do not deform. Linear continuum hybrid elements (type C3D8H) are used to capture incompressible deformation. Finally,

the strips are assumed to be stress free in the reference configuration. An illustration defining the axial and circumferential test specimens is given in Figure 3.9 (left).

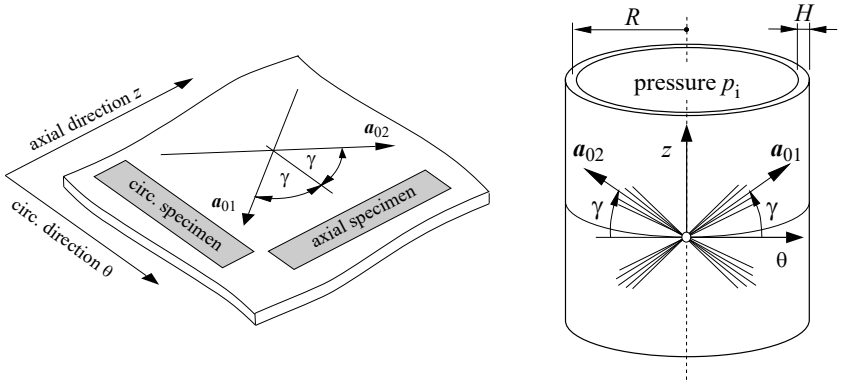


Figure 3.9: Schematic of arterial segments used to evaluate the fibre-reinforced hyperelastic material model. (Left) definition of axial and circumferential specimens for simulated uniaxial tensile tests. (Right) cylindrical artery definition for inflation testing. Highlighted are mean orientations and dispersion of collagen fibres. Image adapted from [4].

Given that the simulation strategy represents a physical test setup under load control, typical load-displacement data can be numerically obtained. Using this data, determining the stress-stretch relationship of the material can be determined following the methods originally described by Raghavan et al. [164] and again by Holzapfel et al. [165].

The stretch ratio λ was computed as l/L, where l and L are the prescribed gauge lengths in the loaded and unloaded configurations, respectively.

Based on global equilibrium, the incompressibility condition, and the numerical force-displacement data, it is possible to determine the associated Cauchy stress, denoted here as σ. Incompressibility requires $LWT = lwt$ (the dimensional parameters of the strip being analysed, in the unloaded and loaded configurations, respectively). Thus, $\sigma = f/wt$, and therefore the Cauchy stress is computed as

$$\sigma = \frac{f}{WT}\lambda \tag{3.16}$$

where f is the computed tensile force as output during the finite element analysis.

To evaluate the utility of this test case, the stress-stretch behaviour of three groups of ascending thoracic aortic tissue was assessed, with material properties based on experimental data reported by Haskett et al. [163]. Specifically, the three groups of tissue

correspond to three different age categories. The material parameters used to define the arterial behaviour for each group are given Table 3.7.

Table 3.7: HGO material parameters for ascending thoracic aortic tissue as reported in [163].

Group	C_{10} (kPa)	k_1 (MPa)	k_2	κ	$\gamma\,(^\circ)$
Ascending 1 $(0-30\ yrs)$	20.9	0.71	0.40	0.8	44.4
Ascending 2 $(30-60\ yrs)$	16.6	0.79	3.13	0.13	44.1
Ascending 3 $(60+yrs)$	44.6	2.07	93.33	0.18	45.5

By correctly implementing the fibre-reinforced hyperelastic material model in Abaqus, the stress-stretch response of arterial tissue to loading can be evaluated. As demonstrated in Figure 3.10, it is possible to study the stress state of arterial tissue. Indeed, the general results shown here are in agreement with those reported by Gasser et al. [4]. Regarding the particular stress distribution reported, it is expected that as the material is (very) non-linear, edge-effects can be anticipated due to the prescribed loading conditions. It is likely that the global stress distribution is thus influenced by such edge-effects. In any case, the resulting stress comes primarily from the collagen fibres, such that some of the fibres are highly stretched at the simulated arterial strip ends.

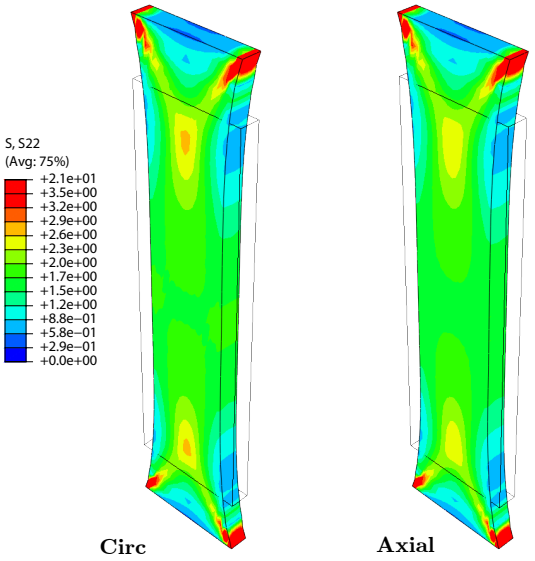


Figure 3.10: Finite element analysis of representative ascending thoracic aortic tissue strips subjected to uniaxial tensile load. Results shown are Cauchy stress (MPa) in the direction of applied load for Ascending Group 3: (left) circumferential direction, (right) axial direction. Stress-free reference configuration shown as a wireframe.

Comparatively, a more valuable output of this simulation strategy is revealed when assessing the stress-stretch response of the three age groups investigated in this test case, as seen in Figure 3.11. The behaviour reported here shows the nearly equivalent loading response of ascending thoracic aortic tissue in both the circumferential and axial directions, as well as the increased stiffness in arterial tissue with aging. These numerical results are in direct agreement with Haskett et al. [163] and have also been reported by other groups (for example, see [166, 167]).

For the remainder of the work presented throughout this Chapter where ascending thoracic aortic tissue is considered, the material properties of Ascending Group 3 are used.

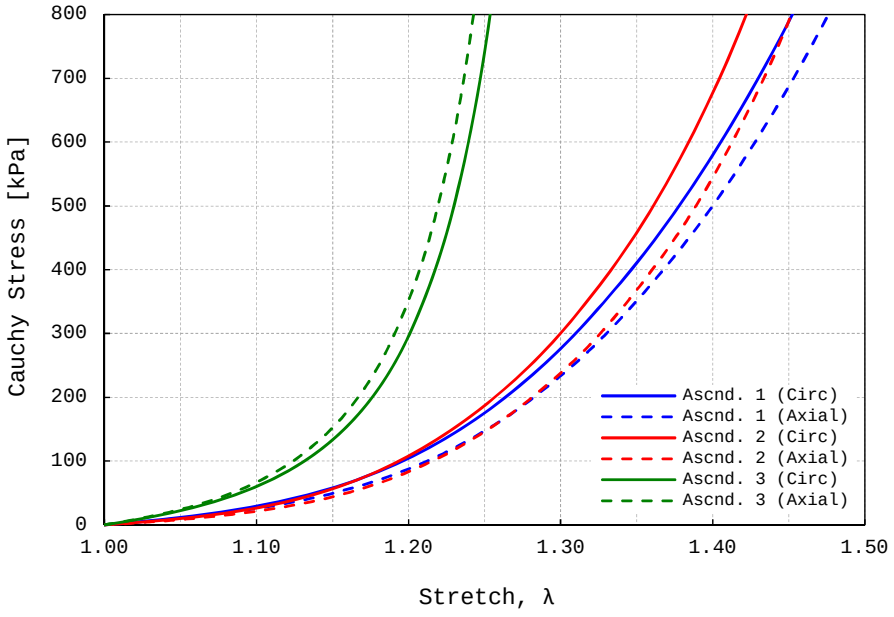


Figure 3.11: Simulated uniaxial stress-stretch response of ascending thoracic aortic tissue in the circumferential and axial directions for three age groups.

To elaborate the arterial modelling techniques described above, an additional simulation strategy is developed to represent a scenario more relevant to investigating stent-graft behaviour. Specifically, a cylindrical arterial segment subjected to physiological blood pressure is considered. A representative illustration is shown in Figure 3.9 (right). Such a simulation is of particular importance given that it is the expansion and contraction of the vessel (due to blood pressure) which dominates the fatigue life of stent-graft devices. As such, accurately capturing this response is critical when assessing stent-graft behaviour.

For the case of vessel loading due to blood pressure, a simple cylindrical artery was considered. Appropriate boundary conditions were imposed on the ends of the arterial segment to restrict its motion to the radial direction. In a single analysis step, a uniform pressure distribution was applied onto the internal arterial surface. Multiple systolic/diastolic pressures were considered to capture a range of vessel inflation behaviour. Specifically, four simulations were conducted at: 50-90mmHg, 80-120mmHg, 110-150mmHg, and 80-160mmHg applied pressure. To accurately capture the response of the arterial segment (considering the fibre-reinforced hyperelastic material model employed) a local coordinate system was assigned to each (artery) finite element, as to correctly account for fibre orientation. Specific details are provided below.

As reported by Auricchio and co-workers, and described here for completeness, if considering the artery as a cylindrical tube, its geometry can be described by using a cylindrical coordinate system defined by three unit vectors e_1, e_2, e_3, which correspond to the radial, circumferential and axial directions, respectively. Under this idealisation, collagen fibres are supposed to be helically disposed with respect to the circumferential direction. In the undeformed configuration, the fibre orientations are locally defined by two unit vectors a_{01} and a_{02} lying in the plane tangent to the cylindrical surface which contains the circumferential and the axial directions, e_2, e_3. In this plane, the unit vectors a_{01} and a_{02} form constant angles $\pm\gamma$ with the circumferential direction. For this particular case, the components of the unit vectors a_{01} and a_{02} with respect to the cylindrical coordinate system (e_1, e_2, e_3) are as follows:

$$a_{01} = (0, \cos\gamma, \sin\gamma)\,, \quad a_{02} = (0, \cos\gamma, \text{-}\sin\gamma)\,. \tag{3.17}$$

Therefore, the definition of the fibre orientation is related to the definition of the local coordinate system e_1, e_2, e_3, and γ [168].

To assess the response of the arterial segment to inflation, specific nodal coordinates are tracked on the inner surface of the finite element mesh to compute the change in vessel diameter. Using this data, it is possible to quantify the response of an artery to pressure loading. Specifically, distensibility [169] and compliance [72] are reported here and take the form

$$Distensibility = \frac{maximum\ lumen\ area\ - minimum\ lumen\ area}{minimum\ lumen\ area\ \times pulse\ pressure}\ [\mathrm{mmHg}^{-1}] \quad (3.18)$$

where *pulse pressure* is calculated as the difference between prescribed systolic and diastolic pressure, and

$$\frac{\%Compliance}{100\ \mathrm{mmHg}} = \frac{(D_{P2} - D_{P1}) \times 10^4}{(D_{P1}\,(P_2 - P_1))} \quad (3.19)$$

where D_{P1} is the inner vessel diameter at diastolic pressure P1, and D_{P2} is the inner vessel diameter at systolic pressure P2 (with pressures in mmHg).

As can be seen in Figure 3.12, the behaviour of the cylindrical arterial segment demonstrates an increased stiffness when subjected to an increased pressure range, in agreement with the results reported in Figure 3.11. Furthermore, the quantified values of distensibility and compliance are in agreement with those reported in the literature [169] and used by regulatory agencies [72].

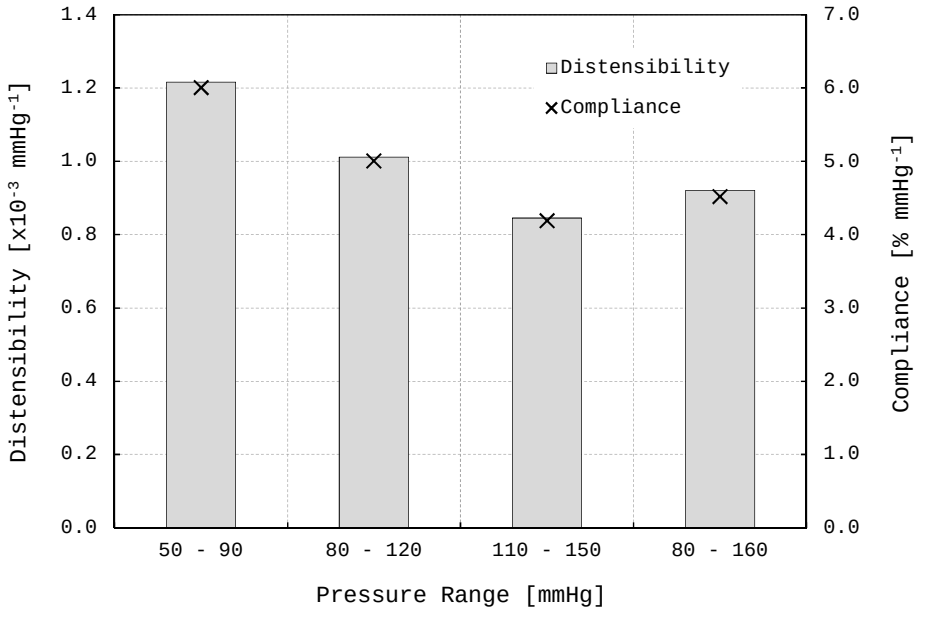


Figure 3.12: Simulated response of a cylindrical ascending thoracic aortic tissue segment subjected to internal pressurisation. Distensibility and compliance values at four pressure ranges for Ascending Group 3.

3.2 Stent-Graft Performance

Using the fundamental building blocks established in the previous section, it is possible to investigate key performance characteristics of stent-graft devices using numerical techniques of increasing complexity. In this section, three FEA strategies to evaluate stent-graft behaviour are established. Specifically, simulations to assess stent crimping, stent-graft bending, and stent deployment into an artery are presented. To demonstrate the utility of these computational tools, the direct comparison of two representative devices closely mimicking commercially available stent-grafts used in the treatment of TAAs is performed.

3.2.1 Stent Crimping

The principal characteristic of a stent is its ability to be packaged into a delivery catheter for minimally invasive surgery. As such, an analysis of the stresses and strains within a stent component - as experienced during packaging - is essential to ensure that the device will behave as expected once deployed. For example, material plasticity should be minimized such that the device will indeed recover its original shape. In the same manner, it is necessary to examine the radial outward forces exerted by a stent, and hence determine possible fixation strengths. A simulated stent crimping test is well suited to examine these characteristics. The methods described in this section are based upon the reported methodologies of De Bock et al. [79], and are concerned with analysing typical Z-stent designs.

To detail the function of the simulation, a study investigating radial crimping of different Z-stent geometries and materials is presented hereafter. Specifically, the maximum von Mises stress for both a 12- and 5-unit stent ring geometry, and for 316L stainless steel and nitinol (NiTi) material selections, are assessed at a 70% diameter reduction. Likewise, the radial outward force exerted by a stent during crimping and subsequent deployment is determined for both stent rings. The graft is not considered in this analysis.

3.2.1.1 Materials and methods

Stent geometry: To begin, it is first necessary to define the geometry of the stent structure. Demanget et al. [120] demonstrated that this can be achieved using a set of parametric equations where design features such as stent height, stent radius, and number of "repeating units" can be controlled. In the case of Z-stent designs, a triplet of coordinates (x, y, z) defining the midline of a stent geometry can be generated using the following equations:

$$x = R_s \cos \beta, \tag{3.20}$$

$$y = R_s \sin \beta, \tag{3.21}$$

$$z = \frac{H_s}{2} \sin \left(\beta N_p \right), \tag{3.22}$$

where R_s is the radius of the stent, H_s the stent height, N_p the number of repeating units, and β representing the angle between the first and current point in the xy-plane as incremented from 0 to 2π.

These equations can effectively be implemented in the Abaqus/CAE software package via a dedicated Python script to represent the Z-stent in a virtual environment. Using Abaqus/CAE, it is also possible to discretise the stent structure into a number of finite elements, also known as a finite element (FE) mesh. As stents are predominantly loaded in bending, the reduced integration linear hexahedron element (type C3D8R) can capture its physical behaviour with minimal computational cost, and so was employed here. The visualisation of the stent geometry parameters described above and their realisation as an FE mesh in Abaqus are illustrated in Figure 3.13.

The stents analysed in this study approximate two commercially available designs: the Cook Zenith TX2 (Cook Medical, Bloomington, IN, USA) and the Medtronic Valiant (Medtronic Inc., Santa Rosa, CA, USA). Geometries of these devices have been adapted from the available literature [53] and are presented in Table 3.8.

Material properties: Two typical stent materials, as described in Section 3.1, have been investigated in this study. For the Medtronic Valiant device, the calibrated nitinol user material subroutine whose parameters are defined in Table 3.3 was used. For the Cook

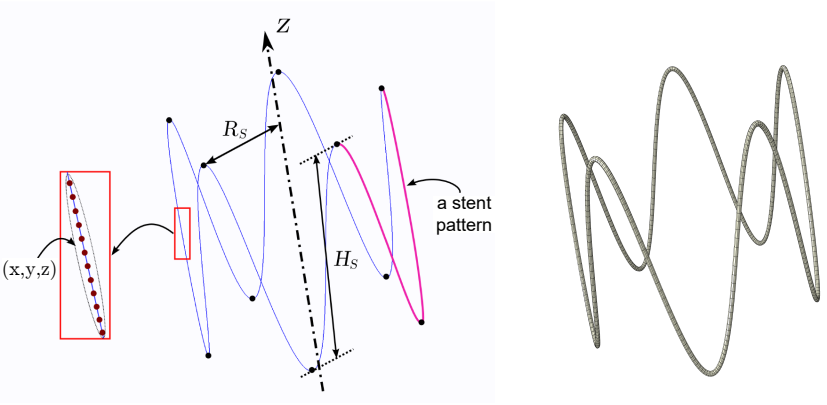


Figure 3.13: Virtual stent development for computational analysis. (Left) Z-stent geometry definition as described by Demanget et al., and (right) corresponding finite element mesh generated in Abaqus. Image adapted from [120].

Table 3.8: Stent geometric and computational features (adapted) [53].

Parameter	Cook Zenith TX2	Medtronic Valiant
Stent height H_s	14 mm	14 mm
Stent radius R_s	16 mm	16 mm
Number N_p	12	5
Wire radius	0.175 mm	0.175 mm
Material	316L Stainless Steel	Nitinol
Number of elements	26112	16000

Zenith TX2 device, the use of 316L stainless steel was considered, and an elastic-perfectly plastic material model was defined based on properties specified in Table 3.4.

Numerical implementation: To perform radial crimping of a stent, a so-called virtual "crimp tool" was created in Abaqus/CAE. This tool was modelled with rigid surface elements (type SFM3D4R) and moved in displacement control whereby its effective opening diameter could be defined. Stents were concentrically positioned within this tool and so were subjected to contact-driven crimping via the inward radial displacements of the crimping elements, as illustrated in Figure 3.14. Deployment was subsequently simulated via outward radial displacements of the tool (i.e. increasing its effective opening diameter from the crimped position), allowing the stent to recover any elastic deformations. Stents were discretised using approximately 26112 and 16000 C3D8R elements

(Zenith TX2 and Valiant, respectively), with six elements across the geometry thickness. A mesh density study was performed confirming the accuracy of mesh refinement (details reported in Appendix A). To prevent rigid body motion, one node of the stent was fixed in the z- and θ-directions.

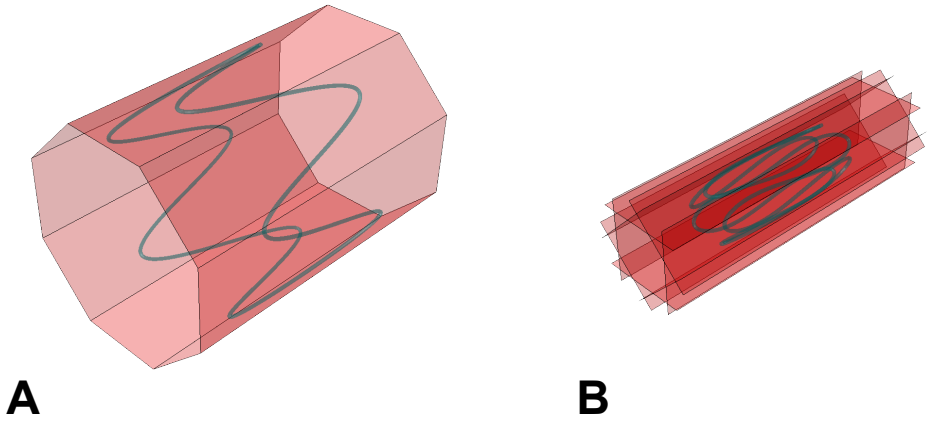


Figure 3.14: Representative stent crimping via rigid surface elements forming a so-called "crimp tool". (A) The stent is positioned concentrically with the crimp tool, and (B) is subjected to contact-driven crimping via the inward radial displacements of the crimping elements. Deployment simulated via outward radial displacements of the tool (i.e. increasing the effective opening diameter from the crimped position; not shown). Image adapted from [79].

Contact conditions defined during the simulation included device contact with the rigid crimp tool elements (note that stent self-contact was not evident in these analyses). Contact was implemented using the contact pairs algorithm in Abaqus with finite sliding and surface-to-surface contact discretisation. Contact constraints were enforced via the penalty method.[3] Behaviour in the normal direction was defined using a linear "hard" contact pressure-overclosure relationship, with a stiffness scaling factor of $S_f = 0.1$. Behaviour in the tangential direction was defined using a penalty friction formulation, with a coefficient of friction $\mu = 0.1$.

Maximum von Mises stress was determined at the final crimped position equivalent to a diameter reduction of 70%. The radial outward force exerted by the stent (i.e. the equivalent force exerted onto an artery wall due to device oversizing) was calculated by summing the radial force vectors imposed onto each crimp tool surface during the crimping/deployment steps.

[3]The penalty method is a stiff approximation of hard contact.

Simulations were performed using the general-purpose solver employing an implicit integration scheme (Abaqus/Standard v2017), and were implemented as a nonlinear static analysis. Automatic incrementation was applied, with an initial increment size of $t = 0.01$ and a maximum increment size of $t = 0.1$.

3.2.1.2 Results and discussion

Maximum von Mises stress: The maximum von Mises stress experienced during radial compression for the Zenith TX2 and Valiant stents are given in Table 3.9.

Table 3.9: Maximum von Mises stress of Zenith and Valiant stents at 70% diameter reduction.

Cook Zenith TX2	Medronic Valiant
1550 MPa	840 MPa

Employing the use of a so-called crimp tool makes it possible to evaluate the stresses and strains experienced by a stent device during loading. For the test case presented here, it is not appropriate to make a direct comparison between devices given the differences in material behaviour. A more useful implementation of this specific simulation methodology would be to assess the effects of geometrical changes to a specific device design. Nevertheless, it is possible to note that plasticity has been induced in the Zenith TX2 while the Valiant device remains (super)elastic. These results are further expanded upon by assessing the radial outward force, as discussed below.

Radial outward force: The crimping-deployment (loading-unloading) curves quantifying the radial outward force of both Zenith TX2 and Valiant stent devices are given in Figure 3.15.

Assessing these results, it is possible to make several observations. From a material performance perspective, it is obvious that the Valiant device exhibits the aforementioned superelastic behaviour, in that it fully recovers to its original diameter following the typically loading/unloading path. Comparatively, the Zenith TX2 device is loaded beyond its elastic limit, and therefore exhibits permanent deformation upon unloading. From a functional perspective, it is apparent that the Valiant device exerts significantly less radial outward force than its Zenith TX2 counterpart. This is attributed to the fact that the material of the Valiant device (nitinol) is far less stiff than that of the Zenith TX2

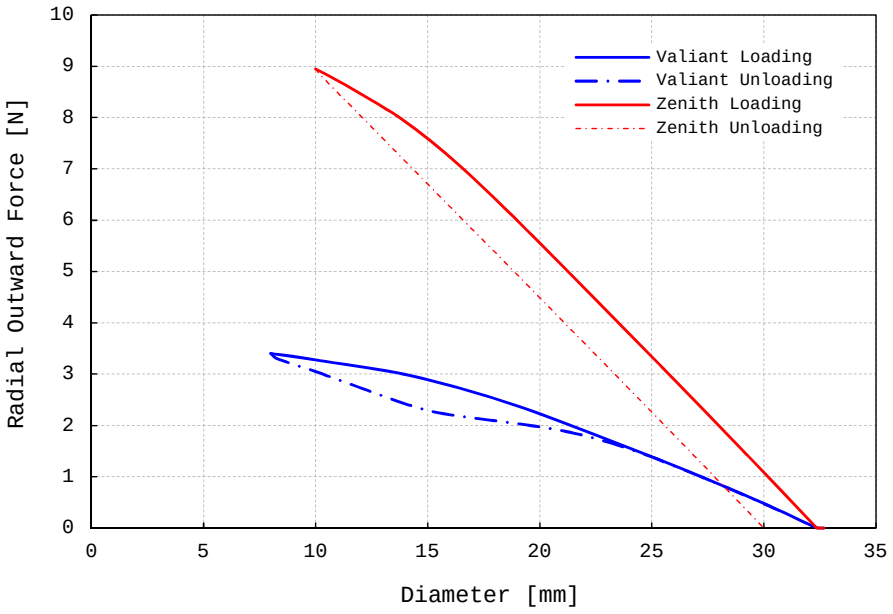


Figure 3.15: Numerically determined radial outward force of representative Cook Zenith TX2 and Medtronic Valiant stent devices subjected to radial loading to 70% diameter reduction followed by unloading.

(stainless steel). This is an important observation when considering stent-graft design, as it is essential that the device exhibits sufficient radial force to maintain fixation with the vessel wall, but does not induce vessel damage due to excessive loads.

In addition to assessing the global behaviour of devices when subjected to radial load, it is also possible to investigate the local behaviour of a device during any portion of the loading cycle. For example, the behaviour of a device can be assessed in regions of interest, such as the apices (commonly known as stent "crowns"), where maximal stresses and strains are likely to occur. Such a global-local inspection has been performed for the Valiant device, and is illustrated in Figure 3.16.

Assessing the region of interest in detail, it is possible to extract the specific stress-strain response on an element-by-element basis to assess material behavior. Indeed, analysing the performance of the Valiant stent reveals the distinctive superelastic stress-strain behaviour in the region of interest, as demonstrated in Figure 3.17.

Summary: A strategy to simulate stent crimping has successfully been implemented using Abaqus. Using these techniques, the influence of stent geometry and materials on anticipated stress distributions and radial forces can be investigated in detail.

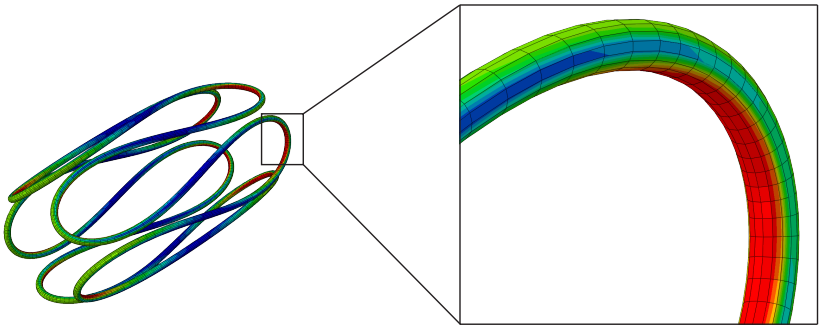


Figure 3.16: Computed stress distribution due to radial load. (Left) global evaluation of representative 5-unit Medtronic Valiant stent ring, and (right) local evaluation of a specified region of interest. *Note*: crimp tool not shown.

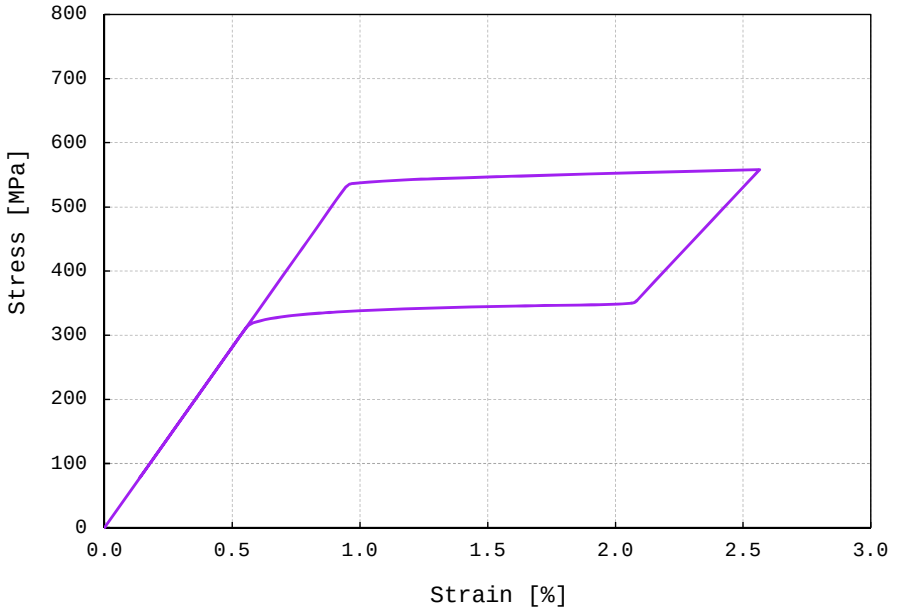


Figure 3.17: Computed stress-strain data at a single finite element located at a specified region of interest (stent apex) in a representative Medtronic Valiant Z-stent.

3.2.2 Stent-Graft Bending

Stent-graft flexibility is a primary consideration in device design: the stent-graft should accurately conform to the target vessel anatomy and should not impede blood flow. A stent-graft bending test is well suited to evaluate this behaviour. The methods described in this section are based upon the reported methodologies of Demanget et al. [53, 120], and are concerned with analysing both the Zenith TX2 and Valiant stent-graft designs described above.

To demonstrate the utility of this simulation, a study reporting on stent-graft response to bending is presented. To quantify the effects of device design on bending characteristics, the metrics *lumen reduction* (LR) and *torque required for bending* (TRB) are employed.

3.2.2.1 Materials and methods

For these (considerably larger) simulations, stent deformations were assumed to be elastic (i.e. plasticity not included within the prescribed material models). Likewise, stent structures were modelled with linear Timoshenko beam elements (type B31 in Abaqus), which have been demonstrated to give similar results to continuum elements with greater computational efficiency [170]. The graft was considered to be a cylindrical shell discretised with 59000 shell elements (type S4R), whose behaviour is described by the elastic orthotropic plane stress model outlined in Section 3.1.2. The stent-grafts were modelled to be 120mm in length, and were each constructed with six stent rings uniformly distributed along the graft length. A surface-based tie constraint was imposed between the stents and graft to ensure connection between meshes, mimicking suture attachments.

Numerical implementation: To simulate stent-graft bending, the stent ring at each graft extremity was considered to be a rigid body controlled by a reference point. Motions were applied directly onto the reference points, and consequently the two rigid bodies. Opposite rotations were applied about the x-axis, until a bending angle (α) of 135° was reached. Rotations in the y- and z-axes were constrained, as were translations along the x- and y-axes to avoid rigid body motions. Translation along the z-axis was left free so as to prevent erroneous tension in the longitudinal direction. These boundary conditions are illustrated in Figure 3.18. All contact was enforced using the general contact algorithm, with frictionless tangential behaviour. Self-contact was imposed in order to eliminate self-penetration of the stent-graft components. Simulations were performed using the general-purpose solver employing an explicit integration scheme with automatic incrementation (Abaqus/Explicit v2017). The explicit solver was chosen to avoid convergence issues as the analysis consists of complex geometric, material, and contact nonlinearities. Mass scaling was applied such that the stable time increment remained larger than 2.5e−06 throughout the analysis (step time of $t = 5s$). Simulations were considered to be a quasi-static analysis with negligible kinetic energy.

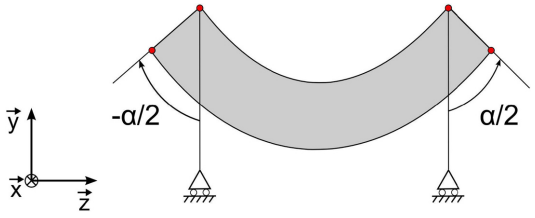


Figure 3.18: Schematic illustration of boundary conditions imposed for simulated stent-graft bending. Image adapted from [120]. *Note*: α = bending angle.

3.2.2.2 Results and discussion

The bending behaviour of representative Zenith TX2 and Valiant devices is illustrated in Figure 3.19. From a qualitative perspective, it is apparent that stent design influences stent-graft deformation during bending. For example, the Zenith TX2 design - consisting of 12 repeating units - suffers from greater lumen reduction when bent (i.e. a decrease in cross-sectional area) when compared to its Valiant counterpart (which has fewer repeating units). This suggests that decreasing the number of repeating units may improve device performance when used in highly curved regions such as the aortic arch (i.e. reduce the likelihood of impeding blood flow). In the same manner, it is apparent that decreasing the number of repeating units in the stent design may offer better conformability, following the natural vascular anatomy more closely (as made evident by the smoother inner curvature of the Valiant device when bent).

In addition to qualitatively assessing device behaviour, the quantitative measures *lumen reduction* and *torque required for bending*, as proposed in [120], are adopted here. Briefly, to evaluate lumen reduction, a dedicated workflow is implemented capable of tracking the cross-sectional area of the inner graft surface at a region of interest throughout bending. The quantitative metric is calculated using the equation

$$LR = 100 \times \left(1 - \frac{S}{S_o}\right) [\%] \tag{3.23}$$

where S_o corresponds to the cross-sectional area in the undeformed state (i.e. prior to bending initiation), and S corresponds to that cross-sectional area at the maximal bending state (i.e. $\alpha = 135°$). The maximum lumen reduction of the Zenith TX2 was determined to be 24%, while that of the Valiant device was determined to be 11%. This

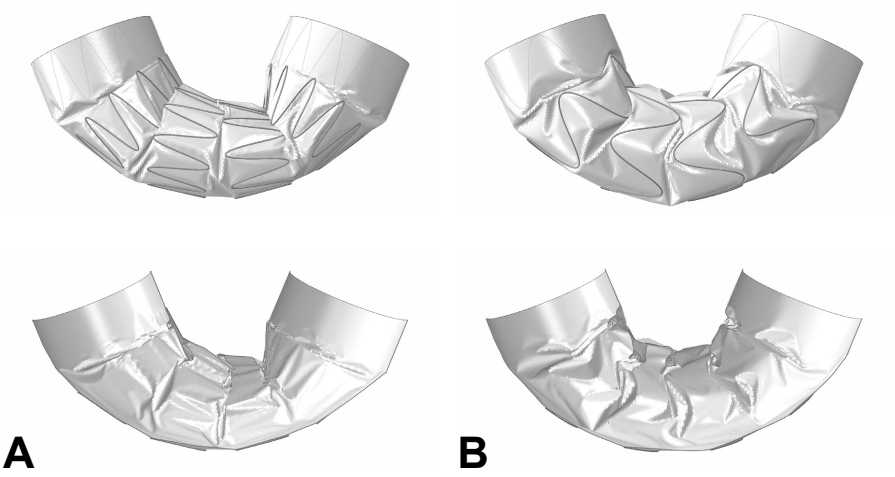


Figure 3.19: Simulated stent-graft behaviour during bending: (A) Zenith TX2 and (B) Valiant devices. Shown are deformed finite element meshes of the full devices (*top panel*), and device cross-sections (*bottom panel*) revealing inner graft lumen.

again suggests the potential clinical superiority of the Valiant device over the Zenith TX2 when subjected to excessive bending. Results are shown in Figure 3.20.

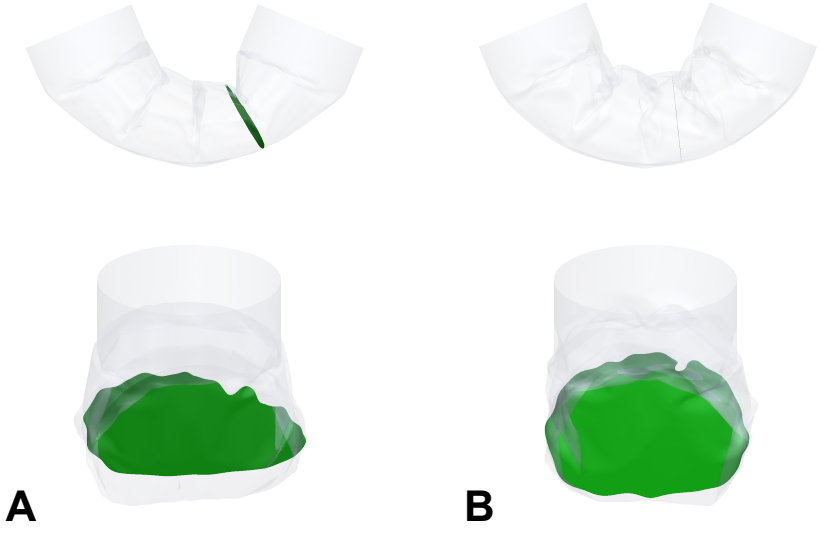


Figure 3.20: Stent-graft lumen reduction during bending. Comparison of (A) Zenith TX2, and (B) Valiant devices at $\alpha = 135°$. Highlighted are tracked graft cross-sections (*green*).

To evaluate the torque required for bending, reaction moments were computed at the reference points controlling the rigid body stents (as output by Abaqus). The evolution of the reaction moments for both the Zenith TX2 and Valiant devices are given in Figure 3.21. The apparent "softening" of the Zenith device (i.e. reduction in TRB

for $\alpha > 105°$) is associated with stent deformation behaviour during bending. Up to $\alpha = 105°$, Zenith stents generally maintain their circular cross-section. Beyond $\alpha = 105°$, these stents experience non-radial lumen reductions (as demonstrated in Figure 3.20) to which this softening is attributed.

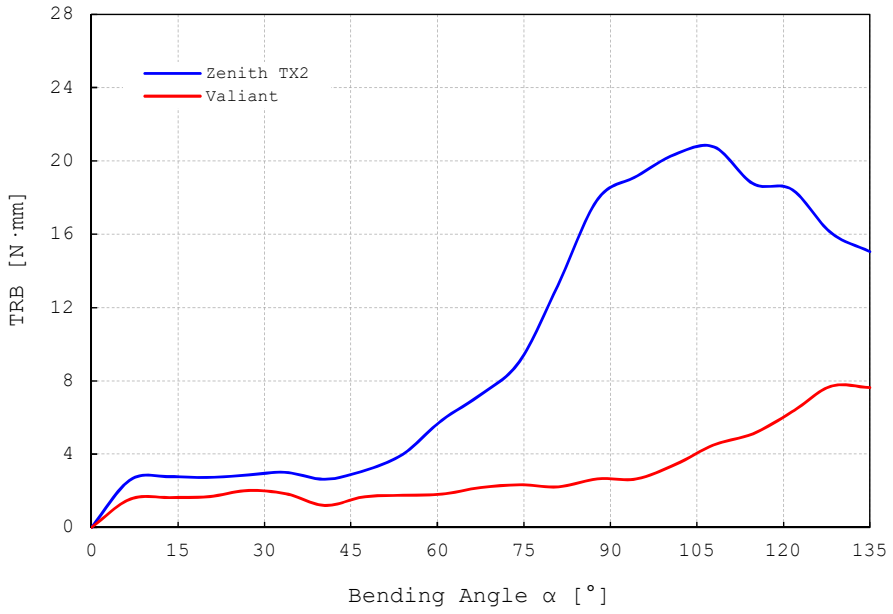


Figure 3.21: Quantitative assessment of stent-graft flexibility. Computed torque required for bending (TRB) for Zenith TX2 and Valiant stent-graft devices to $\alpha = 135°$.

Similar to the trends of lumen reduction, the representative Valiant device demonstrates the potential for clinical superiority, as it can be considered to have greater flexibility (i.e. less force required to induce bending) than its Zenith TX2 counterpart. This performance metric certainly has clinical relevance: a more flexible device will exhibit superior conformability to the vessel wall, in turn improving the likelihood of sealing the diseased portion of the aorta [81]. Furthermore, a more flexible device is less likely to artificiality 'straighten' the vessel, lending to a more natural anatomy after implantation.

Summary: A strategy to simulate stent-graft bending has been successfully implemented in Abaqus based upon the methods proposed by Demanget et al. [120]. Indeed, the procedures described above enable the analysis of both stent and graft contributions to the overall behaviour of a stent-graft device.

3.2.3 Stent Deployment into an Artery

Employing the crimping methodologies outlined in Section 3.2.1, it is also possible to simulate stent deployment into an artery. Conducting such a simulation enables the effect of stent design on the resulting (post-implantation) arterial wall stresses to be evaluated. This is of clinical significance given that excessive radial forces on the arterial wall, and thus wall stresses, can lead to vessel damage and aortic neck dilation [77, 78]. The methods described in this section are based upon the reported methodologies of Azaouzi et al. [150], however, are concerned with analysing typical Z-stent designs.

To demonstrate the utility of this simulation, a study analysing the effects of device type and oversizing on arterial wall stresses is presented below. Specifically, maximal arterial stresses are compared for the two Z-stent designs implanted into a cylindrical artery segment at 10%, 20%, 30%, and 40% oversizing (i.e. with a nominal stent outer diameter greater than vessel inner diameter, as is common in clinical practice). For simplicity, the graft is not considered in this simulation as it does not directly influence stent, and therefore artery, behaviour upon deployment.

3.2.3.1 Materials and methods

Model geometry: The Z-stent geometries were identical to those presented in the sections above. Arteries were modelled as simple cylinders and discretised with hybrid continuum elements (type C3D8H in Abaqus), with four elements across its (wall) thickness. Again, a mesh density study was performed confirming the accuracy of mesh refinement. For the sake of simplicity, arteries were assumed to comprise only a single arterial layer (i.e. the independent behaviour of the arterial layers was not accounted for). Note that the artery diameter is varied to define the level of oversizing, while the stent geometry remains constant.

Material properties: Both Zenith TX2 and Valiant devices are considered whose deformations are assumed to be elastic (i.e. plasticity not included within the prescribed material models). The mechanical behaviour of the artery was described using the anisotropic fibre-reinforced hyperelastic constitutive model detailed in Section 3.1.3. Note that the artery is assumed to be in a stress-free state in the initial configuration.

Numerical implementation: To virtually implant a stent into an artery, a simplified deployment procedure was performed. Briefly, the oversized stent was positioned concentrically over the target artery. The crimp tool methodology described in Section 3.2.1 was then employed to crimp the stent to an effective outer diameter less than that of the artery inner diameter (here, the crimp tool was discretised with 100 elements around its circumference). Then, the diameter of the crimp tool was gradually increased, allowing the stent to expand (deploy) into the arterial wall as it recovers its elastic deformations.

Contact conditions for the device include contact with the crimp tool and stent-artery contact (note that stent self-contact was not evident in these analyses, and so was not specified). In the first step of the analysis (stent crimping), only contact between the crimp tool and stent was activated. In the second step (stent deployment), contact between the artery and stent was activated, thereby "implanting" the device (note that no contact was defined between the crimp tool and artery). All contact was implemented using the contact pairs algorithm with finite sliding and surface-to-surface contact discretisation. Contact constraints were enforced via the penalty method, as described in Section 3.2.1.1. Boundary conditions, including crimp tool displacements, were defined in the cylindrical coordinate system. To prevent rigid body motion, one node of the stent was fixed in the z- and θ-directions. Likewise, artery ends were constrained in the axial and tangential directions, only allowing radial displacements. Von Mises stress distributions in the artery after stent deployment were determined. The deployment procedure is illustrated in Figure 3.22. As per section 3.2.1.1, simulations were performed as a nonlinear static analysis using Abaqus/Standard v2017.

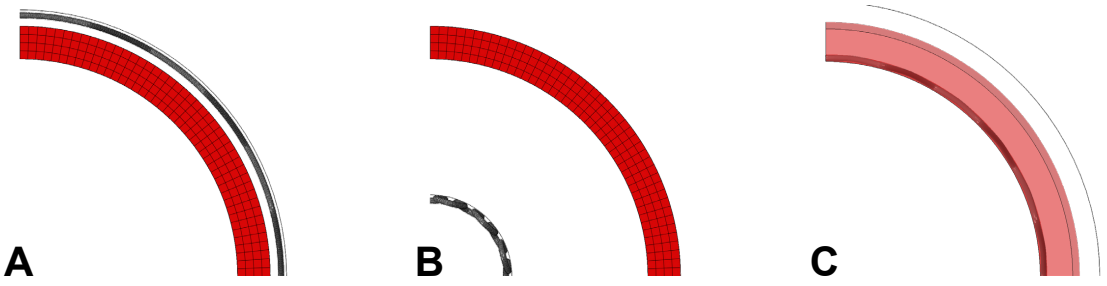


Figure 3.22: Simulation procedure for stent deployment into an artery. Depicted are the stent, artery, and crimp tool. (A) *Initial condition*: oversized stent and crimp tool positioned concentrically outside the target artery. (B) *Step 1*: stent diameter reduced via crimp tool contact. (C) *Step 2*: crimp tool radially expanded and stent-artery contact activated to effectively "implant" the stent (note: artery shading is translucent for stent visualisation, and no contact defined between crimp tool and artery). Quarter sections shown, as viewed along the longitudinal axis.

3.2.3.2 Results and discussion

The maximum von Mises stress in the arterial wall resulting from deployment of representative Z-stent type devices at various degrees of oversizing are reported in Figure 3.23. These findings demonstrate that deployment of the Valiant device results in lower arterial stresses at all oversizing configurations when compared to its Zenith TX2 counterpart. Furthermore, the difference in maximum arterial stresses between device types becomes (somewhat) more pronounced as the amount of oversizing increases. For completeness, the maximum device stress post-deployment is also reported.

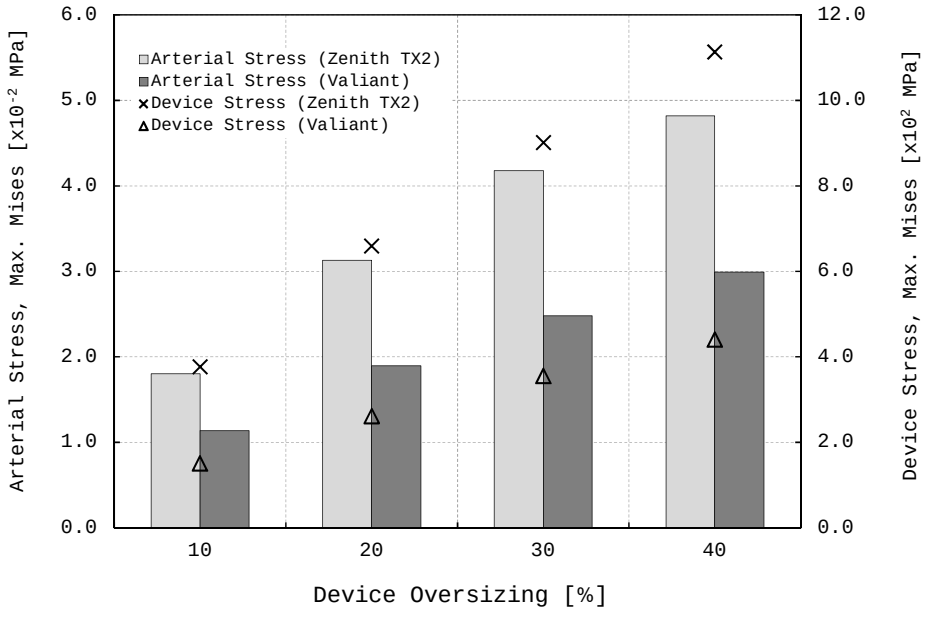


Figure 3.23: Maximum arterial and device von Mises stress resulting from Zenith TX2 and Valiant stent deployment into a cylindrical thoracic aortic segment at four levels of oversizing.

The underlying mechanism which can account for this behaviour is the difference in radial outward force exerted by the different stent types onto the artery. The distribution of arterial stresses due to stent deployment are given in Figure 3.24. From this plot, it is evident that the 5-unit Valiant design does not result in areas of localized stress concentrations, whereas the 12-unit Zenith TX2 design concentrates outward stent forces at the device apices. These findings have clinical implications: stent deployment should not impart excessive forces, and thus stresses, on the vessel wall, but rather only those necessary to prevent device migration.

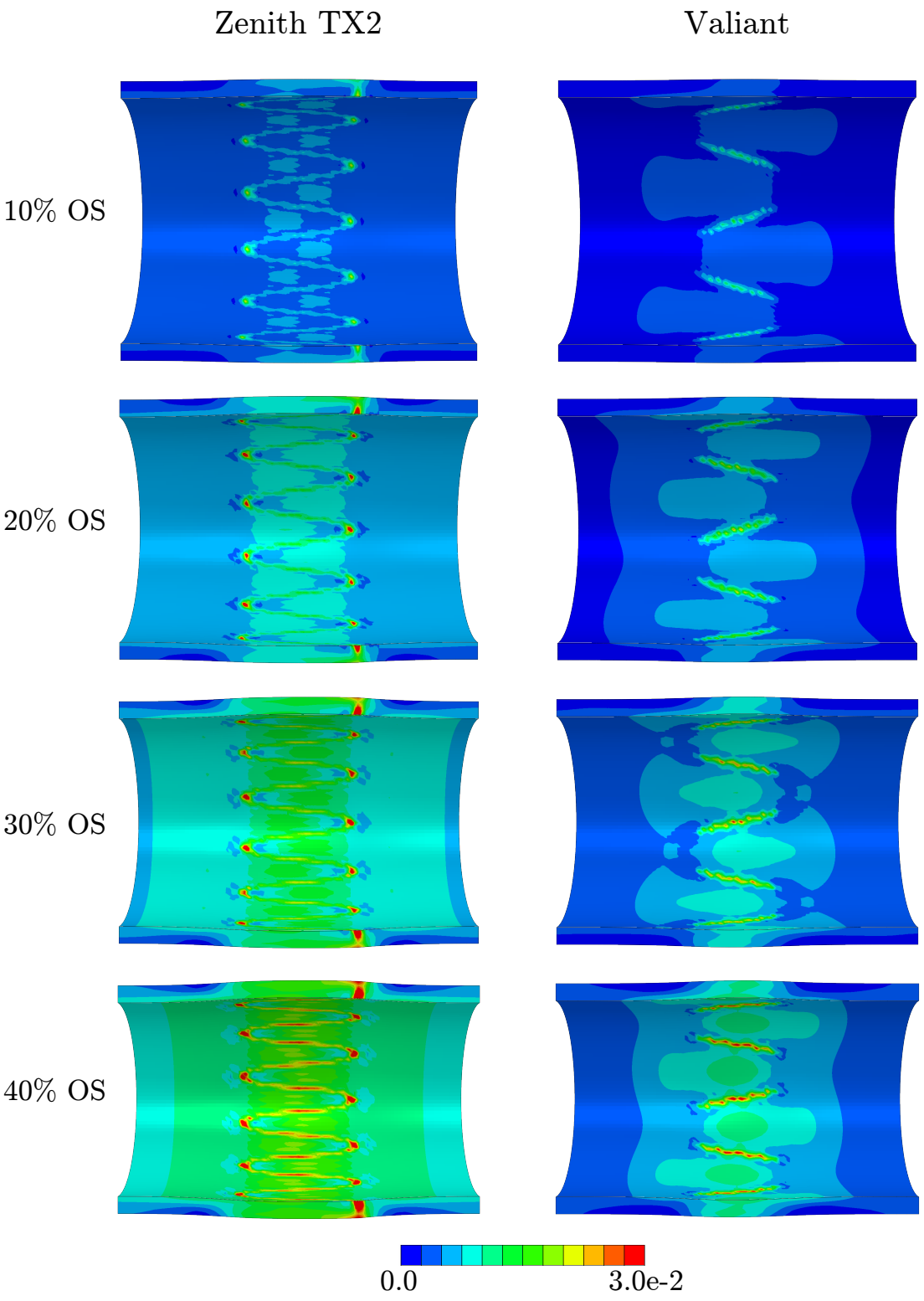


Figure 3.24: Influence of stent design and oversizing (OS) on arterial stresses post-device implantation. Von Mises stress contour plots (MPa) of an ascending thoracic aortic segment at 10%, 20%, 30%, and 40% OS for (*left*) Zenith TX2 and (*right*) Valiant device types. Shown are the arterial cross-sections, as viewed perpendicular to the longitudinal axis.

Summary: Building upon the methods described in Section 3.2.1 and employing the material model described in Section 3.1.3, techniques to virtually implant a stent into an artery have been successfully established.

3.3 Parallel Stent-Graft Deployment

Employing the previously described methods, a novel study is now introduced investigating the behaviour of stent-graft devices deployed in a so-called "parallel" configuration. First, the clinical motivation for analysing such behaviour is presented. Subsequently, the computational tools to conduct the analysis are outlined. Finally, results comparing the aforementioned Zenith TX2 and Valiant devices when deployed in a parallel configuration with a secondary device are reported and discussed.

3.3.1 Clinical Motivation

The push within interventional radiology to provide endovascular treatment in more and in increasingly complex cases has been met with numerous challenges. Indeed, TEVAR of aneurysms located along the ascending aorta and aortic arch is associated with significant risk due to the complex biomechanics and morphology of the vascular anatomy in this region. Nevertheless, cases are found in the literature reporting on the use of conventional stent-grafts devices to treat ascending and aortic arch aneurysms [46]. These procedures involve the deployment of stent-grafts in a parallel configuration, and have been termed chimney thoracic endovascular aortic repair (ch-TEVAR) [45]. A representative illustration of this surgical technique is shown in Figure 3.25.

When electing to perform such a procedure, the correct selection of both the main graft (MG) and chimney graft (CG) is of paramount importance. Should the devices be inappropriately sized or present with excessive radial outward force, there is significant risk of: (*i*) the formation of so-called "gutters", (*ii*) excessive compression of the chimney graft, and/or (*iii*) endograft infolding. Gutters refer to the apparent gaps which may form between the MG, CG, and artery wall, thereby rendering the surgical intervention ineffective (i.e. type 1a endoleak where blood can continue to flow to the aneurysm). Excessive compression of the CG (resulting from excessive forces imposed by the MG) may adversely affect blood flow to the supra-aortic vessels increasing the risk of in-stent

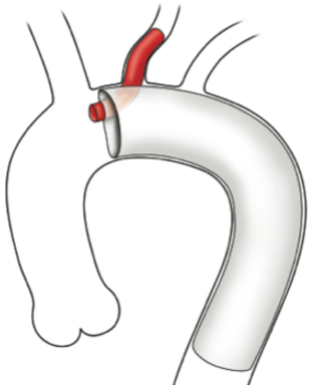


Figure 3.25: Representative illustration of a parallel endograft configuration in the thoracic aorta. The main stent-graft device resides in the aortic arch and extends into the descending aorta. The secondary device (referred to as a "chimney graft") is deployed into the supra-aortic vessel(s) to maintain blood flow to the brain/peripheral vasculature. Image adapted from [171].

thrombosis/device occlusion. Endograft infolding refers to the phenomena where the MG is excessively oversized compared to its parent artery, leading to under-expansion, resulting in an inadequate aortic seal [105].

Indeed, consideration of the risks associated with deploying stent-grafts in a parallel configuration reveals contradictory device requirements. The MG should be appropriately oversized to minimize the risk of gutter formation as well as exert adequate radial force to ensure fixation. However, it should not inadvertently crush the CG, nor exhibit excessive endograft infolding.

Despite the increasing frequency of such procedures [48], to best of this author's knowledge there have yet to be studies reporting on the behaviour of thoracic aortic endografts deployed in parallel configurations assessing the three surgical risks highlighted above. Indeed, the computational tools developed in this Chapter are well suited to analyse ch-TEVAR and compare various device configurations.

3.3.2 Materials and Methods

Representative Zenith TX2 and Valiant stent-grafts are considered in this investigation, maintaining consistency with previous sections. For stent geometries and material properties, refer to Section 3.2.1.1. For simplicity, all stent deformations are assumed to be elastic (i.e. plasticity not included within the prescribed material models). A chimney

graft device, based on a generic design, is also included in the analysis. It too is constructed as a typical Z-stent type, and consists of 7 repeating units having a nominal outer diameter of 10mm. It is considered to be 316L stainless steel, with a graft also of PET. A single stent-graft ring was considered for both the main and chimney grafts. This was deemed to be an appropriate simplification given that the analysed devices are uniform along their length. Likewise, the artery is considered to be a rigid cylinder. Although it is possible to accurately model arterial behavior, as demonstrated in Section 3.1.3 and again in Section 3.2.3, this model reduction was made for the purposes of computational efficiency. Furthermore, as this study was concerned only with the structural interactions of endografts, and not their influence on the surrounding vasculature, including complex artery behaviour was not necessary as a rigid cylinder can be considered equivalent to the inner diameter of a static vessel at equilibrium.

The characteristics of Zenith TX2 and Valiant ch-TEVAR were evaluated at four levels of MG oversizing (10%, 20%, 30%, and 40% OS). It is important to note that the geometry of all stents remain consistent between configurations and that it was the diameter of the representative artery (rigid cylinder) which was adjusted to achieve the desired level of oversizing.

To virtually deploy stent-grafts in parallel, the methodology outlined in Section 3.2.3 was used. Briefly, the so-called crimp tool was employed to control the diameter of the MG, and the simulation was conducted in three analysis steps to (*i*) crimp, (*ii*) deploy, and subsequently (*iii*) pressurise the inner lumen of both devices (to 80mmHg, equivalent to typical diastolic blood pressure). As per Section 3.2.3, appropriate contact conditions were applied across the different analysis steps to enable stent deployment. Of note, the CG does not undergo the crimp/deployment procedure, as it was pre-configured to reside within the rigid artery prior to analysis initialisation.

Here, simulations were performed using Abaqus/Explicit in a quasi-static analysis with negligible kinetic energy. The explicit FEA solver was chosen as to avoid convergence issues, since the analysis involved complex geometric, material, and contact nonlinearities. All contact was implemented using the general contact algorithm via penalty enforcement. Behaviour in the normal direction was defined using a "hard" contact pressure-overclosure relationship, with the "spring" stiffness that relates the contact force to the penetration distance automatically chosen by Abaqus (the default penalty

stiffness is based on a representative stiffness of the underlying elements) [152]. Behaviour in the tangential direction was defined using a penalty friction formulation, with a coefficient of friction $\mu = 0.1$. Mass scaling was applied such that the stable time increment remained larger than 2.5e−06 throughout the analysis (step time of $t = 2s$). The simulated ch-TEVAR configurations are shown in Figure 3.26.

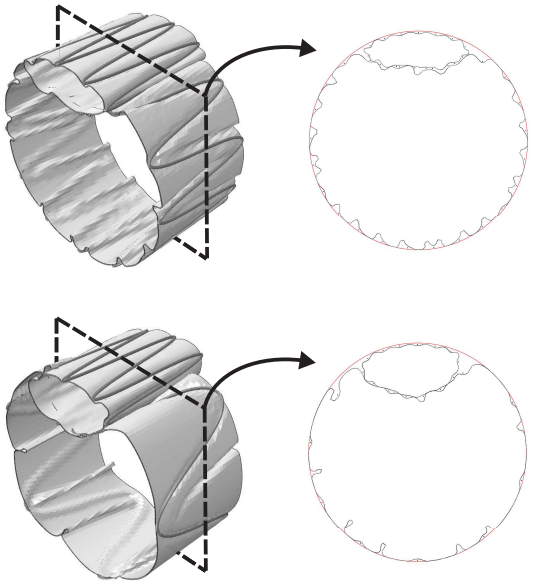


Figure 3.26: Computational analysis of endograft interactions during representative ch-TEVAR. (Left) Zenith TX2 (*top*) and Valiant (*bottom*) main grafts deployed in parallel with a chimney graft (rigid artery not shown). (Right) gutter formation, chimney compression, and endograft infolding at the parallel cross-section (rigid artery shown in red).

To quantify gutter formation, CG compression, as well as endograft infolding, a dedicated analysis workflow was developed. Briefly, nodal data of the deformed graft meshes were output upon completion of the simulation. These data were then post-processed to obtain equivalent surface representations of both MG and CG lumens. Surfaces were then cross-sectioned at a specified region of interest (in this case at a location midway along the graft length), and the resulting cross-sectional areas of both the main and chimney grafts computed.

As the arterial cross-sectional area was pre-specified for the desired level of oversizing and assumed to be rigid (i.e. constant), quantifying gutter formation was straightforward (i.e. evaluated as the cross-sectional area not containing the main or chimney graft lumens). Chimney graft compression was analysed based on the principal of lumen reduction defined in Equation 3.23. Finally, endograft infolding was evaluated by tracking the

nodal positions of the main graft and computing the maximal (inward) nodal distance from the rigid artery wall after pressurisation to diastolic blood pressure.

3.3.3 Results and Discussion

The behaviour of Zenith TX2 and Valiant stent-graft devices deployed in a parallel configuration with a 316L stainless steel chimney graft at four levels of oversizing is shown in Figure 3.27. Assessing the cross-sectional areas of each configuration reveals little intra-device variation at the different levels of oversizing considered. However, there does exist distinct differences between the two MGs analysed. Values for gutter formation, chimney graft compression (lumen reduction), and main endograft infolding are reported below. Across all metrics, lower values are better.

Gutter formation: Total gutter areas as formed between the MG, CG, and rigid artery wall are presented in Table 3.10. This measure is reported as the total free area of the arterial cross-section (i.e. the area not occupied by either the main or chimney graft lumen). Intra-device comparison of the Zenith TX2 at different levels of oversizing does not reveal a significant difference in gutter area. In comparison, the Valiant device demonstrates a (somewhat) decreasing gutter area with increased oversizing (note that the 30% OS data was excluded in this comparison as the computed area is excessively influenced by the stent ring cross-section not accounted for in the calculation); however, this trend is marginal. Critically, there is a notable difference between the two MGs analysed. Based on gutter assessment alone, for the configurations considered here, it appears that a Valiant MG would result in superior performance compared to Zenith, as its deployed state results in comparatively lower gutter areas.

Table 3.10: Comparison of gutter areas between Zenith TX2 and Valiant ch-TEVAR.

Configuration	Zenith TX2 (mm^2)	Valiant (mm^2)
10% OS	29.15	22.65
20% OS	31.70	21.78
30% OS	30.32	27.76
40% OS	30.00	19.39

CG compression: To quantify the functional performance of chimney grafts during ch-TEVAR, CG lumen reduction was evaluated and is reported in Table 3.11. In this

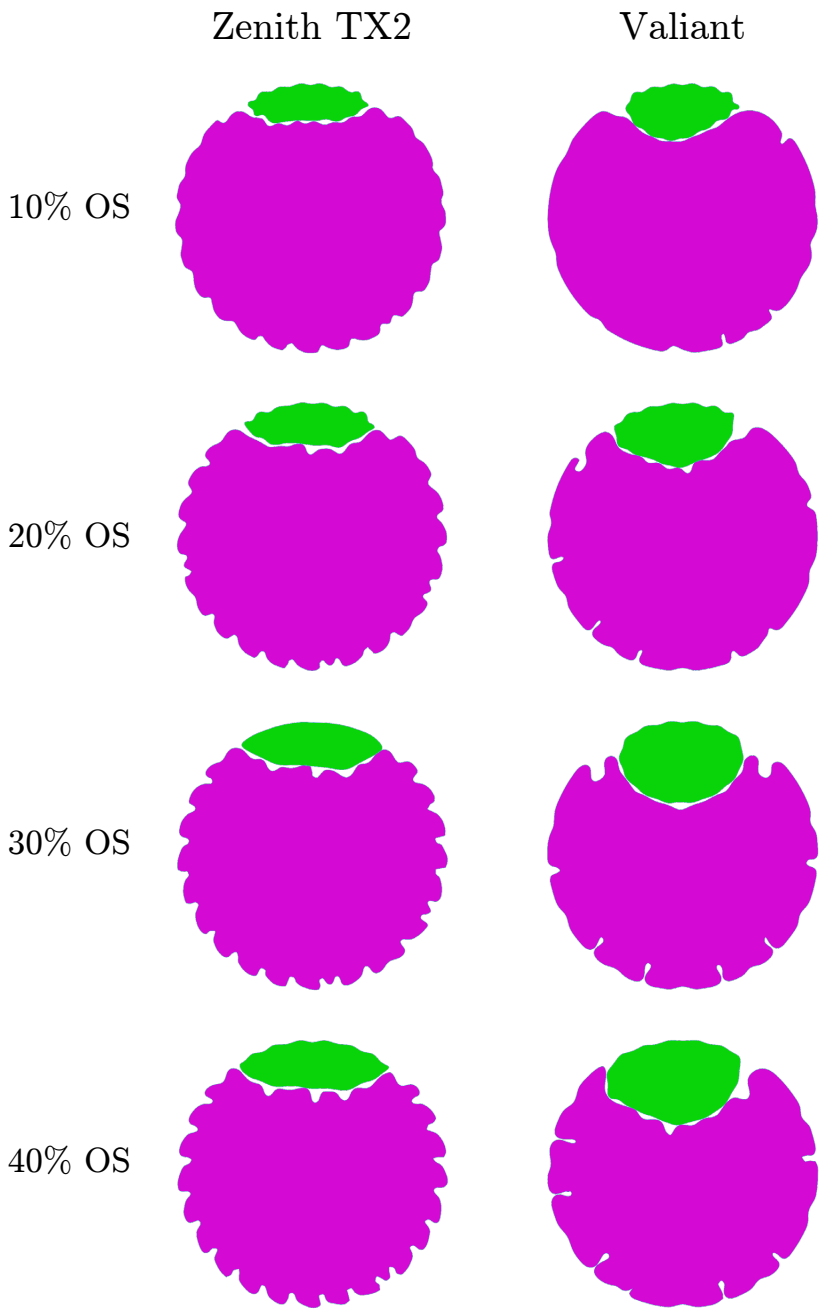


Figure 3.27: Simulated ch-TEVAR configurations at four levels of main graft oversizing. (Left) Zenith TX2, and (right) Valiant device combinations. Cross-sectional areas used for quantifying gutter formation, chimney graft compression, and endograft infolding: main graft lumen (*magenta*), and chimney graft lumen (*green*); rigid artery wall not shown.

analysis, lumen reduction is analogous to CG compression. The results of the simulation show that when the chimney graft is deployed in combination with the Zenith TX2, it exhibits nearly the same level of compression at all levels of oversizing. Comparatively, the CG showed superior predicated behaviour when deployed with the Valiant MG at all levels of oversizing. It is believed that this behaviour is directly linked to the number of MG repeating stent units and the device radial outward force. As the Zenith TX2 consists of a 12-repeating unit stent ring design and exhibits a greater radial outward force, a more uniformly and higher distributed load is applied to the CG, leading to an increase in compression. Conversely, when the Valiant device is considered, it consists of a 5-repeating unit stent ring design as well as a comparatively lower radial outward force, and so the CG experiences a lower degree of compression. Combining these findings with the analysis presented in Section 3.2.1 quantifying MG radial outward force, it becomes clear that when deployed in parallel with a chimney graft, the Valiant will likely demonstrate more desirable behaviour. This observation is based upon the requirement to minimize chimney graft compression.

Table 3.11: Comparison of chimney graft compression (lumen reduction) during ch-TEVAR.

Configuration	Zenith TX2 (%)	Valiant (%)
10% OS	49	34
20% OS	48	29
30% OS	50	16
40% OS	51	22

Endograft infolding: To complete the comparison between the two parallel ch-TEVAR configurations, evaluation of main endograft infolding was conducted. The results of this analysis are presented in Table 3.12. As expected, both MGs experienced increasing levels of endograft infolding with increasing levels of oversizing. Interestingly, this analysis indicates that when using endograft infolding as an evaluation metric, the Zenith TX2 demonstrates superiority over the Valiant. This behaviour is almost certainly dominated by the difference in the number of repeating units with which the devices are designed. As the Zenith TX2 consists of 12 repeating units to which the graft is attached, compared to the 5 repeating units of the Valiant, its graft will remain more closely constrained to the stent frame. In other words, the Valiant's graft is less constrained, and so can more

freely protrude into the vessel lumen. This is an important consideration given that excessive endograft infolding can potentially lead to an increased risk of thromboembolic events resulting from flow disturbances.

Table 3.12: Comparison of maximum infolding between Zenith TX2 and Valiant ch-TEVAR.

Configuration	Zenith TX2 (mm)	Valiant (mm)
10% OS	1.20	2.29
20% OS	1.29	2.65
30% OS	1.57	3.38
40% OS	1.58	3.75

The findings reported in this section are corroborated by the results presented by Mestres and colleagues [105, 106] who undertook an *in vitro* study to examine various conditions of chimney endografting for abdominal aortic aneurysms. Indeed, the general findings of this numerical work are in agreement with those of Mestres: parallel configurations incorporating MGs with greater radial outward force should be avoided in chimney type procedures, and that 30% main graft oversizing appears to an appropriate trade-off between gutter formation, chimney graft compression, and endograft infolding. The computational framework presented herein is the first of its kind to report on the behaviour of representative thoracic aortic stent-graft devices deployed in a parallel configuration. These methods makes it possible to evaluate complex surgical procedures such as ch-TEVAR and to determine the most suitable device selection to increase the likelihood of surgical success.

Summary: Considering the results discussed in this Section along with those reported in Section 3.2, it is apparent that rigorously analysing stent-graft devices is no trivial task. Based on the analysis presented, comparing device behaviour when subjected to radial crimping, bending, deployment into an artery, and when used in a parallel configuration, a Valiant type device appears to demonstrate mechanical superiority over its Zenith TX2 counterpart. Nevertheless, the current generation of stent-grafts continue to exhibit numerous challenges, particularly when used during complex endografting procedures. As such, detailed investigations reporting on the behaviour of endografts remain critical. Improving these devices and surgical strategies can reduce the risk of treatment, working to benefit patients, physicians, and health-care providers alike.

3.4 Summary

In this Chapter, a computational framework to evaluate stent-graft devices has been presented. The phenomenological material models describing nitinol, PET, and arterial tissue have been detailed. An experimental study was undertaken to calibrate a dedicated user material subroutine describing nitinol behavior, with the implementation of PET and arterial tissue models based on data available in the literature.

Three simulation strategies employing the finite element analysis method have been established. Using these numerical tools, the *in silico* performance of two representative stent-grafts devices used in the treatment of thoracic aortic aneurysms have been compared.

Finally, a novel computational study investigating the structural behaviour of stent-grafts deployed in a parallel configuration has been proposed, with clinically relevant evaluation metrics such as gutter formation, stent compression, and endograft infolding numerically predicted and analysed.

Chapter 4

Parallel Stent-Graft Behaviour When Subjected to Uniform Radial Load

In this Chapter, the behaviour of stent-graft devices when deployed in a parallel configuration and subjected to uniform radial load is investigated. First, a conventional benchtop technique is used to characterise four commercially available endografts: two main thoracic aortic devices, and both self- and balloon-expandable covered chimney stents. The benchtop protocol is then extended to evaluate the loading response and mechanical deformations of endografts during representative chimney thoracic endovascular aortic repair (ch-TEVAR). Finally, taking advantage of the available experimental setup, a baseline validation of the finite element analysis methods employed in the previous Chapter is included as a supplement to the primary study.

4.1 Introduction

To ensure a complete aortic seal and to minimize risk of device migration during minimally invasive endovascular repair, stent-grafts should be sufficiently oversized. This oversizing (OS), however, results in radial loads exerted onto the aortic wall. As a consequence of these additional loads, recent studies have reported on microstructural changes to the aortic wall architecture [77] as well as aortic diameter enlargement [78], potentially compromising long-term treatment efficacy.

In an effort to assist interventional radiologists and surgeons, endograft manufacturers prescribe recommended device sizes corresponding to patient anatomy. These recommendations, however, are strictly limited to so-called "on-label" device use: patient, anatomy, and disease state profiles with demonstrated clinical evidence. In the case

of complex endovascular procedures, whereby devices are often used in an "off-label" fashion (i.e. outside of their prescribed indication), no such guidance exists.

Indeed, management of aortic arch aneurysms presents as one of the most technically challenging subsets of endovascular repair. To treat select patients, radiologists have augmented traditional endografting techniques using standard devices in an off-label manner. Known as chimney thoracic endovascular aortic repair (ch-TEVAR), this procedure employs multiple off-the-shelf devices deployed in a parallel configuration: a main endograft (MG) to exclude the diseased aorta from arterial blood flow, and peripheral chimney grafts (CGs) to maintain supra-aortic branch perfusion [45].

Although the technical feasibility and mid-term outcomes of ch-TEVAR have established its utility, this technique still suffers from high-risk complications [48]. Specifically, the formation of so-called "gutters", gaps which form between the endografts and aortic wall leading to type 1a endoleak, can render the treatment ineffective. To minimize the risk of gutter formation, radiologists often resort to deploying excessively oversized main grafts; it is thought that the additional main graft circumference will better conform to both the aortic wall and chimney graft lumen(s), enhancing the aortic seal.

Currently, there exists no consensus as to the optimal device combination or sizing strategy when performing such complex procedures in the aortic arch [42] . A series of reports have presented various methodologies for main graft sizing in the case of ch-EVAR (treatment of abdominal aortic aneurysm, AAA), and have been proposed using an analytical approach [172–174]. Recently, Fazzini et al. [175] have described patient-specific ch-TEVAR sizing techniques and reported its use in a small case series of eight patients. Critically, these methods do not consider the potential impact of main graft oversizing nor device type on the resulting radial loads exerted onto the aortic wall.

As such, the aim of this investigation was to: (1) characterise the radial loading behaviour of constituent ch-TEVAR devices individually, (2) determine the radial loading behaviour of parallel endografts representative of typical ch-TEVAR configurations, and (3) quantify the corresponding mechanical deformations of parallel endografts resulting from radial loading in a benchtop setup. It was hypothesised that both device type and configuration would influence ch-TEVAR interactions.

Finally, owing to the availability of the experimental setup used in this study, additional testing was conducted and used to: (4) evaluate the influence of stent ring design on radial loading response, and (5) validate previously described finite element analysis (FEA) methods typically used to predict stent behaviour. Methods, results, and a brief discussion are included as a supplement presented at the end of this Chapter.

4.2 Materials and Methods

4.2.1 Endografts

In this study, four commercially available endografts commonly used in ch-TEVAR were investigated. The main endografts included a self-expandable (SE) Conformable TAG Thoracic Endoprosthesis (W.L. Gore & Associates Inc., Flagstaff, AZ, USA) and a SE Valiant Thoracic Stent-Graft (Medtronic Inc., Santa Rosa, CA, USA). The chimney endografts included a SE Viabahn (W.L. Gore & Associates Inc., Flagstaff, AZ, USA) and a balloon-expandable (BE) BeGraft (Bentley Innomed GmbH, Hechingen, Germany). Deployed devices are shown in Figure 4.1.

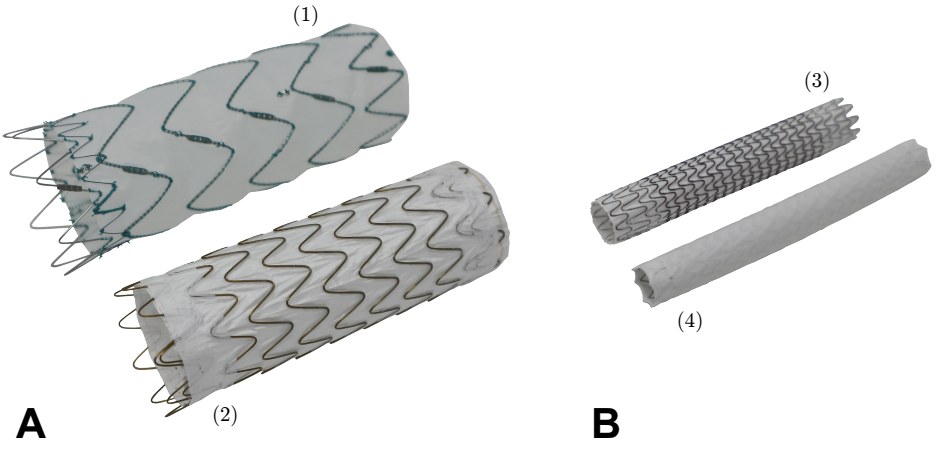


Figure 4.1: Endovascular devices considered in benchtop ch-TEVAR investigations. (A) Main endograft devices, including Medtronic Valiant (*1*) and Gore TAG (*2*); (B) chimney graft devices, including Gore Viabahn (*3*), and Bentley BeGraft (*4*). *Note:* devices shown are not to scale.

The endovascular devices investigated in this study differ greatly in both design and materials used. Considering the main endografts, the TAG consists of a single helical nitinol wire extending along the entire device length, while the Valiant consists of discrete

nitinol stent rings. Furthermore, there are two distinct differences in proximal device design between the main grafts: (1) the amount of uncovered stent (TAG incorporating a partially covered stent design versus the long "FreeFlo" bare stent incorporated by the Valiant), and (2) the method of graft fixation (TAG employing an ePTFE "sealing cuff" versus the fine nitinol wire and sutures employed by the Valiant). Considering the chimney grafts, the key difference between devices is the deployment mechanism: the Viabahn is self-expandable, whilst the BeGraft is balloon-expandable. Further device specifications and characteristics are given in Table 4.1.

Table 4.1: Specifications and characteristics of the four endovascular devices investigated.

Device Feature	Main Endograft		Chimney Graft	
	TAG	Valiant	Viabahn	BeGraft
Labelled diameter (mm)	34.0	40.0	8.0	7.0
Measured length (mm)	105.0	117.0	50.0	55.0
IFU vessel dia. (mm)	27 - 32	35, 36	6.6 - 7.5	7.0
Degree OS range (%)	6.3 - 25.9	11.1, 14.3	6.7 - 21.2	n/a
Delivery diameter (Fr)	22	24	8	6
Stent material	Nitinol	Nitinol	Nitinol	CoCr
Graft material	ePTFE/FEP	PET	ePTFE/FEP	ePTFE
Deployment type	SE	SE	SE	BE
Stent frame type	Helical	Rings	Helical	Open Cell

IFU - instructions for use; *OS* - oversizing; 1 Fr = 1/3mm; *CoCr* - cobalt-chromium; *ePTFE* - expanded polytetrafluoroethylene; *FEP* - fluorinated ethylene propylene; *PET* - polyethylene terephthalate; *SE* - self-expandable; *BE* - balloon-expandable

4.2.2 Device Characterisation

Each device was individually characterised by means of a conventional radial force test [176] synonymous to crimping (loading) and deployment (unloading) of self-expanding stents. In this mechanical loading regime, a uniform load is directed perpendicular to the longitudinal axis of a cylinder and applied to the outer cylindrical surface of the device. All testing was performed using an MSI RX650 Radial Expansion Force System (Machine Solutions Inc., Flagstaff, AZ, USA). The test system consists of a twelve-plate segmental compression mechanism, driven by a linear actuator, which is used to control

the diameter of the testing aperture. An integrated load cell and encoder register the resulting diameter-load data.

Devices were deployed and subsequently placed into the testing system (initial aperture diameter set to deployed device diameter plus 1mm). SE stents were subjected to a single load-unload cycle, compressing to a level approaching their labelled delivery diameter where possible. The BeGraft was subjected to a stepped multi-cycle test: the initial loading increment was equivalent to an 8% diametric compression, followed by four 0.2mm loading increments, and a final load cycle equivalent to a 50% diameter reduction. All experiments were run in displacement control at a rate of 0.1mm/s in a temperature-controlled heating chamber set at 37±2°C (i.e. physiological temperature). The complete test setup is shown in Figure 4.2. Similar experimental systems and protocols have been described elsewhere to assess the radial loading behaviour of transcatheter aortic valves as well as venous stents [177–179].

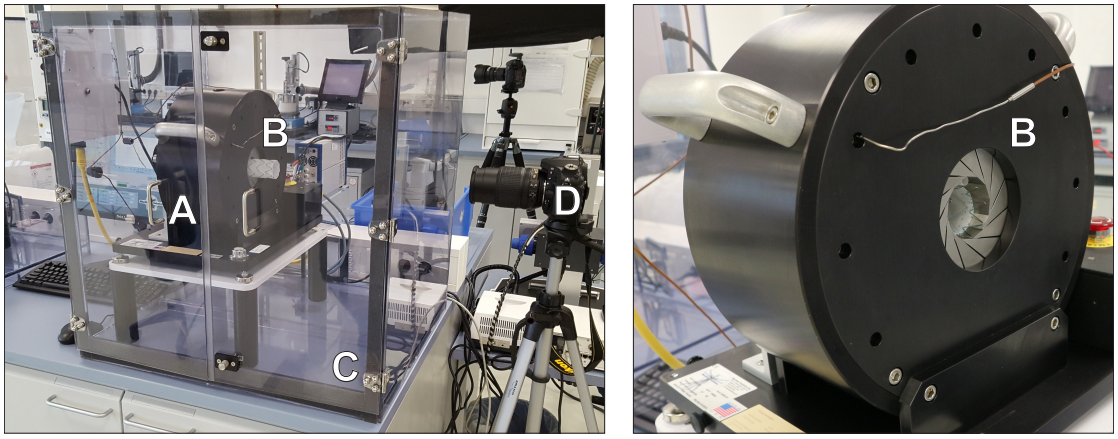


Figure 4.2: Benchtop radial loading test setup. (A) MSI RX650 radial force testing system measurement head; (B) twelve plate segmental compression mechanism; (C) enclosed heating chamber maintained at physiological temperature; (D) video acquisition aligned to the level of the compression mechanism aperture. *Note*: Valiant endograft partially inserted into compression mechanism at (*B, left*) for illustrative purposes only.

Characterisation was based upon analysis of the resulting radial load profiles normalized by measured device length. For SE devices, the chronic outward force (COF) and the radial resistive force (RRF) [144] were quantified. The COF is the continual opening force of the SE device acting on the vessel wall at a specified diameter, as measured from the unloading portion of the radial load profile (i.e. during expansion). The RRF is the associated force generated by the SE device to resist compression, as measured from

the loading portion of the radial load profile (i.e. during crimping). BE devices do not possess a COF or RRF per se, and thus BE stent radial strength is reported herein. To determine radial strength, the steepest portion of a substantially linear unloading curve is offset in a parallel manner so that its diametric intercept is at a specific diameter of interest. The intersection of the offset unloading line with the radial load profile establishes the device radial strength for a specified radial compression (which would have resulted in the plastic deformation of interest) [176]. For the sake of comparison, the BE unloading line was offset to the diameter equivalent to the maximum device oversizing of its SE counterpart.

4.2.3 Radial Loading During ch-TEVAR

To assess radial loads during ch-TEVAR, four single chimney combinations (TAG and Valiant main grafts with either Viabahn or BeGraft chimney grafts) and two double chimney combinations (TAG-Viabahn 2x and Valiant-Viabahn 2x) were subjected to radial loading-unloading in a manner similar to that described above. Specific details are provided below.

For ch-TEVAR combinations containing SE chimney grafts, the initial test aperture diameter was set to be 1mm less than the combined MG-CG diameter (i.e. radial loading initiated under a slightly compressed condition to ensure device-device interaction stability). Devices were positioned such that the chimney graft(s) extended 1-2mm proximal to the main graft covering, and chimneys were aligned to lie between proximal main graft stent struts where possible. In the case of double ch-TEVAR, chimney grafts were aligned in an adjacent fashion. Devices were radially loaded to a diameter equivalent to 60% main graft oversizing, followed by unloading. A representative schematic of a SE single chimney initial configuration is given in Figure 4.3.

For BE ch-TEVAR, main grafts were first radially loaded to a diameter equivalent to 60% main graft oversizing and maintained at the crimped diameter. Subsequently, a balloon-catheter mounted BE stent was positioned and deployed between the crimped main graft and test aperture. To facilitate BE device access, a 0.035" Lunderquist Extra-Stiff Wire Guide (Cook Medical, Bloomington, IN, USA) was used. Chimney grafts were positioned 1-2mm proximal to the main graft covering, and aligned to lie between proximal main graft stent struts where possible. Following BE stent deployment, the parallel devices

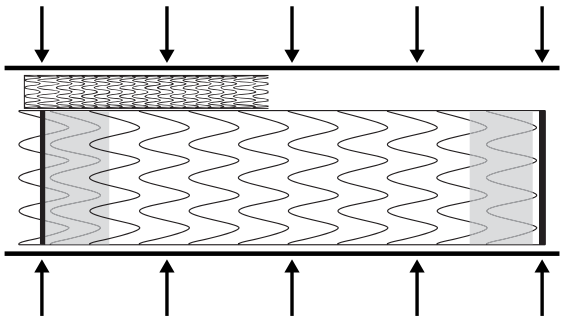


Figure 4.3: Schematic of representative TAG-Viabahn single chimney TEVAR subjected to uniform radial load. Illustrated is the apparent side view of the MSI RX650 tester; only two of the radial loading plates shown.

were unloaded from the crimped configuration. Due to test system availability, double BE ch-TEVAR combinations could not be considered in this study.

As per Section 4.2.2, all testing was performed in displacement control at a loading rate of 0.1mm/s in a temperature controlled chamber set at 37±2°C. Given that only the unloading profiles of BE ch-TEVAR combinations capture parallel endograft behaviour, only unloading profiles and corresponding COF values are reported herein for each configuration. Values are normalized by measured main graft length.

4.2.4 Mechanical Deformations of Parallel Endografts

Mechanical deformations were evaluated via image analysis of video data acquired during the load-unload cycles. Briefly, a video recorder (Nikon D7100, Minato, Tokyo, Japan) was positioned in line with the test system, as shown in Figure 4.2. A purpose-built Matlab code (vR2016b, The MathWorks Inc., Natick, MA, USA) was developed to effectively sync both video and radial force (timestamp) data, and output corresponding video frames (images) at specified compression levels (diameters) of interest. Select video frames were then analysed using the open-source ImageJ2 image analysis software package (Fiji distribution) [180, 181].

Three measures, as originally described by Mestres et al., were used to quantify clinically-relevant endograft deformations [105, 106]. Specifically, gutter area, chimney graft compression, and endograft infolding were assessed. In addition, main graft compression was also evaluated. These metrics are defined below.

Gutter area was calculated as the total area of gaps forming between the main graft, chimney graft, and test aperture boundaries, assessed as a percentage of equivalent lumen area. A lower gutter area represents reduced risk of adverse clinical events (i.e. type 1a endoleak).

Chimney graft compression was calculated as relative decrease of visible chimney graft lumen area to the nominal labelled lumen area: CG compression = (1 - Measured/Nominal) x 100%. This metric is analogous to lumenal reduction as described by Demanget et al. [120]. Higher percentage values reflect increased device compression (i.e. loss of lumen area), and represent potential increased risk of adverse clinical events (e.g. loss of chimney graft patency).

Graft infolding was calculated as the maximal inward deflection of the main graft covering into the lumenal area (in areas other than the chimney graft location), assessed as a percentage of lumen radius. Reduced graft infolding may represent reduced risk of potential adverse clinical events (e.g. thromboembolic events resulting from flow disturbances).

Main graft compression was calculated as relative decrease of visible main graft lumen area to the ideal ch-TEVAR main graft lumen area (i.e. the ideal main graft outcome, conforming to both the vessel wall and chimney graft). Lower values (i.e. less lumen reduction) represent better conformability.

All measurements were performed manually and were taken at the proximal edge of the corresponding graft covering at a single "ideal" aortic diameter (i.e. one level of oversizing). Details specifying the numerically determined ideal aortic diameter are provided below.

4.2.5 "Ideal" Aortic Diameter

As both main and chimney graft sizes were predetermined (i.e. diameters set based upon device availability), it was necessary to prescribe an equivalent aortic diameter at which radial loads and endograft deformations were to be explicitly compared. A straightforward geometric analysis was performed to determine the ideal aortic diameter for the available endograft sizes. The methodology adopted here is analogous to the sizing strategy proposed by Kölbel et al. [174]. However, it was necessary to determine

the corresponding aortic diameter, rather than main graft size, in this study. As such, the inverse problem was considered.

In the case of single chimney TEVAR, it was assumed that the parallel devices would follow the ideal configuration illustrated in Figure 4.4 (inset) whereby the aorta and chimney graft are considered to be circular in cross-section, and the main graft is sized in a manner such that it conforms to the chimney. By simple geometric approximation of each segment, it is possible to determine the corresponding main graft size (perimeter) for a given aortic diameter and chimney graft size [174], as illustrated in Figure 4.4A. To solve the inverse problem (i.e. determine the aortic diameter for a given main and chimney graft size), a numerical scheme was implemented in Matlab as no exact (analytical) solution exists. Briefly, the ideal aortic diameter for the single chimney case can be obtained by solving an equality of the form

$$P_{MG} = 2R\pi + 2\alpha r + 2x - 2R\beta \tag{4.1}$$

where P_{MG} is the known main graft perimeter, r is the known chimney graft radius, and R is the ideal aortic radius to be solved. Following the convention presented in Figure 4.4A, the aortic radius can be numerically determined by applying the following trigonometric relationships (i.e. the law of sines):

$$\gamma = \arcsin\left(\left(\frac{R-r}{r}\right)\sin\alpha\right) \qquad \beta = \pi - \alpha - \gamma \qquad x = \left(R\,\frac{\sin\beta}{\sin\alpha}\right) - r.$$

By extension, the double chimney case as presented in Figure 4.4B can also be assessed. The ideal aortic diameter can be obtained by solving an equality of the form

$$P_{MG} = 2R\pi + 2\left(x + \alpha r + \theta r\right) + t - 2R\left(\beta + \delta\right) \tag{4.2}$$

where P_{MG} is the main graft perimeter, r is the chimney graft radius, and R is the ideal aortic radius to be solved. The trigonometric relationships defining γ, β, and x are identical to the aforementioned single chimney case, while the additional terms δ, λ, θ, ϵ, s, and t are necessary to account for the second (adjacent) chimney graft. Likewise,

the following trigonometric relations apply:

$$\delta = \arcsin\left(\frac{r}{R-r}\right) \qquad \lambda = \frac{\pi - 2\delta}{2} \qquad \epsilon = \lambda - \theta \qquad s = r\cos\theta \qquad t = 2r - 2s.$$

For consistency with the methodology presented by Kölbel et al., an α angle of 135° is assumed and the main graft perimeter appropriately adjusted to reflect an equivalent 15% oversizing. The ideal aortic diameter for each ch-TEVAR combination and the associated main graft oversizing are given in Table 4.2.

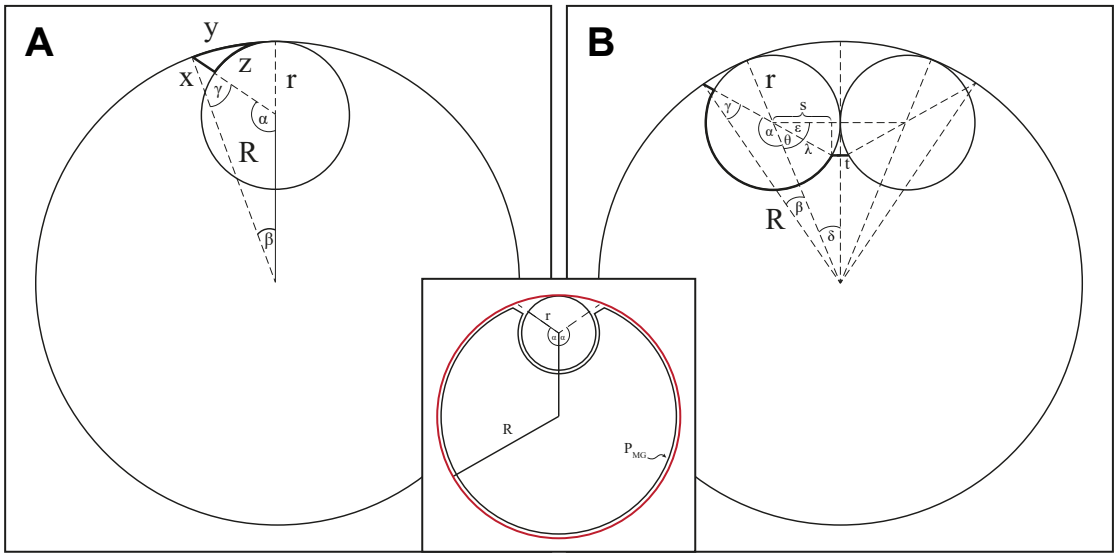


Figure 4.4: Geometric approximation model to determine the "ideal" aortic diameter based upon main and chimney graft sizes. (Inset) ideal conformability of MG to CG and aortic wall (*red*) in single chimney case; (A) ideal configuration in single chimney TEVAR; (B) ideal configuration in double chimney TEVAR. Adapted from [174].

Table 4.2: ch-TEVAR combinations and associated "ideal" aortic diameter and MG oversizing.

Combination	"Ideal" Aortic Diameter (mm)	MG Oversizing (%)
TAG-Viabahn	25.2	35
TAG-BeGraft	25.7	32
Valiant-Viabahn	30.4	32
Valiant-BeGraft	30.9	29
TAG-Viabahn (2x)	26.8	27
Valiant-Viabahn (2x)	31.6	26

4.2.6 Influence of Post-Dilation and Repeatability

In clinical practice, it is common to simultaneously "post-dilate" both main and chimney grafts [182] to facilitate device "remodelling" to the aortic wall. In this study, neither the main endografts nor SE chimney grafts were post-dilated. To assess the influence of SE chimney graft post-dilation on experimental measures, an additional test was performed. Specifically, a Valiant-Viabahn single chimney TEVAR combination was loaded to 60% main graft oversizing, the Viabahn post-dilated using an EverCross PTA Balloon Catheter (ev3 Inc., Plymouth, MN, USA) as per Viabahn instructions for use, and subsequently unloaded. Chimney graft compression at 60% main graft oversizing was measured and compared for both the "pre-" and "post-dilation" cases.

To assess the repeatability of the experimental setup and measurements taken, test data from the initial Valiant-Viabahn loading cycle and the pre-dilation Valiant-Viabahn loading cycle were evaluated (i.e. duplicate, independent test data). Specifically, chimney graft compression areas at 60% main graft oversizing were quantified and compared.

4.3 Results

4.3.1 Device Characterisation

The radial deformation-load profiles of TAG and Valiant main grafts are given in Figures 4.5A and 4.5B, respectively. COF and RRF values at both minimum and maximum instruction for use (IFU) recommended diameters, and for a range of oversizing, are given in Table 4.3. Characteristically, both radial load profiles exhibit "biased stiffness" as associated with nitinol devices, albeit with differing intensity. Considering the indicated sizing for each device, the TAG exerts a COF between 0.15-0.55 N/mm, while the Valiant exerts a COF between 0.17-0.19 N/mm.

The radial deformation-load profiles of the Viabahn and BeGraft chimney grafts are given in Figures 4.6A and 4.6B, respectively. Radial load measures appropriate to SE and BE devices are also reported in Table 4.3. Again, the SE Viabahn device exhibits biased stiffness. It was observed that the COF of the Viabahn device between the minimum and maximum IFU sizing range (0.15-0.58 N/mm) is comparable to the TAG

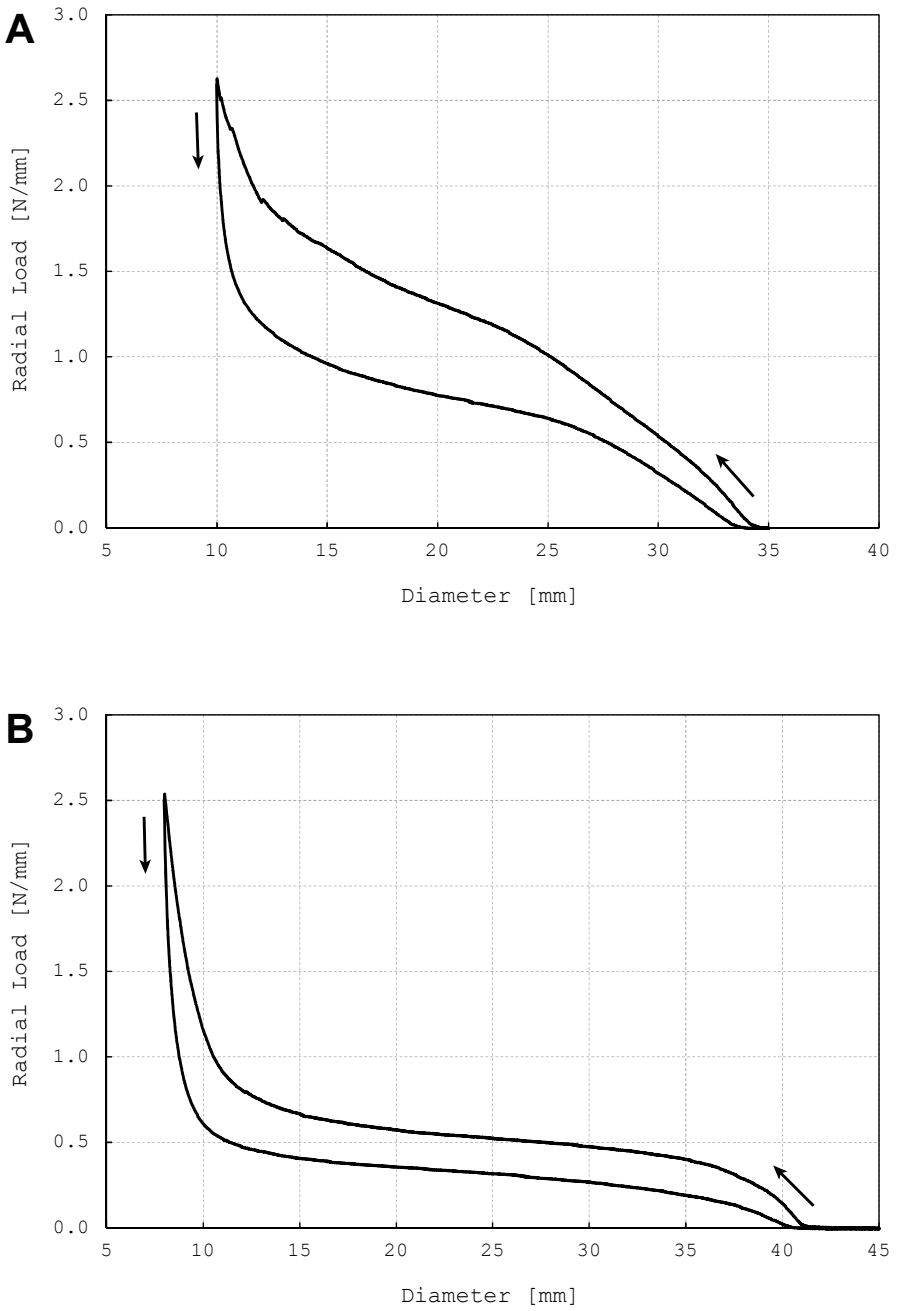


Figure 4.5: Main endograft characterisation. Radial deformation-load profiles of the (A) Gore TAG thoracic endoprosthesis, and (B) Medtronic Valiant thoracic aortic stent-graft. Arrows denote loading-unloading directionality; loading corresponds to radial resistive force (RRF), unloading corresponds to chronic outward force (COF).

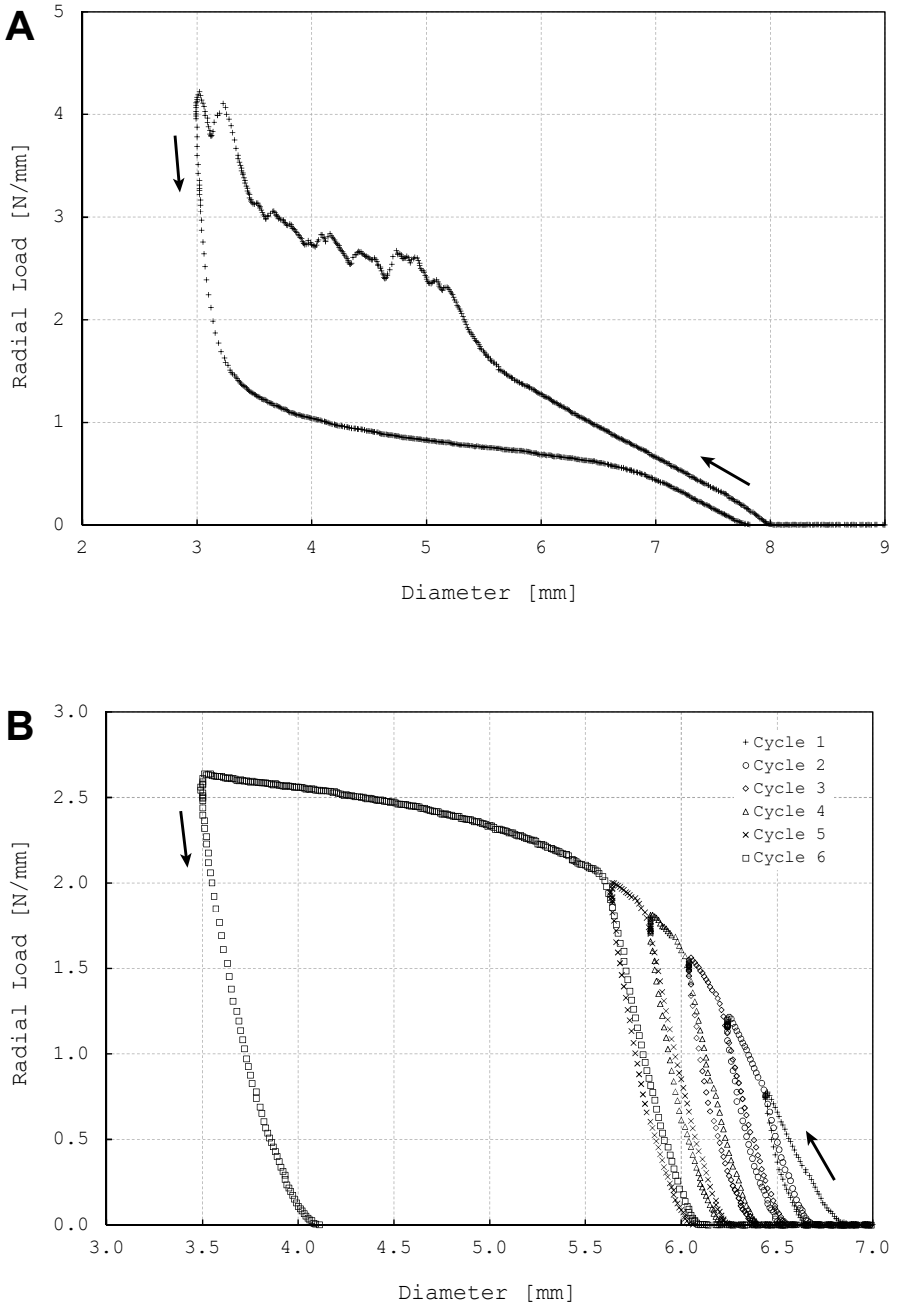


Figure 4.6: Chimney graft characterisation. Radial deformation-load profiles of the (A) Gore Viabahn self-expandable, and (B) Bentley BeGraft balloon-expandable chimney grafts. Arrows denote loading-unloading directionality. In the case of Viabahn, loading corresponds to radial resistive force (RRF), unloading corresponds to chronic outward force (COF). In the case of BeGraft, radial strength (RS) determined via unloading line offset.

Table 4.3: Endograft COF, RRF, and RS characterisation. All values reported as N/mm.

Oversizing	TAG		Valiant		Viabahn		BeGraft
	COF	RRF	COF	RRF	COF	RRF	RS*
Min. OS (IFU)	0.15	0.32	0.17	0.37	0.16	0.36	0.76
Max. OS (IFU)	0.55	0.83	0.19	0.40	0.58	0.90	
10% OS	0.25	0.45	0.16	0.36	–	–	
20% OS	0.45	0.70	0.22	0.43	–	–	
30% OS	0.59	0.91	0.26	0.46	–	–	
40% OS	0.66	1.07	0.28	0.49	–	–	
50% OS	0.71	1.18	0.30	0.51	–	–	
60% OS	0.75	1.25	0.32	0.52	–	–	

COF = chronic outward force; *RRF* = radial resistive force; *RS* = radial strength; *OS* = oversizing; *IFU* = instructions for use
*RS reported for unloading line-load profile intercept at 6.6mmOD

main graft device. The BE BeGraft device exhibits typical elastoplastic behaviour. Importantly, it was observed via the stepped multi-cycle test that the last unloading line is approximately parallel to all other unloading lines and to all reloading lines. When compressed to a diameter equivalent to the maximum oversizing diameter of its SE counterpart (6.6mmOD), the BeGraft's radial strength was found to be 0.76 N/mm; at 50% diameter reduction the radial strength was 2.64 N/mm.

4.3.2 Radial Loading Profiles of ch-TEVAR

Radial deformation-load profiles of single ch-TEVAR combinations are given in Figures 4.7A (TAG-Viabahn/BeGraft) and 4.7B (Valiant-Viabahn/BeGraft). Radial load profiles of double ch-TEVAR combinations are given in Figures 4.8A (TAG-Viabahn) and 4.8B (Valiant-Viabahn). COF values for all configurations across a range of main graft oversizing, including the ideal aortic diameter, are reported in Table 4.4.

An increase in COF was observed for all ch-TEVAR combinations. This upward shift is exacerbated at increased levels of main graft oversizing, such as those typically encountered during ch-TEVAR. In the case of TAG ch-TEVAR, the SE configuration exhibited 5.1 times COF (from 0.15 to 0.77 N/mm) while the BE configuration exhibited 4.6 times

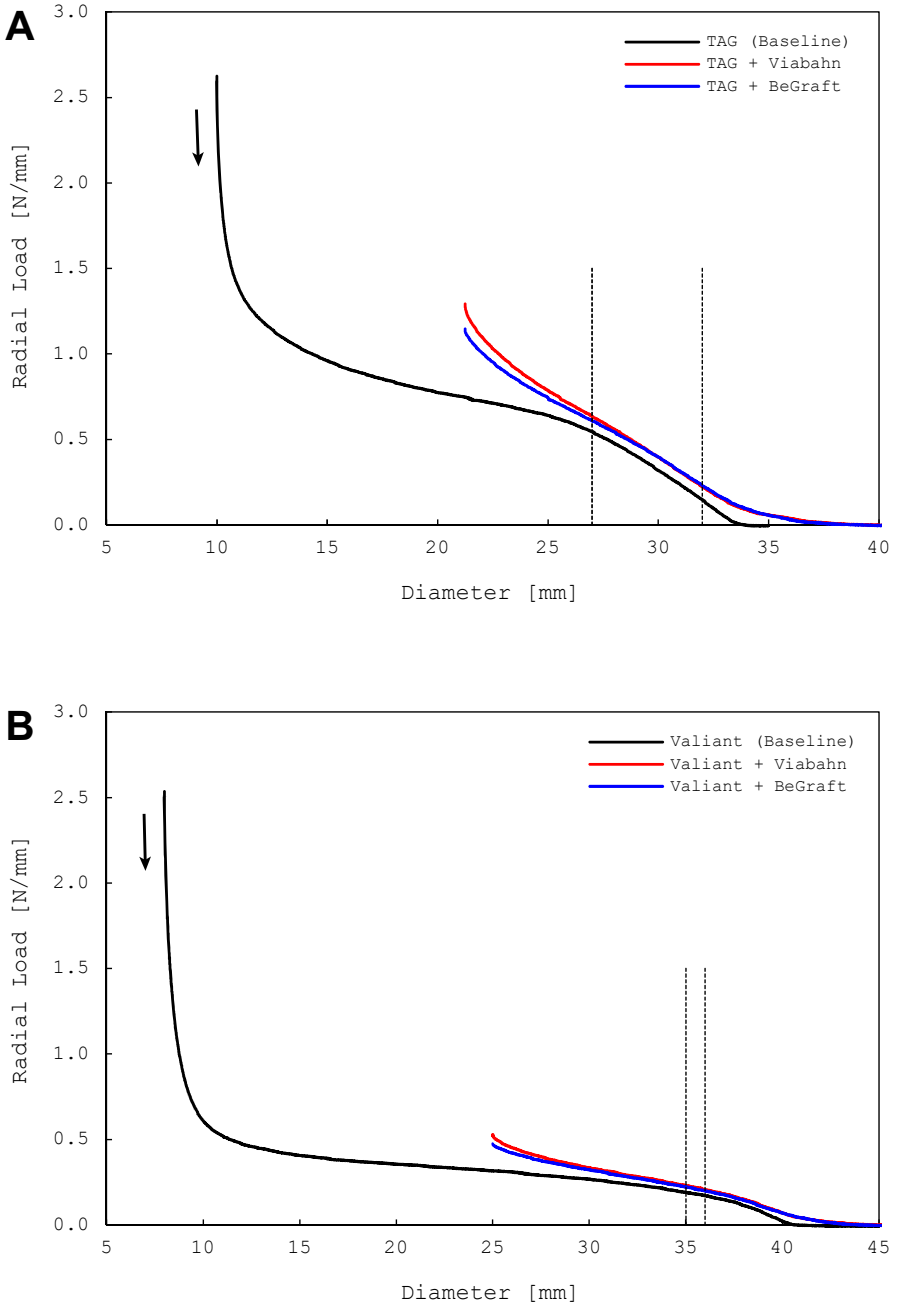


Figure 4.7: Radial deformation-load profiles of single chimney TEVAR. (A) TAG-Viabahn and TAG-BeGraft, and (B) Valiant-Viabahn and Valiant-BeGraft configurations. Arrows denote unloading directionality and correspond to chronic outward force (COF). Unloading curves obtained from main graft characterisation are included to provide a baseline measure. Vertical lines indicate manufacturer IFU oversizing range for standard TEVAR.

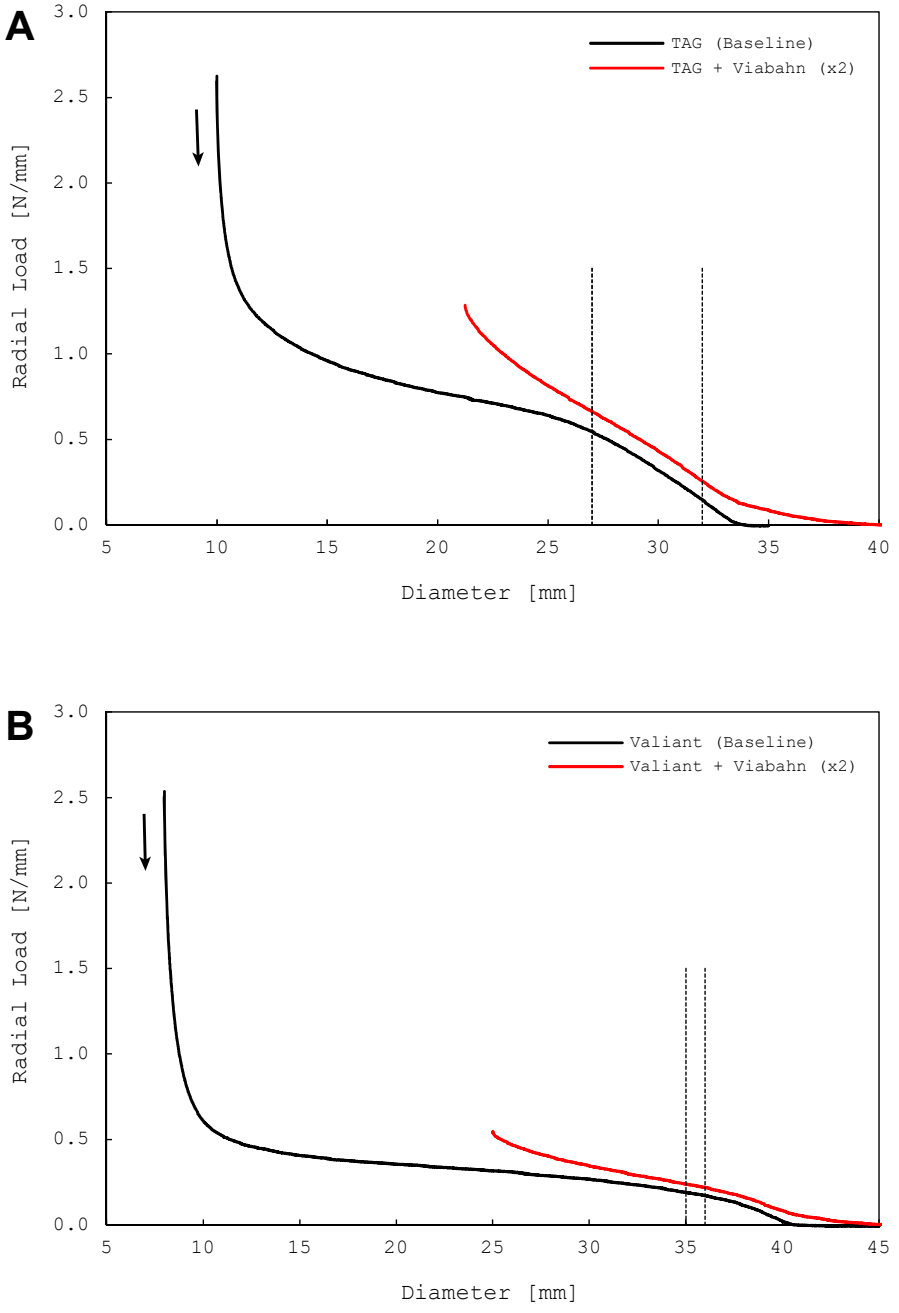


Figure 4.8: Radial deformation-load profiles of double chimney TEVAR. (A) TAG-Viabahn (2x), and (B) Valiant-Viabahn (2x) configurations. Arrows denote unloading directionality and correspond to chronic outward force (COF). Unloading curves obtained from main graft characterisation are included to provide a baseline measure. Vertical lines indicate manufacturer IFU oversizing range for standard TEVAR.

Table 4.4: Chronic outward force of ch-TEVAR at the "ideal" aortic diameter and for a range of oversizing.

Oversizing	Chronic Outward Force (N/mm)					
	TAG-Viabahn	TAG-BeGraft	Valiant-Viabahn	Valiant-BeGraft	TAG-Viabahn (2x)	Valiant-Viabahn (2x)
"Ideal" OS	0.77	0.69	0.33	0.31	0.68	0.31
Min. OS (IFU)	0.22	0.23	0.21	0.20	0.26	0.22
Max. OS (IFU)	0.63	0.61	0.23	0.22	0.66	0.24
10% OS	0.32	0.32	0.20	0.19	0.36	0.21
20% OS	0.53	0.52	0.27	0.26	0.56	0.27
30% OS	0.70	0.67	0.32	0.31	0.73	0.33
40% OS	0.85	0.80	0.37	0.35	0.87	0.38
50% OS	1.01	0.93	0.42	0.40	1.03	0.44
60% OS	1.29	1.15	0.53	0.47	1.28	0.54

"Ideal" aortic diameter determined as per Section 4.2.5 as based on Kölbel et al. [174];
OS – oversizing; *IFU* – manufacturer instructions for use

COF (from 0.15 to 0.69 N/mm) compared to standard TEVAR at minimum IFU oversizing. Considering Valiant ch-TEVAR, the SE configuration exhibited 1.9 times COF (from 0.17 to 0.33 N/mm) while the BE configuration exhibited 1.8 times COF (from 0.17 to 0.31 N/mm) compared to baseline.

Similar to the previously described single chimney cases, an increase in COF is observed for both double chimney TEVAR combinations. Again, this upward shift is exacerbated at increased levels of main graft oversizing. In the case of TAG double chimney TEVAR, 4.5 times COF was measured (from 0.15 to 0.68 N/mm). Considering Valiant double chimney TEVAR, 1.8 times COF was measured (from 0.17 to 0.31 N/mm). Notably, no appreciable difference was observed between COF values between single chimney and double chimney cases (e.g. 0.77 vs. 0.68 N/mm and 0.33 vs. 0.31 N/mm for TAG-Viabahn and Valiant-Viabahn cases, respectively), with the decrease in COF associated with the reduced level of main graft oversizing required to achieve the ideal aortic diameter in the double chimney configuration.

4.3.3 Deformation Behaviour of Parallel Endografts

All single chimney TEVAR combinations exhibited gutters, both chimney and main graft compression, as well as main graft infolding. Endograft deformations resulting from radial (un)loading to an ideal ch-TEVAR vessel diameter are shown in Figure 4.9. Measured deformation values are reported in Table 4.5. The absolute largest total gutter area was determined to be 52.5mm^2, or 7.0% of lumen area, and was associated with the Valiant-BeGraft combination. Conversely, smaller gutter areas were associated with the SE chimney grafts, with the TAG-Viabahn combination resulting in the lowest measured gutter area equivalent to 3.2mm^2, or 0.6% of lumen area.

Chimney graft compression was most evident in configurations with Viabahn devices. The highest degree of compression was associated with the TAG-Viabahn combination, with a 67% chimney lumen cross-section reduction. Both BeGraft combinations exhibited lower compression in ch-TEVAR, with lumenal reductions of 39% and 44% for the TAG and Valiant configurations, respectively.

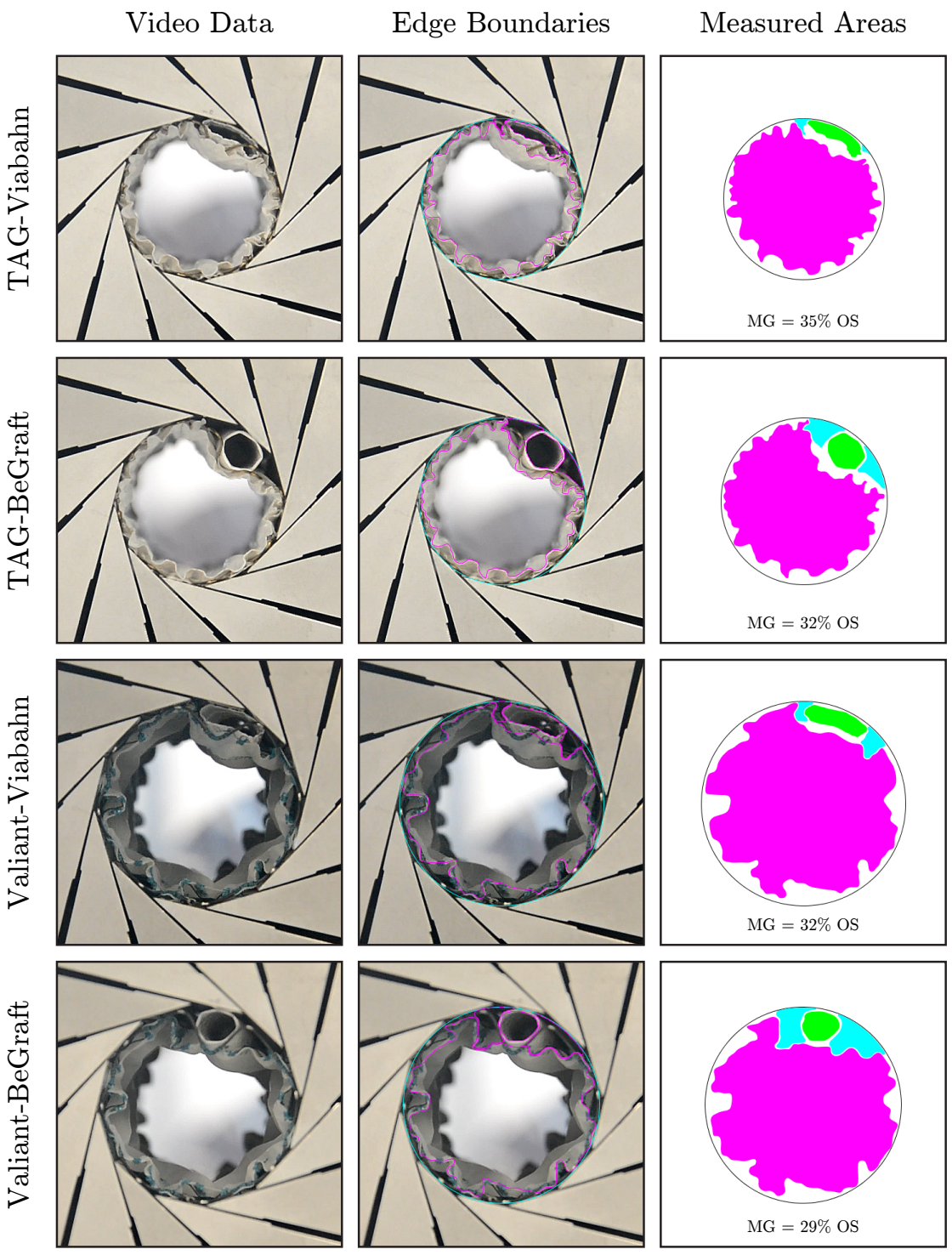


Figure 4.9: Deformations of single chimney parallel endografts. (Left) Synced video frame at the ideal aortic diameter; (center) constructed edge boundaries of MSI RX650 inscribed diameter, graft lumens, and gutter boundaries; (right) measured gutter (*cyan*), main graft (*magenta*), and chimney graft (*green*) areas. Equivalent main graft (MG) oversizing (OS) reported with respect to ideal aortic diameter.

Table 4.5: Deformation measures of parallel endografts in a single chimney configuration at the ideal aortic diameter for the MG-CG combination. Data reported as raw values (normalized).

	Gutter Area (mm^2)	Chimney Graft Area (mm^2)	Main Graft Area (mm^2)	Max. Graft Infolding (mm)
TAG-Viabahn	3.2 (0.6%)	16.7 (67%)	378.3 (15%)	3.2 (26%)
TAG-BeGraft	24.3 (4.7%)	23.6 (39%)	366.4 (24%)	2.8 (22%)
Valiant-Viabahn	13.4 (1.9%)	21.9 (56%)	556.6 (17%)	4.2 (28%)
Valiant-BeGraft	52.5 (7.0%)	21.7 (44%)	558.7 (21%)	4.1 (26%)

Normalizations: Lower is better across all metrics

Regarding main graft deformation behaviour, parallel configurations containing Viabahn chimneys exhibited lower lumen reduction, and thus higher levels of conformability, compared to BeGraft configurations. Between chimney graft pairs, conformability was measured to be 15% and 17% for TAG/Valiant-Viabahn and 24% and 21% for TAG/Valiant-BeGraft. When considering main graft infolding, Valiant combinations exhibited the highest absolute measures (4.1mm and 4.2mm for BeGraft and Viabahn combinations, respectively). When normalized to lumen radius, infolding ranged from 22-28% across all combinations.

Gutters, graft compression, and main graft infolding were also observed in the double chimney configurations considered in this study. Parallel endograft deformations resulting from radial (un)loading to an ideal aortic diameter are shown in Figure 4.10. Measured deformation values are reported in Table 4.6.

Table 4.6: Deformation measures of parallel endografts in a double chimney (Viabahn 2x) configuration at the ideal aortic diameter for the MG-CG combination. Data reported as raw values (normalized).

	Gutter Area (mm^2)	CG_1 Area (mm^2)	CG_2 Area (mm^2)	MG Area (mm^2)	Max. Infolding (mm)
TAG	9.4 (1.7%)	35.9 (29%)	35.2 (30%)	369.2 (18%)	3.2 (24%)
Valiant	15.0 (1.9%)	32.7 (35%)	27.1 (46%)	578.6 (14%)	4.0 (25%)

Normalizations: Lower is better across all metrics;
CG_1: left hand side Viabahn; CG_2: right hand side Viabahn

In both cases, four gutters were identified, and similar total gutter areas measured when normalized to lumenal area. However, total gutter area tripled in the double chimney

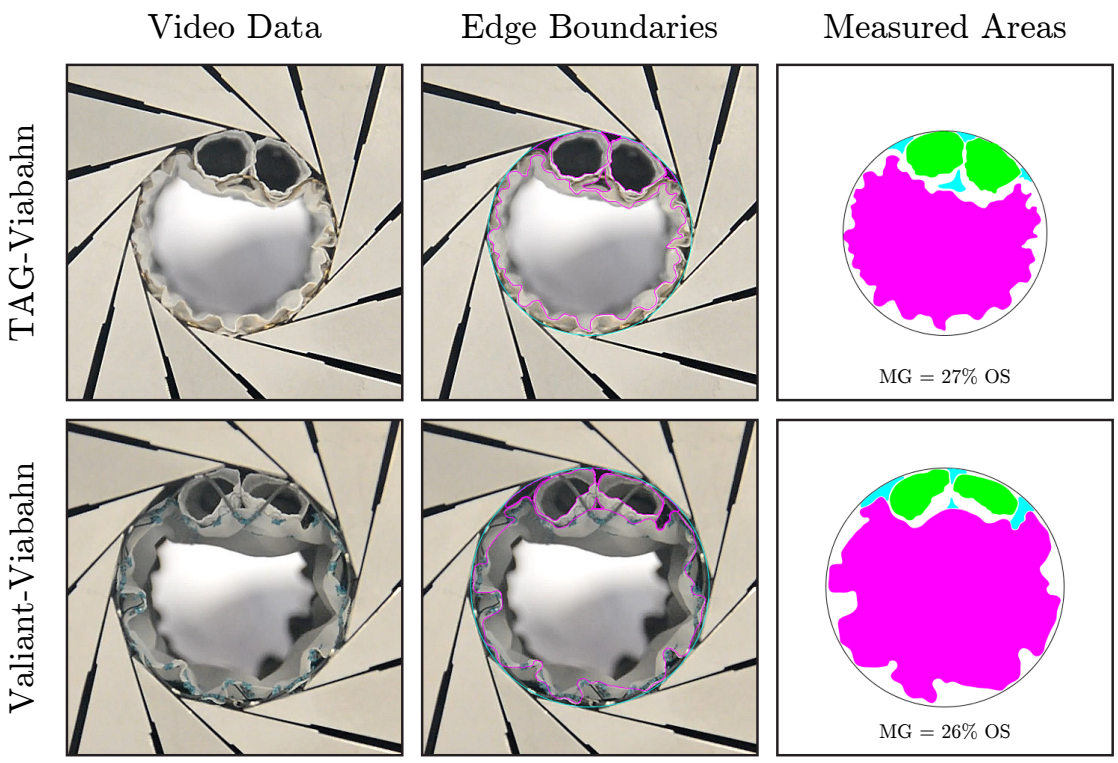


Figure 4.10: Deformations of double chimney parallel endografts. (Left) Synced video frame at the ideal aortic diameter; (center) constructed edge boundaries of MSI RX650 inscribed diameter, graft lumens, and gutter boundaries; (right) measured gutter (*cyan*), main graft (*magenta*), and chimney graft (green) areas. Equivalent main graft (MG) oversizing (OS) reported with respect to ideal aortic diameter.

TAG-Viabahn case compared to its single chimney counterpart (0.6% vs. 1.7% of lumen area), whereas gutter area remained constant in the case of double chimney Valiant-Viabahn compared to its single chimney counterpart (1.9% lumen area in both cases). Notably, chimney graft compression was lessened in the case of TAG-Viabahn double chimney TEVAR (29% and 30%, versus 67% in the single chimney case). A similar observation was made in the case of the Valiant-Viabahn, although to a lesser extent (35% and 46%, versus 56% in the single chimney case).

Regarding main graft deformation, the TAG-Viabahn and Valiant-Viabahn double chimney combinations exhibited 18% and 14% conformability, respectively. The degree of double chimney main graft infolding normalized to lumen radius was measured to be 24% and 25% in the Valiant and TAG cases, respectively.

4.3.4 Influence of Post-Dilation and Repeatability

Quantified lumen areas for the Valiant-Viabahn single chimney configuration, pre- and post-dilation, at 60% main graft oversizing are given in Figure 4.11. Repeatability was assessed comparing data presented in Figures 4.11A and 4.11B. Influence of post-dilation was assessed comparing data presented in Figures 4.11B and 4.11C.

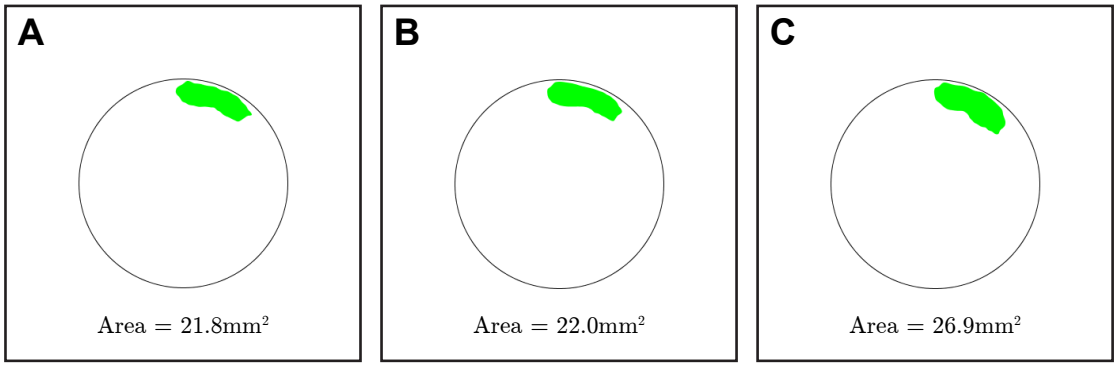


Figure 4.11: Influence of post-dilation and experimental repeatability. Quantified Viabahn lumen area (*green*) at 60% main graft oversizing. (A) Original test data, (B) secondary test data pre-dilation, and (C) secondary test data post-dilation. Comparison between A and B used as repeatability measure.

The test system and protocol, analysis technique, and observer repeatability showed agreement between seemingly identical experimental runs (measured chimney graft lumen areas of 21.8mm^2 and 22.0mm^2). It can be noted that post-dilation of the chimney graft results in a modest increase in chimney graft lumen area. As such, it is plausible that the degree of chimney graft compression reported herein may be overestimated in the circumstance that post-dilation is performed *in vivo*. Qualitatively, however, the lumenal shape remains similar between pre- and post-dilation cases.

4.4 Discussion

4.4.1 Device Characterisation

Four commercially available endografts have been characterised according to their mechanical response to uniform radial load. The main grafts investigated represent two

distinct stent-graft types: a continuous helical undulating wire frame design with a partially uncovered proximal stent (Gore TAG), and a discrete multiple stent ring design with a flared proximal bare stent (Medtronic Valiant). Likewise, the chimneys represent two distinct chimney graft types: a SE helical undulating wire frame design (Gore Viabahn), and a BE open-cell frame design (Bentley BeGraft). As such, this work captures a number of relevant device combinations.

The results of the present study emphasize the significantly different radial load profiles, and hence device-artery interactions, of endografts used in clinical practice. Considering the main grafts and the associated COFs reported here, use of the TAG endograft can result in a threefold increase in radial load exerted onto an aortic wall if compared to a separate procedure which may employ a Valiant device. Notably, the main grafts investigated in this study exhibit considerably different behaviour at increasing levels of oversizing: the TAG demonstrates a generally constant increase in radial load values, whereas the Valiant tends towards a plateau over a similar range. In other words, the devices exhibit differing rates of radial load increase per radial compression (i.e. slope), with the COF of Valiant relatively insensitive to increases in oversizing. Clinically, this suggests that inadvertent/excessive oversizing is potentially less detrimental with Valiant compared to TAG.

The non-uniform loading profile of the Viabahn device past the recommended sizing level was attributed to the intricate structure of the Viabahn stent frame, whereby adjacent struts were believed to have come into contact and subsequently deflect to accommodate further diameter reduction. This behaviour occurred at radial compression levels in excess of 50% oversizing, and so deemed inconsequential to the *in vivo* scenario (where the maximum indicated oversizing is approximately 20%) or subsequent ch-TEVAR experiments as such excessive radial compression was not observed. Similarly, the sharp increase in radial load of both main grafts at excessively high levels of compression (i.e. those approaching delivery diameter) was attributed to stent/graft self-contact.

In general, the behaviour reported here is consistent with trends described by De Bock et al. [79] and Morris et al. [80] for AAA devices, specifically regarding the biased stiffness during loading-unloading and the distinct differences between endograft types. Recently, Matsumoto et al. [183] reported radial force measurements of three thoracic

aortic endografts, including TAG and Valiant types. In that study, a different experimental technique was employed and radial deformation-load profiles were not reported, preventing direct comparisons. Nonetheless, the general observations of that study corroborate the findings here: TAG endografts exert higher radial loads onto the aortic wall compared to Valiant devices.

Regarding the chimney grafts investigated in this study, two different sizes (diameters) were intentionally selected. Specifically, the SE Viabahn was chosen to be one size larger than the BE BeGraft, as per clinical practice at our institution. The mechanical behaviour of peripheral stents has been reported in a select number of studies. However, those studies do not report response to uniform radial load [184–186], nor do they give detailed descriptions of the experimental/reporting methods used [183, 187], limiting their utility when evaluating ch-TEVAR.

The chimney graft characterisation presented here highlights the distinct and fundamental differences of endograft types and serves to clarify differing qualitative descriptions of parallel endograft behaviour found in the literature. Numerous studies have described the behaviour of chimneys based on their supposed "radial force" (see, for example, [105, 106, 175]), however, such ambiguous terminology confounds meaningful analysis of ch-TEVAR device combinations when comparing SE and BE chimney graft types. As made evident here, BE devices do not exert a radial force per se; their behaviour is strictly governed by their radial strength (i.e. ability to withstand deformation), whilst SE devices intrinsically have no radial strength limitation (i.e. they will elastically recover even after complete flattening/radial crushing) [188]. Thus, the more appropriate comparator is chimney graft radial stiffness: the resistance to diametric compression due to radial load. By simple consideration of the governing material behaviour of BE versus SE devices, a BE device will always have higher radial stiffness compared to a comparable SE device. The detailed device characterisation and associated COF, RRF, and RS profiles reported in this study serve as the on-label baseline values to which the off-label ch-TEVAR configurations can be compared.

4.4.2 Benchtop ch-TEVAR

Recently, a series of *in vitro* studies have reported on the behaviour of parallel endografts used to treat challenging AAAs [105–108, 110, 189, 190]. These studies, which provide

compelling insights into the behaviour of devices during chimney type procedures, have solely focused on presenting geometrical data (and in the case of Boersen et al. [190], volumetric flow) and so were strictly limited to qualitative observations regarding device-device and device-artery interactions. The distinctly unique aspect of this investigation is the coupling of radial load profiles and corresponding mechanical deformations with the use of a radial force testing system and video (image) analysis. Given the device sizes available, the ideal aortic diameter for which a device combination would be selected in clinical practice was numerically determined based upon the method proposed by Kölbel et al. [174]; with its intuitive geometric underpinnings and applicability to an *in vitro* context, this approach was deemed most suitable for this study. Dependent on device combination, the level of oversizing analysed here ranged from 26 - 35%, representing the upper oversizing range seen in clinical practice [49, 111, 191, 192].

It should be noted, however, that the oversizing approach applied does not account for deformations of chimney stents, but rather assumes lumen cross-sections remain circular. Such an assumption is directly valid for BE chimney devices, which in general retain their circular shape. However, as made evident in Figure 4.9 and reported elsewhere (see, for example, [105]), SE devices will inevitably undergo a degree of deformation (compression) during chimney procedures. For the sake of simplicity, and to apply a constant sizing approach across all device types, this compression was not accounted for during oversizing determination. Likewise, some groups have reported reinforcing SE chimney grafts with additional stents to promote a circular cross-section [111], further justifying this assumption.

Mechanical deformation measures have been normalized in a manner similar to that described by Mestres et al. [105, 106]. Of note, the deformed main graft area has also been reported here and has been normalized using the calculated ideal ch-TEVAR main graft lumen area. Finally, as all previously reported *in vitro* chimney studies have relied on CT reconstructions where it is not possible to explicitly identify graft edge boundaries, this is the first study to provide quantitative data on the degree of main graft infolding. Similarly, gutters and both chimney and main graft lumen areas reported here are based on clearly defined graft edge boundaries.

4.4.3 Chronic Outward Force During ch-TEVAR

The results presented here demonstrate a marked increase in COF during both single and double ch-TEVAR, and for both SE and BE chimney graft types, compared to that anticipated in standard TEVAR. Dependent on configuration, ch-TEVAR can result in a fivefold increase in COF. In general, rates of COF increase per radial compression (i.e. slope) were observed to follow baseline measures between the minimum and maximum IFU indicated levels of oversizing. The increase in COF over baseline was further exacerbated at increased levels of oversizing (i.e. in the off-label scenario), as would typically be encountered in ch-TEVAR. Moreover, COF was consistently higher for TAG compared to Valiant across all combinations, with more than a twofold difference at the ideal aortic diameter. Although there exists no clearly defined "safe" COF threshold, apart from the implied manufacturer specified maximum oversizing, a systematic review by Canaud et al. [193] demonstrated that increased endograft oversizing (and hence COF) translated to an increased risk of aortic wall damage (as manifested by retrograde type A aortic dissection). The COFs reported here highlight the device dependent variability in potential aortic wall loading during ch-TEVAR procedures. Indeed, clinicians may need to exercise more caution with TAG oversizing in the presence of chimney grafts as COFs are up to 3x as affected by oversizing compared to Valiant.

There was found to be a minimal difference in COF between SE and BE ch-TEVAR. This finding is of particular interest given that BE endografts do not possess a radial force per se, whilst SE devices inherently do. The quasi-static nature of the experimental setup necessitates that force interactions between devices and the test aperture (analogous to a rigid vessel wall) must be balanced. Inspection of Figure 4.9 reveals that SE chimney grafts devices are prone to deformation. This deformation leads to a more uniformly distributed chimney graft contact against the apparent aortic wall. In contrast, the BE device retains its circular shape, limiting total contact area. Therefore, it follows that BE type chimney grafts may result in COF localizations onto the adjacent aortic segment, potentially leading to aortic wall stress concentrations.

4.4.4 Mechanical Deformations During ch-TEVAR

This study illustrates that endograft deformations during ch-TEVAR are dependent on device type. Combinations employing BE chimney grafts exhibit larger gutter areas whilst maintaining their circular cross-sections. Conversely, combinations employing SE chimney grafts presented with comparatively lower gutter areas, however, increased rates of lumen compression. Such behaviour is attributed to the difference in radial stiffness between chimney types. The direct comparison of results presented here to those reported by other groups is not wholly appropriate due to the differences in main grafts studied (TAA vs. AAA), experimental setup (RX650 tester vs. silicone models), and imaging techniques used (video vs. CT analysis). Nevertheless, these trends are similar to those of *in vitro* ch-EVAR and further corroborate the notion that SE compression leads to reduced gutter areas by deforming into the free (gutter) space [105, 106].

Notably, this is the first study to present detailed depictions of endograft inflow areas, as the methods employed here allow for exact delineation of the endograft boundary. The distinct variability in inflow shape between device types is attributed to the differences in stent design (for both main and chimney grafts) as well as graft attachment mechanisms (for main grafts). Interestingly, in the case of Valiant configurations it was observed that the fine nitinol support wire at the proximal edge of the graft covering deflected into the lumenal area. Moreover, in the case of the BeGraft combination, this deflection contributed towards an increase in gutter area. However, the difference in stent design/graft attachment mechanism did not influence maximal endograft infolding; although the Valiant device presented with the highest absolute degree of infolding, when normalized to lumen radius, both main graft types exhibited nearly equivalent measures.

Finally, this is the first study to report deformation data on multiple parallel endografts arranged in an adjacent fashion as would be anticipated in some cases of double ch-TEVAR. The salient observations here pertain to chimney compression: in the case of double ch-TEVAR, adjacent chimney grafts appear to radially reinforce each other, limiting the degree of chimney compression. This reinforcement effect, however, was somewhat mitigated in the Valiant configuration due to chimney graft interactions with the proximal bare stent. These observations, when coupled with the behaviour of lumen

deformations in the single chimney case, provide compelling insights into the potential best *in vivo* arrangement of endografts during double chimney TEVAR.

4.4.5 Limitations

Considering the benchtop nature of the work presented in this investigation, results should be viewed within the experimental context described herein and its associated limitations. First, the inherent elasticity of the aorta is not accounted for in this study due to the necessary rigid nature of the test system. As such, the deformations quantified here may differ *in vivo*. Similarly, experiments have been run in displacement control in a seemingly continuous loading-unloading fashion. Although endograft deformations have been evaluated in an essentially quasi-static manner, oversizing has been achieved by loading each endograft from an unconstrained state, and subsequently unloading to the analysis diameter. Accordingly, the apparent endograft deformations are dependent on the previous time instance, which is not the case in the clinical scenario.

Secondly, the test setup does not account for aortic pressure, nor pulsatile blood flow. It is anticipated that internal pressures and flow acting on the endograft covering would likely influence its configuration, and thus the associated measures reported in this study.

Finally, a limited number of devices were investigated, restricting quantitative findings to the specific devices and configurations described. Specifically, the main grafts used in this investigation (which were limited in availability to our group) cannot provide a like-for-like comparison given their differing nominal diameters. Nevertheless, the observations reported here do allow for meaningful comparisons across a wide anatomical range. Similarly, devices were reused with the potential of accumulated plasticity between loading cycles. Of note, the Gore TAG comes constrained in an ePTFE sleeve which remains implanted upon device deployment. For the sake of simplicity, and to isolate the effects of the endoprosthesis alone, this sleeve was removed. Likewise, owing to the experimental setup, it was only possible to deploy the BE devices in an orientation such that its distal end was subject to evaluation. Chimney grafts were also assumed to have landed parallel to each main graft, while they may in fact take oblique routes *in vivo*. It is also recognized that the endografts used in this study are current generation devices, with some next-generation devices already in clinical use.

4.5 Supplement: Stent Ring Design & FEA Validation

Owing to the availability of the experimental setup presented in this study, a supplemental experiment and computational analysis are included within this Chapter. First, results of additional radial force testing of two stent-graft rings of varying design are presented, serving to highlight the influence of stent design on loading response. Subsequently, a baseline validation of the finite element analysis (FEA) methods employed in the previous Chapter is presented.

4.5.1 Stent Ring Design

As previously described, the Medtronic Valiant comprises discrete stent rings of "Z-stent" type sutured to a graft covering. Conspicuously, there exists two distinct stent ring designs within a single device: the proximal "FreeFlo" stent ring incorporates an eight-apex design, whilst the "Main Body"stent ring incorporates a five-apex design.

To isolate the individual radial deformation-load response of each stent design, stent rings were carefully removed from a 34mmOD Valiant device not included in the primary study.[1] Using the RX650 test setup as detailed above, individual stent rings were subjected to a load-unload cycle, radially compressed to a diameter equivalent to the labelled delivery profile (24Fr). Experiments were run in displacement control at a loading rate of 0.5mm/s and with the test temperature maintained at 37±2°C. The resulting radial deformation-load profiles are given in Figure 4.12

Four observations are made evident here. First, stent ring design influences the apparent radial deformation-load profile. Secondly, the Freeflo and Main Body stent rings are of different unconstrained diameter. As such, it is not wholly appropriate to directly compare radial load values. Furthermore, differences in material properties between stent rings (if any) are unknown. Nevertheless, the obvious difference in apparent profile illustrates the influence of stent design on radial loading response. Interestingly, it is observed that the COF values of both stent rings are equivalent at the indicated IFU size range (29-31mm native vessel inner diameter). However, the FreeFlo stent COF

[1] Although sharing the same nominal diameter of the Gore TAG device studied, the 34mmOD Valiant was > 200mm in length, which the RX650 test aperture could not accommodate

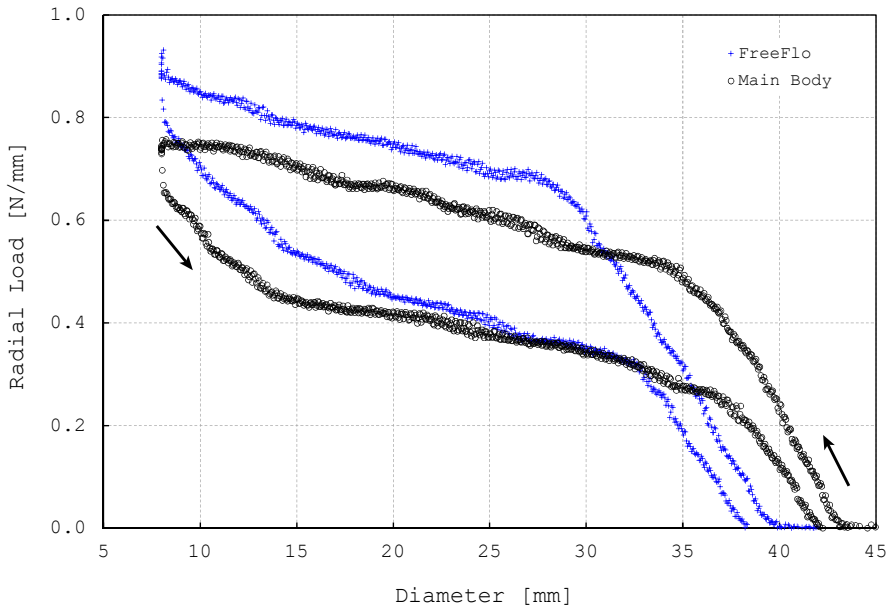


Figure 4.12: Medtronic Valiant stent ring characterisation. Radial deformation-load profiles of FreeFlo and Main Body stents. Arrows denote loading-unloading directionality; loading corresponds to radial resistive force (RRF), unloading corresponds to chronic outward force (COF).

comparatively increases at increasing levels of oversizing, such as those which may be experienced during ch-TEVAR.

Following this, it was observed that some permanent deformation (accumulated plasticity) occurs upon (re)loading the stent rings to the delivery diameter at physiological temperature. Finally, when sutured to its accompanying graft, the stent rings of the Valiant device are constrained and so (already) subjected to a "baseline" mean strain prior to device implantation (i.e. the diameters reported here are markedly greater than the labelled nominal outer diameter).

The results presented in Section 4.3.1 illustrate the distinctly different radial load profiles between endografts (e.g. TAG vs. Valiant). Here, it is made evident in the case of Valiant, that device-artery (and in ch-TEVAR, device-device) interactions may vary along device length resulting from the differing behaviour of constituent stent rings.

4.5.2 FEA Validation

In Chapter 3, a computational framework was presented to study the behaviour of stent-graft devices via finite element analysis (FEA). To evaluate the robustness of those

methods, a validation exercise is presented here whereby the ability of a computational model to match (predict) the response of a physical system is demonstrated.

To begin, the exact geometry of a 34mmOD Medtronic Valiant main body stent ring was obtained via high resolution micro-computed tomography (μCT). Briefly, the (untested) detached stent ring was scanned using a NSI IMAGIX system (North Star Imaging, Rogers, MN, USA) and a corresponding reconstruction obtained. Using the Simpleware ScanIP software package (vN-2018.03, Synopsys Inc., Mountain View, CA, USA), the stent ring centerline was computed and its representation visualized as a cubic spline [194]. Centerline data was subsequently exported in IGES format, and re-imported into the Abaqus Unified FEA software package (Dassault Systèmes Simulia Corp., Providence, RI, USA). The process of translating the physical stent ring into its digital representation is illustrated in Figure 4.13.

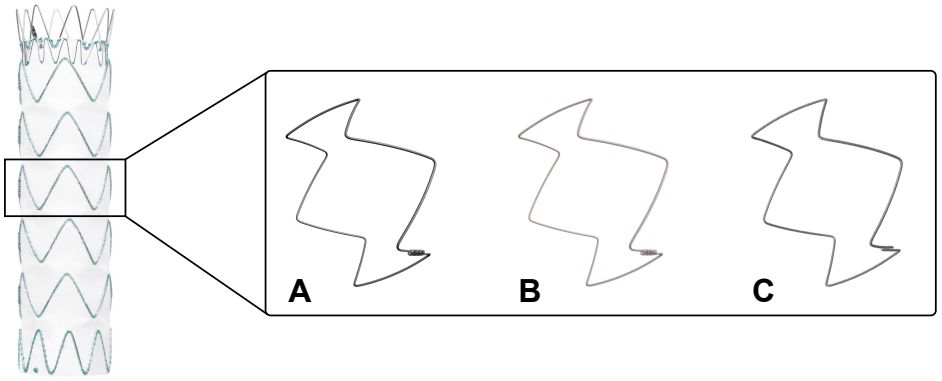


Figure 4.13: Medtronic Valiant main body stent ring mesh generation. (A) Volumetric geometry reconstruction from μCT scan data; (B) centerline extraction (computed centerline depicted in red with stent ring geometry set to transparent); (C) resulting Abaqus mesh rendering.

As per the methods outlined in Chapter 3, the stent ring geometry was meshed in Abaqus using linear Timoshenko beam elements (type B31) with a circular cross-section. These elements have been demonstrated to give similar results to continuum elements with greater computational efficiency [170], and so have been implemented in this validation. Analogous to the experimental method, a virtual "crimp tool" was created and modelled as twelve discrete rigid plates. Matching the experimental protocol, the crimp tool was moved in displacement control whereby its effective opening diameter was specified. The stent representation was positioned within the crimp tool, and so was subjected to radial deformation driven by displacement of the rigid crimp tool elements. Contact was

implemented using the general contact algorithm. Contact constraints were enforced via the penalty method. Behaviour in the normal direction was defined using a linear "hard" contact pressure-overclosure relationship, with a stiffness scaling factor of $S_f = 0.01$. Behaviour in the tangential direction was defined using a penalty friction formulation, with a coefficient of friction $\mu = 0.1$. The stent ring was appropriately constrained as to prevent rigid body motion and stent ring wire ends were effectively connected using a tie constraint to mimic the stent wire fastening sleeve (which was not explicitly modelled here). A representative illustration of the simulated radial loading experiments is provided in Figure 4.14.

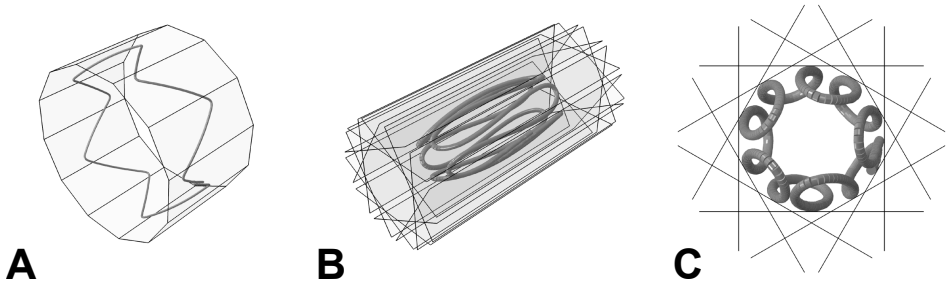


Figure 4.14: Medtronic Valiant stent ring virtual crimping experiment. (A) Pre-loaded state; (B) loaded state; (C) loaded state in axial view.

FE calculations were performed using the general-purpose solver employing an implicit integration scheme (Abaqus/Standard v2018-HF2) and were implemented as a nonlinear static analysis. The radial loading profile was computed by summing the reaction force vectors exerted onto each of the 12 crimping plates during a load-unload cycle. Of note, the exact material properties of the nitinol stent ring was unknown, and so were manually adjusted to match the available experimental data. The inbuilt nitinol material model available in Abaqus was used, which is based upon the model described by Auricchio et al. [153, 154]. The resulting computationally determined radial load profile is given in Figure 4.15. Agreement was obtained between experimental and FEA data. The nitinol material model parameters used to match radial force data are reported in Table 4.7.

Admittedly, this validation is intrinsically dependent on the nitinol material model inputs, which have been manually adjusted to the available experimental data.[2] Due to the proprietary nature of endograft devices, exact material specifications are unknown.

[2]It is recognized that the difference between start/end transformation loading (and unloading) is likely to be artificially high.

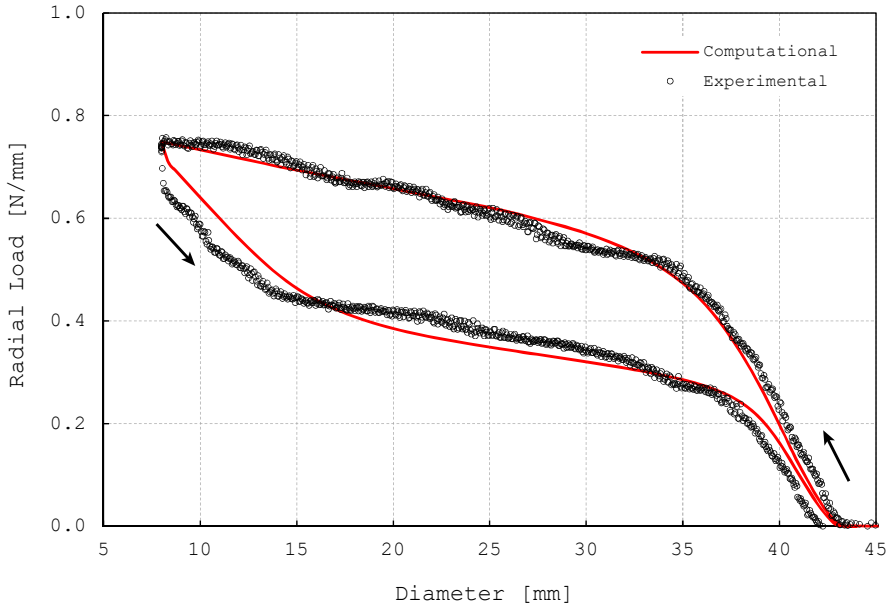


Figure 4.15: Finite element analysis validation. Medtronic Valiant Main Body stent ring radial deformation-load profiles for both experimental (*black*) and computational (*red*) methods. Arrow denotes loading-unloading directionality.

Table 4.7: Nitinol material model parameters used for Valiant stent ring FEA validation.

Parameter	Value
Calibrated Nitinol UMAT	
Density ρ	6500 Kg/m^3
Austenite elasticity E_A	59000 MPa
Austenite Poisson's ratio ν_A	0.33
Martensite elasticity E_M	24750 MPa
Martensite Poisson's ratio ν_M	0.33
Transformation strain ε^L	0.042
Loading $(\delta\sigma/\delta T)_L$	4.77 MPa/°C
Start of transformation loading σ_L^S	260 MPa
End of transformation loading σ_U^E	600 MPa
Temperature T_o	37°C
Unloading $(\delta\sigma/\delta T)_U$	4.77 MPa/°C
Start of transformation unloading σ_U^S	260 MPa
End of transformation unloading σ_L^E	120 MPa
Transformation stress (compression) σ_{CL}^S	400 MPa

Indeed, the (minor) discrepancies seen between the physically measured behaviour of the stent ring and that which is predicated by FEA are attributed to the lack of exact material model parameters (e.g. accumulated plasticity upon unloading). Nevertheless, it is made evident here, and as reported elsewhere (for example, see [79, 83, 119]), that it is possible to accurately predict the behaviour of stent-graft devices using computational techniques. To the best of this author's knowledge, this is the first report of FEA predicted thoracic aortic stent ring behaviour validated with experimental data.

4.6 Summary

In this study, four single chimney and two double chimney TEVAR configurations have been evaluated when subjected to uniform radial load. The chronic outward force (COF) of each configuration has been assessed, revealing notable differences between main endograft types as well as a distinct increase over the baseline characterisation. Critically, this study quantifies the increase in COF at the ideal aortic ch-TEVAR diameter compared to the manufacturer recommend range. Compelling differences were observed between various ch-TEVAR device combinations, most notably in the level of gutter area forming between self-expanding and balloon-expanding configurations. Finally, the finite element methods employed in the previous Chapter have been validated as demonstrated by the excellent agreement between the experimentally measured radial load profile of a single stent-graft ring and its numerical prediction.

4.7 Acknowledgements

The experiments presented in this Chapter were performed in the test laboratory of Admedes GmbH (Pforzheim, Germany). Discussions with Dr. Philipp Hempel and Christoph Degel, as well as technical support from Hannes Feldman, are greatly acknowledged. BeGraft samples were generously provided by Bentley Innomed GmbH (Hechingen, Germany).

Chapter 5

In Vitro Quantification of Stent-Graft Behaviour During ch-TEVAR

In this Chapter, the previously described experimental techniques to investigate parallel stent-graft interactions are elaborated to a more clinically relevant case. Specifically, representative double chimney TEVAR procedures are performed in a physiological model of the thoracic aorta with retrospective electrocardiography-gated computed tomography used to evaluate endograft behaviour. First, the clinical context for this study is provided. Following this, the experimental setup and procedural protocol are described. A rigorous analysis of the *in vitro* ch-TEVAR procedures is then presented, with particular attention given to the quantification of gutter dynamics and endograft deformations at critical time points during the cardiac cycle. Finally, a detailed discussion of the findings is provided, highlighting the influence of endograft design and configuration on device behaviour.

5.1 Introduction

Aneurysmal disease of the ascending aorta and aortic arch (aTAA) is a life-threatening condition which necessitates intervention in patients who present with a high likelihood of rupture. Traditionally, aTAA pathologies have been treated via an open surgical approach. Such procedures, however, are associated with significant risk thereby precluding those patients who present with multiple comorbidities and are unfit for invasive procedures [195–197]. In an effort to treat these patients, minimally invasive thoracic endovascular aortic repair (TEVAR) techniques, which are well established for diseases of the descending thoracic aorta, have been refined to address the complex biomechanical and morphological challenges of the aortic arch [41].

In recent years, fenestrated [198] and branched [199] TEVAR procedures have been successfully reported as potential treatment options. Unfortunately, such devices are typically patient-specific, and therefore costly with lengthy manufacturing times, where patients remain at risk of rupture. The so-called chimney technique (ch-TEVAR) provides an off-the-shelf solution.

Originally reported by Greenberg [30] and Criado [43, 44] as a so-called "bail-out" procedure, this endovascular approach employs the use of standard devices deployed in a "parallel" fashion. Specifically, chimney stent-grafts (CGs) are placed in the supra-aortic branch vessels, sized with sufficient length to extend proximally into the ascending aorta/arch, and run parallel to the primary endograft. The intended result is a sufficient aortic seal zone excluding the diseased aorta whilst maintaining supra-aortic branch vessel perfusion. Recent registries [46] and single-center studies [47–49] reporting on technical success and midterm outcomes illustrate the utility of this approach in treating high-risk patients, particularly in an emergent setting.

Despite its demonstrated feasibility, complications such as endoleak and chimney graft occlusion persist. Regarding endoleak in ch-TEVAR, this phenomenon is predominantly associated with the formation of so-called "gutters": channels/gaps between the aortic wall and non-conforming endografts, through which blood continues to flow, compromising the aortic seal.[1] Conversely, CG occlusion is thought to result from excessive lumenal compression stemming from deployment next to the primary endograft, inadvertently disrupting blood flow potentially causing in-stent thrombosis. These two complications are particularly relevant in the case of double chimney TEVAR configurations, whereby multiple devices are deployed across the aortic arch leading to increasingly complex device-device and device-artery interactions.

Recently, a series of benchtop studies have reported on the behaviour of stent-grafts when used to treat challenging abdominal aortic aneurysms (ch-EVAR) [105–108, 110, 189, 190, 200] and aortoiliac occlusive disease [201]. However, to date, no experimental studies of ch-TEVAR have been reported in the literature. As such, the purpose of this investigation was to: (1) establish a fully characterised, physiological, *in vitro* vascular model subjected to pulsatile flow at our institution, (2) perform representative double chimney TEVAR procedures using both balloon-expandable (BE) and self-expandable

[1] Illustration of gutter formation presented in Chapter 1 (see Figure 1.7).

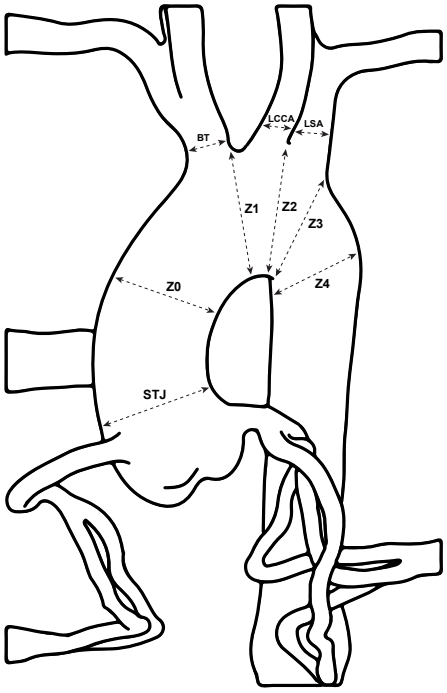
(SE) covered chimney stents, and (3) quantify gutter volume and endograft deformations at critical time points during the cardiac cycle using retrospective electrocardiography-gated computed tomography (ECG-gated CT). It was hypothesised that both device type and cardiac pulsatility would influence the geometric and dynamic behaviour of ch-TEVAR configurations.

5.2 Methods

5.2.1 *In Vitro* Thoracic Aortic Model

An *in vitro* thoracic aortic model, based on a post-mortem vascular cast and manufactured from silicone, was obtained from Elastrat Sàrl (Geneva, Switzerland). The healthy anatomy includes the full thoracic aorta (ascending, arch, descending segments) as well as supra-aortic branch vessels (brachiocephalic trunk, left and right carotids, left and right subclavians, and left and right vertebrals). Fluid flow was accommodated via an inlet located at the posterior surface of the ascending aorta, approximately 20mm distal to the sinotubular junction. Essential model geometry for the purposes of performing representative ch-TEVAR procedures is illustrated in Figure 5.1. Of note, the thoracic model was connected to a secondary silicone abdominal aortic segment, including femoral arteries (United Biologics Inc., Santa Ana, CA, USA) to provide typical endovascular access. The principal mechanical properties and anatomical structure of the model were fully characterised, as described below.

To assess the behaviour of the model under pulsatile loading conditions, changes in inner vessel lumen between end-diastolic (minimum) and peak-systolic (maximum) pressure were measured from retrospectively ECG-gated CT scans. Full details of the pulsatile flow system and imaging protocol are described in the subsequent sections (see Sections 5.2.2 and 5.2.3, respectively). Briefly, individual CT reconstructions at equivalent end-diastolic and peak-systolic aortic pressure of the unstented silicone model were analysed with the 3Mensio Vascular software package (v9.1, Pie Medical, Bilthoven, The Netherlands). Measurements were taken perpendicular to the flow lumen (i.e. over a constructed central lumen line, CLL) for each vessel.



STJ: 33.5mm
Zone 0: 32.5mm
Zone 1: 34.2mm
Zone 2: 31.8mm
Zone 3: 30.4mm
Zone 4: 27.3mm
BT: 10.5mm
LCCA: 7.0mm
LSA: 10.2mm

Figure 5.1: Geometry of the *in vitro* thoracic aortic model used for ch-TEVAR experiments. Dimensions reported as mean inner vessel diameter at 120 ± 40mmHg. (*STJ*) Sinotubular junction; (*BT*) brachiocephalic trunk; (*LCCA*) left common carotid artery; (*LSA*) left subclavian artery. Landing zones defined as per Ishimaru's aortic arch map [202]. Zone 0 defined as the midpoint between the STJ and Z1, as no additional anatomical landmarks (i.e. bifurcation of the pulmonary trunk) present. Note: complex 3D aortic lumen curvature not depicted.

Model distensibility, as based on the standard definition [169, 203, 204], was determined at each proximal landing zone (see Figure 5.1) and was calculated as

$$Distensibility = \frac{maximum\ lumen\ area\ - minimum\ lumen\ area}{minimum\ lumen\ area\ \times pulse\ pressure}\left[\mathrm{mmHg}^{-1}\right]. \quad (5.1)$$

To provide an additional pulsatile behaviour quantification metric, the circumferential cyclic strain at each proximal landing zone was also determined, using the Green-Lagrange strain tensor [162] and was calculated as

$$E_{\theta\theta} = \frac{1}{2}\left(\frac{C_S^2}{C_D^2} - 1\right), \quad (5.2)$$

where C_S denotes the peak-systolic circumference and C_D denotes the end-diastolic circumference. In this formulation it is assumed the deformation through the model wall and in the axial direction is small when compared to the circumferential deformation, as described by Morrison and colleagues [205].

It is important to note that the model lumen boundary at each region of interest was defined as a 2D closed curve, constructed via a series of user-defined spline points (*polygon region of interest* tool embedded within 3Mensio Vascular [190]). Consequently, it is the equivalent lumen circumference which was used in the aforementioned diametric calculations, and not the diameters (again, see [205]).

The morphology of the model was characterised as per the geometrical parameters of the aortic arch recently described by Marrocco-Trischitta et al. [206]. Specifically, the radius of arch curvature, aortic arch tortuosity index, β-angle, and τ-angle (tortuosity angle) for both end-diastolic and peak-systolic aortic pressures were determined.

To determine the radius of arch curvature and aortic arch tortuosity index, a series of four "landmark" points were assigned in 3Mensio (denoted A-D). Following the methodology of Marrocco-Trischitta, these points were specified in axial view at the level of Zone 0. Points A and B were defined along the CLL of the ascending and descending aorta, respectively. Points C and D were assigned on adjacent lumenal surfaces (i.e. minimal distance between ascending and descending aortic segments). Simply, the radius of arch curvature was defined as half the distance between C and D. The aortic arch tortuosity index was calculated as the CLL length between A and B divided by the shortest distance between points A and B.

To determine the β-angle (i.e. the angle between the flow axis and the hypothetical body of the lesion/aneurysm to treat [207]), tangent lines were constructed using the most proximal point of each landing zone and a point 40mm distally (both on the CLL), and the resulting angle computed using the tangent angle function in 3Mensio.

In a similar fashion, the τ-angle of each landing zone was quantified using the tortuosity angle function. This metric is the resulting angle between two connected line segments, whose endpoints fall on the CLL (noting that the end of the first line segment and the start of the second line segment are common; line segment length was 15mm).

For completeness, the model wall thickness was also quantified. Briefly, a single CT reconstruction (unstented, peak-systole) was analysed using the Simpleware ScanIP software package (vN-2018.03, Synopsys Inc., Mountain View, CA, USA). A series of segmentation, Boolean operations, and manual editing techniques were performed to obtain a complete vessel wall surface representation. The wall thickness was computed based on the triangulation of the resulting vessel wall surfaces [194].

5.2.2 Hemodynamic Circuit

To replicate physiological conditions, the silicone vascular model was incorporated into a hemodynamic circuit capable of generating pulsatile flow. The system, a Portable Pulse Duplicator (Medical Implant Testing Lab Inc., Irvine, CA, USA), consists of two main components: (1) a flow channel block, and (2) a controller. The flow channel block was configured in a such a manner as to replicate left heart function. A detailed schematic of the block is given in Figure 5.2. Pulsatile flow was driven by a linear voice coil actuator at the location of the left ventricle, with the vascular model inflow connected as part of the systemic compliance and return flow (from the supra-aortic branch vessels) connected as part of the peripheral compliance. A pressure transducer (PX309, OMEGA Engineering Inc., Manchester, UK) was located at the level of the right subclavian artery, and systemic pressure was monitored and recorded using a custom LabVIEW program (v2015, National Instruments, Austin, Texas, USA). For simplicity, a sinusoidal pressure profile was applied, with the controller and both systemic and peripheral resistances used to tune the pressure range.

In this study, a "worst-case" experimental approach was adopted for specifying the *in vitro* boundary conditions. Hence, a diastolic pressure of 80mmHg and a systolic pressure of 160mmHg was used, with a heart rate of 70 beats per minute (noting that the specified heart rate was due to retrospective ECG-gating requirements).

A blood analogue fluid of consisting of 55% deionized water : 45% glycerol by weight [208] was circulated throughout the model, and its temperature controlled at 37°C.

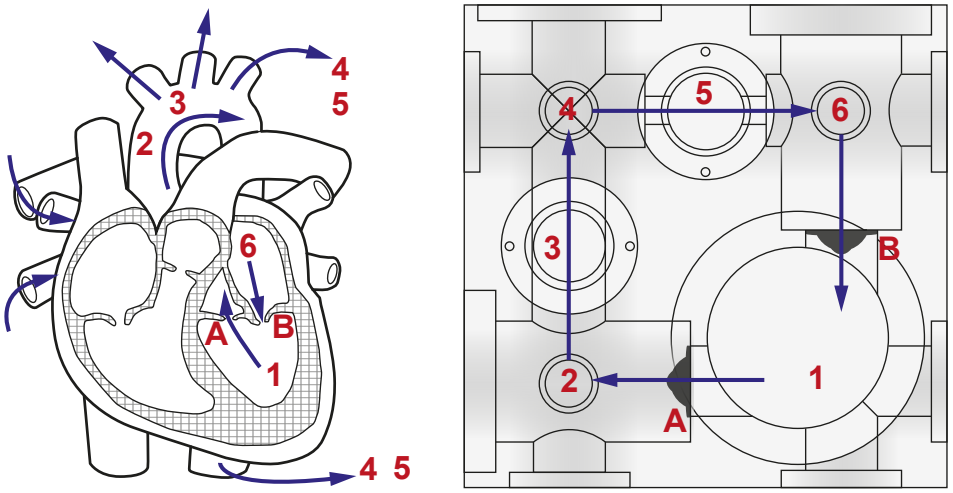


Figure 5.2: Schematic of the left heart and corresponding configuration of the Portable Pulse Duplicator flow channel block. (*Blue Arrows* →) Direction of flow; (*1*) left ventricle, including heating probe; (*2*) systemic compliance; (*3*) tunable systemic resistance of larger arteries; (*4*) peripheral compliance of all peripheral vessels; (*5*) tunable resistance of peripheral vessels; (*6*) left atrium; (*A*) aortic valve; (*B*) mitral valve. *Source: Medical Implant Testing Lab Inc.*

5.2.3 Image Acquisition: ECG-Gated CT

All experiments were conducted within the Interventional Radiology Unit at the John Radcliffe Hospital (Oxford, UK). Computed tomography imaging was performed using a 64 detector CT scanner (GE Healthcare, Chicago, IL, USA), with a standard gated cardiac helical scan protocol (80-kV tube voltage, 100-mA tube current, 0.24:1 pitch, 40mm detector coverage, 0.35s rotation time) and a slice thickness of 0.625mm. An idealised external "heart beat" of 70 beats per minute was provided to the system for the purposes of retrospective ECG-gated reconstructions, with 10 equally spaced phases acquired over the cardiac cycle. The complete setup is shown in Figure 5.3.

5.2.4 *In Vitro* ch-TEVAR Procedures

In this study, two different ch-TEVAR configurations were implanted by an experienced interventional radiologist (Dr. R Uberoi, supported by interventional registrar Dr. M Hadi). Both configurations used a single 44mmOD Ankura device, resulting in an equivalent oversizing of 35%, as the primary endograft (TAA4438B180; Lifetech Scientific Co. Ltd., Shenzhen, China). Either balloon-expandable (BE) or self-expandable (SE) chimney grafts (CGs) were implanted into the brachiocephalic trunk (BT) and left common

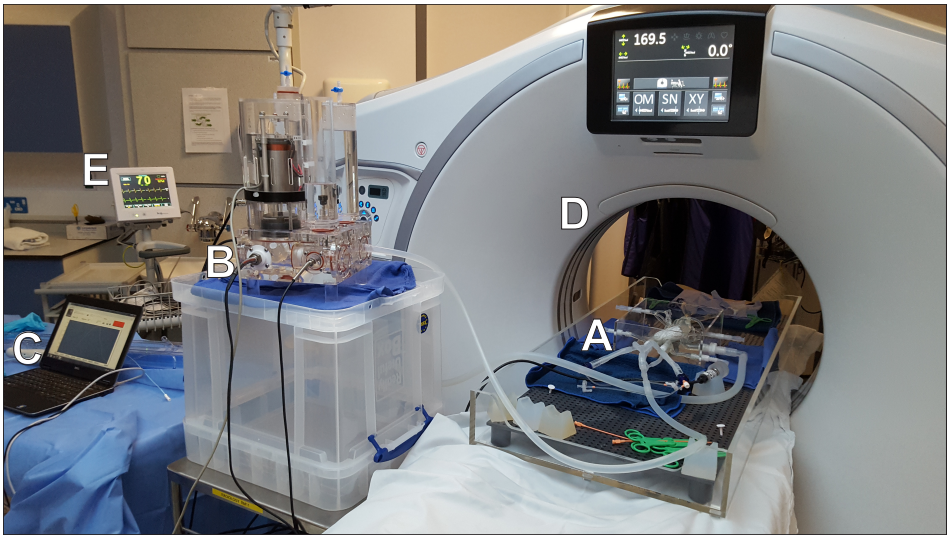


Figure 5.3: *In vitro* ch-TEVAR setup at the John Radcliffe Hospital. (*A*) Thoracic aortic vascular model, including pressure transducer at the level of the right subclavian artery; (*B*) Portable Pulse Duplicator; (*C*) pressure profile monitoring and data acquisition; (*D*) CT scanner; (*E*) external cardiac cycle for retrospective ECG-gating.

carotid artery (LCCA), representative of double chimney TEVAR. Procedural steps are detailed below.

In the vascular model, femoral access was obtained via a large-bore hemostatic valve capable of accommodating a 24Fr delivery system. Supra-aortic branch access into the brachiocephalic trunk and left common carotid was obtained using Tuohy Borst-type valves and standard introducer sheaths, approximating brachial access. The Ankura device was advanced over a 0.035" Lunderquist Extra-Stiff Wire Guide (Cook Medical, Bloomington, IN, USA) as per standard practice, positioned, and deployed at a predefined landing zone. Branch vessels were then cannulated using either 0.018" or 0.035" access wires as appropriate (i.e. as according to CG requirements). To facilitate cannulation, a supporting guide catheter (Codman, Johnson & Johnson, New Brunswick, New Jersey, USA) was used in some instances.

In the first configuration, 10mmOD x 57mm and 7mmOD x 57mm balloon-expandable BeGraft covered stents (Bentley Innomed GmbH, Hechingen, Germany) were implanted into the BT and LCCA, respectively, as per the instructions for use (IFU). Two devices, in an overlapping fashion, were deployed in each artery (i.e. four devices total). Following CG implantation, both the endograft and CGs were simultaneously post-dilated. A compliant endograft remodelling balloon (Tri-Lobe, W.L. Gore & Associates Inc.,

Flagstaff, AZ, USA) was used to ensure the Ankura device adapted to the model aortic wall. ECG-gated imaging was performed as described in Section 5.2.3. Post-imaging, the BeGrafts were radially crushed and removed from the model using a retrieval snare (pfm medical, Cologne, Germany), leaving the main endograft deployed within the model. It was noted that during BeGraft removal, there was a slight distal shift in Ankura positioning caused by model manipulation.

In the second configuration, the supra-aortic vessels were re-cannulated in a similar fashion, with 11mmOD x 5cm and 8mm x 10cm self-expanding Viabahn covered stents (W.L. Gore & Associates Inc., Flagstaff, AZ, USA) deployed into the BT and LCCA, respectively. In this procedure, only a single device was deployed in each artery (i.e. two devices total). Again, both the endograft and CGs were simultaneously post dilated. Opta Pro PTA dilation catheters (Cordis, Milpitas, CA, USA) were used to prevent CG compression and were sized as per the Viabahn IFU.

It is important to note that during cannulation of the supra-aortic vessels, exact positioning of the guidewires were not strictly controlled. That is, the guidewire paths running parallel to the Ankura device were dictated by "the path of least resistance". As a result, CG deployment locations between configurations differed. Representative CT reconstructions resulting from the *in vitro* double chimney TEVAR procedures are shown in Figure 5.4.

5.2.5 Evaluation of ch-TEVAR Gutters

To assess the geometry and dynamic behaviour of the resulting ch-TEVAR gutters, it was first necessary to identify the two phases in each CT series relating to the equivalent end-diastolic and peak-systolic aortic pressure. It was assumed that maximal variation in gutter geometries would occur between minimum/maximum aortic pressures, and so intermediate pressure ranges were not explicitly assessed. Using a standard interventional radiology reporting station (TeraRecon, Foster City, CA, US), each CT series was reviewed by radiologists and the appropriate phases identified by means of diametrical comparison at a defined location in an unstented portion of the ascending aorta. In addition, apparent gutters between the aortic wall and endograft fabrics were also identified as part of this preliminary step.

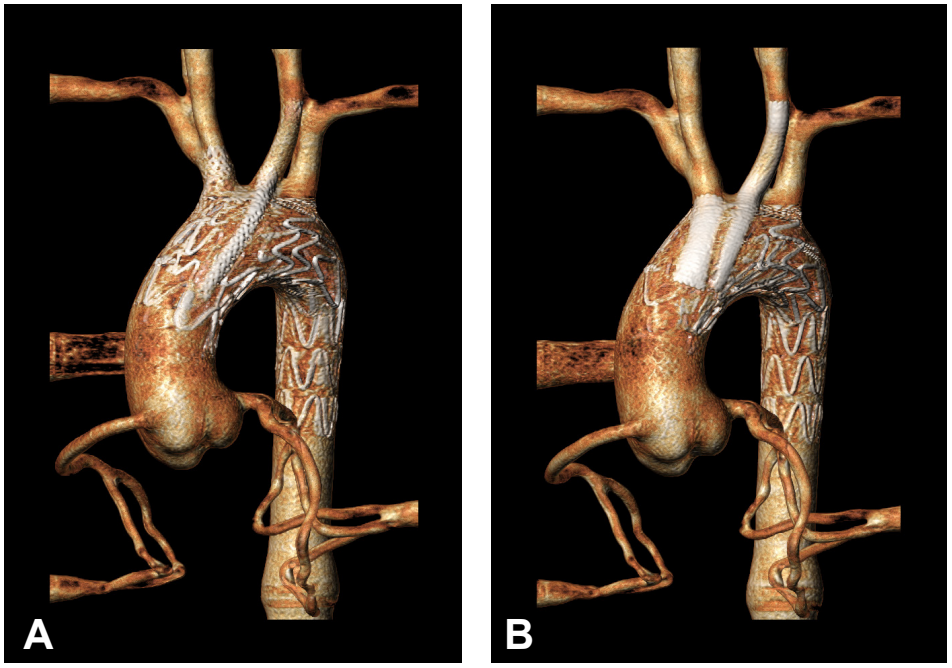


Figure 5.4: Representative CT reconstructions of *in vitro* double chimney TEVAR: (A) Ankura-BeGraft, and (B) Ankura-Viabahn configurations.

Upon identification, imaging data of each phase was exported as a CT DICOM stack and subsequently analysed using a specialized workflow developed in Simpleware ScanIP. Details of each analysis step are provided below.

To begin, data was preprocessed by means of a Median filter to reduce noise. This filter was selected as it is robust to the presence of grey-level outliers; the value of each output pixel is computed as the statistical median of the neighborhood of values around the corresponding input pixel [194, 209].

The aortic vessel wall, as well as endograft and CG stent frames were then segmented. Subsequently, any remaining artefact (e.g. excessive noise attenuated by radiopaque markers) was manually removed via 3D editing techniques (primarily via morphological erosion and feature deletion). Of note, it was not possible to strictly define the boundaries of endograft coverings, as these features were not identifiable via CT imaging used in this study. As such, endograft and CG lumens were estimated based on the spatial positioning of the metallic stent frames and radiopaque markers.

Next, the axial slice at the level of the proximal edge of the main endograft covering was selected. Based upon the gutter identification made in the preliminary step, apparent

gutter (pixel-based) areas were subsequently identified, quantified, and stored. Representative images highlighting the segmented aortic wall, endograft, CGs, and quantified gutter areas of both experimental configurations are given in Figure 5.5. Gutter areas were quantified every 3-5 slices as appropriate, to a predefined axial slice at the level of the fourth endograft stent marker.

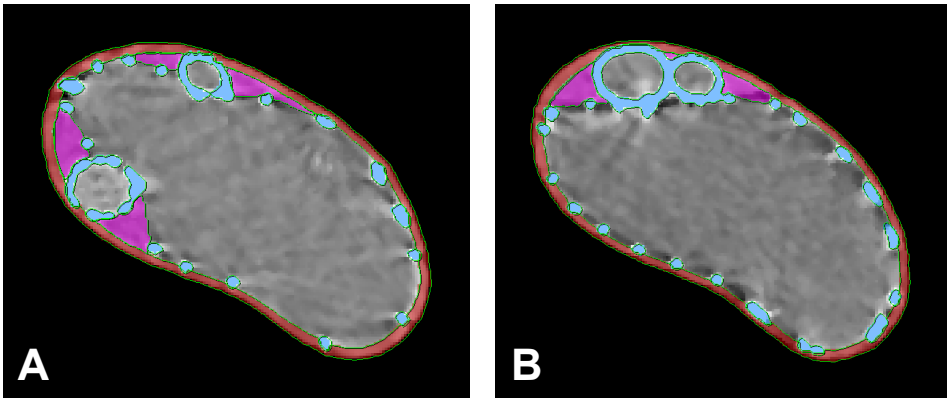


Figure 5.5: Representative axial CT slices used for gutter evaluation in Simpleware ScanIP: (A) Ankura-BeGraft, and (B) Ankura-Viabahn double chimney TEVAR configurations. (*Red*) Aortic wall; (*blue*) stent struts; (*magenta*) gutter areas; (*green*) segmentation contours.

Using the stored gutter areas (i.e. gutter cross-sections on a single imaging plane), the gutter (voxel-based) volume was then constructed by performing a slice-by-slice interpolation between target areas.

To correct for the "axial slice" approach described above, the data was effectively resliced along a centerline generated through the aortic lumen, on to which a finite plane was constructed at the level of the proximal endograft covering. Any gutter volume proximal to the plane was removed resulting in a gutter "inlet" perpendicular to the flow axis at the level of the main endograft covering (note that the distal gutter geometry was unmodified).

Finally, the voxel-based gutter was converted into a surface-based representation, from which the resulting gutter volume was calculated and reported herein. As mentioned, analysis was performed for two CT phases per experimental configuration (i.e. four sets in total). The gutter volume analysis workflow is summarized in Figure 5.6.

Workflow 1: Gutter Volume Analysis

1. Identify required CT phases (TeraRecon) and export data
2. Import CT DICOM stack into ScanIP
3. Reduce noise (grey-level outliers) via Median filter
4. Segment artery wall, endograft and CG stent frames
5. Remove excessive imaging artefacts
6. Select axial slice at level of proximal endograft covering
7. Quantify and store gutter areas; repeat every 3-5 slices
8. Interpolate between quantified areas to generate voxel-based gutter
9. Reslice gutter volume at level of proximal endograft cover
10. Convert gutter voxels to surface based representation
11. **Compute gutter volume**

Figure 5.6: Simpleware ScanIP workflow developed to generate surface-based gutter geometries and quantify volumes. Phase identification and data export (CT DICOM stacks, Step 1) performed by the John Radcliffe Hospital Interventional Radiology Unit.

In this manner, it is possible to quantify, and subsequently compare, both the dynamic behaviour of the gutter geometry during the cardiac cycle at minimum and maximum aortic pressure as well as the difference in gutter formation between different CG combinations.

In addition to quantifying gutter volumes at equivalent diastolic/systolic phases, the effective change in gutter geometry was also assessed. Using the surface-based gutter representations, in a new workflow, both the diastolic and systolic gutter surfaces were imported into Simpleware ScanIP. (Note that as both CT phases share the same global coordinate system, the imported surfaces (qualitatively) show the displacement of the *in vitro* model.)

Briefly, both surfaces were co-registered using a landmark-based registration algorithm. The diastolic surface was specified as the moving object while the systolic surface specified as the fixed object. A minimum of three landmarks were defined per gutter pair. To improve registration, an iterative closest point algorithm was then employed.

Subsequently, the effective surface deviation was quantified by computing the distance from a grid of sampling points distributed across one gutter surface to the nearest

point on the other gutter surface [194]. Here, the systolic gutter was defined as the reference surface (the surface from which the measurements were made) and the diastolic gutter defined as the test surface (the surface which measurements are made to). The surface deviation analysis workflow is summarized in Figure 5.7. This analysis was performed as a means to evaluate the apparent geometric variation of all gutters between minimum/maximum aortic pressure.

Workflow 2: Surface Deviation Analysis

1. Import systolic gutter surface
2. Import diastolic gutter surface
3. Perform landmark based registration (fixed object: systolic surface)
4. Perform iterative closest point surface registration
5. Assign reference surface (systolic gutter)
6. Assign test surface (diastolic gutter)
7. **Compute distance between reference and test surfaces**

Figure 5.7: Simpleware ScanIP workflow implemented to quantify geometric variation of gutters at minimum/maximum aortic pressure.

5.2.6 Evaluation of Device Interactions (Deformations)

To evaluate device interactions, graft lumen deformation was measured for both the endograft and CGs. Using 3Mensio, CLLs were constructed for each individual device at both phases of the cardiac cycle. Graft lumen boundaries were then defined in a plane perpendicular to the flow axis using the *polygon region of interest* tool, similar to the approach described in Section 5.2.1. The degree of graft deformation was quantified as the ratio between major and minor axis of the graft lumenal area, known as the D-Ratio. A D-Ratio of 1 indicates a perfectly circular lumen, while a D-Ratio > 1 indicates an elliptical (compressed) shape [110, 190, 201]. Note that the major and minor axes used in D-ratio calculations both pass through a centroid defined by the 2D closed curve of the graft lumen boundary. Representative images demonstrating D-Ratio analysis for both experimental configurations are given in Figure 5.8. Measurements were performed for each CT slice beginning at the proximal device (covered) edge and at subsequent 2mm intervals, to a level deemed sufficient to fully capture device behaviour (e.g. in

the case of Ankura devices, to a position distal to the LCCA where no CG interactions remain).

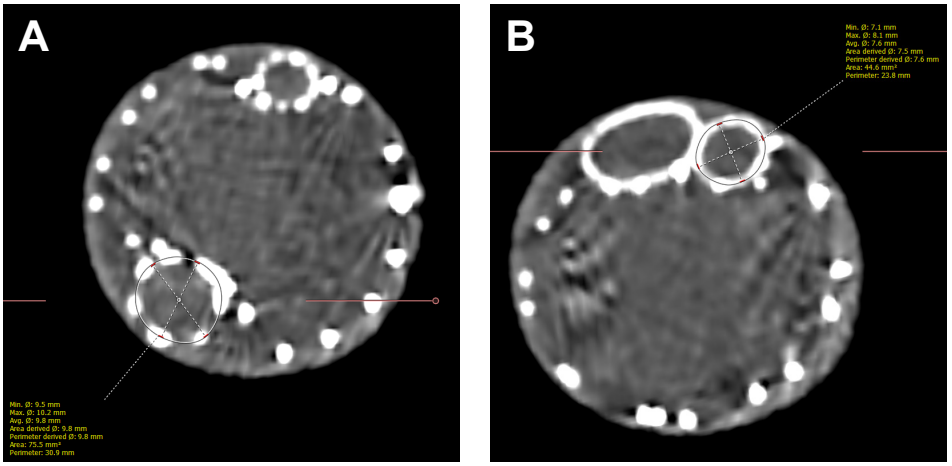


Figure 5.8: Representative resliced CT images (perpendicular to flow axis) used for D-Ratio analysis: (A) Ankura-BeGraft, and (B) Ankura-Viabahn combination. Shown are CG lumen boundary, and major- and minor-axis for BeGraft (BT) and Viabahn (LCCA) calculations.

5.2.7 Statistical Analysis

For statistical comparisons, a two-tailed Student's t-test was used to assess significance between measures. In cases of intra-configuration comparisons (i.e diastolic *vs.* systolic phases), a paired test was used. In cases of inter-configuration comparisons (i.e. BE *vs.* SE chimney stents), a two-sample equal variance (homoscedastic) test was used. The significance threshold was set as $p < 0.05$, and analysis was performed using Microsoft Excel (v1807, Microsoft Corporation, Washington, USA).

Of note, measurements were performed by a single observer. As such, interobserver variability was not considered in this study. Similarly, intraobserver variability was not formally quantified (e.g. using Bland-Altman plots, as described elsewhere). Rather, to demonstrate repeatability, D-ratio measurements for a single dataset (Viabahn-BT, systolic) were conducted three times and variability qualitatively examined.

5.3 Results

5.3.1 *In Vitro* Model Characterisation

Characterisation metrics of the thoracic aortic model are reported in Table 5.1. In addition to characterising the model at proximal landing zone boundaries (Zones 0 - 4, according to Ishimaru's aortic arch map [202]), the unstented model was also characterised at the actual level of the Ankura device landing zone (midpoint of the most proximal radiopaque marker, approximately 4mm proximal to Zone 0, as determined post deployment).

Table 5.1: *In vitro* thoracic aortic model characterisation, including pulsatile behaviour and anatomical geometry.

	Distensibility (10^{-3} mmHg^{-1})	Circ. Cyclic Strain (%)	β-angle (deg)	τ-angle (deg)	CLL Length (mm)
Landing Zone	1.95	7.81	50/50	12/15	
Zone 0	1.98	7.93	56/54	12/13	39.1/39.6
Zone 1	2.24	8.46	83/77	30/26	8.0/9.0
Zone 2	2.44	9.30	75/76	37/37	13.1/13.0
Zone 3	1.78	6.39	61/63	28/28	20.0/20.0
Zone 4	1.73	6.97	26/25	12/10	

β-angle, τ-angle, and central lumen line (CLL) length values reported as diastolic/systolic

Model distensibility ranged from 1.73 - 2.44 (mean: 2.02) (10^{-3} mmHg^{-1}), with a tendency towards increasing distensibility in the proximal aortic arch. Spatial variation in model behaviour when subjected to pulsatile flow was attributed to differences in model wall thickness. As shown in Figure 5.9 the model exhibits a degree of wall thickness heterogeneity throughout, and in particular a thinner wall in the aortic arch. The mean model wall thickness was determined to be 1.96mm.

The model exhibits an increase in both β- and τ-angles moving distally from the landing zone to Zone 1, followed by a decrease in both values moving further distal into the descending (straight) segment of the thoracic aorta. Variation was observed in values between equivalent end-diastolic and peak-systolic aortic pressures, with the largest variation occurring at Zone 1 (a decrease of 6° and 4° in the β- and τ-angles, respectively).

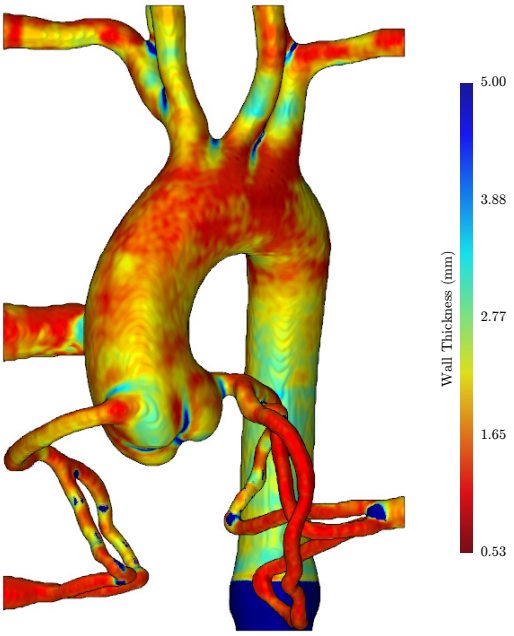


Figure 5.9: Thoracic aortic model wall thickness (mean: 1.96mm). Computed based on the triangulation of vessel wall surfaces as segmented from CT data. *Note:* vessel wall at level of descending thoracic - abdominal aorta junction (blue) not included in mean thickness analysis.

Model geometrical indices are presented in Table 5.2. The radius of arch curvature decreased between varying aortic pressures, as attributed to lumen distension. Notably, the radius of arch curvature was found to be < 20mm, indicating a steep aortic arch angulation. Such an anatomy may represent a contraindication to standard TEVAR procedures [206]. This value, however, was derived based on a Zone 0 landmark defined as the mid-point between the sinotubular junction and Zone 1, as typical anatomical landmarks were not available (e.g. pulmonary trunk bifurcation). If assessing the radius of arch curvature at the level of the inlet flow, for example, a systolic radius of arch curvature of 22.3mm can be reported, demonstrating the suitability of the model for *in vitro* ch-TEVAR.

The aortic arch tortuosity index was found to be 1.44 and 1.41 at minimum and maximum aortic pressure, respectively. This variation is attributed to an increase in the shortest distance length between landmark points A-B, with the difference in CLL length between the same two points relatively negligible (data not shown). The variation in aortic arch tortuosity, coupled with the decrease in both β- and τ-angles at Zone 1 serve to demonstrate the dynamic motion of the ascending aortic segment of the model. This

motion, in addition to cardiac pulsatility, is best described as a anterior-lateral movement of the aortic root, with a slight caudal translation. This movement is attributed to location of the fluid inlet, the (relatively) unconstrained attachment of the model at this location, and the absence of the heart.

Table 5.2: *In vitro* thoracic aortic model geometric indices.

Index	Value
Radius of Curvature	16.5/15.6
Aortic Arch Tortuosity	1.44/1.41

Values reported as diastolic/systolic

A stable pulsatile pressure profile, cycling between 120 ± 40 mmHg, was generated using the Portable Pulse Duplicator, as demonstrated in Figure 5.10.

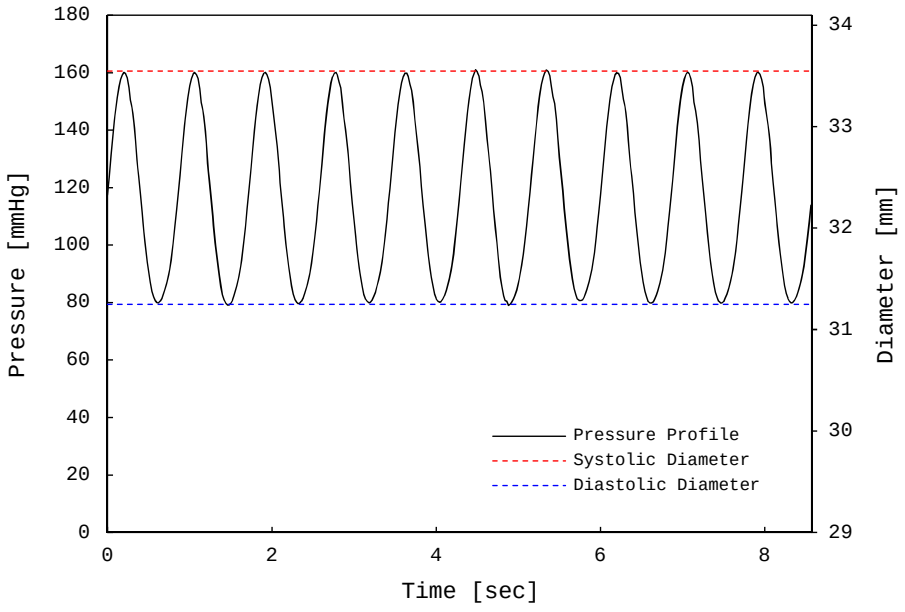


Figure 5.10: Representative pressure profile (10 cycles) recorded at the level of the right subclavian artery as generated by the pulse duplicator. Average peak-systolic and end-diastolic lumen diameters at the level of the landing zone are included for reference.

5.3.2 Gutter Phenomena During the Cardiac Cycle

Double chimney TEVAR employing BE covered stents (Ankura-BeGraft) resulted in four gutters, while double chimney TEVAR employing SE covered stents (Ankura-Viabahn)

resulted in the formation of three gutters. The identified gutters and corresponding surface-based volumetric reconstructions for each configuration are shown in Figure 5.11. Quantified gutter volumes, changes in gutter volume during the cardiac cycle, and degree of gutter volume increase are reported in Table 5.3.

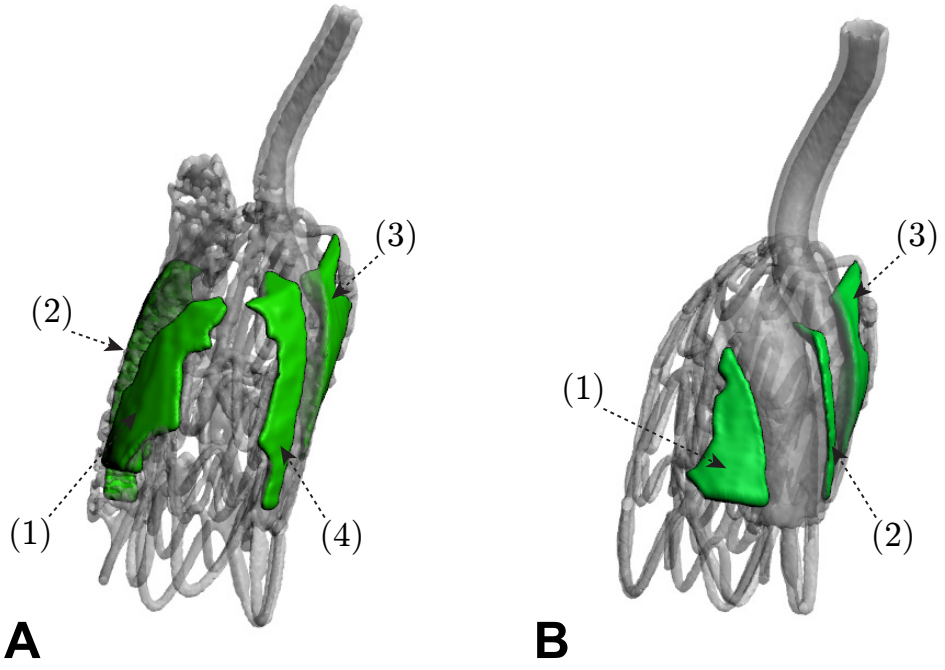


Figure 5.11: *In vitro* gutters identified and resulting surface-based volume reconstructions in the (A) Ankura-BeGraft, and (B) Ankura-Viabahn double chimney TEVAR configurations. Gutters shown are at peak-systolic pressure.

The absolute largest gutter volumes were determined to be 1593.2mm^3 and 559.6mm^3 in the BE and SE configurations, respectively. All gutter volumes were found to increase from end-diastolic to peak-systolic aortic pressure, with largest volumetric increase found in the BE configuration (Gutter 1, 385.9mm^3).

Differences in gutter volumes between configurations were not found to be statistically significant for either end-diastolic or peak-systolic aortic pressures (p=0.2 and p=0.12, respectively). Change in gutter volume between diastole and systole was statistically significant for the BE configuration (p=0.014), but was not significant for the SE configuration (p=0.098). Differences in gutter volume change during the cardiac cycle between configurations were found to be (nearly) significant (p=0.0504).

Table 5.3: Gutter volumes at end-diastolic and peak-systolic aortic pressure.

	Diastole (mm^3)	Systole (mm^3)	Difference	Factor
Ankura-BeGraft				
Gutter 1	531.7	917.7	385.9	1.73
Gutter 2	1286.2	1593.2	307.1	1.24
Gutter 3	503.4	650.0	146.6	1.29
Gutter 4	396.6	623.6	227.1	1.57
TOTAL	**2717.9**	**3784.5**	**1066.7**	**1.39**
Ankura-Viabahn				
Gutter 1	406.2	559.6	153.4	1.38
Gutter 2	43.4	84.8	41.4	1.95
Gutter 3	423.6	515.7	92.1	1.22
TOTAL	**873.3**	**1160.2**	**286.9**	**1.33**

A total of seven gutter pairs were overlaid, co-registered, and subsequently analysed using the surface deviation approach to quantify the behaviour of the gutter geometry at end-diastolic and peak-systolic pressure. A representative analysis case is illustrated in Figure 5.12. For clarity, all co-registered gutters are presented in Figure 5.13.

Surface deviation results between diastolic-systolic gutter geometry pairs are reported in Table 5.4. Note that negative values indicate a test (diastolic) surface lying within the reference (systolic) surface, whilst positive values indicate a test surface lying outside the reference surface. Assessment of mean positive and mean negative surface deviations reveal that diastolic gutters predominately lie within the systolic surface.

Maximum negative surface deviations of -5.26mm and -4.49mm were found for the BE and SE configurations, respectively. These large deviations are associated with geometric changes located in the distal region of the gutter, approaching the aortic arch. Mean surface deviations were found to be -0.43mm and -0.34mm in the BE and SE configurations, respectively. Differences in mean surface deviations between BE and SE configurations were not determined to be statistically significant ($p=0.52$).

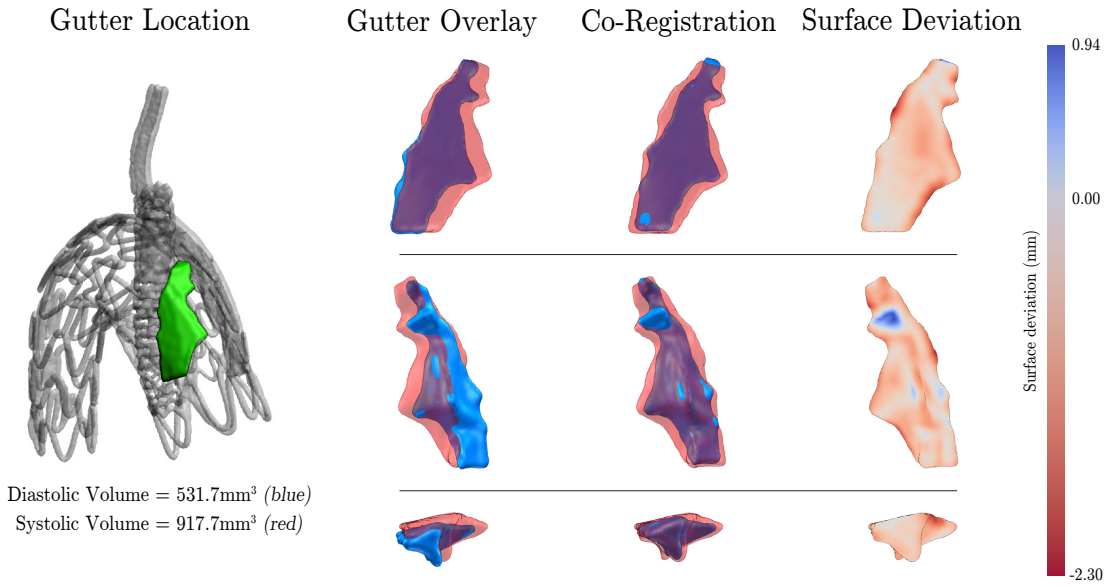


Figure 5.12: Representative case of geometrical gutter analysis (Gutter 1, Ankura-BeGraft) including diastolic (*blue*) and systolic (*red*) gutter overlay, co-registration, and surface deviation quantification. Gutter as viewed to (*top*) vessel-bound surface aspect; (*middle*) endograft-bound surface aspect; (*bottom*) inlet at level of Ankura graft covering. Gutter location included for reference. Note: surface deviation map displayed on systolic gutter surface; positive surface deviation indicates regions where diastolic gutter lies external to systolic gutter.

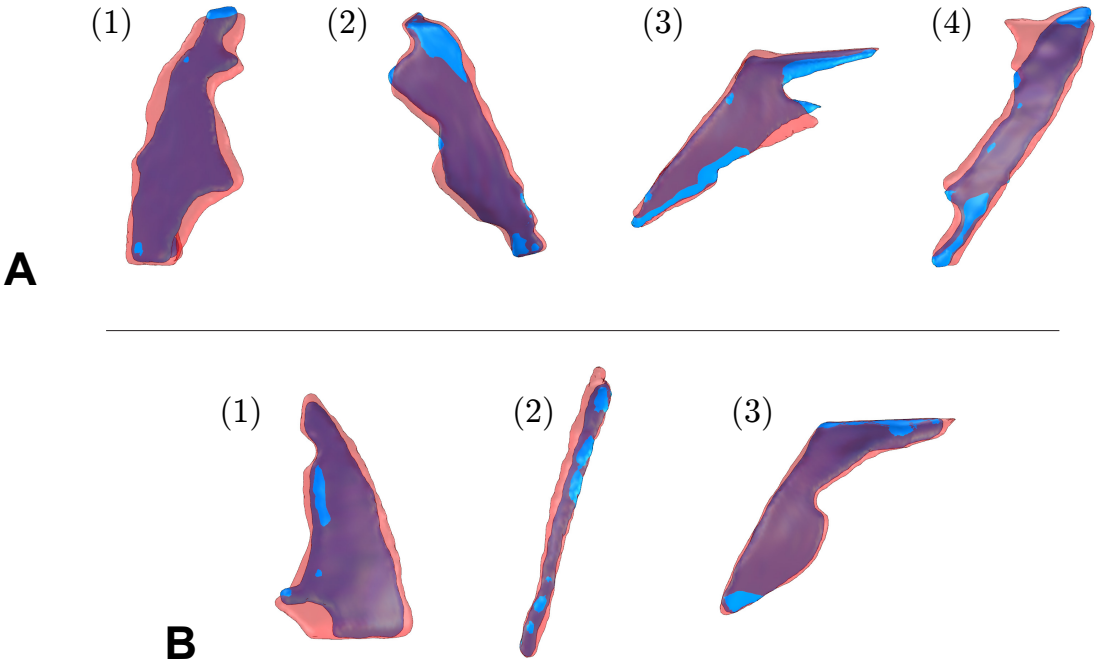


Figure 5.13: Co-registration of diastolic (*blue*) and systolic (*red*) gutters in: (A) Ankura-BeGraft, and (B) Ankura-Viabahn combinations. Gutter labels as per Figure 5.11 and orientated as viewed to vessel-bound surface aspect.

Table 5.4: Geometrical variation (surface deviation) in gutter volumes between diastolic and systolic cardiac phases. Data reported as mean (maximum) values of co-registered gutter pairs.

	Mean Positive Deviation (mm)	Mean Negative Deviation (mm)	Mean Deviation (mm)
Ankura-BeGraft			
Gutter 1	0.01 (0.94)	-0.63 (-2.30)	-0.62
Gutter 2	0.03 (0.73)	-0.34 (-1.84)	-0.30
Gutter 3	0.04 (0.63)	-0.31 (-2.26)	-0.28
Gutter 4	0.02 (0.59)	-0.53 (-5.26)	-0.51
Ankura-Viabahn			
Gutter 1	0.01 (0.41)	-0.35 (-2.87)	-0.35
Gutter 2	0.01 (0.20)	-0.50 (-4.49)	-1.74
Gutter 3	0.01 (0.19)	-0.19 (-1.74)	-0.18

Mean positive - the mean average of all positive deviation points found by the analysis
Mean negative - the mean average of all negative deviation points found by the analysis
Mean - the mean average deviation found by the analysis

5.3.3 Endograft Compression During the Cardiac Cycle

The D-ratios for both experimental configurations are presented in Figure 5.14. Key measures along the constructed CLLs including maximum, minimum, and average D-ratios, as well as the change between end-diastolic and peak-systolic aortic pressure, are reported in Table 5.5.

For the BE double chimney configuration, the Ankura device exhibited the largest D-ratio (1.99, end-diastolic pressure), with the change between end-diastolic and peak-systolic behaviour determined to be statistically significant ($p<0.001$). BeGraft devices deployed into the BT and LCCA experienced absolute maximal D-ratio changes of 0.03 and 0.06, respectively. These changes, however, were not statistically significant ($p=0.17$ and $p=0.38$, respectively). When considering positional variation, both BeGrafts exhibited relatively uniform D-ratios along their length, whilst the Ankura device exhibited a consistent downward trend.

In the SE double chimney configuration, the Viabahn device deployed into the BT exhibited the largest (and largest overall) D-Ratio ratio (2.17, end-systolic pressure). However, in a manner similar to the BE configuration, only changes in the Ankura D-ratio

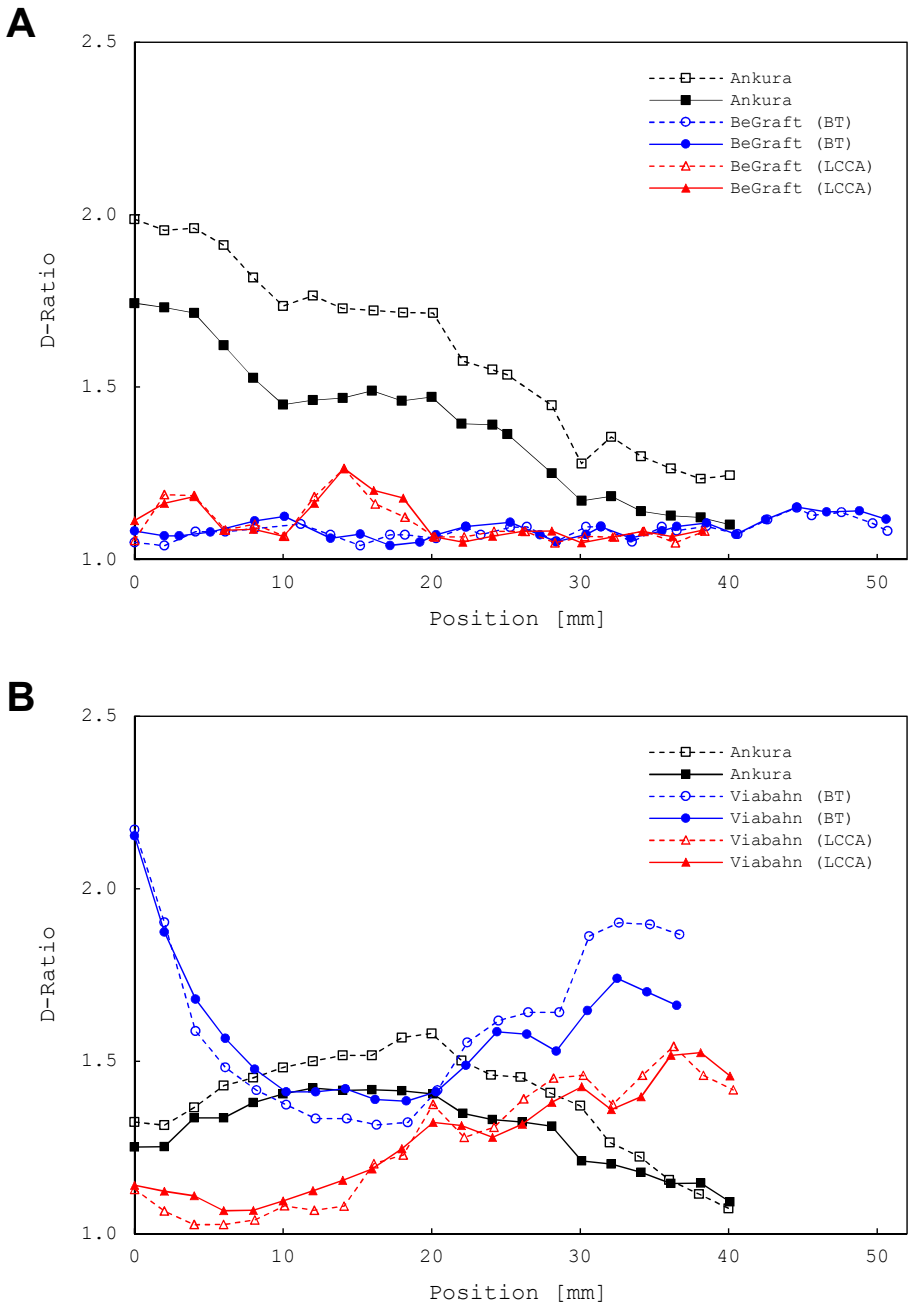


Figure 5.14: D-ratios of (A) Ankura-BeGraft, and (B) Ankura-Viabahn double chimney TEVAR configurations at end-diastolic (*dashed line*) and peak-systolic (*solid line*) aortic pressures measured along the central lumen lines. (*BT*) Device deployed into brachiocephalic trunk; (*LCCA*) device deployed into left common carotid artery. Position 0mm refers to the proximal covered edge of each device.

Table 5.5: Key measures of main and chimney endograft D-ratios between end-diastolic and peak-systolic aortic pressure as measured along the central lumen lines.

Endograft	Diastolic D-Ratio	Systolic D-Ratio	Dia-Sys Change
Ankura (BeGraft)			
Maximum	1.99	1.74	0.30
Minimum	1.23	1.10	0.11
Difference	0.75	0.64	–
Average	1.61	1.40	0.21
BeGraft (BT)			
Maximum	1.15	1.15	0.03
Minimum	1.04	1.04	0.00
Difference	0.11	0.11	–
Average	1.09	1.09	0.01
BeGraft (LCCA)			
Maximum	1.26	1.26	0.06
Minimum	1.05	1.05	0.00
Difference	0.21	0.22	–
Average	1.11	1.11	0.02
Ankura (Viabahn)			
Maximum	1.58	1.42	0.18
Minimum	1.07	1.09	0.01
Difference	0.51	0.33	–
Average	1.38	1.30	0.09
Viabahn (BT)			
Maximum	2.17	2.15	0.22
Minimum	1.32	1.38	0.00
Difference	0.86	0.77	–
Average	1.61	1.58	0.09
Viabahn (LCCA)			
Maximum	1.54	1.53	0.08
Minimum	1.03	1.07	0.01
Difference	0.52	0.46	–
Average	1.26	1.27	0.04

BT - brachiocephalic trunk; *LCCA* - left common carotid artery

between end-diastolic and peak-systolic aortic pressure were deemed to be statistically significant ($p<0.001$). When considering positional variation, it can be observed that the D-ratios of both SE devices noticeably change along their length.

When comparing inter-experimental results, only differences between Ankura D-ratio changes were statistically significant ($p<0.001$), whilst changes in CG D-ratios were not ($p=0.12$ and $p=0.85$, respectively).

As previously mentioned, guidewire positioning during chimney graft placement was not strictly controlled, whereby guidewires followed "the path of least resistance" during positioning. Consequently, a distinct inflection is observed in the BT Viabahn D-ratio, for both end-diastolic and peak-systolic phases. This distinctive change in D-ratio is associated with the adjacent positioning of the SE chimney devices; it appears self-expandable devices tend to support each other, maintaining their inherent circular cross-sections, when deployed in parallel. In the case of the (larger) Viabahn device deployed into the BT, at its most proximal position, which was completely unopposed by either the main endograft or its parallel counterpart, it exhibited the largest level of lumen compression. However, as the LCCA device came into contact (noting that the LCCA was deployed slightly distally, see Figure 5.4), both SE devices tended towards their (designed) circular cross-sections (i.e. decreasing D-ratios). Notably, another secondary inflection in D-ratio was observed for SE devices. Specifically, both Viabahn D-ratios increased further distally into the aortic arch as devices lost contact departing into their target deployment sites. This observation further corroborates the notion that self-expandable covered stents maintain their designed circular lumen if deployed in an adjacent double chimney configuration.

For completeness, the measured major and minor axes for all devices, from which the D-ratio is derived, is provided in Figure 5.15. When considering the axial variation in D-Ratio of the Ankura (in both BE and SE ch-TEVAR configurations) and both Viabahn devices, inspection of the major and minor axes reveals that the change in D-ratio is primarily driven by changes in the minor axes.

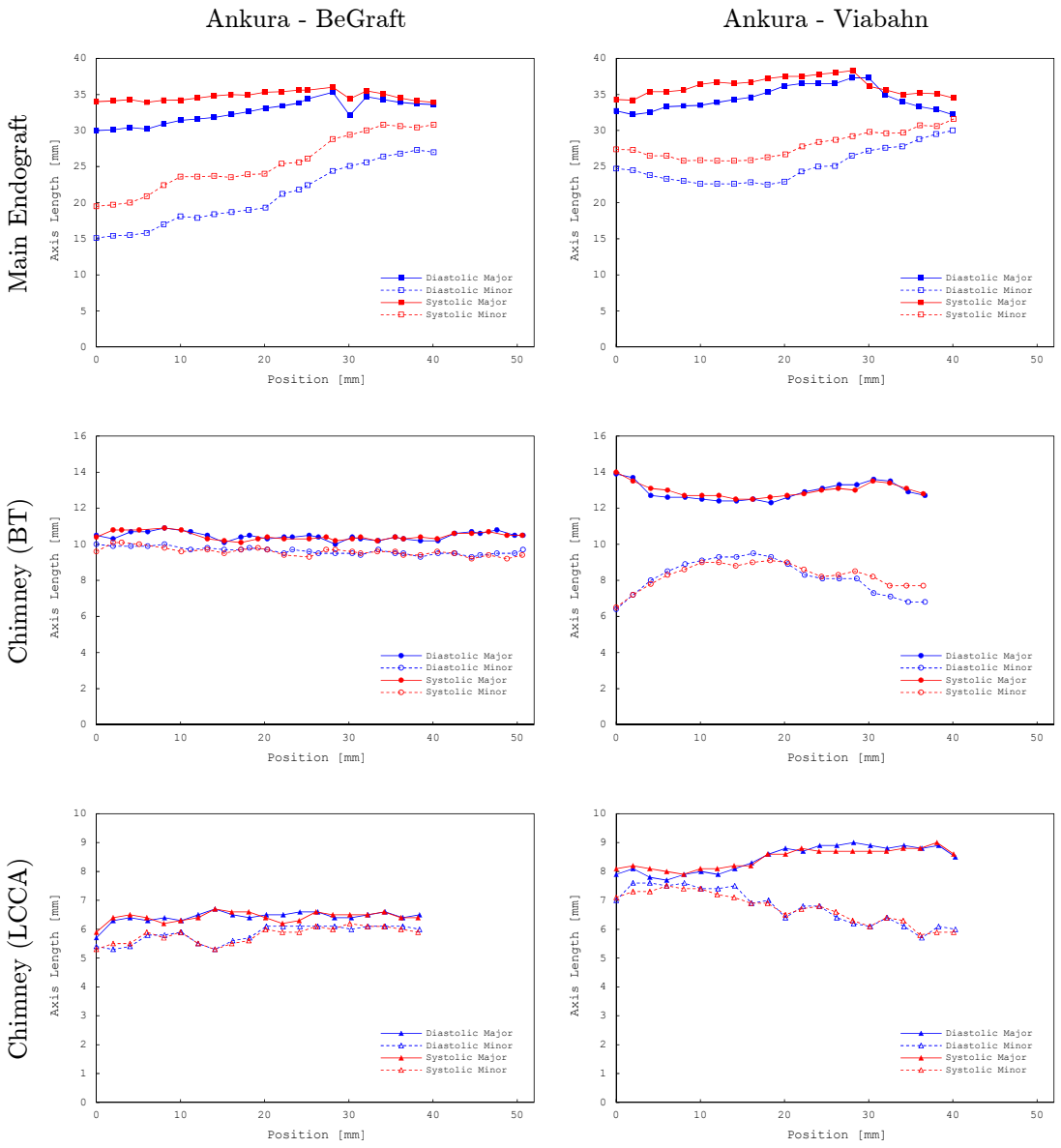


Figure 5.15: Endograft lumen major and minor axes. (*Blue*) End-diastolic pressure; (*red*) peak-systolic pressure). (*BT*) Device deployed into brachiocephalic trunk; (*LCCA*) device deployed into left common carotid artery. Position 0mm refers to the proximal edge of each device.

5.3.4 Repeatability

To demonstrate the stable and repeatable performance of the pulse duplicator used in this study, representative pressure profiles for each experimental configuration are given in Figure 5.16. Excellent agreement between all experiments was found. The slight offset recorded during the diastolic phase of the Ankura-BeGraft experiment was attributed to the distal landing position of the BeGraft device in the brachiocephalic trunk. The deployed device reached the level of brachiocephalic bifurcation (see Figure 5.4A) partially covering the right subclavian to which the pressure transducer was connected. This deployment was deemed to have a negligible impact on tuning the pulse duplicator to the desired pressure range, as made evident in the profiles below. The deployment outcome, however, led the team to subsequently deploy only single SE devices in the Ankura-Viabahn configuration. This ensured perfusion to the pressure transducer whilst not inadvertently confounding gutter/D-ratio results by analysing an excessively overlapped SE configuration (i.e. a secondary SE with overly proximal deployment).

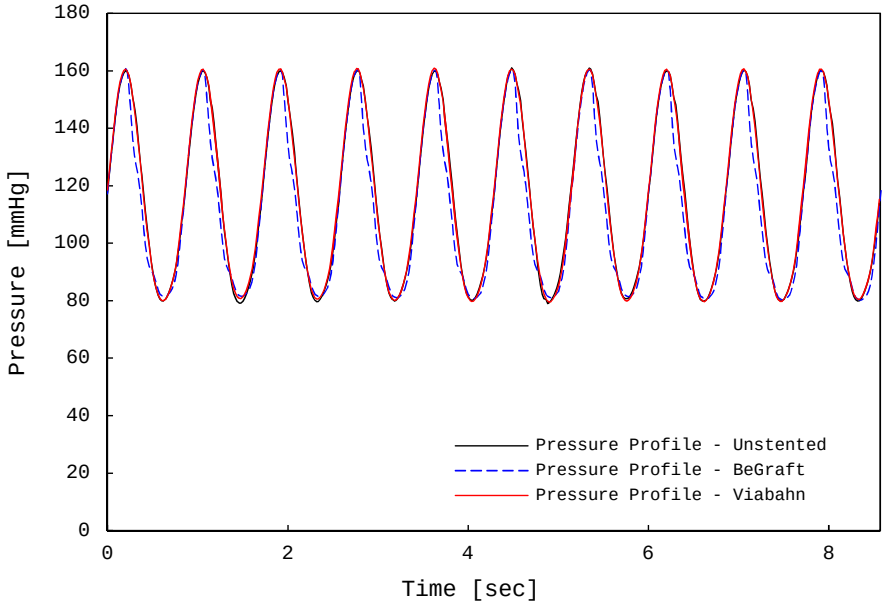


Figure 5.16: Pulse duplicator repeatability. Representative pressure profiles measured at the level of the right subclavian artery of unstented (*black*), Ankura-BeGraft (*blue*), and Ankura-Viabahn (*red*) configurations.

To assess the repeatability of CT data measurements made (relevant to the gutter volumes, surface deviations, and D-ratio values reported in this study), three sets of repeated measurements were made for a representative case. The endograft lumen of the

Viabahn device deployed in the BT at peak-systolic pressure, as used to report the D-ratio, was selected. This data represented one of the unique findings of this study (i.e. a positionally varying profile) and so was deemed appropriate to assess repeatability. The resulting measurements are given in Figure 5.17. Qualitatively, it was determined that there was minimal variation between measurements.

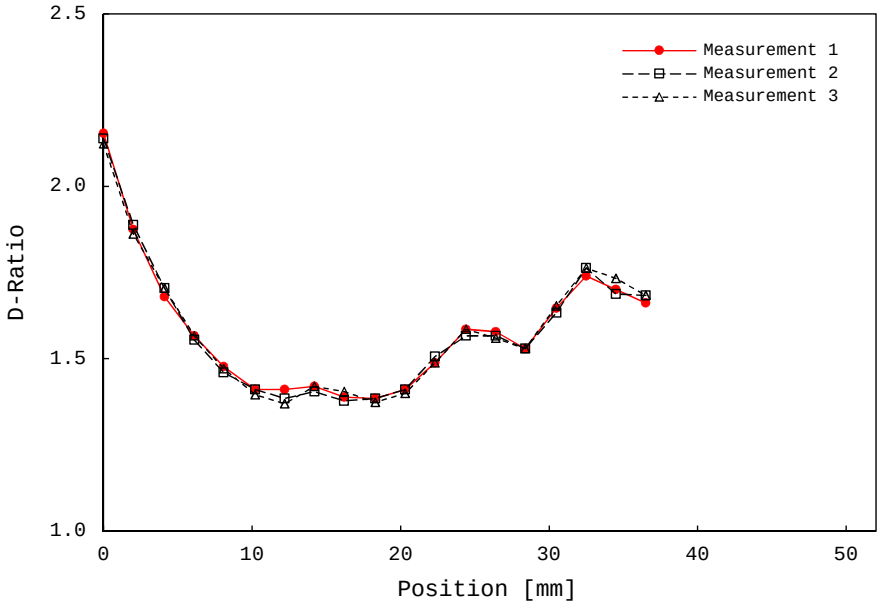


Figure 5.17: CT data measurement repeatability: D-ratio of SE device deployed into brachiocephalic trunk at peak-systolic pressure (Ankura-Viabahn configuration).

5.4 Discussion

Open surgical repair of aneurysmal disease involving supra-aortic branch vessels is associated with high rates of morbidity and mortality. To treat patients unfit for these procedures, conventional endovascular techniques have been augmented to extend their utility into the region of the ascending aorta and aortic arch. Specifically, the use of off-the-shelf devices deployed in a parallel configuration, known as chimney TEVAR, has been described to treat patients both in emergent and elective settings. Despite a growing level of experience with these procedures, peri- and post-operative complications still persist, namely in the form of type 1a endoleak and CG compression. Although the technical feasibility and mid-term outcomes of ch-TEVAR have established its effectiveness, results of contemporary registries and pooled data in current meta-analysis

report rates of type 1a endoleak and CG occlusion in 11% and 2% of cases, respectively [46–48]. A recent single-center study describing outcomes after double chimney TEVAR procedures reported incidents of type 1a endoleaks in 13% and CG compression in 4.3% of cases, respectively [210]. These complication rates require a deeper understanding of how endograft devices interact in the complex anatomy of the ascending aorta and aortic arch. In this study, representative *in vitro* double chimney TEVAR procedures have been performed to elucidate the dynamic behaviour of endografts during complex aortic repair.

The use silicone vascular models to investigate stent-graft behaviour is well established (see, for example, [80, 104, 211–214]). The *in vitro* model employed within this work, when integrated into a hemodynamic flow circuit replicating left heart function, exhibited distensibility and circumferential cyclic strain at the upper physiological range [169, 205]. Its anatomy was categorized as a Type 1 aortic arch [215], with a steep aortic angulation [206]. Considering the level of model characterisation described herein, the physiological behaviour and anatomy were deemed suitable for this study based on its mechanical response to pulsatile load. Interestingly, the model also exhibited dynamic, non-pulsatile, motion as made evident during experimentation and quantified via the various geometric parameters such as the aortic arch tortuosity index and changes in both β- and τ-angles at Zone 1. Although not strictly physiological (i.e. as induced by cardiac and respiratory dynamics, but rather as an unintended consequence of inlet potion and vessel connections), such additional motions do add a level of realism to the *in vitro* setup when comparing its behaviour to the dynamics of the *in vivo* thoracic aorta. Specifically, the aortic root is pulled in an anterior and caudal direction during systole mimicking native thoracic behaviour as described by Suh et al. [216] and again by Hirotsu et al. [217]. As a result, these three dimensional motions are, to a degree, manifested in the resulting gutter volumes, D-ratios, and surface deviations determined in this study, thus enhancing the quality of data collected.

Critically, nearly all reported studies employ physiological resting conditions in benchtop experiments. In this work, an aggressive physiological testing environment (120 $\pm$ 40 mmHg aortic pressure) was employed to assess behaviour at worst-case boundary conditions. Such an approach was taken to be inline with test protocols typically required by regulatory agencies (e.g. the FDA) when evaluating the mechanical performance of

endovascular devices (for example, see [72]). As such, the observations in this work are viewed in the light of such worst-case boundary conditions.

The results of the present study demonstrate that both balloon-expandable (BE) and self-expandable (SE) covered chimney stents, when deployed in a double ch-TEVAR configuration, result in gutter formation. Notably, the BE configuration resulted in three times the total gutter volume in comparison to its SE counterpart, which extends the results of previously reported ch-EVAR/EVAS studies [105, 106, 108, 110] to the ch-TEVAR case. Indeed, gutters may be inherent to this endovascular technique [190], regardless of chimney graft type or anatomical location. Quantitatively, it is not appropriate to compare absolute gutter volumes between other reported studies given the difference in devices used, target branch vessels (anatomy), and the various measurement techniques employed. Nevertheless, Niepoth et al. [107] reported total gutter volumes up to 960mm^3 over a seal zone of 20mm for a single balloon expandable ch-EVAR case (resulting in two identifiable gutters). Considering additional gutters have been identified in the model employed here (four gutters in the case of BE ch-TEVAR), as well as longer seal zones (up to approximately 45mm in case of Gutter 2), the total gutter volumes for both BE and SE configurations appear entirely reasonable.

Importantly, it was shown that ch-TEVAR gutter volumes vary dynamically between end-diastolic and peak-systolic phases of the cardiac cycle, corroborating a recent ch-EVAR study by Overeem et al. [110]. The most substantial change in gutter volume between end-diastolic and peak-systolic aortic pressure was associated with the BE configuration, with only a small change in gutter volume noted in the SE case. These findings further support the recommendation that ECG-gated CT, or similar, should be used during follow-up of patients treated with chimney grafts to better identify persistent endoleaks which may otherwise go undetected [110].

The difference in gutter volume changes during the cardiac cycle were also evaluated in this work. The nearly significant difference in cardiac-induced changes between BE and SE configurations suggests that either chimney type or deployed arrangement (opposite clock-face orientation *vs.* adjacent), or both, influence how gutters may behave *in vivo*. Such influences could in turn affect the risk of type 1a endoleak. Given the low sample size in this study, and uncontrolled implant positioning between groups, exact inferences could not be made. Nevertheless, these findings further support the notion

that there exists an underlying structure-function relation, primarily attributed to the native properties of nitinol [144], that may influence the optimal configuration of devices in chimney-type procedures [106, 190].

To the best of this author's knowledge, there exists only a single report to date illustrating a volumetric reconstruction of an *in vitro* chimney related gutter [107], and no reports on either the geometrical changes during the cardiac cycle, or specific to ch-TEVAR. Accordingly, this investigation provides compelling insights into the dynamic geometrical behaviour of gutters. Qualitatively, it can be observed in the ch-TEVAR cases presented here that distinct gutter geometries exist at different phases of the cardiac cycle. Again, it is postulated that this dynamic behaviour is likely owing to both spatial positioning and device type. Recent reports have described the treatment of chimney-related type 1a endoleak using embolic agents [218]. Indeed, the illustrative observations reported here, coupled with the quantification of surface deviations, may serve to better inform how type 1a endoleaks are treated using such techniques.

Similarly, there have been no *in vitro* studies or clinical reports describing chimney deformation when devices are deployed in an adjacent fashion parallel to a primary endograft. In general, the D-ratios reported here follow trends reported elsewhere [110, 190], namely: self-expandable covered chimney grafts exhibit higher degrees of deformation (i.e. higher D-ratios) compared to their balloon-expandable counterparts. Again, this behaviour is attributed to mechanical differences inherent to these devices. The distinctly unique findings of this study, however, are derived from the observed interactions of the adjacent self-expandable CGs deployed into the brachiocephalic trunk and left common carotid artery, as manifested by their varying lumen deformations (Figure 5.14B). When in contact, chimney grafts appear to support each other, and as such, tend towards a more consistently circular shape. Indeed, this *in vitro* behaviour corroborates the benchtop data presented in Chapter 4 of this thesis: adjacent CGs appear to radially reinforce each other, limiting the degree of chimney compression. Such observations warrant further investigation, as adjacent deployment of CGs in double chimney TEVAR may reduce incidence of device compression thereby improving long-term patency rates.

Limitations. Considering the benchtop nature of the work presented in this Chapter,

results should be viewed within the experimental context described herein and their associated limitations. First, a single, healthy thoracic aortic model was used for simulated double chimney TEVAR. As such, it was not possible to assess the aforementioned gutter behaviour or endograft deformations in a wide range of diseased states/anatomies. To address these concerns, a detailed analysis of model anatomy and behaviour was performed to provide context to a wider patient population. Regarding the experimental setup, it should also be noted that flow rates were not quantified, nor was a truly physiological pressure profile used. These were deemed acceptable omissions given the structural nature of the study, and that only end-diastolic and peak-systolic time points were considered (i.e. intermediate time points during the cardiac cycle neglected).

Secondly, contrast agent was not used during imaging. Inclusion within the experimental protocol may have improved intensities between the lumen, vessel wall, and endograft frames, however initial CT data collection revealed the data to be of sufficient quality. Likewise, the variance in material properties between BE and SE chimney devices may result in differences in attenuated imaging signal, affecting both gutter and D-ratio measurements. Critically, gutter measurements and D-ratios were performed by a single observer. Although repeatability was qualitatively assessed, additional measurements with additional observers would strengthen the data reported.

Finally, only a single primary endograft was considered in this study, limiting observations to the specific device combinations discussed. Similarly, the Ankura device has limited use in European interventional centers. Notably, however, the most recent study describing double chimney TEVAR outcomes employed the Ankura device in 65% of cases [210], demonstrating its adoption in complex endovascular procedures.

5.5 Summary

In this study, two different double chimney TEVAR configurations have been evaluated in a fully characterised *in vitro* thoracic aortic model. The dynamic behaviour of the resulting gutters and endograft deformations have been assessed, revealing compelling differences between balloon-expandable and self-expandable chimney graft types. Notably, this is the first report to include detailed volumetric reconstructions of ch-TEVAR gutter volumes at critical time points during the cardiac cycle, describe gutter surface

deviation as a metric to characterise dynamic gutter phenomena, as well as describe the phenomenon of decreased chimney stent lumen and gutter deformation when there are multiple chimney grafts adjacent to each other.

5.6 Acknowledgements

The experiments presented in this Chapter were performed within the Interventional Radiology Unit at the John Radcliffe Hospital (Oxford, UK). The clinical expertise and collaboration with Drs. R. Uberoi and M. Hadi enabling this work are greatly acknowledged. Special thanks to JR Radiology staff Helen Nicole, Lesley Brougham, and Kader Benadel for their support. Materials and equipment were generously provided by Elastrat Sàrl (Geneva, Switzerland), United Biologics Inc. (Santa Ana, CA, USA), Medical Implant Testing Lab Inc. (Irvine, CA, USA), Lifetech Scientific Co. Ltd. (Shenzhen, China), and Bentley Innomed GmbH (Hechingen, Germany).

Chapter 6

Simulating Ascending Aorta Endografting in a Dynamic Heart Model

In this Chapter, realistic simulation strategies for evaluating ascending aortic endografting are described. The computational framework presented in Chapter 3 employs traditional analysis methods whereby devices and procedures are simulated in a quasi-static manner neglecting cardiac biomechanics. Here, a complete finite element representation of an adult male human heart and its surrounding vasculature is detailed. The dynamic response of the heart is governed by realistic electrical, structural, and fluid flow physics via a sequentially coupled electrical-mechanical analysis. Results investigating the use of such a model for evaluating multiple chimney thoracic endovascular aortic repair (ch-TEVAR) configurations are presented and discussed.

6.1 Introduction

A series of *in vitro* studies have recently reported on the various mechanical interactions associated with chimney endografting procedures to identify optimal device and oversizing configurations [105, 106], serving as the de facto guidelines used by the clinical community. Although these works have provided real physical insights into device behaviour during chimney endografting, they are limited in scope due to their experimental nature. Specifically, they do not capture physiological phenomena, such as aortic wall stress response to endograft deployment, nor do they adequately reflect the *in vivo* conditions of the ascending aorta/aortic arch.

Computational simulations offer the ability to investigate these interactions in detail, beyond the level possible with conventional experimental or imaging techniques. Multiple

studies of have been described in the literature presenting numerical analyses of various endovascular procedures, establishing the utility of finite element analysis (FEA) to accurately predict stent-graft behaviour (for example, see [119, 123, 124, 142]). However, FEA has yet to be used for analysing complex procedures such as chimney TEVAR. Moreover, the reported studies do not consider cardiac-induced vascular motion.

As such, the aim of this investigation was to: (1) describe the key mechanical aspects of a dynamic heart model and quantify its ascending aorta/arch behaviour, (2) develop a computational strategy for simulating representative chimney TEVAR procedures using the model, and (3) characterise the influence of both endograft properties and configurations on clinically relevant device-device and device-artery interactions over the entire cardiac cycle. To the best of this author's knowledge, this is the first study to present computational simulations of complex ascending aortic endografting accounting for realistic vascular boundary conditions.

6.2 Materials and Methods

6.2.1 The Living Heart Human Model

This study is based upon the "Living Heart Human Model" (LHHM) cardiac modelling framework, as originally developed by Dassault Systèmes (Providence, RI, USA). Briefly, the LHHM is a dynamic model of a normal, 4-chamber adult male human heart. The response of the LHHM is governed by realistic electrical, structural, and fluid (blood) flow physics via a sequentially coupled electrical-mechanical analysis. Complete details of the framework, including the continuum model of electro-mechanical coupling, the balance equations, and the constitutive equations have been described by Baillargeon and colleagues [219–221]. Here, only the most relevant (mechanical) details, as pertaining to the simulation of complex endografting, are presented for completeness.

Anatomy and finite element representation. The model geometry is based upon computed tomography and magnetic resonance images of a healthy, 21-year old, 50^{th} percentile US male at 70% diastole. Captured within the model are well-defined anatomical structures including: two atria, two ventricles, all four heart valves (tricuspid, pulmonary, mitral, aortic), chordae tendineae, coronary arteries and veins, as well as the

major vessels (superior vena cava, pulmonary arteries, and the ascending aorta/aortic arch). To create a finite element representation of the anatomy, Abaqus/CAE (Dassault Systèmes Simulia Corp., Providence, RI, USA) was used to discretise the model into 449,215 linear tetrahedral elements and 135,162 nodes (resulting in 485,790 degrees of freedom). Incorporated within the LHHM is a thickness-dependent, helically wrapped cardiac muscle fibre arrangement, which is defined via 449,215 local fibre and sheet directions at the centroid of each element. Regarding the aortic anatomy, the lumen diameters of the ascending aorta and brachiocephalic trunk are 29.5 and 13.4mm, respectively, with a wall thickness of 2mm. The complete model is illustrated in Figure 6.1.

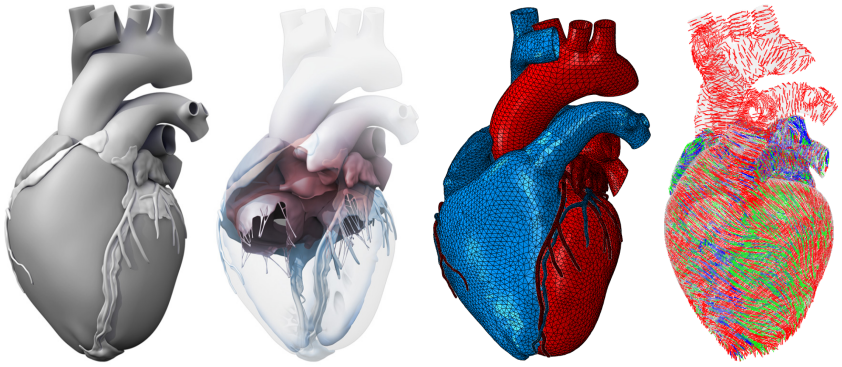


Figure 6.1: The Living Heart Human Model. (Left) Anatomical model created from computed tomography and magnetic resonance images of a healthy adult male. (Middle, left) Geometric model with the two atria, the two ventricles, the four valves, chordae tendineae, coronaries, and the major vessels. (Middle, right) Finite element discretisation with 449,215 linear tetrahedral elements and 135,162 nodes. (Right) Element level fibre orientations interpolated from the geometric reconstruction. Image adapted from [221, 222].

Constitutive modelling. The mechanical behaviour of the LHHM (i.e. the total stress response) is split into passive and active contributions along both the fibre and sheet directions. As such, the total stress developed in the fibre direction, σ_f, is equal to the passive stress, σ_{pf}, plus the active stress, σ_{af}:

$$\sigma_f = \sigma_{pf} + \sigma_{af}. \tag{6.1}$$

Similarly, the total stress in the sheet direction, σ_s, is equal to the passive stress, σ_{ps}, plus a fraction of the active stress in the fibre direction $n_s \cdot \sigma_{af}$:

$$\sigma_s = \sigma_{ps} + n_s \cdot \sigma_{af} \tag{6.2}$$

where n_s is a scalar value less than 1.0 and describes the interaction between adjacent muscle fibres. This factor accounts for cross-fibre stress development which cannot be attributed to fibre dispersion or deformation effects alone [223]. Notably, this contribution affects both the total contractility of the chambers as well as the degree of twist developed in the chamber during the cardiac cycle. This value has been previously tuned such that the contractility of each chamber leads to an appropriate ejection fraction (further details can be found in [221]).

The passive material response of the cardiac tissue is described using an anisotropic hyperelastic formulation based on that originally proposed by Holzapfel and Ogden [224], whose constitutive parameters are outlined in Table 6.1. The deviatoric response is governed by the following strain energy potential:

$$\Psi_{dev} = \frac{a}{2b}\mathrm{e}^{b(I_1-3)} + \sum_{i=f,s}\frac{a_i}{2b_i}\left\{\mathrm{e}^{b_i(I_{4i}-1)^2}-1\right\} + \frac{a_{fs}}{2b_{fs}}\left\{\mathrm{e}^{b_{fs}\left(I_{8fs}\right)^2}-1\right\}, \tag{6.3}$$

with the volumetric response governed by:

$$\Psi_{vol} = \frac{1}{D}\left(\frac{J^2-1}{2} - \ln(J)\right). \tag{6.4}$$

Table 6.1: Constitutive parameters of the passive cardiac material response.

Parameter	Description
a, b	Governs the isotropic response of the tissue
a_f, b_f	Governs additional stiffness in the fibre direction
a_s, b_s	Governs additional stiffness in the sheet direction
a_{fs}, b_{fs}	Governs coupling stiffness in the fibre and sheet directions
I_1	The first deviatoric strain invariant
I_{4i}	A pseudo-invariant defined as $A_i \cdot C \cdot A_i$
I_{8fs}	A pseudo-invariant defined as $A_f \cdot C \cdot A_s$
C	The Right Cauchy-Green tensor
A_i	Vector in direction i
D	Multiple of Bulk modulus ($K = 2/D$)
J	The third deformation gradient invariant

The active tissue response, which also embeds the proportional behaviour between the strength of the heart's systolic contraction to its diastolic expansion in the LHHM (known as the Frank-Starling effect), is governed by a time-varying elastance model following Walker et al. [225]. In this model, the active stress is defined as:

$$\sigma_{af}(t, E_{ff}) = \frac{T_{max}}{2} \frac{[\mathrm{Ca}]_0^2}{[\mathrm{Ca}]_0^2 + E[\mathrm{Ca}]_{50}^2(E_{ff})} \Big(1 - \cos\Big(\omega(t, E_{ff})\Big)\Big), \tag{6.5}$$

where the length-dependent calcium sensitivity is given by:

$$E[\mathrm{Ca}]_{50}(E_{ff}) = \frac{[\mathrm{Ca}]_{0_{max}}}{\sqrt{\mathrm{e}^{B\left(l(E_{ff}) - l_0\right)} - 1}}, \tag{6.6}$$

and

$$\omega(t, E_{ff}) = \begin{cases} \pi \frac{t}{t_0} & \text{when } 0 \leq t \leq t_0 \\ \pi \frac{t - t_0 + t_r\left(l(E_{ff})\right)}{t_r} & \text{when } t_0 \leq t \leq t_0 + t_r\left(l(E_{ff})\right) \\ 0 & \text{when } t \geq t_0 + t_r\left(l(E_{ff})\right). \end{cases} \tag{6.7}$$

The duration of relaxation, t_r, is a linear function of sarcomere length as given by:

$$t_r(l) = ml + b. \tag{6.8}$$

Finally, sarcomere length is related to fibre strain by the following relation:

$$l(E_{ff}) = l_r\sqrt{2E_{ff} + 1}. \tag{6.9}$$

Essentially, the cardiac tissue's active response is governed by the local sarcomere length, l, and is dependent on the cardiac action potential (i.e. an electrical excitation controlling the effective calcium concentration, $[\mathrm{Ca}]_0$). The time dependence defined by Equation 6.7 leads to a smooth yet steep transition from zero to peak active tension at time t_0, followed by a smooth decline back to zero for the specified relaxation time t_r [221]. This behaviour is illustrated in Figure 6.2. The constitutive parameters of the model are described in Table 6.2.

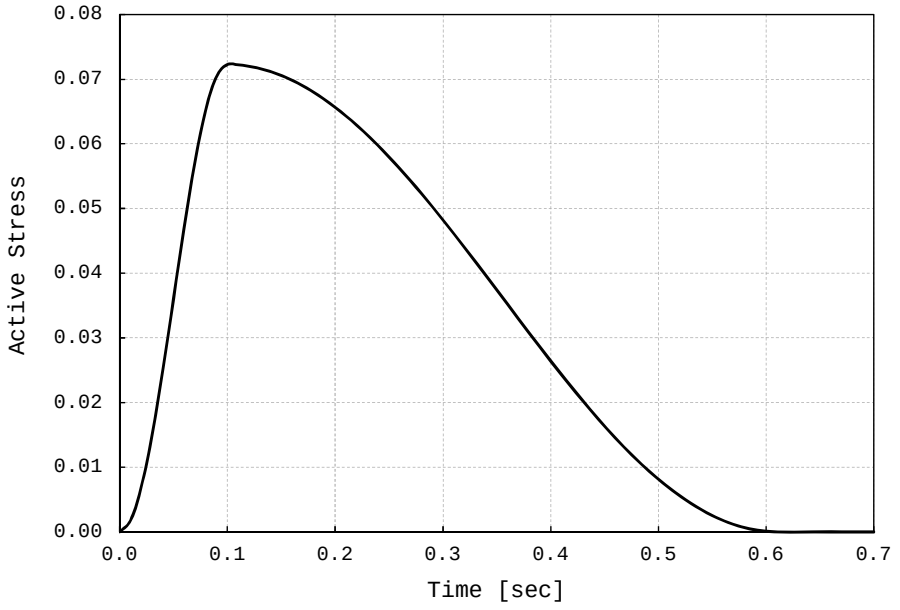


Figure 6.2: Generalized active stress response of cardiac tissue. Shown is the smooth yet steep transition from zero to peak active tension at time t_0 and then a smooth decline back to zero for the specified relaxation time t_r, as described by Sack et al. [221]. Image adapted from [226].

Table 6.2: Constitutive parameters of the active cardiac material response.

Parameter	Description
T_{max}	Constitutive law contractility scaling factor (value directly scales ejection fraction)
$[\mathrm{Ca}]_0$	The intracellular calcium concentration
$[\mathrm{Ca}]_{50}$	The intracellular calcium concentration required to produce 50% of the peak contraction
$[\mathrm{Ca}]_{0_{max}}$	The maximum peak intracellular calcium concentration
$E[\mathrm{Ca}]_{0_{max}}$	Length-dependent calcium sensitivity
B	Governs the shape of the peak isometric tension-sarcomere length relation
l_0	The sarcomere length below which no active force develops
l_r	The initial sacromere length
t_0	Time to reach peak tension
t_r	Duration of relaxation
m, b	Coefficients that govern the shape of the linear relaxation duration and sarcomere length relaxation
E_{ff}	Lagrangian strain tensor component aligned with the local muscle fibre direction

Of note, the major vessels (i.e. superior vena cava, pulmonary arteries, and the ascending aorta/aortic arch) behave passively, and so the material model active stress contribution in these structures is effectively suppressed throughout the cardiac cycle. Regarding the ascending aorta/arch, the anisotropic hyperelastic formulation has been tuned to reflect the material behaviour of ascending aortic tissue. The stress-stretch response of the implemented material model is illustrated in Figure 6.3. For comparative purposes, the behaviour of ascending aortic tissue in the circumferential direction for three different age-group populations as reported by Haskett et al. [163] is also presented.

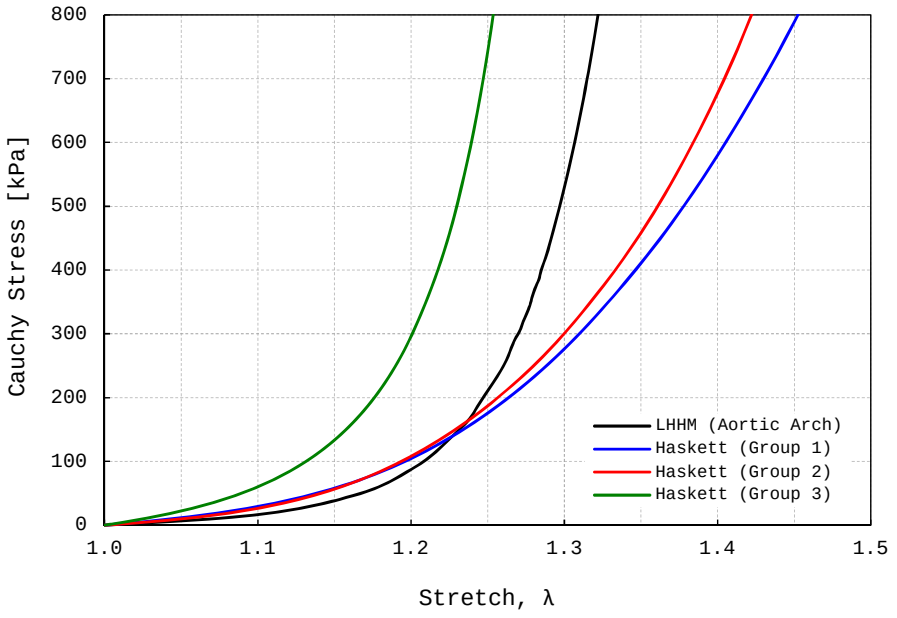


Figure 6.3: Stress-stretch behaviour of ascending thoracic aortic tissue as implemented in the Living Heart Human Model. Also shown is the equivalent circumferential behaviour of three different age-group populations as reported by Haskett et al. [163]. Age groups categorized as 0-30, 31-60, and 61+ y/o, respectively.

Boundary and initial conditions. Prior to initiating the mechanical analysis (i.e. simulating the cardiac/vascular deformations of the heart and major vessels throughout a complete heart beat), an electrical analysis is performed during which the cardiac action potential across the atria and ventricles is computed. This electrical potential serves as an input into the mechanical model, providing the excitation source for the active stress throughout the cardiac cycle as described above. Specific details of the electrical analysis can be found in [227].

As a preliminary step, it is necessary to determine the initial stress state of the structure.

Specifically, the initially discretised geometry is in a stress-free configuration and must be updated to reflect the actual *in vivo* loaded state at which imaging was performed. This procedure involves solving an inverse problem where the corresponding zero-stress state geometry is computed and subsequently pressurised to physiological levels corresponding to 70% diastole, prior to initiating the electrical excitation in the mechanical analysis.

The heart model is constrained in space via Dirichlet boundary conditions at the geometrical cut planes of the major vessels (e.g. at the inflow regions of the superior vena cava, and outflow regions of the pulmonary trunk, supra-aortic branches, and descending aorta). To ensure physiological motion/compliance of the vasculature, these regions are free to move relative to a fixed reference point via a distributing coupling with an appropriately tuned elastic stiffness.

To account for blood flow within the LHHM, a hybrid lumped parameter representation is employed where the compliance and contractility of the atria and ventricles are governed by the mechanical model using surface-based fluid cavities and fluid exchange definitions. Using this approach, a natural coupling between the structural deformation and the fluid pressure is obtained; blood flow is therefore described in terms of temporally varying blood pressure within each of the four chambers. Of note, the major vessels are excluded from the lumped parameter model. To impose physiological conditions within the ascending aorta/arch, the LHHM is modified via the direct specification of an additional time dependent pressure load within the aortic surface-based fluid cavity. The pressure profile was derived from the corresponding arterial compliance of the lumped parameter model, and is shown in Figure 6.4.

Analysis steps. The complete cardiac cycle is simulated over two computational steps using the Abaqus/Explicit finite element solver. In the first step, the cardiac action potential as computed in the electrical analysis drives the mechanical deformation of the cardiac structures (i.e. atrial/ventricular contraction) and consequently the major vessels. In the second step, the electrical potential of the entire heart is set to the resting potential (i.e. no active stress contribution) and the mechanical deformations follow their corresponding (un)loading paths. The entire cycle occurs over 1s (equivalent to a heart rate of 60bpm), with $t = 0.0s$ corresponding to 70% diastole. Mass scaling was applied such that the stable time increment remained larger than 2.5e−06 throughout the analysis.

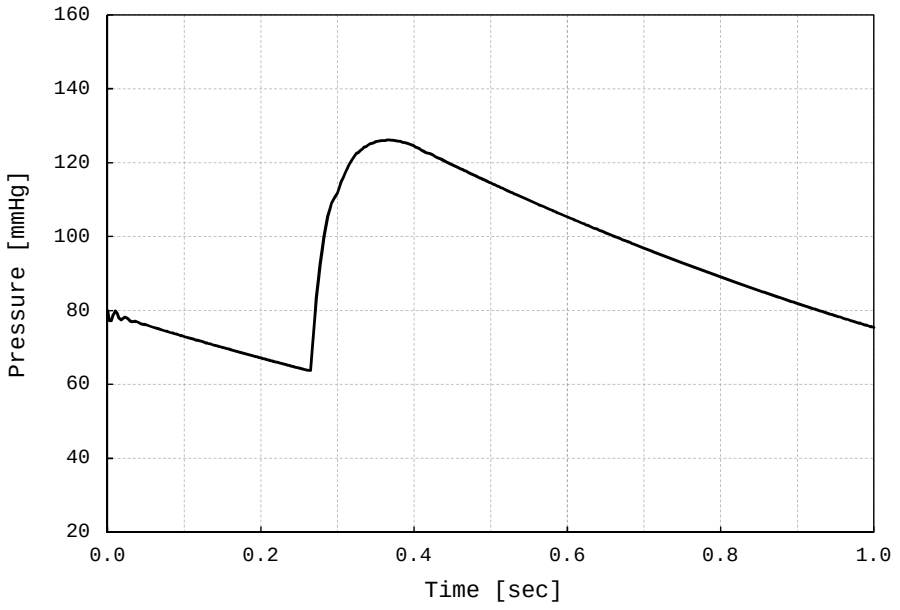


Figure 6.4: Aortic arch pressure in the Living Heart Human Model. The profile is derived from the arterial compliance of the lumped parameter model, and is uniformly applied to the entire surface-based fluid cavity of the aorta.

6.2.2 Chimney TEVAR in the LHHM

Representative single chimney TEVAR procedures were simulated in the Living Heart Human Model following the computational strategies previously described (see Sections 3.2 and 3.3). Specific modelling details are presented below.

Endograft geometries. For simplicity, both main and chimney endografts were considered to be idealised structures (i.e. representing a generic stent design). Using an in-house Python script, stent geometries were defined using a set of parametric equations where design features such as stent length, diameter, and "number of repeating units" were controlled. The main graft (MG) was constructed with a nominal diameter equivalent to 20% oversizing relative to the ascending aorta of the LHHM, and the chimney graft (CG) constructed with a nominal diameter equivalent to 10% oversizing relative to the brachiocephalic trunk. The MG was intentionally sized as to increase the likelihood of (identifiable) gutter formation (i.e. relatively undersized compared to the configurations described in Chapters 4 and 5). The CG was constructed such that its length was greater than the MG, allowing for a more proximally positioned CG edge relative to the MG, reflecting the clinical scenario. Stents were discretised with linear Timoshenko

beam elements (type B31 in Abaqus, a first-order, three-dimensional element). Grafts were considered to be a cylindrical shell modelled with linear triangular elements (type S3R in Abaqus, a 3-node triangular general-purpose element with reduced integration). Geometric and computational features of the stent geometries are presented in Table 6.3.

Table 6.3: Geometric and computational features of main and chimney endografts.

Parameter	Main Graft	Chimney Graft
Stent length	14 mm	16 mm
Stent diameter	36 mm	15 mm
Repeating units	12	7
Wire radius	0.175 mm	0.175 mm
No. elements (B31)	648	378
No. elements (S3R)	8602	4158

For the sake computational efficiency, only a single endograft ring for both the main and chimney grafts was considered in this study. Although such a configuration would not be seen in the clinical scenario, it is in fact the most proximal endograft sections (i.e. those at the landing zone) which dominate surgical outcomes (e.g. gutter formation, chimney graft compression, and endograft infolding). As such, this simplification is wholly appropriate within the analysis context presented here.

Material properties. Two typical stent materials have been investigated in this study. Endografts were considered to be either 316L stainless steel or nitinol. Material behaviour was implemented using a simple and standard linear elastic model (i.e. neglecting plasticity in 316L stainless steel and superelasticity in nitinol). This simplification was deemed appropriate for the sake of computational efficiency when incorporating endografts into the LHHM the first instance. Grafts were considered to be polyethylene terephthalate (PET) whose behaviour was described using an elastic orthotropic plane stress model. Properties of 316L stainless steel and PET are based on those reported in the literature [53], with nitinol properties based upon uniaxial tensile test data described in Section 3.1.1. Material model parameters for the stent and graft components are given in Table 6.4. Of note, the implemented PET model has been appropriately scaled such that the graft behaves in a realistic manner upon deployment and throughout the cardiac cycle.

Table 6.4: Material properties of main and chimney endografts.

Parameter	Value
316L stainless steel	
Young's modulus E	210000 MPa
Poisson's ratio ν	0.3
Nitinol	
Austenite elasticity E_A	56000 MPa
Austenite Poisson's ratio ν	0.33
PET	
Longitudinal elastic modulus E_L	225 MPa
Transverse elastic modulus E_C	1000 MPa
Shear modulus G_{LC}	3.6 MPa
Poisson's ratio ν_{LC}	0.2

Boundary conditions and analysis steps. Stent-graft deployment was simulated using a simplified approach. Prior to analysis initiation, both endografts were positioned in Zone 0 of the LHHM ascending aorta (as per Ishimaru's aortic arch map [202]) based upon the spatial positioning of the loaded anatomy at 70% diastole. Devices were orientated using local coordinate systems, and the CG was arranged in such a manner that it was pre-configured to reside within the ascending aorta without the need for a prescribed deployment procedure. Virtual deployment of the main graft was achieved using a so-called "crimp tool". This tool was modelled with rigid surface elements (type SFM3D4R in Abaqus) and moved in displacement control whereby its effective opening diameter was specified. As such, the main graft was subjected to radial deformation driven by displacement of the crimp tool elements.

The ch-TEVAR deployment procedure was carried out in three phases to: (*i*) crimp, (*ii*) deploy, and subsequently (*iii*) pressurise the inner lumen of both devices. Main graft crimping was performed concurrently with the anatomy pressurisation step. MG deployment and subsequent lumen pressurisation were performed during two newly introduced analysis steps prior to the cardiac cycle. During graft pressurisation, a nominal pressure load was applied to the internal graft lumens as to realistically deform the grafts in their deployed (oversized) states, without imposing erroneous loads onto the aortic wall.

During the crimping, deployment, and graft pressurisation steps, the MG and CG stent

rings were appropriately constrained as to prevent rigid body motion (i.e. a single MG and CG stent node fixed in the local $z-$ and $\theta-$directions). Grafts were effectively attached to their corresponding stent via a tie constraint.

Contact conditions were appropriately handled to allow for stent deployment and were implemented using the general contact algorithm via penalty enforcement as described in Section 3.3.2 (here, the coefficient of friction was specified as $\mu = 0.3$). In the first analysis step, only contact between the crimp tool and MG was activated. In the second step, contact between the crimp tool and MG remained active with interactions between the MG, CG, and aortic arch added to the contact domain, thereby "implanting" the endografts (note that no contact was defined between the crimp tool and ascending aorta). During the pressurisation step, the MG, CG, and aorta interactions were propagated, while the crimp tool excluded from the contact domain. Stent and graft self-contact was also active throughout the entire analysis.

Following device deployment and graft pressurisation, the cardiac cycle of the LHHM as described above was initiated. Throughout the cycle all displacement-type stent boundary conditions were removed. As such, endograft behaviour was solely governed by the device-device interactions and contact with the aortic wall.

6.2.3 Experimental Design

To fully exploit the capabilities of the Living Heart Human Model, and to quantify the influence of both endograft properties and configurations on clinically relevant device-device and device-artery interactions over the cardiac cycle, a parametric study was performed. Four different ch-TEVAR configurations were simulated in the LHHM, varying the endograft stiffness (via the material assignment), as outlined in Table 6.5. All other conditions were held constant across each simulation run.

The resulting FEA data was post-processed and compared between each ch-TEVAR configuration. To assess device-device interactions, the structural deformations of both the main and chimney endografts were qualitatively assessed. To analyse device-artery interactions, both the contact normal forces (i.e. forces imparted onto the aortic wall) and aortic wall stresses were computed and compared. The contact normal forces were quantified as the sum of all vector values for the individual surface pairs included in

Table 6.5: Experimental design for studying ch-TEVAR in the LHHM.

	Main Graft	Chimney Graft
Case 1	Stainless steel	Stainless steel
Case 2	Nitinol	Nitinol
Case 3	Nitinol	Stainless steel
Case 4	Stainless steel	Nitinol

the analysis domain (i.e. the inner aortic wall at Zone 0), and were visualized as the resultant vector in the consolidated data set. The peak aortic wall stress for each ch-TEVAR configuration was also compared against the baseline (unstented) case.

6.3 Results

6.3.1 Mechanical Behaviour of the LHHM

The mechanical response of the unstented LHHM throughout the cardiac cycle is shown in Figure 6.5. The model exhibits a spatio-temporal evolution of mechanical displacements across the heart and major vessels. Maximal cardiac deformations, as quantified using maximum principal logarithmic strains, occur as a result of atrial and ventricular contraction at approximately $t = 0.4s$.

The ascending aorta/arch exhibits a realistic behaviour throughout the heart beat. The prevailing motion can be described as an anterior-caudal displacement (i.e. a forward-downward motion), whose maximum magnitude corresponds with the aforementioned atrial/ventricular contraction. A computed 3D displacement field of the aortic anatomy (see Figure 6.5, middle panel) reveals a maximal anterior-caudal motion of approximately 7.8mm in the most proximal region of the ascending aorta with respect to the initial position (i.e. at 70% diastole). Moving distally into the aortic arch/descending aorta, the motion diminished. For clarity, an overlay of the ascending aorta/arch anatomy throughout the cardiac cycle with respect to its initial position is also provided (see Figure 6.5, bottom panel).

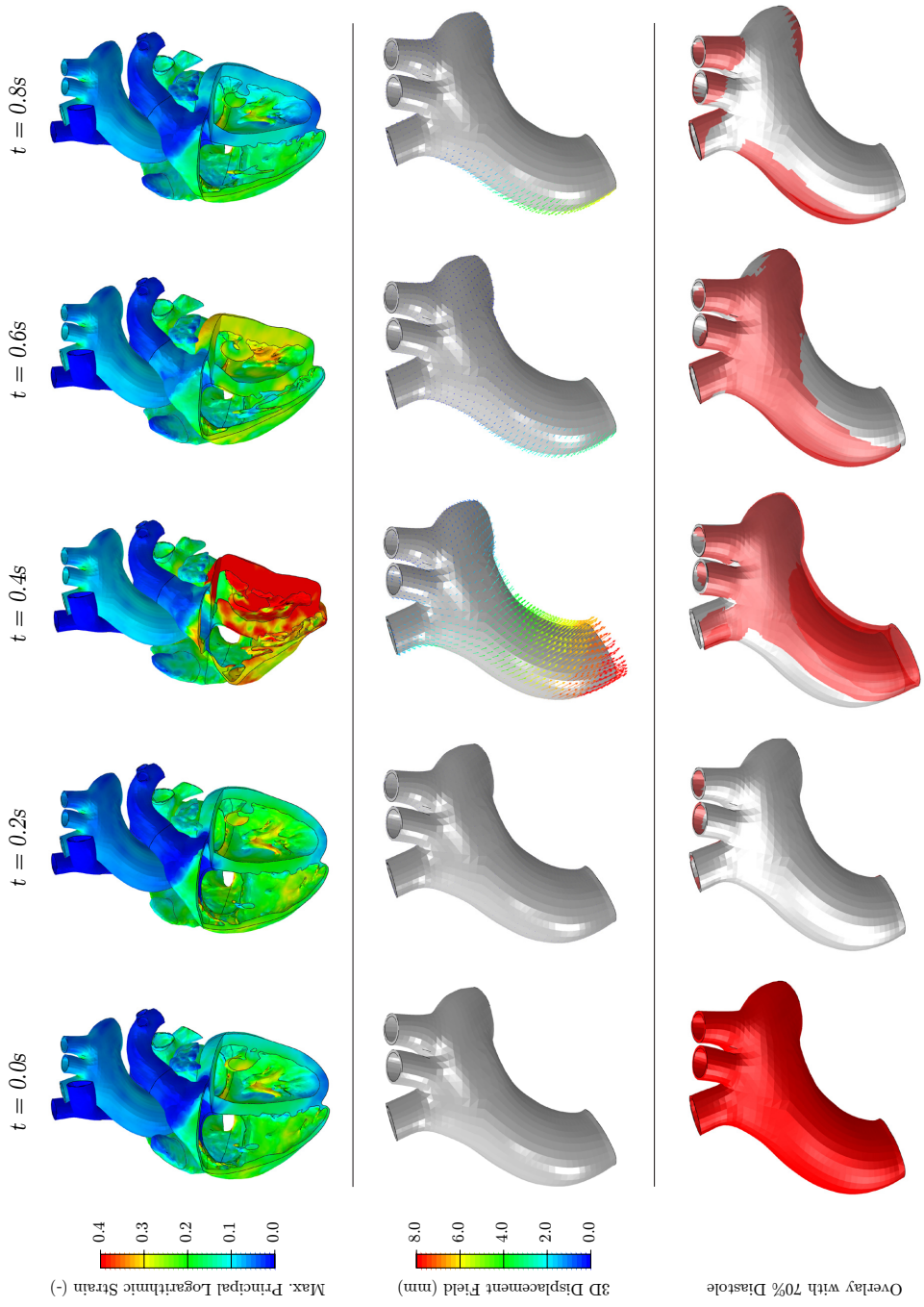


Figure 6.5: Mechanical response of the unstented Living Heart Human Model. (Top panel) Entire model with cut section depicting atrial and ventricular contraction/relaxation (valves, chordae tendineae, and coronaries suppressed for clarity). (Middle panel) 3D displacement field of the ascending aorta/arch with respect to $t = 0.0$s. (Bottom panel) Aortic motion overlay with respect to its initial position. *Notes:* initial position is at 70% diastole; the cardiac cycle is 1 second in duration (i.e. an equivalent heart rate of 60bpm).

Pulsatile behaviour of the ascending aorta throughout the cycle was quantified by tracking nodal coordinates on the inner aortic surface. Using these nodal positions, the corresponding lumen diameter was computed. The variation in aortic diameter across the heart beat is shown Figure 6.6. Combining this diametric distention data with the aortic pressure given in Figure 6.4, the LHHM exhibits an aortic compliance of 5.18 (% $mmHg^{-1}$).

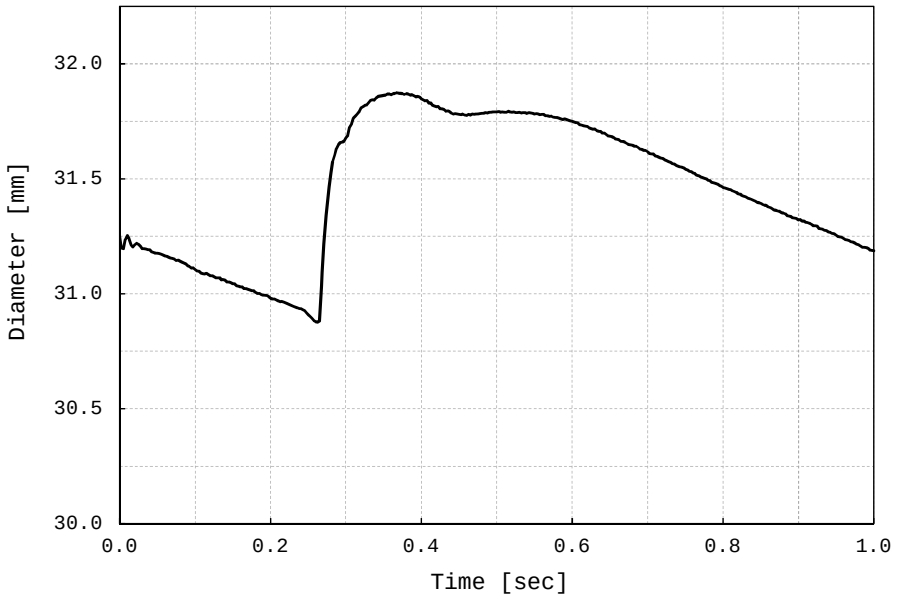


Figure 6.6: Pulsatile behaviour of the LHHM ascending aorta. Vessel lumen diameter reported at Zone 0 as computed from nodal coordinates tracked on the inner aortic surface during the cardiac cycle.

6.3.2 Simulating ch-TEVAR in the LHHM

The resulting single chimney TEVAR configurations, demonstrating the utility of the adopted simulation strategy, are shown in Figure 6.7. One complete cardiac cycle (including the crimp, deployment, and lumen pressurisation steps) took approximately 6hrs and 45mins of walltime on one compute node containing two Intel Xeon Platinum P-8124 processors each containing 18 cores (3.00GHz processor base frequency, Skylake microarchitecture).

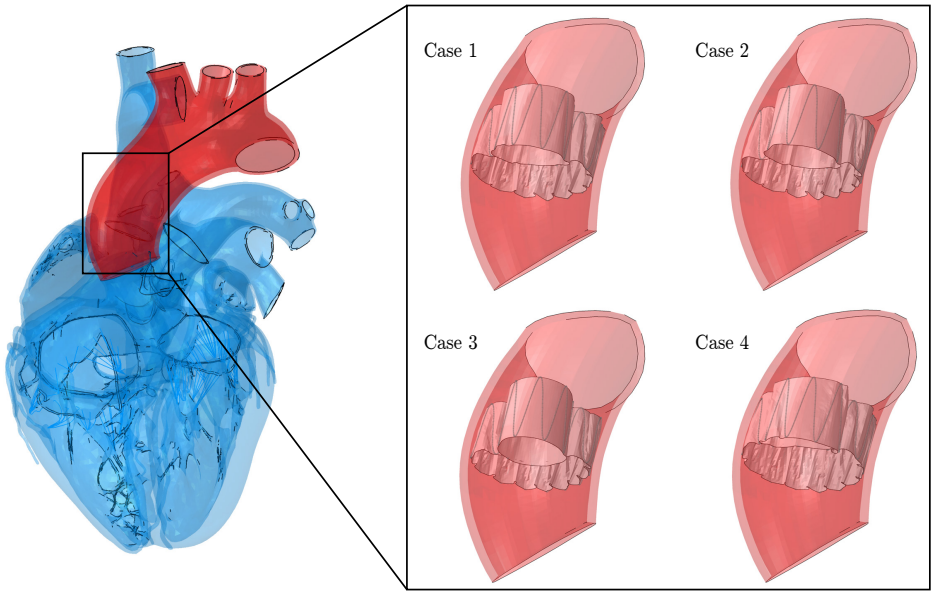


Figure 6.7: Single chimney TEVAR in the Living Heart Human Model. (Left) Translucent view of the LHHM with the ascending aorta/aortic arch highlighted in red. (Right) Resulting single chimney TEVAR deployments of the four endograft configurations considered in the parametric study. Shown is the deformation state for each case at $t = 0.0s$ (i.e. 70% diastole).

All four simulated ch-TEVAR cases exhibited gutters, both chimney and main graft compression, as well as main graft infolding. The mechanical deformations of each case throughout the cardiac cycle are shown in Figure 6.8. Qualitatively, Cases 1 and 2 exhibited relatively similar behaviour, which is attributed to the balanced stiffness of both endografts (i.e. both the MG and CG share the same material properties and a common stent frame design). Case 3 presented with the largest gutter formation and most circular (non-deformed) chimney cross-section. This behaviour is due to the fact that the CG is stiffer than the MG (316L stainless steel vs. nitinol). Conversely, in Case 4, the CG (nitinol) experienced significant lumen compression, and consequently

minimal gutter areas, as the MG (316L stainless steel) presented with a higher stiffness; this radial stiffness mismatch results in significant CG deformation during deployment.

Endograft behaviour in each ch-TEVAR case was observed to be temporally dependent. Thus, the associated gutters, lumen compression, and main graft infolding were found to vary with the cardiac cycle. The most notable deformations were associated with maximal aortic displacement at $t = 0.4s$ (i.e. atrial/ventricular contraction). Case 3 was found to be most affected by aortic motion, whilst Case 4 exhibited the least dependence.

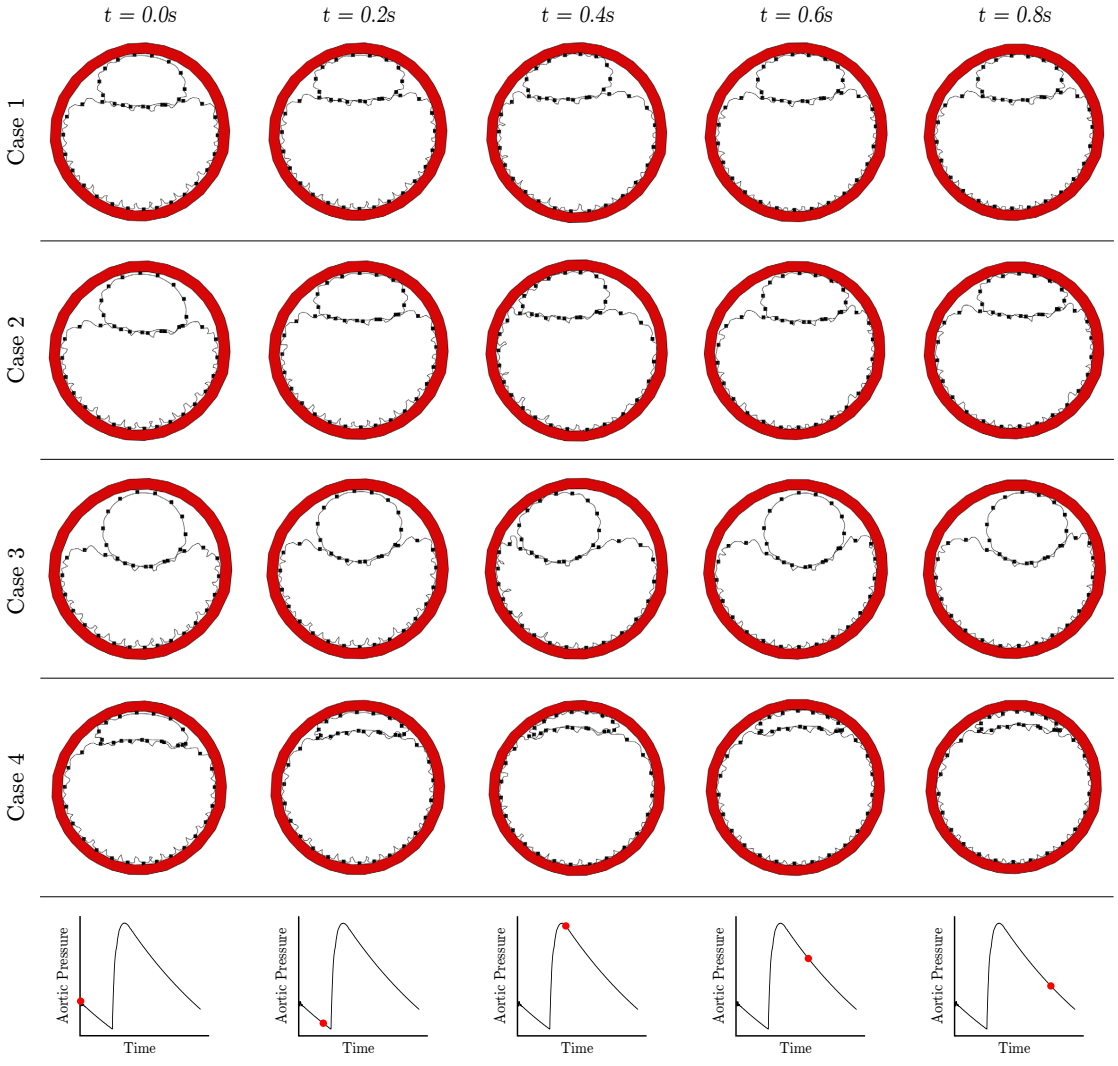


Figure 6.8: Mechanical deformations of endografts during the cardiac cycle. Shown are the aortic cross-sections at the midpoint of the devices for each ch-TEVAR case. The aortic wall is shown in red, with both stent and graft boundaries shown in black. Observable are gutters, chimney graft compression, as well as endograft infolding. For reference, the aortic pressure at each time interval is provided. *Note:* stent profiles depicted as squares due to visualization outputs from Abaqus; actual profiles are circular.

The device-artery interactions, as quantified using contact normal forces, are shown in Figure 6.9. For clarity, the displayed vectors have been normalized by the maximum computed contact normal force across all cases and time points. The range of peak contact normal forces during the cardiac cycle are reported in Table 6.6.

Table 6.6: Range of peak contact normal force on the aortic wall.

	Peak Contact Normal Force (N)	
	Minimum	Maximum
Case 1	0.20	0.24
Case 2	0.06	0.09
Case 3	0.07	0.11
Case 4	0.19	0.23

Similar to the observed device-device interactions, device-artery interactions were found to be both dependent on ch-TEVAR configuration and the cardiac cycle. Cases 1 and 4 exhibited the highest contact normal forces across the heart beat. On average, these configurations resulted in a 2.7 times increase in contact normal forces imparted onto the aortic wall compared to Cases 2 and 3. Again, this behavior can be attributed to endograft properties; higher contact normal forces were associated with configurations employing stiffer stents.

The magnitude of the contact normal forces remained relatively consistent throughout the cardiac cycle. However, the aortic region in which the maximal contact forces occurred was temporally dependent. In general, maximal contact forces were determined to act on the posterior surface of the aortic wall at the start of the cardiac cycle. The region of maximal contact forces then transitions to the anterior surface due to (peak) aortic motion. It is also observable that the configurations whose CGs experience increased lumen compression, and are therefore more evenly distributed along the aortic circumference, experience reduced contact normal forces in the region of the chimney graft. In other words, those configurations whose CGs tend to retain their circular shape impart greater contact normal forces at the location of CG-artery contact. This behaviour is, for example, seen comparing Cases 1 and 4 at $t = 0.2s$.

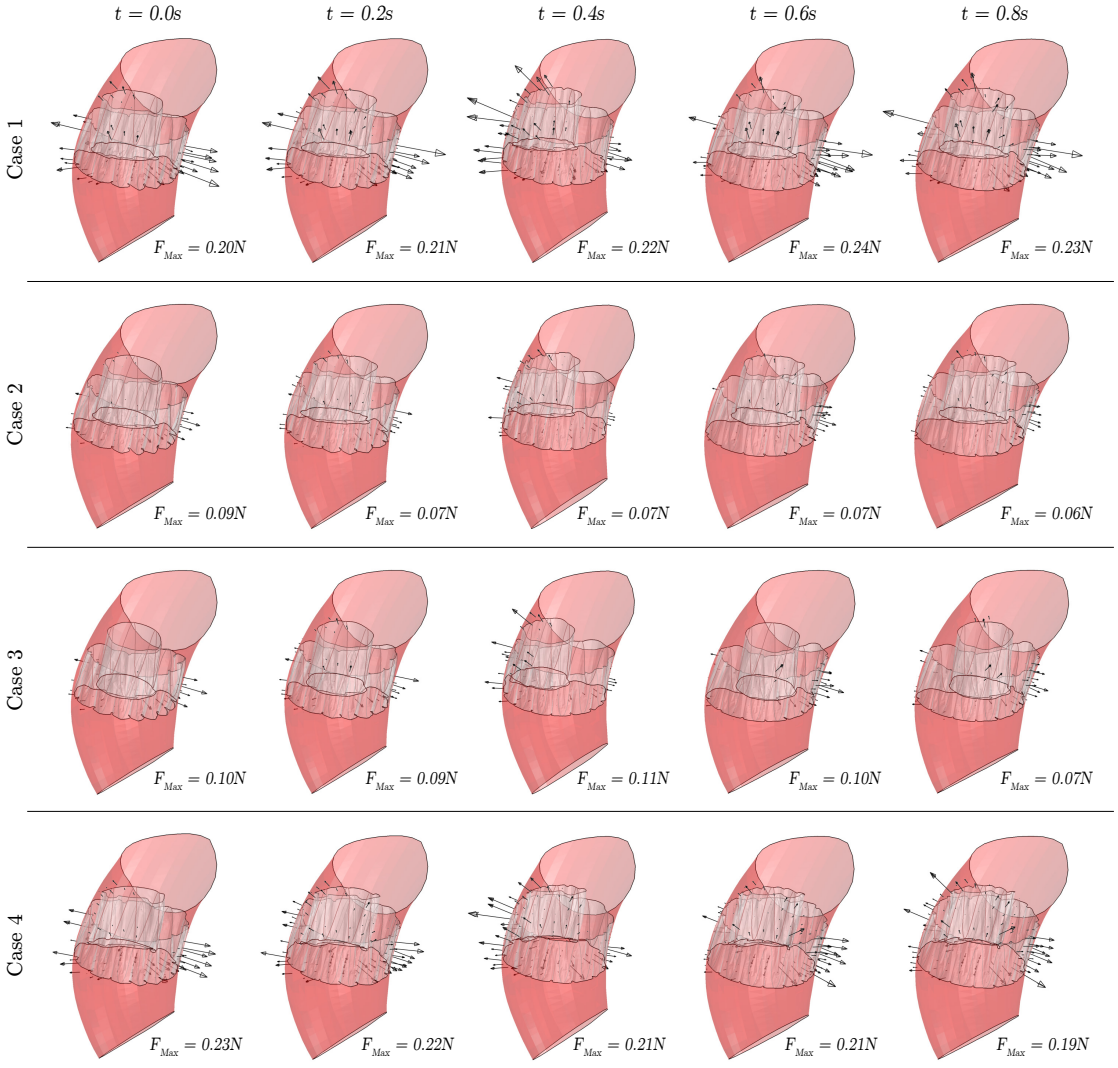


Figure 6.9: Contact normal forces acting on the aortic wall during the cardiac cycle. Shown is the anterior surface view of the ascending aorta for each ch-TEVAR case. Contact normal force vectors are plotted in black with the corresponding peak force reported below each configuration. *Note:* vectors have been normalized by the maximum computed contact normal force across all cases and time points ($F_{Max} = 0.24N$).

Peak maximum principal stresses for each ch-TEVAR case throughout the cardiac cycle are reported in Table 6.7. A representative ch-TEVAR stress distribution contour plot for the ascending aortic inner surface is presented in Figure 6.10 and is compared against the baseline (i.e. unstented) LHHM simulation.

Table 6.7: Peak maximum principal stress (kPa) at the ascending aortic lumen surface.

	Peak Maximum Principal Stress (kPa)				
	$t = 0.0s$	$t = 0.2s$	$t = 0.4s$	$t = 0.6s$	$t = 0.8s$
Baseline	254	215	350	321	276
Case 1	295	266	389	351	323
Case 2	254	217	354	325	281
Case 3	255	218	356	326	281
Case 4	286	252	373	331	295

Aortic wall stresses were found to be temporally dependent in both the baseline and ch-TEVAR cases. In the baseline case, maximum principal stress ranged from 215 - 350 kPa, with the maximum stress associated with both peak aortic displacement and pressure. This predicted stress response is intuitive: at $t = 0.4s$ the ascending aortic segment experiences its maximal longitudinal stretch due to anterior-caudal aortic motion (where the supra-aortic branches are relatively constrained) as well as the (nearly) maximal circumferential stretch due to pulsatile pressure load. It was also observed that the peak wall stress consistently occurred on the anterior aortic surface.

Chimney TEVAR procedures employing stiffer main endografts were found to substantially increase aortic wall stress. Deployment of the endografts considered in Cases 1 and 2 led to increases in maximum stress by 1.24 and 1.17 times over the baseline case, respectively. This maximum increase occurred at $t = 0.2s$ and was primarily attributed to the decreased baseline stress at this interval due to the (minimal) aortic pressure. Matching the behaviour of the unstented case, peak wall stress was associated with maximal aortic displacement and pressure. It was noted, however, that in Case 1 the peak wall stress occurred on the posterior surface of the ascending aorta (see Figure 6.10, right panel). Finally, the ch-TEVAR configurations considered Cases 2 and 3 were not associated with an increase in wall stress, owing to the comparatively compliant behaviour of the main endograft.

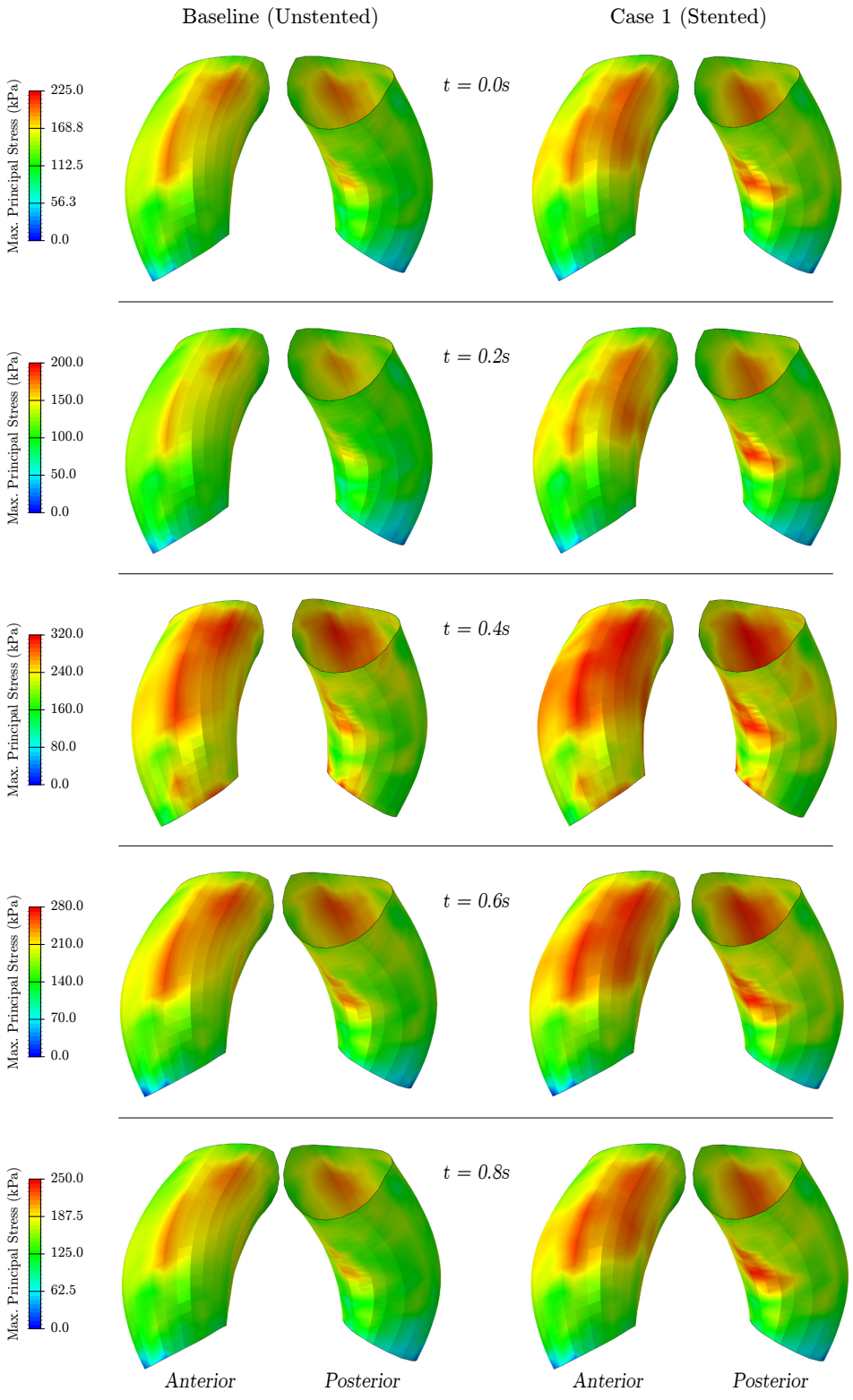


Figure 6.10: Representative case of maximum principal stress distribution and temporal evolution at the inner wall of the ascending aorta during the cardiac cycle. (Left panel) Baseline characterisation of the Living Heart Human Model. (Right panel) Case 1 ch-TEVAR configuration. Shown are both the anterior (*left*) and posterior (*right*) surface views. Scales have been set to enable differentiation at each interval.

6.4 Discussion

The Living Heart Human Model is a robust computational framework capable of simulating complex cardiac mechanics. To date, the LHHM has been used to investigate a wide range of cardiovascular conditions including the treatment of ischemic mitral regurgitation [220], heart failure [221], and calcified aortic valve disease [228]. Given the inclusion of the aortic anatomy within the model, the LHHM provides a platform for analysing challenging endografting procedures such as chimney TEVAR. Thus, to elucidate endograft mechanics throughout the cardiac cycle, this study sought to: (1) characterise the behaviour of the LHHM ascending aorta/arch to establish the suitability of the model, (2) extend the modelling framework to simulate endograft deployment, and (3) use the model to characterise device-device and device-artery interactions of several ch-TEVAR configurations.

Aortic characterisation. The electro-mechanical behaviour of the LHHM has been described in detail by Baillargeon and colleagues [219–221]. Those studies, however, have been dedicated to the cardiac, rather than vascular, characteristics of the model. Extending those works, this study establishes the realism of the ascending aortic/arch behaviour. In the first instance, the stress-stretch response of the aortic material model agrees suitably well with the experimentally reported behaviour of ascending aortic tissue as described by Haskett et al. [163]. Similarly, the implemented pulsatile behaviour of the aortic model described here, as characterised by dynamic compliance, agrees with the generally accepted range used to evaluate stent-graft devices [229]. Regarding LHHM dynamics, the computed 3D displacement field reveals an anterior-caudal motion of the ascending aorta. The determined maximal displacement of 7.8mm is in close agreement with Beller et al. [230] who reported a downward aortic root motion of 8.9mm. Similar boundary conditions have been used in other computational studies of ascending aorta/aortic arch behaviour [231]. Of note, the displacement reported here is not strictly at the aortic root, rather in the region of the sinotubular junction. Finally, the peak ascending aortic wall stress is in the range of values reported elsewhere [232–234]. It is not wholly appropriate to make direct comparisons between the reported stress values and those determined here given the differences in aortic geometries, material models/parameters, and computational techniques employed. To the best of this author's knowledge, this is the first study to couple the time-varying longitudinal and

circumferential deformations of the ascending aorta in an endografting analysis. Given that the aortic behaviour of the LHHM accurately represents physiological conditions, it is appropriate to use the model for studying dynamic stent-graft behaviour in the ascending aorta.

ch-TEVAR in the LHHM. Representative single chimney TEVAR was simulated in the LHHM using a simplified deployment approach similar to the methods described by Auricchio et al. [124] in their study of ascending aortic endografting. For the sake of computational efficiency, the ch-TEVAR configurations analysed here only consider the most proximal segments of the endografts, neglecting phenomena which may occur distally into the aortic arch/descending aorta. Although these modelling assumptions do not strictly reflect the complete *in vivo* scenario, the resulting mechanical interactions realistically capture the behaviour of the endografts at the ascending aortic landing zone (i.e. at the level of the endograft inflow). Indeed, the simulated ch-TEVAR deployments reported here (Figure 6.8) reflect those determined experimentally as presented in Chapter 4 and described elsewhere [105, 106]. Specifically, gutters, endograft compression, as well as endograft infolding could be identified. This comparison with the available *in vitro* results serves as a (crude) validation of the adopted simulation strategy. It should be recognized that a direct validation is not possible; nevertheless, the predicted endograft behaviour in the LHHM generally agrees with mechanical deformations determined experimentally (additional details are discussed in the following section). Furthermore, given that device-related complications are most likely to be associated with device behaviour at the landing zone, limiting the computational analysis to the most proximal endograft segments was deemed to be appropriate.

ch-TEVAR interactions. The parametric analysis included in this study clearly illustrates that device-device and device-artery interactions are dependent on both chTEVAR configuration and the dynamic aortic motions associated with the cardiac cycle. As shown in Figure 6.8, dissimilar MG-CG combinations result in substantially different mechanical deformations, as made evident by inspection of the lumen cross-sections. Notably, when a radially compliant MG is deployed in parallel to a comparatively stiff CG (Case 3), the CG retains its circular profile resulting in large gutter areas. Conversely, when a stiff MG is deployed in parallel to a radially compliant CG, the CG experiences substantial lumen compression leading to a reduction in gutter area. Clinically, this suggests that ch-TEVAR employing MG-CG combinations with balanced radial stiffnesses

may offer a reasonable compromise between CG lumen compression and gutter area. Again, these predicated mechanical interactions are in direct agreement with the experimental determined trends presented in Chapter 4. Elaborating on that experimental work, this numerical analysis also reveals a distinct variation in mechanical interactions throughout the cardiac cycle.

Recently, Nardi and Avrahami [130] presented a computational fluid dynamics study reporting on the hemodynamic outcomes of various treatment approaches for aortic arch aneurysm, including the chimney technique. In that study, the mechanical interactions between both the MG and CG were not considered. As such, the effects of *in vivo* phenomena such as gutter formation and endograft compression on clinically relevant hemodynamic parameters were neglected. Considering the realistic device-device interactions presented here, it intuitively follows that different ch-TEVAR configurations, at different intervals of the cardiac cycle, will influence aortic hemodynamics. Given the trend towards patient-specific treatment planning for endovascular repair [121, 122], this study represents a first step towards capturing the true behaviour of devices during complex ascending aortic endografting, which can serve as more realistic inputs into hemodynamic studies, enhancing clinical decision-making.

To provide a comprehensive mechanical analysis of ch-TEVAR, device-artery interactions and their associated physiological phenomena have also been reported in this study. Following the approach of De Bock et al. [119], the contact normal forces experienced by the ascending aortic wall have been analysed, and the influence of ch-TEVAR on peak aortic wall stress quantified. In a manner similar to the device-device behaviour described above, contact forces and wall stress are both dependent on ch-TEVAR configuration and the cardiac cycle. The results also suggest an association between these two metrics: chimney TEVAR combinations imparting greater forces onto the aortic wall lead to an increase in peak wall stress, which is a physically intuitive response. Notably, this behaviour holds physiological relevance, as forces imparted onto the aortic wall (e.g. through stent-graft deployment and oversizing) can lead to arterial injury [77]. Indeed, the ability to accurately predict such phenomena has the potential to significantly improve both next-generation device design and treatment planning.

Limitations. Considering the computational nature of the work presented in this Chapter, results should be viewed within the numerical context described herein and their

associated simplifications/limitations. First, the LHHM represents a healthy aortic anatomy and behaviour. As such, this study did not consider the influence of aneurysmal aortic geometries nor the properties of diseased tissue. Similarly, the aortic wall thickness and material properties were considered to be uniform across the aorta, and did not account for layer-specific heterogeneity. These were deemed to be acceptable omissions in the first instance given that only the ch-TEVAR landing zone was considered (which requires a suitably healthy aortic segment *in vivo*).

Secondly, the applied aortic arch pressure profile is decoupled from the lumped parameter model for the sake of simplicity. More importantly, the LHHM blood flow analogy only considers structural deformations and fluid pressures; it does not account for true hemodynamic effects such as pressure variations or shear stresses. As such, the mechanical behaviour of the ch-TEVAR configurations analysed here is purely driven by structural interactions, which may differ under the influence of fluid effects. It should also be recognized that mass scaling has been applied uniformly throughout the mechanical analysis. The specified amount of mass scaling substantially improves run-time performance of the model while having a negligible effect on heart mechanics. However, this scaling is also applied to the endografts and may inadvertently influence the accuracy of stent-graft mechanics reported herein (i.e. due to the relatively refined stent mesh compared to the LHHM, the added stent mass may be artificially high).

Finally, incorporating full endograft models and a clinically representative deployment procedure would serve to enhance the modelling approach and allow for analysis of secondary interactions occurring distally in the aortic arch/descending aorta. Likewise, the endografts and associated material models employed here were idealizations, limiting observations to the specific designs and device combinations discussed.

Addressing these limitations represent a significant opportunity to enhance the Living Heart Human Model and further its realism for simulating true endograft procedures to treat complex aortic disease.

6.5 Summary

In this study, a sophisticated finite element representation of the human heart and major vessels has been detailed and its use for simulating chimney TEVAR procedures

described. The aorta incorporated within the model exhibits realistic cardiac biomechanics and thus is a suitable computational tool for analysing device behaviour during ascending aortic endografting. Four idealised ch-TEVAR configurations have been assessed, with clinically relevant device-device and device-artery interactions found to be both device and temporally dependent. Notably, this numerical study is the first of its kind to report on dynamic endograft mechanics throughout the cardiac cycle.

6.6 Acknowledgments

The work presented in this Chapter was performed as part of the Dassault Systèmes Living Heart Project. Technical discussions with Brian Baillargeon, Jiang Yao, Praveen Sridhar, and Clint Davies-Taylor are greatly acknowledged.

Chapter 7

Conclusions and Future Work

This thesis has investigated the structural device-device and device-artery interactions which are inherent to complex endografting procedures. A computational framework has been described and elaborated in which stent-graft mechanics can be quantitatively assessed in a virtual environment. Advanced experimental techniques have been employed to detail the behaviour of stent-graft devices *in vitro*. Using these sophisticated tools, a range of devices and surgical scenarios has been characterised according to clinically relevant performance metrics. Indeed, the results presented here demonstrate that the structure-function relationship of endografts affect their suitability for use in the management of ascending aorta and aortic arch aneurysms.

This concluding Chapter consolidates the main findings and original contributions presented throughout the thesis, which are summarized according to the stated research objectives of this dissertation. Prospective directions for continued work in the field of stent-graft mechanics and the treatment of complex aortic disease are also outlined.

7.1 Conclusions

7.1.1 A Computational Framework for Stent-Graft Modelling

> **Objective 1:** to establish a computational framework employing the finite element method able to predict thoracic aortic stent-graft behaviour.

The phenomenological material models describing nitinol, PET, and arterial tissue, comprising the principal components of the "stent-graft-artery" analysis domain, have been detailed. An experimental study was undertaken to calibrate a dedicated user material subroutine describing nitinol behavior, with the implementation of PET and arterial tissue models derived from data available in the literature. Based on these fundamental material descriptions, three numerical case studies employing the finite element method have been established to examine various aspects of stent-graft performance. Specifically, methodologies to numerically characterise radial outward force, lumen reduction due to bending, and aortic wall stress resulting from stent deployment have been reported for thoracic aortic stent-grafts.

To quantify the influence of design on anticipated stent-graft behaviour, two commercially representative devices were assessed using the computational framework. It was demonstrated that stent design significantly affects behaviour. Devices constructed with superelastic materials and employing a structurally sparse stent frame were predicted to have superior *in vivo* performance compared to their stiffer, compact counterparts. Indeed, it has been shown that a 5 repeating unit nitinol stent-graft design results in lower radial outward forces, minimal lumen reduction, and a lowered aortic wall stress response compared to its 12 repeating unit stainless steel counterpart.

The computational framework was expanded to establish the suitability of numerical techniques for evaluating chimney thoracic endovascular aortic repair (ch-TEVAR). It was demonstrated that computational tools can effectively be used to quantify clinically relevant performance metrics such as so-called gutter formation, endograft compression, and main graft infolding in the first instance. Again, it was shown that differing device designs used during ch-TEVAR are predicted to have different clinical outcomes.

7.1.2 Radial Loading of Parallel Endografts

> **Objective 2:** to characterise the loading response of thoracic stent-grafts alone and in combination with chimney stents. In the case of parallel configurations, to quantify mechanical deformations in terms of clinically relevant metrics.

The mechanical behaviour of four commercially available endografts when subjected to uniform radial load was characterised using established experimental techniques. The results presented here clearly illustrate significantly different radial load profiles between various endografts commonly used in clinical practice. Given the range of devices and techniques available to surgeons, such differences may have clinical implications. Based on the findings reported here, radial loads exerted onto an aortic wall can vary up to threefold depending on the stent-graft selected. These general observations corroborate the numerical predictions in this thesis and serve to validate the previously established computational tools.

The experimental techniques were extended to evaluate the loading response and mechanical deformations of endografts in various chimney TEVAR configurations. For the first time, coupled radial load and deformation behaviour of parallel endografts has been reported. This study reveals an increase in chronic outward force during ch-TEVAR, and therefore increased radial loads exerted onto the aortic wall over what is to considered to be the recommended range. Marked differences in mechanical deformations between chimney TEVAR configurations were observed, primarily in the form of gutter formation. It was found that balloon-expandable ch-TEVAR results in larger gutter areas compared to self-expandable configurations, with this behaviour attributed to the difference in radial stiffness between chimney graft types.

Significantly, it has been described for the first time here that use of balloon-expandable chimney grafts may lead to increased radial force localizations onto the adjacent aortic segment *in vivo*, as they tend to retain their circular shape when deployed in parallel configurations. Such behaviour is not anticipated with self-expandable chimney grafts, as these devices are prone to deformation and therefore more uniformly conform to the aortic wall.

7.1.3 *In Vitro* Evaluation of ch-TEVAR

> **Objective 3:** to evaluate thoracic aortic chimney endografting in an *in vitro* model accounting for cardiac biomechanics.

Representative double chimney TEVAR procedures have been performed in a physiological thoracic aortic model with retrospective electrocardiography-gated computed tomography used to evaluate endograft behaviour. The resulting device interactions were characterised according to gutter volume and endograft deformation. For the considered conditions, it was found that ch-TEVAR employing balloon-expandable covered chimney stents results in three times the total gutter volume in comparison to its self-expandable counterpart. Gutter volumes were observed to vary dynamically between the end-diastolic and peak-systolic phases of the cardiac cycle, with the most substantial change associated with the balloon-expandable chimney configuration. The findings reported here support the recommendation that electrocardiography-gated computed tomography, or similar, should be used during follow-up of patients treated with chimney grafts to better identify device related complications.

Chimney graft deformations were dependent on device type, with self-expandable devices exhibiting up to twice the degree of deformation as balloon-expandable devices. A distinctly unique finding of this study was observed in the interactions of adjacent self-expandable chimney grafts, as manifested by their varying lumen deformations: when in contact, self-expandable chimneys appear to support each other, and as such, tend towards a more consistently circular shape. Such an observation warrants further investigation, as adjacent deployment of chimney grafts in double chimney TEVAR may improve long-term patency rates and reduce incidence of device compression and subsequent chimney graft occlusion.

Finally, this is the first report to include detailed volumetric reconstructions of ch-TEVAR gutter volumes at critical time points during the cardiac cycle, and furthermore, to describe gutter surface deviation as a metric to characterise dynamic gutter phenomena.

7.1.4 Realistic Simulation of Ascending Aortic Endografting

> **Objective 4:** to describe advanced numerical simulations, elaborating on the methods developed in Objective 1 and the behaviour characterised in Objectives 2 and 3, to assess aspects of complex endografting in a dynamic FEA model.

Employing the Living Heart Human Model cardiac modelling platform, the device-device and device-artery interactions of single chimney TEVAR configurations have been quantified. The ascending aortic behaviour of the model has been implemented such that it exhibits cardiac-induced vascular biomechanics, including realistic material behaviour, pulsatility, and motion, as compared to experimental results reported elsewhere. Notably, this is the first study to couple the time-varying longitudinal and circumferential deformations of the ascending aorta in an endografting analysis. As the mechanical behaviour of the aortic model accurately represents physiological conditions, it was used to quantify the dynamic interactions of four ch-TEVAR configurations, significantly extending the capabilities of the initially described computational framework.

Again, it was observed that both device-device and device-artery interactions are dependent on ch-TEVAR configuration, and hence, stent-graft design. Configurations employing devices with matched stiffnesses tended toward balanced deformations. Conversely, those with devices exhibiting a radial stiffness mismatch lead to either excessive gutter formation or significant chimney graft compression. It was also found that both device-device and device-artery interactions are temporally dependent. Peak contact force vectors and aortic wall stresses varied with the cardiac cycle, and were associated with the maximal anterior-caudal displacement of the ascending aorta.

7.2 Future Work

7.2.1 Enhancing the Computational Framework

The numerical analysis presented here is, to a degree, limited by the modelling simplifications and idealizations applied. To extend the computational framework, incorporating the true geometry and material behaviour of devices used in clinical practice, as well as implementing a clinically representative deployment strategy, would enhance the realism

of the simulation techniques. Furthermore, the inclusion of patient-specific aneurysmal anatomies and diseased aortic tissue properties would add the level of sophistication required to make patient-specific prediction of complex endovascular procedures possible. Combining these enhancements into an automated and efficient workflow would enable the use of computational models to support clinical decision-making in the field of chimney TEVAR.

7.2.2 Hemodynamics and Fluid-Structure Interactions

The focus of this research has been solely placed on the mechanical interactions of stent-graft devices. As such, their influence on aortic blood flow has not been considered. Broadening the analysis domain to couple both the mechanical and hemodynamic aspects of complex ascending aortic endografting via fluid-structure interaction techniques would elaborate the clinical significance of this work. Indeed, endovascular devices specifically tailored for chimney type procedures do not exist. Combining the structural behaviour described here with hemodynamic analyses is the logical next step to determine the ideal endograft configuration for complex endografting and to propose optimised chimney-specific device designs.

7.2.3 Validation with Clinical Data

The findings presented in this thesis are based upon *in vitro* experiments and *in silico* analyses. To fully translate this work to the *in vivo* scenario, corroboration with clinically observed phenomena is required. Given the current clinical trend towards stent-graft deployment in the ascending aorta/aortic arch and the adoption of the chimney technique, there is a growing body of clinical data which illuminates the behaviour of stent-grafts when deployed in parallel configurations. Performing a comprehensive validation of the findings here against the available clinical data represents a significant research opportunity to further elucidate the effect of device design and chimney configuration on long-term treatment outcomes.

Appendix A

Mesh Convergence

To ensure the accuracy of FEA results reported in Chapter 3, a mesh convergence study was conducted by means of a representative stent crimping simulation. Briefly, a Cook Zenith TX2 stent ring segment was radially compressed via a cylindrical rigid surface following the methods described in Section 3.2.1 (here, the 316L stainless steel material properties were assumed to be elastic). The maximum von Mises stress was computed and evaluated for a series of identical stent segments each with an increasingly refined FE mesh. Results show that the maximum von Mises stress converges at approximately $2.8{\times}10^3$ MPa, as illustrated in Figure A.1. As such, a mesh discretisation of 2172 elements per stent ring segment, with six elements across the geometry thickness, was chosen as an appropriate compromise between computational accuracy and cost (run time). Additional details regarding stent modelling best practices can be found in [235].

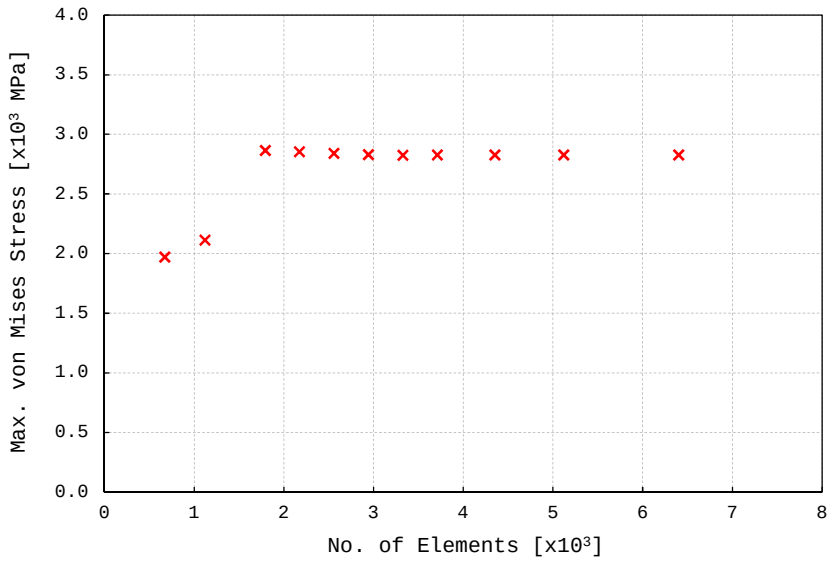


Figure A.1: Stent mesh convergence study. Maximum von Mises stress in a Cook Zenith TX2 stent ring segment subjected to radial crimping at increasing levels of mesh refinement.

Similarly, a convergence study was conducted to determine an appropriate level of mesh refinement for the arterial models reported herein. Following the methods outlined in Section 3.1.3, a representative ascending thoracic aortic arterial segment was subjected to an inflation pressure equivalent to 160mmHg (i.e. systolic blood pressure). The maximum von Mises stress in the arterial wall was computed and evaluated for a series of identical arterial segments each with an increasingly refined FE mesh. Results show that the maximum von Mises stress converges at approximately 1.9×10^{-1} MPa, as seen in Figure A.2. As such, a uniformly structured mesh discretisation with four elements across the geometry thickness (20640 elements for the arterial segment considered here) was chosen as an appropriate compromise between computational accuracy and cost.

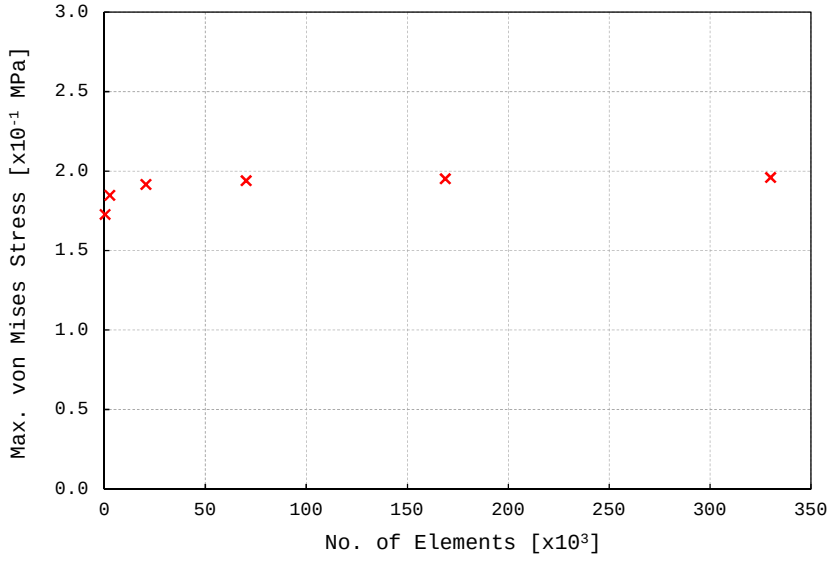


Figure A.2: Artery mesh convergence study. Maximum von Mises stress in an ascending thoracic aortic arterial segment subjected to inflation at increasing levels of mesh refinement.

References

[1] Alwan A et al. *Global status report on noncommunicable diseases 2010*. World Health Organization, 2011.

[2] Ritchie H and Roser M. Causes of Death (Online). `https://ourworldindata.org/causes-of-death`, 2018. Accessed: 05.06.2018.

[3] Holzapfel GA, Gasser TC, and Ogden RW. A new constitutive framework for arterial wall mechanics and a comparative study of material models. *Journal of Elasticity*, 61(1-3):1–48, 2000.

[4] Gasser TC, Ogden RW, and Holzapfel GA. Hyperelastic modelling of arterial layers with distributed collagen fibre orientations. *Journal of the Royal Society Interface*, 3(6):15–35, 2006.

[5] Kleinstreuer C, Li Z, and Farber M. Fluid-structure interaction analyses of stented abdominal aortic aneurysms. *Annual Review of Biomedical Engineering*, 9:169–204, 2007.

[6] Johnston KW, Rutherford RB, Tilson MD, et al. Suggested standards for reporting on arterial aneurysms. *Journal of Vascular Surgery*, 13(3):452–458, 1991.

[7] Elefteriades J, Olin J, Halperin J, and Ziganshin B. Diseases of the aorta. In *Hurst's The Heart*, pages 2157–2194. McGraw-Hill Education, 14th edition, 2017.

[8] Aneurysm Treatment (Online). `https://uvahealth.com/services/aneurysm-treatment`, Accessed: 09.08.2014.

[9] Katzen BT, Dake MD, MacLean AA, and Wang DS. Endovascular repair of abdominal and thoracic aortic aneurysms. *Circulation*, 112(11):1663–1675, 2005.

[10] Schlatmann TJ and Becker AE. Histologic changes in the normal aging aorta: Implications for dissecting aortic aneurysm. *American Journal of Cardiology*, 39 (1):13–20, 1977.

[11] Ziganshin BA and Elefteriades JA. Mechanisms of disease and natural history. In *Endovascular Aortic Repair – Current Techniques with Fenestrated, Branched and Parallel Stent-Grafts*, pages 19–43. Springer, 2017.

[12] Abraha I, Romagnoli C, Montedori A, and Cirocchi R. Thoracic stent graft versus surgery for thoracic aneurysm. *Cochrane Database of Systematic Reviews*, 6, 2016.

[13] Clouse WD, Hallett JW, Schaff HV, et al. Improved prognosis of thoracic aortic aneurysms: a population-based study. *Journal of the American Medical Association*, 280(22):1926–1929, 1998.

[14] Bickerstaff LK, Pairolero PC, Hollier LH, et al. Thoracic aortic aneurysms: a population-based study. *Surgery*, 92(6):1103–1108, 1982.

[15] Johansson G, Markstrm U, and Swedenborg J. Ruptured thoracic aortic aneurysms: a study of incidence and mortality rates. *Journal of Vascular Surgery*, 21(6):985–988, 1995.

[16] Moreno-Cabral CE, Miller DC, Mitchell RS, et al. Degenerateive and atherosclerotic aneurysms of the thoracic aorta - determinants of early and late stage surgical outcome. *Journal of Thoracic and Cardiovascular Surgery*, 88(6):1020–1032, 1984.

[17] Debakey ME, McCollum CH, and Graham JM. Surgical treatment of aneurysms of the descening thoracic aorta: Long term results in 500 patients. *Journal of Cardiovascular Surgery*, 19(6):571–576, 1978.

[18] Hilgenberg AD, Rainer WG, and Sadler TR. Aneurysm of the descending thoracic aorta: replacement with the use of a shunt or bypass. *Journal of Thoracic and Cardiovascular Surgery*, 81(6):818–824, 1981.

[19] Coady MA, Ikonomidis JS, Cheung AT, et al. Surgical management of descending thoracic aortic disease: Open and endovascular approaches – A scientific statement from the American Heart Association. *Circulation*, 121(25):2780–2804, 2010.

[20] Thurnher SA and Grabenwoger M. Endovascular treatment of thoracic aortic aneurysms: A review. *European Radiology*, 12(6):1370–1387, 2002.

[21] Buth J and Harris P. Endovascular treatment of aortic aneurysms. In *Rutherford: Vascular Surgery*, chapter 101. Elsevier/Saunders, 6th edition, 2005.

[22] Riambau V, Böckler D, Brunkwall J, et al. Management of descending thoracic aorta diseases: Clinical practice guidelines of the European Society for Vascular Surgery (ESVS). *European Journal of Vascular and Endovascular Surgery*, 53(1): 4–52, 2017.

[23] Swan H, Maaske C, Johnson M, and Grover R. Arterial Homografts: II. Resection of thoracic aortic aneurysm using a stored human arterial transplant. *AMA Archives of Surgery*, 61(4):732–737, 1950.

[24] Lam CR and Aram HH. Resection of the descending thoracic aorta for aneurysm - a report of the use of a homograft in a case and an experimental study. *Annals of Surgery*, 134(4):743–752, 1951.

[25] DeBakey ME and Cooley DA. Successful resection of aneurysm of thoracic aorta and replacement by graft. *Journal of the American Medical Association*, 152(8): 673–676, 1953.

[26] Coselli JS, de la Cruz K, Preventza O, and LeMaire SA. Descending and thoracoabdominal aortic aneurysms. In *Cardiac Surgery in the Adult*, chapter 49, pages 1075–1099. McGraw-Hill Education, 5th edition, 2018.

[27] Isselbacher EM. Thoracic and abdominal aortic aneurysms. *Circulation*, 111(6): 816–28, 2005.

[28] Svensson LG, Kouchoukos NT, Miller DC, et al. Expert consensus document on the treatment of descending thoracic aortic disease using endovascular stent-grafts. *Annals of Thoracic Surgery*, 85(1):S1–S41, 2008.

[29] Williamson WK, Nicoloff AD, Taylor Jr LM, et al. Functional outcome after open repair of abdominal aortic aneurysm. *Journal of Vascular Surgery*, 33(5):913–920, 2001.

[30] Greenberg RK, Clair D, Srivastava S, et al. Should patients with challenging anatomy be offered endovascular aneurysm repair? *Journal of Vascular Surgery*, 38(5):990–996, 2003.

[31] Parodi JC, Palmaz J, and Barone H. Transfemoral intraluminal graft implantation for abdominal aortic aneurysms. *Annals of Vascular Surgery*, 5(6):491–499, 1991.

[32] Dake MD, Miller DC, Semba CP, et al. Transluminal placement of endovascular stent-grafts for the treatment of descending thoracic aortic aneurysms. *New England Journal of Medicine*, 331(26):1729–1734, 1994.

[33] Cheng D, Martin J, Shennib H, et al. Endovascular aortic repair versus open surgical repair for descending thoracic aortic disease: A systematic review and meta-analysis of comparative studies. *Journal of the American College of Cardiology*, 55(10):986–1001, 2010.

[34] Jonker FH, Trimarchi S, Verhagen HJ, et al. Meta-analysis of open versus endovascular repair for ruptured descending thoracic aortic aneurysm. *Journal of Vascular Surgery*, 51(4):1026–1032, 2010.

[35] Czerny M, Funovics M, Sodeck G, et al. Long-term results of thoracic endovascular aortic repair in atherosclerotic aneurysms involving the descending aorta. *The Journal of Thoracic and Cardiovascular Surgery*, 140(6, Supplement):S179–S184, 2010.

[36] Fattori R, Russo V, Lovato L, Buttazzi K, and Rinaldi G. Endovascular management of thoracic aortic aneurysms. *Cardiovascular and Interventional Radiology*, 34(6):1137–1142, 2011.

[37] Hiraoka A, Chikazawa G, Tamura K, et al. Clinical outcomes of different approaches to aortic arch disease. *Journal of Vascular Surgery*, 61(1):88–95, 2015.

[38] Tsilimparis N, Debus ES, von Kodolitsch Y, et al. Branched versus fenestrated endografts for endovascular repair of aortic arch lesions. *Journal of Vascular Surgery*, 64(3):592–599, 2016.

[39] Anthony Lee W. Status of branched grafts for thoracic aortic arch endovascular repair. *Seminars in Vascular Surgery*, 29(1):84–89, 2016.

[40] Rana MA and Oderich GS. Current device designs to incorporate supra-aortic arch trunks for endovascular repair. In *Endovascular Aortic Repair – Current Techniques with Fenestrated, Branched and Parallel Stent-Grafts*, pages 501–506. Springer, 2017.

[41] Spanos K, Tsilimparis N, Rohlffs F, et al. Total endovascular arch repair is the procedure of the future. *The Journal of Cardiovascular Surgery*, 59(4):559–571, 2018.

[42] Czerny M, Schmidli J, Adler S, et al. Current options and recommendations for the treatment of thoracic aortic pathologies involving the aortic arch: An expert consensus document of the European Association for Cardio-Thoracic Surgery

(EACTS) & the European Society for Vascular Surgery (ESVS). *European Journal of Vascular and Endovascular Surgery*, 57(2):165–198, 2019.

[43] Criado FJ, Barnatan MF, Rizk Y, Clark NS, and Wang CF. Technical strategies to expand stent-graft applicability in the aortic arch and proximal descending thoracic aorta. *Journal of Endovascular Therapy*, 9(Suppl II):II–32–II–38, 2002.

[44] Criado FJ. A percutaneous technique for preservation of arch branch patency during thoracic endovascular aortic repair (TEVAR): Retrograde catheterization and stenting. *Journal of Endovascular Therapy*, 14(1):54–58, 2007.

[45] Criado FJ. Parallel stent graft techniques to facilitate endovascular repair in the aortic arch. In *Endovascular Aortic Repair – Current Techniques with Fenestrated, Branched and Parallel Stent-Grafts*, pages 543–554. Springer, 2017.

[46] Bosiers MJ, Donas KP, Mangialardi N, et al. European multicenter registry for the performance of the chimney/snorkel technique in the treatment of aortic arch pathologic conditions. *The Annals of Thoracic Surgery*, 101(6):2224–2230, 2016.

[47] Lindblad B, Bin Jabr A, Holst J, and Malina M. Chimney grafts in aortic stent grafting: Hazardous or useful technique? Systematic review of current data. *European Journal of Vascular and Endovascular Surgery*, 50(6):722–731, 2015.

[48] Ahmad W, Mylonas S, Majd P, and Brunkwall JS. A current systematic evaluation and meta-analysis of chimney graft technology in aortic arch diseases. *Journal of Vascular Surgery*, 66(5):1602–1610.e2, 2017.

[49] Voskresensky I, Scali ST, Feezor RJ, et al. Outcomes of thoracic endovascular aortic repair using aortic arch chimney stents in high-risk patients. *Journal of Vascular Surgery*, 2017.

[50] Pecoraro F, Lachat M, Cayne NS, et al. Mid-term results of chimney and periscope grafts in supra-aortic branches in high risk patients. *European Journal of Vascular and Endovascular Surgery*, 54(3):295–302, 2017.

[51] Lally C, Kelly D, and Prendergast P. Stents. *Wiley Encyclopedia of Biomedical Engineering*, 2006.

[52] Bolton Medical Relay Stent-Graft (Online). `http://www.boltonmedical.com`, Accessed: 11.08.2014.

[53] Demanget N, Duprey A, Badel P, et al. Finite element analysis of the mechanical performances of 8 marketed aortic stent-grafts. *Journal of Endovascular Therapy*, 20(4):523–535, 2013.

[54] Stoeckel D, Bonsignore C, and Duda S. A survey of stent designs. *Minimally Invasive Therapy & Allied Technologies*, 11(4):137–147, 2002.

[55] Holton A, Walsh E, Anayiotos A, Pohost G, and Venugopalan R. Comparative MRI compatibility of 316L stainless steel alloy and nickel-titanium alloy stents. *Journal of Cardiovascular Magnetic Resonance*, 4(4):423–430, 2002.

[56] Gawenda M and Brunkwall J. Comparison of CE approved TEVAR devices. *Journal of Cardiovascular Surgery*, 51(2):157–68, 2010.

[57] Diagnostic and Interventional Cardiology: TEVAR Stent Grafts Comparison Chart (Online). `https://www.dicardiology.com/compare`, Accessed: 08.02.2018.

[58] Endovascular Today European Device Guide: Thoracic Stent Grafts (Online). `http://evtoday.com/device-guide/europe`, Accessed: 08.02.2018.

[59] Scali ST, Beck AW, Torsello G, et al. Identification of optimal device combinations for the chimney endovascular aneurysm repair technique within the PERICLES registry. *Journal of Vascular Surgery*, 68(1):24–35, 2018.

[60] Donas KP, Usai MV, Taneva GT, et al. Impact of aortic stent-graft oversizing on outcomes of the chimney endovascular technique based on a new analysis of the PERICLES registry. *Vascular*, Article in Press.

[61] Illig KA, Ohki T, Hughes GC, et al. One-year outcomes from the international multicenter study of the Zenith Alpha Thoracic Endovascular Graft for thoracic endovascular repair. *Journal of Vascular Surgery*, 62(6):1485–1494.e2, 2015.

[62] Matsumura JS, Cambria RP, Dake MD, et al. International controlled clinical trial of thoracic endovascular aneurysm repair with the Zenith TX2 Endovascular Graft: 1-year results. *Journal of Vascular Surgery*, 47(2):247–257, 2008.

[63] Fairman RM, Tuchek JM, Lee WA, et al. Pivotal results for the Medtronic Valiant Thoracic Stent Graft System in the VALOR II trial. *Journal of Vascular Surgery*, 56(5):1222–1231.e1, 2012.

[64] Farber MA, Lee WA, Szeto WY, Panneton JM, and Kwolek CJ. Initial and midterm results of the Bolton Relay Thoracic Aortic Endovascular Pivotal Trial. *Journal of Vascular Surgery*, 65(6):1556–1566.e1, 2017.

[65] Zipfel B, Zaefferer P, Riambau V, et al. Worldwide results from the RESTORE II on elective endografting of thoracic aneurysms and dissections. *Journal of Vascular Surgery*, 63(6):1466–1475, 2016.

[66] Makaroun MS, Dillavou ED, Kee ST, et al. Endovascular treatment of thoracic aortic aneurysms: Results of the phase II multicenter trial of the Gore TAG Thoracic Endoprosthesis. *Journal of Vascular Surgery*, 41(1):1–8, 2005.

[67] Desai M, Eaton-Evans J, Hillery C, et al. AAA stent-grafts: Past problems and future prospects. *Annals of Biomedical Engineering*, 38(4):1259–1275, 2010.

[68] Jacobs TS, Won J, Gravereaux EC, et al. Mechanical failure of prosthetic human implants: A 10-year experience with aortic stent graft devices. *Journal of Vascular Surgery*, 37(1):16–26, 2003.

[69] Rudarakanchana N and Jenkins M. Hybrid and total endovascular repair of the aortic arch. *BJS*, 105(4):315–327, 2018.

[70] Roselli EE, Arko Iii FR, and Thompson MM. Results of the Valiant Mona LSA early feasibility study for descending thoracic aneurysms. *Journal of Vascular Surgery*, 62(6):1465–1471.e3, 2015.

[71] Patel HJ, Dake MD, Bavaria JE, et al. Branched endovascular therapy of the distal aortic arch: Preliminary results of the feasibility multicenter trial of the Gore Thoracic Branch Endoprosthesis. *The Annals of thoracic surgery*, 2016.

[72] ASTM International. *ASTM F2477-07 (Reapproved 2013): Standard Test Methods for* in vitro *Pulsatile Durability Testing of Vascular Stents*. West Conshohocken, PA, USA, 2013.

[73] Center for Devices and Radiological Health, Food and Drug Administration. *Guidance for Industry and FDA Staff: Non-Clinical Engineering Tests and Recommended Labeling for Intravascular Stents and Associated Delivery Systems*. Silver Spring, MD, USA, 2010.

[74] International Organization for Standardization. *Cardiovascular implants - Endovascular devices - Part 1: Endovascular prostheses (ISO 25539-1:2017)*. Geneva, Switzerland, 2017.

[75] International Organization for Standardization. *Cardiovascular implants and extracorporeal systems - Vascular prostheses - Tubular vascular grafts and vascular patches (ISO 7198:2016)*. Geneva, Switzerland, 2017.

[76] Kenny S and McDermott E. Simulated testing in medical device design. *Medical Device Technology*, 17(4):22–25, 2006.

[77] Sincos IR, da Silva ES, Belczak SQ, et al. Histologic analysis of stent graft oversizing in the thoracic aorta. *Journal of Vascular Surgery*, 58(6):1644–1651, 2013.

[78] Alberta HB, Secor JL, Smits TC, et al. Comparison of thoracic aortic diameter changes after endograft placement in patients with traumatic and aneurysmal disease. *Journal of Vascular Surgery*, 59(5):1241–1246, 2014.

[79] De Bock S, Iannaccone F, De Beule M, et al. Filling the void: A coalescent numerical and experimental technique to determine aortic stent graft mechanics. *Journal of Biomechanics*, 46(14):2477–82, 2013.

[80] Morris L, Stefanov F, Hynes N, Diethrich EB, and Sultan S. An experimental evaluation of device/arterial wall compliance mismatch for four stent-graft devices and a multi-layer flow modulator device for the treatment of abdominal aortic aneurysms. *European Journal of Vascular and Endovascular Surgery*, 51(1):44–55, 2016.

[81] Canaud L, Cathala P, Joyeux F, et al. Improvement in conformability of the latest generation of thoracic stent grafts. *Journal of Vascular Surgery*, 57(4):1084–1089, 2013.

[82] Canaud L, Alric P, Laurent M, et al. Proximal fixation of thoracic stent-grafts as a function of oversizing and increasing aortic arch angulation in human cadaveric aortas. *Journal of Endovascular Therapy*, 15(3):326–334, 2008.

[83] Demanget N, Latil P, Orgeas L, et al. Severe bending of two aortic stent-grafts: An experimental and numerical mechanical analysis. *Annals of Biomedical Engineering*, 40(12):2674–2686, 2012.

[84] Guan Y, Lin J, Dong ZH, and Wang L. Comparative study of the effect of structural parameters on the flexibility of endovascular stent grafts. *Advances in Materials Science and Engineering*, page 10, 2018.

[85] Pasta S, Scardulla F, Rinaudo A, et al. An in vitro phantom study on the role of the bird-beak configuration in endograft infolding in the aortic arch. *Journal of Endovascular Therapy*, 23(1):172–181, 2016.

[86] Bosman W, van der Steenhoven TJ, Suarez DR, et al. The proximal fixation strength of modern EVAR grafts in a short aneurysm neck. An in vitro study. *European Journal of Vascular and Endovascular Surgery*, 39(2):187–192, 2010.

[87] Melas N, Saratzis A, Saratzis N, et al. Aortic and iliac fixation of seven endografts for abdominal-aortic aneurysm repair in an experimental model using human cadaveric aortas. *European Journal of Vascular and Endovascular Surgery*, 40(4): 429–435, 2010.

[88] Rahmani S, Grewal IS, Nabovati A, et al. Increasing angulation decreases measured aortic stent graft pullout forces. *Journal of Vascular Surgery*, 63(2):493–499, 2016.

[89] Chiang CH, Yeh ML, Chen WL, and Kan CD. Apparatus for comparison of pullout forces for various thoracic stent grafts at varying neck angulations and oversizes. *Annals of Vascular Surgery*, 31:196–204, 2016.

[90] Corbett TJ, Callanan A, O'Donnell MR, and McGloughlin TM. An improved methodology for investigating the parameters influencing migration resistance of abdominal aortic stent-grafts. *Journal of Endovascular Therapy*, 17(1):95–107, 2010.

[91] Corbett TJ, Callanan A, and McGloughlin TM. In vitro measurement of the axial migration force on the proximal end of a bifurcated abdominal aortic aneurysm stent-graft model. *Proceedings of the Institution of Mechanical Engineers Part H-Journal of Engineering in Medicine*, 225(H4):401–409, 2011.

[92] Corbett TJ, Molony DS, Callanan A, and McGloughlin TM. The effect of vessel material properties and pulsatile wall motion on the fixation of a proximal stent of an endovascular graft. *Medical Engineering & Physics*, 33(1):106–111, 2011.

[93] Hinchliffe RJ, Natarajan S, and Hopkinson BR. In vitro analysis of modular aortic stent-graft failure. *Journal of Endovascular Therapy*, 13(1):77–84, 2006.

[94] Cinà DP, Grant G, Peterson M, et al. A study of pullout forces of the components of modular multi-manufacturer hybrid endografts used for aortic aneurysm repair. *European Journal of Vascular and Endovascular Surgery*, 37(6):671–680, 2009.

[95] Grenville J, Tan KT, Tse LW, Rajan DK, and Lindsay TF. Bridging stent-graft pullout force analysis. *Journal of Endovascular Therapy*, 18(2):161–168, 2011.

[96] Zhou SS, How TV, Vallabhaneni SR, et al. Comparison of the fixation strength of standard and fenestrated stent-grafts for endovascular abdominal aortic aneurysm repair. *Journal of Endovascular Therapy*, 14(2):168–175, 2007.

[97] Scurr JR, How TV, McWilliams RG, Lane S, and Gilling-Smith GL. Fenestrated stent-graft repair: which stent should be used to secure target vessel fenestrations? *Journal of Endovascular Therapy*, 15(3):344–348, 2008.

[98] Oshin OA, How TV, Brennan JA, et al. Magnitude of the forces acting on target vessel stents as a result of a mismatch between native aortic anatomy and fenestrated stent-grafts. *Journal of Endovascular Therapy*, 18(4):569–575, 2011.

[99] Scurr JR, McWilliams RG, and How TV. How secure is the anastomosis between the proximal and distal body components of a fenestrated stent-graft? *European Journal of Vascular and Endovascular Surgery*, 44(3):281–286, 2012.

[100] Crawford SA, Itkina M, Doyle MG, et al. Structural implications of fenestrated stent graft misalignment. *The Surgeon*, 16(2):89–93, 2018.

[101] Schurink GW, Aarts NJ, van Baalen JM, Schultze Kool LJ, and van Bockel JH. Stent attachment site-related endoleakage after stent graft treatment: An in vitro study of the effects of graft size, stent type, and atherosclerotic wall changes. *Journal of Vascular Surgery*, 30(4):658–667, 1999.

[102] Leigh L, Rabkin D, Berbaum K, et al. Impact of graft material configuration on stent-graft endoleak in vitro. *Journal of Vascular and Interventional Radiology*, 12(12):1423–1427, 2001.

[103] Albertini JN, Macierewicz JA, Yusuf SW, Wenham PW, and Hopkinson BR. Pathophysiology of proximal perigraft endoleak following endovascular repair of abdominal aortic aneurysms: a study using a flow model. *European Journal of Vascular and Endovascular Surgery*, 22(1):53–56, 2001.

[104] Sulaiman A, Boussel L, Taconnet F, et al. In vitro non-rigid life-size model of aortic arch aneurysm for endovascular prosthesis assessment. *European Journal of Cardio-Thoracic Surgery*, 33(1):53–57, 2008.

[105] Mestres G, Uribe JP, Garca-Madrid C, et al. The best conditions for parallel stenting during EVAR: An in vitro study. *European Journal of Vascular and Endovascular Surgery*, 44(5):468–473, 2012.

[106] Mestres G, Yugueros X, Apodaka A, et al. The best in vitro conditions for two and three parallel stenting during endovascular aneurysm repair. *Journal of Vascular Surgery*, 66(4):1227–1235, 2017.

[107] Niepoth WW, de Bruin JL, Yeung KK, et al. A proof-of-concept in vitro study to determine if endoanchors can reduce gutter size in chimney graft configurations. *Journal of Endovascular Therapy*, 20(4):498–505, 2013.

[108] de Bruin JL, Yeung KK, Niepoth WW, et al. Geometric study of various chimney graft configurations in an in vitro juxtarenal aneurysm model. *Journal of Endovascular Therapy*, 20(2):184–190, 2013.

[109] Boersen JT, Donselaar EJ, Groot Jebbink E, et al. Benchtop quantification of gutter formation and compression of chimney stent grafts in relation to renal flow in chimney endovascular aneurysm repair and endovascular aneurysm sealing configurations. *Journal of Vascular Surgery*, 2016.

[110] Overeem SP, Donselaar EJ, Boersen JT, et al. In vitro quantification of gutter formation and chimney graft compression in chimney evar stent-graft configurations using electrocardiography-gated computed tomography. *Journal of Endovascular Therapy*, 25(3):387–394, 2018.

[111] Mangialardi N, Serrao E, Kasemi H, et al. Chimney technique for aortic arch pathologies: an 11-year single-center experience. *Journal of Endovascular Therapy*, 21(2):312–323, 2014.

[112] Zhang R, Crawford S, Forbes T, Cole JH, and King MW. In vitro fatigue evaluation of chimney endovascular aneurysm repair: A case study. *Journal of Vascular Surgery*, 68(3):e92, 2018.

[113] Bussmann A, Heim F, Delay C, et al. Textile aging characterization on new generations of explanted commercial endoprostheses: A preliminary study. *European Journal of Vascular and Endovascular Surgery*, 54(3):378–386, 2017.

[114] Lin J, Wang L, Guidoin R, et al. Stent fabric fatigue of grafts supported by z-stents versus ringed stents: An in vitro buckling test. *Journal of Biomaterials Applications*, 28(7):965–977, 2014.

[115] Chenesseau B, Heim F, Pidancier C, et al. How compression inside a delivery system can degrade the cover of aortic endografts. *Annals of Vascular Surgery*, 51:150–159, 2018.

[116] Jayet J, Heim F, Coggia M, Chakfe N, and Coscas R. An experimental study of laser in situ fenestration of current aortic endografts. *European Journal of Vascular and Endovascular Surgery*, 56(1):68–77, 2018.

[117] Schlösser FJ, Hogendoorn W, and Muhs BE. Midterm results of thoracic endovascular aortic repair with periscope graft revascularization of the left subclavian artery. *Journal of Endovascular Therapy*, 20(6):735–737, 2013.

[118] Gupta A, Sett S, Varahoor S, and Wolf B. Investigation of interaction between guidewire and native vessel using finite element analysis. In *Proceedings of the 2010 Simulia Customer Conference*, 2010.

[119] De Bock S, Iannaccone F, De Santis G, et al. Virtual evaluation of stent graft deployment: A validated modeling and simulation study. *Journal of the Mechanical Behavior of Biomedical Materials*, 13:129–139, 2012.

[120] Demanget N, Avril S, Badel P, et al. Computational comparison of the bending behavior of aortic stent-grafts. *Journal of the Mechanical Behavior of Biomedical Materials*, 5(1):272–282, 2012.

[121] Perrin D, Badel P, Orgas L, et al. Patient-specific numerical simulation of stent-graft deployment: Validation on three clinical cases. *Journal of Biomechanics*, 48 (10):1868–1875, 2015.

[122] Perrin D, Badel P, Orgeas L, et al. Patient-specific simulation of endovascular repair surgery with tortuous aneurysms requiring flexible stent-grafts. *Journal of the Mechanical Behavior of Biomedical Materials*, 63:86–99, 2016.

[123] Romarowski R, Conti M, Morganti S, et al. Computational simulation of TEVAR in the ascending aorta for optimal endograft selection: A patient-specific case study. *Computers in biology and medicine*, 103:140–147, 2018.

[124] Auricchio F, Conti M, Marconi S, et al. Patient-specific aortic endografting simulation: From diagnosis to prediction. *Computers in Biology and Medicine*, 43(4): 386–394, 2013.

[125] Romarowski R, Faggiano E, Conti M, et al. A novel computational framework to predict patient-specific hemodynamics after TEVAR: Integration of structural and fluid-dynamics analysis by image elaboration. *Computers & Fluids*, In Press.

[126] Vad S, Eskinazi A, Corbett T, McGloughlin T, and Vande Geest JP. Determination of coefficient of friction for self-expanding stent-grafts. *Journal of Biomechanical Engineering – Transactions of the ASME*, 132(12):10, 2010.

[127] Lam S, Fung G, Cheng S, and Chow K. A computational study on the biomechanical factors related to stent-graft models in the thoracic aorta. *Medical & Biological Engineering & Computing*, 46(11):1129–1138, 2008.

[128] Figueroa CA, Taylor CA, Yeh V, Chiou AJ, and Zarins CK. Effect of curvature on displacement forces acting on aortic endografts: A 3-Dimensional computational analysis. *Journal of Endovascular Therapy*, 16(3):284–294, 2009.

[129] Figueroa CA, Taylor CA, Chiou AJ, Yeh V, and Zarins CK. Magnitude and direction of pulsatile displacement forces acting on thoracic aortic endografts. *Journal of Endovascular Therapy*, 16(3):350–358, 2009.

[130] Nardi A and Avrahami I. Approaches for treatment of aortic arch aneurysm, a numerical study. *Journal of Biomechanics*, 50:158–165, 2017.

[131] Chiu T, Tang AY, Cheng SW, and Chow K. Analysis of flow patterns on branched endografts for aortic arch aneurysms. *Informatics in Medicine Unlocked*, 13:62–70, 2018.

[132] van Bakel TM, Arthurs CJ, van Herwaarden JA, et al. A computational analysis of different endograft designs for Zone 0 aortic arch repair. *European Journal of Cardio-Thoracic Surgery*, 2018.

[133] Prasad A, To LK, Gorrepati ML, Zarins CK, and Figueroa CA. Computational analysis of stresses acting on intermodular junctions in thoracic aortic endografts. *Journal of Endovascular Therapy*, 18(4):559–568, 2011.

[134] Li Z and Kleinstreuer C. A comparison between different asymmetric abdominal aortic aneurysm morphologies employing computational fluid-structure interaction analysis. *European Journal of Mechanics - B/Fluids*, 26(5):615–631, 2007.

[135] Li Z and Kleinstreuer C. Blood flow and structure interactions in a stented abdominal aortic aneurysm model. *Medical Engineering & Physics*, 27(5):369–382, 2005.

[136] Li Z and Kleinstreuer C. Analysis of biomechanical factors affecting stent-graft migration in an abdominal aortic aneurysm model. *Journal of Biomechanics*, 39 (12):2264–2273, 2006.

[137] Li Z and Kleinstreuer C. Computational analysis of Type II endoleaks in a stented abdominal aortic aneurysm model. *Journal of Biomechanics*, 39(14):2573–2582, 2006.

[138] Prasad A, Xiao N, Gong XY, Zarins CK, and Figueroa CA. A computational framework for investigating the positional stability of aortic endografts. *Biomechanics and Modeling in Mechanobiology*, 12(5):869–887, 2013.

[139] Pelton AR, Schroeder V, Mitchell MR, et al. Fatigue and durability of nitinol stents. *Journal of the Mechanical Behavior of Biomedical Materials*, 1(2):153–164, 2008.

[140] Robertson SW, Launey M, Shelley O, et al. A statistical approach to understand the role of inclusions on the fatigue resistance of superelastic nitinol wire and tubing. *Journal of the Mechanical Behavior of Biomedical Materials*, 51:119–131, 2015.

[141] Allegretti D, Berti F, Migliavacca F, Pennati G, and Petrini L. Fatigue assessment of nickeltitanium peripheral stents: Comparison of multi-axial fatigue models. *Shape Memory and Superelasticity*, 4(1):186–196, 2018.

[142] Kleinstreuer C, Li Z, Basciano CA, Seelecke S, and Farber MA. Computational mechanics of nitinol stent grafts. *Journal of Biomechanics*, 41(11):2370–2378, 2008.

[143] Pathmanathan P, Gray RA, Romero VJ, and Morrison TM. Applicability analysis of validation evidence for biomedical computational models. *Journal of Verification, Validation and Uncertainty Quantification*, 2(2):021005, 2017.

[144] Duerig TW, Tolomeo DE, and Wholey M. An overview of superelastic stent design. *Minimally Invasive Therapy & Allied Technologies*, 9(3-4):235–246, 2000.

[145] Pelton AR, DiCello J, and Miyazaki S. Optimisation of processing and properties of medical grade Nitinol wire. *Minimally Invasive Therapy & Allied Technologies*, 9(2):107–118, 2000.

[146] Stoeckel D. Nitinol medical devices and implants. *Minimally Invasive Therapy & Allied Technologies*, 9(2):81–88, 2000.

[147] Robertson S, Pelton A, and Ritchie R. Mechanical fatigue and fracture of nitinol. *International Materials Reviews*, 57(1):1–37, 2012.

[148] Maleckis K, Anttila E, Aylward P, et al. Nitinol stents in the femoropopliteal artery: A mechanical perspective on material, design, and performance. *Annals of biomedical engineering*, pages 1–21, 2018.

[149] Bonsignore C. Present and future approaches to lifetime prediction of superelastic nitinol. *Theoretical and Applied Fracture Mechanics*, 92:298–305, 2017.

[150] Azaouzi M, Makradi A, and Belouettar S. Deployment of a self-expanding stent inside an artery: A finite element analysis. *Materials & Design*, 41:410–420, 2012.

[151] Duerig T and Zadno R. An engineer's perspective of pseudoelasticity. In Duerig TW, Melton KN, Stöckel D, and Wayman CM, editors, *Engineering Aspects of Shape Memory Alloys*, pages 369 – 393. Butterworth-Heinemann, 1990.

[152] Dassault Systèmes Simulia Corp. *Abaqus User's Manual*. Providence, RI, USA, 2018.

[153] Auricchio F and Taylor RL. Shape-memory alloys: modelling and numerical simulations of the finite-strain superelastic behavior. *Computer Methods in Applied Mechanics and Engineering*, 143(1-2):175–194, 1997.

[154] Auricchio F, Taylor RL, and Lubliner J. Shape-memory alloys: macromodelling and numerical simulations of the superelastic behavior. *Computer Methods in Applied Mechanics and Engineering*, 146(34):281–312, 1997.

[155] ASTM International. *ASTM F2516-14: Standard Test Method for Tension Testing of Nickel-Titanium Superelastic Materials*. West Conshohocken, PA, USA, 2014.

[156] Pelton AR, Fino-Decker J, Vien L, et al. Rotary-bending fatigue characteristics of medical-grade Nitinol wire. *Journal of the Mechanical Behavior of Biomedical Materials*, 27:19–32, 2013.

[157] Pelton AR. Nitinol fatigue: A review of microstructures and mechanisms. *Journal of Materials Engineering and Performance*, 20(4-5):613–617, 2011.

[158] Bonsignore C. Nitinol Design Concepts. 10.5281/zenodo.583328, May 2017. Accessed: June 2017.

[159] Aycock K. Design of a Generic IVC Filter (Online). github.com, May 2017. Accessed: June 2017.

[160] Lin J, Guidoin R, Du J, et al. An in vitro twist fatigue test of fabric stent-grafts supported by z-stents vs. ringed stents. *Materials*, 9(2):19, 2016.

[161] Demanget N. *Analyse des performances mécaniques des endoprotheses aortiques par simulation numérique: Application au traitement des anévrismes tortueux.* PhD thesis, MINES Saint-Étienne, 2012. In French.

[162] Holzapfel G. *Nonlinear solid mechanics: a continuum approach for engineering.* Wiley, 2000.

[163] Haskett D, Johnson G, Zhou A, Utzinger U, and Vande Geest J. Microstructural and biomechanical alterations of the human aorta as a function of age and location. *Biomechanics and Modeling in Mechanobiology*, 9(6):725–736, 2010.

[164] Raghavan ML, Webster MW, and Vorp DA. Ex vivo biomechanical behavior of abdominal aortic aneurysm: Assessment using a new mathematical model. *Annals of Biomedical Engineering*, 24(5):573–582, 1996.

[165] Holzapfel GA, Sommer G, and Regitnig P. Anisotropic mechanical properties of tissue components in human atherosclerotic plaques. *Transactions of the ASME-K-Journal of Biomechanical Engineering*, 126(5):657–665, 2004.

[166] Azadani AN, Chitsaz S, Matthews PB, et al. Comparison of mechanical properties of human ascending aorta and aortic sinuses. *The Annals of Thoracic Surgery*, 93 (1):87–94, 2012.

[167] Azadani AN, Chitsaz S, Mannion A, et al. Biomechanical properties of human ascending thoracic aortic aneurysms. *The Annals of Thoracic Surgery*, 96(1):50–58, 2013.

[168] Auricchio F, Conti M, Ferrara A, Morganti S, and Reali A. Patient-specific finite element analysis of carotid artery stenting: a focus on vessel modeling. *International Journal for Numerical Methods in Biomedical Engineering*, 29(6):645–664, 2013.

[169] de Beaufort HWL, Nauta FJH, Conti M, et al. Extensibility and distensibility of the thoracic aorta in patients with aneurysm. *European Journal of Vascular and Endovascular Surgery*, 53(2):199–205, 2017.

[170] Hall GJ and Kasper EP. Comparison of element technologies for modeling stent expansion. *Journal of Biomechanical Engineering-Transactions of the Asme*, 128 (5):751–756, 2006.

[171] Criado FJ and Duson S. Parallel grafts in perspective: definitions and a new classification. *Vascular Disease Management*, 10(1):16–19, 2013.

[172] Lachat M. *Multiple chimneys: Techniques, results and limitations.* Presented at the 33rd CX Symposium. London, UK, 2011.

[173] Chou HW, Chan CY, Wang SS, and Wu IH. How to size the main aortic endograft in a chimney procedure. *The Journal of Thoracic and Cardiovascular Surgery*, 147 (3):1099–1101, 2014.

[174] Kölbel T, Carpenter SW, Taraz A, et al. How to calculate the main aortic graft-diameter for a chimney-graft. *The Journal of Cardiovascular Surgery*, 57(1):66–71, 2016.

[175] Fazzini S, Ronchey S, Orrico M, et al. Over-SIRIX: A new method for sizing aortic endografts in combination with the chimney grafts – early experience with aortic arch disease. *Annals of Vascular Surgery*, 46(Supplement C):285–298, 2018.

[176] ASTM International. *ASTM F3067-14: Guide for Radial Loading of Balloon Expandable and Self Expanding Vascular Stents.* West Conshohocken, PA, USA, 2014.

[177] Cabrera MS, Oomens CWJ, and Baaijens FPT. Understanding the requirements of self-expandable stents for heart valve replacement: Radial force, hoop force and equilibrium. *Journal of the Mechanical Behavior of Biomedical Materials*, 68: 252–264, 2017.

[178] Egron S, Fujita B, Gullón L, et al. Radial force: An underestimated parameter in oversizing transcatheter aortic valve replacement prostheses: In vitro analysis with five commercialized valves. *ASAIO Journal*, 64(4):536–543, 2018.

[179] Dabir D, Feisst A, Thomas D, et al. Physical properties of venous stents: An experimental comparison. *CardioVascular and Interventional Radiology*, 41(6): 942–950, 2018.

[180] Schindelin J, Arganda-Carreras I, Frise E, et al. Fiji: an open-source platform for biological-image analysis. *Nature Methods*, 9(7):676–682, 2012.

[181] Rueden CT, Schindelin J, Hiner MC, et al. ImageJ2: ImageJ for the next generation of scientific image data. *BMC Bioinformatics*, 18(1):529, 2017.

[182] Wang L, Huang Y, Guo D, et al. Application of triple-chimney technique using C-TAG and Viabahn or Excluder iliac extension in TEVAR treatment of aortic arch dilation diseases. *Journal of Thoracic Disease*, 10(6):3783–3790, 2018.

[183] Matsumoto T, Matsubara Y, Aoyagi Y, et al. Radial force measurement of endovascular stents: Influence of stent design and diameter. *Vascular*, 24(2):171–176, 2016.

[184] W.L. Gore & Associates, Inc. *Mechanical Properties of Nitinol Stents and Stentgrafts: Comparison of 6mm Diameter Devices*, 2011.

[185] Teßarek J. *BeGraft peripheral: Stent design and technical aspects.* Presented at the Leipzig Interventional Course. Leipzig, Germany, 2016.

[186] Maleckis K, Deegan P, Poulson W, et al. Comparison of femoropopliteal artery stents under axial and radial compression, axial tension, bending, and torsion deformations. *Journal of the Mechanical Behavior of Biomedical Materials*, 75 (Supplement C):160–168, 2017.

[187] Verhoeven E and Katsargyris A. *First clinical experience with a new balloon-expandable stent graft: Potential advantages for side branch reconstruction during EVAR of complex pathologies.* Presented at the Leipzig Interventional Course. Leipzig, Germany, 2018.

[188] Duerig T and Wholey M. A comparison of balloon- and self-expanding stents. *Minimally Invasive Therapy & Allied Technologies*, 11(4):173–178, 2002.

[189] Niepoth WW, de Bruin JL, Lely RL, et al. In vitro feasibility of a sac-sealing endoprosthesis in a double chimney graft configuration for juxtarenal aneurysm. *Journal of Endovascular Therapy*, 21(4):529–537, 2014.

[190] Boersen JT, Donselaar EJ, Jebbink EG, et al. Benchtop quantification of gutter formation and compression of chimney stent grafts in relation to renal flow in chimney endovascular aneurysm repair and endovascular aneurysm sealing configurations. *Journal of Vascular Surgery*, 66(5):1565–1573, 2017.

[191] Shahverdyan R, Gawenda M, and Brunkwall J. Triple-barrel graft as a novel strategy to preserve supra-aortic branches in arch-tevar procedures: Clinical study and systematic review. *European Journal of Vascular and Endovascular Surgery*, 45(1):28–35, 2013.

[192] Shahverdyan R, Mylonas S, Gawenda M, and Brunkwall J. Single-center mid-term experience with chimney-graft technique for the preservation of flow to the supra-aortic branches. *Vascular*, 26(2):175–182, 2018.

[193] Canaud L, Ozdemir BA, Patterson BO, et al. Retrograde aortic dissection after thoracic endovascular aortic repair. *Annals of Surgery*, 260(2):389–395, 2014.

[194] Synopsys Inc. *Simpleware ScanIP Reference Guide vN-2018.03*, 2017.

[195] Strauch JT, Spielvogel D, Lauten A, et al. Technical advances in total aortic arch replacement. *The Annals of Thoracic Surgery*, 77(2):581–590, 2004.

[196] Walsh SR, Tang TY, Sadat U, et al. Endovascular stenting versus open surgery for thoracic aortic disease: Systematic review and meta-analysis of perioperative results. *Journal of Vascular Surgery*, 47(5):1094–1098, 2008.

[197] Ouzounian M, LeMaire SA, and Coselli JS. Open aortic arch repair: State-of-the-art and future perspectives. *Seminars in Thoracic and Cardiovascular Surgery*, 25 (2):107–115, 2013.

[198] Glorion M, Coscas R, McWilliams RG, et al. A comprehensive review of in situ fenestration of aortic endografts. *European Journal of Vascular and Endovascular Surgery*, 52(6):787–800, 2016.

[199] van Bakel TM, de Beaufort HW, Trimarchi S, et al. Status of branched endovascular aortic arch repair. *Annals of Cardiothoracic Surgery*, 7(3):406–413, 2018.

[200] Franklin RN, Silveira PG, Timi JRR, et al. Tomographic measurement of gutters and analysis of the conformability of stent grafts in the octopus technique for endovascular thoracoabdominal aneurysm repair. *Annals of vascular surgery*, 33: 202–209, 2016.

[201] Groot Jebbink E, Grimme FAB, Goverde PCJM, et al. Geometrical consequences of kissing stents and the covered endovascular reconstruction of the aortic bifurcation configuration in an invitro model for endovascular reconstruction of aortic bifurcation. *Journal of Vascular Surgery*, 61(5):1306–1311, 2015.

[202] Ishimaru S. Endografting of the aortic arch. *Journal of Endovascular Therapy*, 11 (Suppl II):II–62–II–71, 2004.

[203] Redheuil A, Yu WC, Wu CO, et al. Reduced ascending aortic strain and distensibility. *Hypertension*, 55(2):319–326, 2010.

[204] Bell V, Mitchell WA, Sigurosson S, et al. Longitudinal and circumferential strain of the proximal aorta. *Journal of the American Heart Association*, 3(6):e001536, 2014.

[205] Morrison TM, Choi G, Zarins CK, and Taylor CA. Circumferential and longitudinal cyclic strain of the human thoracic aorta: Age-related changes. *Journal of Vascular Surgery*, 49(4):1029–1036, 2009.

[206] Marrocco-Trischitta MM, de Beaufort HW, Secchi F, et al. A geometric reappraisal of proximal landing zones for thoracic endovascular aortic repair according to aortic arch types. *Journal of Vascular Surgery*, 65(6):1584–1590, 2017.

[207] Chaikof EL, Fillinger MF, Matsumura JS, et al. Identifying and grading factors that modify the outcome of endovascular aortic aneurysm repair. *Journal of Vascular Surgery*, 35(5):1061–1066, 2002.

[208] Finn R and Morris L. An experimental assessment of catheter trackability forces with tortuosity parameters along patient-specific coronary phantoms. *Proceedings of the Institution of Mechanical Engineers, Part H: Journal of Engineering in Medicine*, 230(2):153–165, 2016.

[209] Johnson HJ, McCormick MM, Ibáñez L, and the Insight Software Consortium. *The ITK software guide*, 4th edition, 2018.

[210] Wang T, Shu C, ming Li Q, et al. First experience with the double chimney technique in the treatment of aortic arch diseases. *Journal of Vascular Surgery*, 66(4):1018 – 1027, 2017.

[211] Doyle BJ, Corbett TJ, Cloonan AJ, et al. Experimental modelling of aortic aneurysms: Novel applications of silicone rubbers. *Medical Engineering & Physics*, 31(8):1002–1012, 2009.

[212] Knowles M, Pellisar T, Murphy EH, et al. In vitro analysis of type II endoleaks and aneurysm sac pressurization on longitudinal stent-graft displacement. *Journal of Endovascular Therapy*, 18(4):601–606, 2011.

[213] Biglino G, Verschueren P, Zegels R, Taylor AM, and Schievano S. Rapid prototyping compliant arterial phantoms for in-vitro studies and device testing. *Journal of Cardiovascular Magnetic Resonance*, 15, 2013.

[214] Marconi S, Lanzarone E, van Bogerijen GHW, et al. A compliant aortic model for in vitro simulations: Design and manufacturing process. *Medical Engineering & Physics*, 59:21–29, 2018.

[215] Madhwal S, Rajagopal V, Bhatt D, et al. Predictors of difficult carotid stenting as determined by aortic arch angiography. *Journal of Invasive Cardiology*, 20(5): 200–204, 2008.

[216] Suh GY, Beygui RE, Fleischmann D, and Cheng CP. Aortic arch vessel geometries and deformations in patients with thoracic aortic aneurysms and dissections. *Journal of Vascular and Interventional Radiology*, 25(12):1903–1911, 2014.

[217] Hirotsu K, Suh GY, Lee JT, et al. Changes in geometry and cardiac deformation of the thoracic aorta after thoracic endovascular aortic repair. *Annals of Vascular Surgery*, 46:83–89, 2018.

[218] Kolvenbach RR. *Challenging EVAR's: Long term optimization with Onyx.* Presented at the Leipzig Interventional Course. Leipzig, Germany, 2018.

[219] Baillargeon B, Rebelo N, Fox DD, Taylor RL, and Kuhl E. The Living Heart Project: A robust and integrative simulator for human heart function. *European Journal of Mechanics - A/Solids*, 48:38–47, 2014.

[220] Baillargeon B, Costa I, Leach JR, et al. Human cardiac function simulator for the optimal design of a novel annuloplasty ring with a sub-valvular element for correction of ischemic mitral regurgitation. *Cardiovascular Engineering and Technology*, 6(2):105–116, 2015.

[221] Sack KL, Baillargeon B, Acevedo-Bolton G, et al. Partial LVAD restores ventricular outputs and normalizes LV but not RV stress distributions in the acutely failing heart in silico. *The International Journal of Artificial Organs*, 39(8):421–430, 2016.

[222] Genet M, Lee LC, Baillargeon B, Guccione JM, and Kuhl E. Modeling pathologies of diastolic and systolic heart failure. *Annals of Biomedical Engineering*, 44(1): 112–127, 2016.

[223] Peirlinck M, Sack KL, De Backer P, et al. Kinematic boundary conditions substantially impact in silico ventricular function. *International journal for numerical methods in biomedical engineering*, page e3151, 2018.

[224] Holzapfel GA and Ogden RW. Constitutive modelling of passive myocardium: a structurally based framework for material characterization. *Philosophical Transactions of the Royal Society of London A: Mathematical, Physical and Engineering Sciences*, 367(1902):3445–3475, 2009.

[225] Walker JC, Ratcliffe MB, Zhang P, et al. MRI-based finite-element analysis of left ventricular aneurysm. *American Journal of Physiology-Heart and Circulatory Physiology*, 289(2):H692–H700, 2005.

[226] Dassault Systèmes Simulia Corp. *The Active Cardiac Material Model: Living Heart Human Model Verification Suite.* Providence, RI, USA, 2016.

[227] Costabal FS, Hurtado DE, and Kuhl E. Generating Purkinje networks in the human heart. *Journal of biomechanics*, 49(12):2455–2465, 2016.

[228] Marom G, D'Souza K, Ghosh RP, et al. Electro-mechanical modeling of transcatheter aortic valve deployment in the Simulia Living Heart Human Model. In *NAFEMS European Conference*, Copenhagen, Denmark, 2016.

[229] Conti J and Strope E. Radial compliance of natural and mock arteries: how this property defines the cyclic loading of deployed vascular stents. *Biomedical Sciences Instrumentation*, 38:163–172, 2002.

[230] Beller CJ, Labrosse MR, Thubrikar MJ, and Robicsek F. Role of aortic root motion in the pathogenesis of aortic dissection. *Circulation*, 109(6):763–769, 2004.

[231] Garcí-Herrera CM and Celentano DJ. Modelling and numerical simulation of the human aortic arch under in vivo conditions. *Biomechanics and Modeling in Mechanobiology*, 12(6):1143–1154, 2013.

[232] Pasta S, Rinaudo A, Luca A, et al. Difference in hemodynamic and wall stress of ascending thoracic aortic aneurysms with bicuspid and tricuspid aortic valve. *Journal of biomechanics*, 46(10):1729–1738, 2013.

[233] Mousavi SJ and Avril S. Patient-specific stress analyses in the ascending thoracic aorta using a finite-element implementation of the constrained mixture theory. *Biomechanics and Modeling in Mechanobiology*, 16(5):1765–1777, 2017.

[234] Campobasso R, Condemi F, Viallon M, et al. Evaluation of peak wall stress in an ascending thoracic aortic aneurysm using FSI simulations: effects of aortic stiffness and peripheral resistance. *Cardiovascular Engineering and Technology*, 9 (4):707–722, 2018.

[235] Sinha S. Modeling stents. In *Simulia Best Practices*. Shashwat Sinha, Dassault Systèmes Simulia Corp., 2018.